

**Experimental Investigations of Drying Droplets  
Containing Microparticles and of Mixtures of  
Poly(Ethylene Oxide)/Microparticles**

Yohana Msambwa

A thesis submitted in partial fulfillment of the requirements of Nottingham Trent  
University for the degree of Doctor of Philosophy

May 2015

This work is the intellectual property of the author, and may also be owned by the research sponsor(s) and/or Nottingham Trent University. You may copy up to 5% of this work for private study, or personal, non-commercial research. Any re-use of the information contained within this document should be fully referenced, quoting the author, title, university, degree level and pagination. Queries or requests for any other use, or if a more substantial copy is required, should be directed in the first instance to the author.

## Abstract

Ring-stains are seen when droplets of liquid containing particles are left to dry on a surface: a pinned contact line leads to outward radial flow, which is enhanced by the diverging evaporative flux at the contact line. As a result, suspended particles in the drops are transported to the edge of the droplet, and deposited in a circular stain. In the first section of this study, we investigated how the width and height of ring in water droplets containing suspensions of polystyrene microparticles with diameters  $\leq 0.5\mu\text{m}$  vary with experimentally controlled parameters, including particle size, contact angle, concentration, evaporation rate and orientation of the droplets. Our studies found, for the first time, that the drying rate plays an important role in determining the shape of the final deposit which may contribute to a better understanding of a coffee ring effect. At low drying rates, nearly all the particles are deposited in the ring and the width and height of the ring follow a power law. However there is a significant deposition of particles in the center of the droplets at the fastest drying rates.

In the second section, we investigated the drying dynamics of the droplets using optical microscopy and optical coherence tomography both at low and high drying rates. The results indicate that, as expected, the outward capillary flow to the edge dominates for  $0.5\mu\text{m}$  and  $2\mu\text{m}$  particles at low drying rates. However, at the highest drying rates, particle flow is reversed towards the center for  $0.5\mu\text{m}$  and  $2\mu\text{m}$  particles and is attributed to Marangoni flow driven by a high temperature gradient between the edge and apex of the drop. For  $5\mu\text{m}$  at low drying rates, sedimentation is found to be more significant than outward flow and at higher drying rates the outward flow dominates over sedimentation.

The final section involved mixing polystyrene microparticles with Poly(ethylene oxide) (PEO) polymer. Drying droplets of aqueous solutions of PEO is known to form either the familiar "coffee-ring" or a tall "central pillar" depending on the

concentration of the polymer, its molecular weight, humidity and drying rate. The objective of this study was to investigate the effect of particle sizes and concentration on drying of water droplets containing a water/PEO solution mixture. Results show that the four stages in the pillar forming of PEO drying process is disrupted, and even completely destroyed, with the additional of polystyrene microparticles. The extent at which the pillars are destroyed depends on both the concentration and sizes of the polystyrene microparticles as well as on PEO concentration in the mixture. A range of deposit was observed, as a result, including the standard particle ring stain, polymer pillars and puddles. We present a novel and versatile technique, using the skewness of the height profile, to distinguish quantitatively between the various deposits. We show that this simple parameter seems to illustrate the observed deposit types, with a positive skewness for pillars, close to zero for flat puddle deposits and negative skewness for ring stains. The skewness values have the potential to be useful for characterizing deposits in a wide variety of system

## **Declaration**

The experiments described in this thesis were carried out by myself and, where indicated, in collaboration with colleagues. The data analysis and interpretation is my own work. This thesis has been written entirely by myself.

Yohana Msambwa

## **Acknowledgements**

I would like to thank my supervisors Dr. Fouzia Ouali, Dr. David Fairhurst and Prof. Carl Brown for their unrelenting support and guidance throughout this work. I would like to thank Dr. Haida Liang for helping me with appropriate suggestions regarding optical coherence tomography. I would also like to thank my independent assessor Dr. Michael Newton for his valuable inputs and comments on my research work. I wish to thank the technicians, Dave Parker and Stephen Elliot for their help in several occasions and Gordon Arnott for his expertise in scanning electron microscope. I would like to thank all my fellow laboratory mates in particular Naresh Sampara, Kyle Baldwin and Anthony Turner for their support. I greatly appreciate the unconditional love and support from my mother Frida Merere and other family members. I appreciate the financial support of Dar Es Salaam University College of Education, a constituent college of the University of Dar Es Salaam.

# Table of Contents

Abstract .....	iii
Declaration .....	v
Acknowledgements .....	vi
Table of Contents .....	vii
List of Figures .....	xiii
List of Tables.....	xxvi
Notation .....	xxvii
1. Introduction.....	1
1.1 Motivation .....	2
1.2 Liquid-solid interface .....	3
1.2.1 Surface Tension .....	3
1.2.2 Wetting.....	4
1.2.3 Young’s Equation.....	5
1.3 Droplet Evaporation of Pure Liquids .....	8
1.3.1 Theory of Droplet Evaporation .....	8
1.3.2 Modes of Droplet Evaporation. ....	12
1.3.3 Temperature.....	13
1.3.4 Marangoni Flow.....	16
1.3.5 Thermal Conductivity of the Substrate. ....	18
1.3.6 Air Pressure.....	20

1.4 Evaporation of Droplets Containing Particles .....	20
1.4.1 Coffee Ring Effect.....	21
1.4.2 Particle Ring Growth .....	23
1.4.3 Relative Humidity and Ring Stain Formation .....	28
1.4.4 Forces between the particles in solution and the substrate .....	30
1.5 Evaporation of Droplets Containing Polymers.....	34
1.5.1 What is a polymer?.....	34
1.5.2 Behaviour of PEO solutions .....	37
1.5.3 PEO droplets.....	39
1.5.4 PEO and particle droplets .....	42
1.6 The Present Work.....	43
2. Experimental Techniques and Methods .....	46
2.1 Introduction .....	47
2.2 Sample Preparation .....	48
2.2.1 PS Microparticle Suspensions .....	48
2.2.2 PS-PEO Solution.....	48
2.2.3 Substrates.....	49
2.2.4 pH Measurement.....	51
2.2.5 Zeta and Surface Potential Measurement.....	52
2.3 Evaporation of Sessile Droplets.....	52
2.3.1 Experimental Set-up.....	52
2.3.2 Experimental Procedures.....	54
2.3.3 Analysis of the Final Deposits.....	55

2.3.3.1	Surface Morphology Characterization .....	55
2.3.3.2	Surface Depth Profile Characterization .....	56
2.3.3.3	Image J Profile Characterization .....	60
2.4	Kinematics of Droplets Drying.....	60
2.4.1	Optical Coherence Tomography (OCT) .....	61
2.4.1.1	Introduction.....	61
2.4.1.2	Experimental Setup and Measurement .....	63
2.4.1.3	Particle Tracking.....	67
2.4.2	Optical Microscope Imaging Technique.....	67
2.4.3	Measurements of Temperature Variations Across the Drops .....	68
2.5	Evaporation of PS-PEO Droplets. ....	69
2.5.1	Experimental Procedures.....	69
2.5.2	Analysis of Final Deposit.....	70
3.	How Robust is the ring Stain .....	74
3.1	Introduction .....	75
3.2	Experimental Results and Discussions.....	75
3.2.1	Images of the Final Deposits.....	75
3.2.1.1	Effect of Droplet Orientation .....	76
3.2.1.2	Effect of Contact Angle.....	81
3.2.1.3	Reproducibility .....	83
3.2.2	Analysis of the Images/Patterns .....	85
3.2.3	The Scaling Laws.....	89
3.2.3.1	The Effect of Contact Angle.....	89

3.2.3.2	The Effect of Particle sizes and droplet orientation .....	94
3.2.3.3	The Effect of Evaporation Rate .....	99
3.3	Conclusions .....	106
4.	Kinematics of Droplet Drying.....	108
4.1	Introduction .....	109
4.2	Experimental Methods .....	109
4.2.1	Material Preparation .....	109
4.2.2	Kinematics of Droplets Drying by SDOCT.....	111
4.2.3	Kinematics of Droplets Drying by Optical Imaging Microscope .....	116
4.3	Experimental Results and Discussions.....	118
4.3.1:	0.5 $\mu$ m PS Microparticles.....	119
4.3.1.1	Low Drying rate .....	119
4.3.2.2	High Drying rate.....	121
4.3.2:	2 $\mu$ m PS Microparticles .....	126
4.3.2.1	Low Drying rate .....	126
4.3.2.2	High Drying rate.....	129
4.3.3:	5 $\mu$ m PS Microparticles .....	135
4.3.3.1	Low Drying rate .....	135
4.3.3.2	High Drying rate.....	138
4.3	Conclusions .....	142
5.	PS-PEO Droplet Drying .....	145
5.1	Introduction.....	146
5.2	Experimental Results and Discussions .....	147

5.2.1	Images of the Final Deposits.....	148
5.2.1.1	: 0.5 $\mu$ m PS Particles in PEO Solution.....	148
5.2.1.2	: 5 $\mu$ m PS Particles in PEO solution.....	153
5.2.2	Surface Profiles .....	156
5.2.2.1	: 0.5 $\mu$ m PS Particles in PEO Solution.....	157
5.2.2.2	: 5 $\mu$ m PS Particles in PEO Solution .....	159
5.2.3	Effect of PS-PEO concentration and Particle Sizes .....	160
5.3	Conclusions .....	165
6.	Conclusions .....	166
6.1	How Robust is the Ring Stain .....	166
6.1.1	Evaporation Rate.....	166
6.1.2	Contact Angle .....	167
6.1.3	Droplet Orientation and Particle Sizes .....	167
6.2	Kinematics of Droplet Drying.....	168
6.2.1:	0.5 $\mu$ m PS Microparticles .....	168
6.2.2:	2 $\mu$ m PS Microparticles.....	169
6.2.3:	5 $\mu$ m PS Microparticles.....	169
6.3	PS-PEO Droplet Drying .....	170
6.3.1	Effect of PS Particle Sizes .....	170
6.3.2	Effect of PS-PEO Initial Concentration .....	170
6.4	Future Work .....	171
6.4.1	How Robust is the Ring Stain .....	171
6.4.2	Kinematics of Droplet Drying .....	172

6.4.3 PS-PEO Droplet Drying .....	173
Bibliography.....	174
Appendix A: Derivation of the Young Equation.....	193
Appendix B: Radial profile plotting using Image J.....	194
Appendix C: Derivation of ring stain power law predictions .....	196
Appendix D: Determination of coefficient of skewness .....	199
Publications .....	201

## List of Figures

Figure 1.1: The coffee stain affect formed from a spilled and dried coffee droplet on a wooden table. ....	2
Figure 1.2: Schematic illustration of intermolecular forces between molecules in a liquid responsible for surface tension (arrows show attractive forces between the molecules). ....	3
Figure 1.3: Schematic illustration of the wire frame for increasing the surface area of a soap film. ....	4
Figure 1.4: Schematic illustration of a hydrophobic and hydrophilic surface.....	5
Figure 1.5: Schematic illustration of a contact angle and the mechanical equilibrium of interfacial surface tensions of a sessile drop resting on a solid surface .....	5
Figure 1.6: Graphical representation of contact angle hysteresis in terms of the free energy and cosine of apparent contact angle for sessile droplet [36]. ....	7
Figure 1.7: Droplet with the shape of a spherical cap rests on a flat surface. The local height and evaporation flux are $h(r, t)$ and $J(r, t)$ respectively. ....	9
Figure 1.8: The formation of stick-slip in an evaporating droplet with (a) the droplet radius is constant with a pinned triple line while both contact angle and droplet height decreases with time (b) the triple depinns leading to an increased contact angle and droplet height while the radius decreases [56]. ....	13
Figure 1.9: Local evaporation flux and temperature of methanol droplet as a function of location on droplet radius on Al/PTFE substrate [60, 61]. ....	15
Figure 1.10: Internal convective flow in the presence of Marangoni flow. As the droplet evaporates the Marangoni flow decreases and the radial flow dominates [75]. ....	18
Figure 1.11: Dependence of the evaporation flux of droplet of water ( $\theta_0 = 78^\circ$ ) on various substrate thermal conductivity ( $k_s$ ) [48]. ....	19

Figure 1.12: In (a) the absence of microparticles leads the droplet shrink as the it dries and (b) presence of microparticle enables pinning at the contact line [4].  
..... 21

Figure 1.13: (a) Densely packed ring at  $c_0 = 3\%$  (and (b) wispy ring filled with voids at  $c_0 = 0.003\%$  of gold nanoparticles [94]. ..... 24

Figure 1.14: (a) Deposition patterns, (b1) square packed stain, (b2) hexagonal packed stain, (b3) disordered packed stain and (c) Voronoi cells as a function of the distance from the contact line [95]. ..... 25

Figure 1.15: (a) Final deposit left after evaporation of 0.125% SiO<sub>2</sub> particles at 750 mbar showing stick-slip patterns and (b) the change in contact angle and radius of the droplet with time [96]. ..... 26

Figure 1.16: Deposits patterns dried from 0% of ethanol, 100% of water (left) and with binary mixture with 50% of ethanol and 50% of water (right) [97]. ..... 27

Figure 1.17: Relationship between final deposit diameter and the relative humidity [104]. ..... 29

Figure 1.18: Final blood deposits patterns as a function of relative humidity [105]29

Figure 1.19: Schematic interaction energy versus distance profiles of the DLVO interaction. The actual magnitude of the energy  $W$  is proportional to the particle size or interaction area [107]. ..... 33

Figure 1.20: Deposit patterns from a suspension of 0.005% volume fraction of negatively charged PS microparticles and surfactant on (a) negatively charged glass substrate and (b) a positively charged glass substrate [115]. ..... 34

Figure 1.21: Examples of polymer molecule with their monomers as well as the repeating units. .... 35

Figure 1.22: Spherulites showing lamella chain folded platelets [120]. ..... 37

Figure 1.23: Drying stages of PEO solutions and phase separation. Thin lines indicate liquid surfaces, thick regions represent solid deposits. Progress within

each stage is from solid black to dashed dark grey to dotted light grey. Image from [136].....	40
Figure 1.24: The relationship between Péclet number, $P_e$ and the initial concentration, $c_1$ normalized to overlap concentration, $c^*$ . Puddles and pillars are formed with a line roughly between them showing the transition region [137]. .....	41
Figure 1.25: Final deposits from drying polystyrene particles, glass bead in water and when are mixed with 200K and 900K of PEO [140]. .....	43
Figure 1.26: A radial profile of a deposit of a dried droplet showing the ring width, $w_r$ and it height, $h_r$ . .....	44
Figure 1.27: (a) The tall central deposit called pillar forms from drying $c_1 = 10\%$ of PEO and (b) Puddle like deposits when $c_1 = 2\%$ of PEO is dried at atmospheric conditions.....	45
Figure 2.1: Schematic presentation of drop shape analysis system experimental setup. ....	50
Figure 2.2: Schematic presentation of evaporation of sessile droplet experimental setup in a low pressure chamber. ....	53
Figure 2.3: The image shows a surface morphology of $0.5\mu\text{m}$ polystyrene microparticles with $c_0 = 0.25\%$ . .....	56
Figure 2.4: Programmable Dektak 6M Stylus Profiler used to study the surface profile of final deposits after drying droplets. ....	58
Figure 2.5: Final deposits of 1% polystyrene microparticles suspension dried at 0.6 n/s in upright orientation captured with CCD camera reflection mode.....	59
Figure 2.6: Sample of Dektak 6M surface profiles used to extract the ring height, width and diameter.....	59
Figure 2.7: Radial profile plot versus radius for $0.5\mu\text{m}$ particles dried at 0.6 nL/s in upright orientation.....	60

Figure 2.8: (A) Spectral domain Spectral domain optical coherence tomography (SDOCT) system comprising of broadband laser source such superluminescent diode (SLD), single mode fiber (SMF), diffraction grating (G), personal computer (PC), charged-coupled device (CCD) and P represent intensity of power recorded by a photodetector. Also B is the interference signal, C is the rescaled signal and D is the sample depth profile or A-scan [147]..... 62

Figure 2.9: The schematic diagram a part (scanning probe/ Michelson interferometer) of commercial OCT combined with pressure chamber ..... 64

Figure 2.10: Experimental set-up to study the kinematics of the droplets drying employing SDOCT and low pressure chamber..... 65

Figure 2.11: A raw 2D image of a droplet containing 5 $\mu$ m polystyrene microparticles constructed using using SDOCT where  $h_0$  and  $h'$  are real and optical droplet heights respectively. .... 66

Figure 2.12: The final stylus deposit profile containing  $c_1 = 1.6\%$  (PEO) and  $c_0 = 4\%$  (0.5 $\mu$ m PS particles). The left hand side (LHS) peak and right hand side (RHS) peak are well demarcated by an imaginary line of symmetry. The imaginary line of symmetry divides a central peak into two halves of left hand side (LHS) peak and right hand side (RHS) peak. .... 71

Figure 2.13: The final stylus deposit profile containing  $c_1 = 9.6\%$  (PEO) and  $c_0 = 4\%$  (5 $\mu$ m PS particles). .... 72

Figure 2.14: The final stylus deposit profile (folded) containing  $c_1 = 1.6\%$  (PEO) and  $c_0 = 4\%$  (0.5 $\mu$ m PS particles). .... 72

Figure 2.15: The final stylus deposit profile containing  $c_1 = 9.6\%$  (PEO) and  $c_0 = 4\%$  (5 $\mu$ m PS particles). .... 73

Figure 3.1: The final images as a function of initial concentration of polystyrene microparticles and particle sizes dried at  $\sim 0.6$ nl/s with substrate for  $\theta = 35^\circ$  76

Figure 3.2: The final images as a function of initial concentration of polystyrene microparticles and particle sizes dried at $\sim 0.6\text{nL/s}$ with substrate for $\theta = 35^\circ$	78
Figure 3.3: The final images as a function of initial concentration of polystyrene microparticles and particle sizes dried at $>5\text{nL/s}$ with substrate of contact angle $35^\circ$ in upright orientation. ....	79
Figure 3.4: The final images as a function of initial concentration of polystyrene microparticles and particle sizes dried at $>5\text{nL/s}$ .....	81
Figure 3.5: Final deposit left after drying droplets of $0.2\mu\text{m}$ PS particles ( $c_0 = 1\%$ ) at ambient conditions with substrates of contact angle (a) $\theta = 35^\circ$ ( $0.4\text{ nL/s}$ ) (b) $\theta = 18^\circ$ ( $2.6\text{ nL/s}$ ) and (c) $\theta = 5^\circ$ ( $3.4\text{ nL/s}$ ).....	82
Figure 3.6: The five final images showing their reproducibility when dried at $\sim 0.6\text{nL/s}$ with substrate of contact angle $35^\circ$ in upright orientation. ....	84
Figure 3.7: The five final images showing their reproducibility when dried at $\sim 8\text{nL/s}$ with substrate of contact angle $35^\circ$ in upright orientation. ....	85
Figure 3.8: Comparison of deposit profiles showing the height of the deposits in $\mu\text{m}$ using the stylus profilometer (solid black lines) and normalised integrated intensity (in arbitrary units) obtained from ImageJ (red dashed lines). The scale of the latter was adjusted for easy comparison with the profilometry data. The two images are shown underneath. Both droplets contained $0.5\mu\text{m}$ polystyrene particles at initial concentration, $c_0 = 1\%$ at two different drying rates, $0.6\text{nL/s}$ (left) and $5.3\text{nL/s}$ (right) .....	86
Figure 3.9: Deposit profiles obtained with stylus profilimeter of $5\mu\text{m}$ particles dried at $\sim 0.6\text{nL/s}$ . ....	88
Figure 3.10: Deposit profiles of $5\mu\text{m}$ particles dried at $>5\text{nL/s}$ . ....	89
Figure 3.11: The effect of contact angle on ring height $h_r$ for varying concentration, $c_0$ on three different substrates with contact angle values $\theta=5^\circ$ , $18^\circ$ and $35^\circ$ .	

The lines are linear best fit,  $\log(h_r) = n \log(c_o) + \log Q_1$  indicating a power law with an exponent given by the slope of the fits with  $n(5^\circ) = 0.55 \pm 0.05$ ,  $n(18^\circ) = 0.43 \pm 0.03$ , and  $n(35^\circ) = 0.55 \pm 0.03$ ..... 91

Figure 3.12: The effect of contact angle on ring width  $w_r$  for varying concentration,  $c_o$  on three different substrates with contact angle values  $\theta = 5^\circ$ ,  $18^\circ$  and  $35^\circ$ .

The straight lines are best fits indicating a power law dependence with an exponent given by the slope  $m(5^\circ) = 0.34 \pm 0.03$ ,  $m(18^\circ) = 0.39 \pm 0.06$ , and  $m(35^\circ) = 0.31 \pm 0.02$ . For  $\theta = 35^\circ$ . The three data sets coincide and, therefore, for clarity they are offset from each other by multiplying  $\theta = 35^\circ$  data by 0.6 and  $\theta = 18^\circ$  data set by 1.4. .... 92

Figure 3.13: The width of the ring normalized by the droplet radius for varying concentration,  $c_o$  on three different substrates with contact angle values  $\theta = 5^\circ$ ,  $18^\circ$  and  $35^\circ$ .

The straight lines are best fits indicating a power law dependence with an exponent given by the slope  $s(5^\circ) = 0.34 \pm 0.03$ ,  $s(18^\circ) = 0.32 \pm 0.02$ , and  $s(35^\circ) = 0.29 \pm 0.02$ ..... 93

Figure 3.14: The effect of particle size on ring height for varying concentration,  $c_o$  for upright orientation on three PS microparticles sizes  $0.1\mu\text{m}$ ,  $0.2\mu\text{m}$  and  $0.5\mu\text{m}$ .

The straight lines are best fits indicating a power law dependence with an exponent given by the slope  $n(0.1\mu\text{m}) = 0.49 \pm 0.09$ ,  $n(0.2\mu\text{m}) = 0.46 \pm 0.07$ , and  $n(0.5\mu\text{m}) = 0.51 \pm 0.07$ . The three data sets coincide and, therefore, for clarity they are offset from each other by multiplying  $0.2\mu\text{m}$  data set by 1.4 and  $0.1\mu\text{m}$  data set by 0.6. .... 95

Figure 3.15: The effect of particle size on ring width for varying concentration,  $c_o$  for upright orientation on three PS microparticles sizes  $0.1\mu\text{m}$ ,  $0.2\mu\text{m}$  and  $0.5\mu\text{m}$ .

0.5 $\mu\text{m}$ . The straight lines are best fits indicating a power law dependence with an exponent given by the slope  $m(0.1\mu\text{m}) = 0.35 \pm 0.09$  ,  $m(0.2\mu\text{m}) = 0.31 \pm 0.10$  , and  $m(0.5\mu\text{m}) = 0.34 \pm 0.02$  . The three data sets coincide and, therefore, for clarity they are offset from each other by multiplying 0.5 $\mu\text{m}$  data set by 1.4 and 0.1 $\mu\text{m}$  data set by 0.6. .... 96

Figure 3.16: The effect of particle size on ring height for varying concentration  $c_0$  for upside down orientation on three PS microparticles sizes 0.1 $\mu\text{m}$  , 0.2 $\mu\text{m}$  and 0.5 $\mu\text{m}$  . The straight lines are best fits indicating a power law dependence with an exponent given by the slope  $n(0.1\mu\text{m}) = 0.47 \pm 0.09$  ,  $n(0.2\mu\text{m}) = 0.51 \pm 0.07$  , and  $n(0.5\mu\text{m}) = 0.53 \pm 0.06$  . The 0.2 $\mu\text{m}$  data set multiplied by 1.4 and 0.1 $\mu\text{m}$  by 0.6). .... 97

Figure 3.17: The effect of particle size on ring width for varying concentration,  $c_0$  for upside down orientation on three PS microparticles sizes 0.1 $\mu\text{m}$  , 0.2 $\mu\text{m}$  and 0.5 $\mu\text{m}$  . The straight lines are best fits indicating a power law dependence with an exponent given by the slope  $m(0.1\mu\text{m}) = 0.33 \pm 0.04$  ,  $m(0.2\mu\text{m}) = 0.31 \pm 0.05$  , and  $m(0.5\mu\text{m}) = 0.32 \pm 0.03$  . The 0.5 $\mu\text{m}$  data set was multiplied by 1.4 and 0.1 $\mu\text{m}$  data set by 0.6 for clarity. .... 98

Figure 3.18: Data points show the fitted values for the power law exponents describing how the ring width ( $m$  , black squares), ring height ( $n$  , red circles) and initial droplet radius ( $p$  , blue triangles) vary with drying rate. Also shown is the sum of all three exponents  $m+n+p$  . Exponents were determined for a range of PS microparticle sizes, initial contact angles, and droplet orientations. .... 100

Figure 3.19: Scanning electron microscope of deposit left at the interior of the ring from drying (a) 0.25% of 0.5 $\mu\text{m}$  of PS microparticles at 0.6nL/s and (b) 2% of

0.5 $\mu\text{m}$ of PS microparticles at 0.6nL/s. The image in (b) was obtained at higher magnification compared to (a). .....	101
Figure 3.20: Percentage of the deposit in the ring from drying 2% of 0.5 $\mu\text{m}$ PS particles in upright orientation using data from surface stylus profiler. ....	102
Figure 3.21: Percentage of the deposit in the ring as a function of initial concentration $c_0$ for 0.5 $\mu\text{m}$ PS particles in upright orientation (atmospheric conditions).....	103
Figure 3.22: Ring profile data for droplets containing 500 nm particles drying at a pressure of 800 mbar for a range of initial concentrations. Radius and height coordinates are rescaled with concentration using exponents $g = 0.42$ and $n = 0.55$ respectively. The outside of the droplet is in the positive $r^*$ direction. ....	105
Figure 3.23: Scanning electron microscope section of a ring with 0.25% of 0.5 $\mu\text{m}$ PS microparticles with (a) inner most ring and (b) outer most ring. ....	106
Figure 4.1: Schematic illustration of a PS microparticle movement from position 1 to 2 through an instantaneous displacement $\Delta\vec{d}$ .....	112
Figure 4.2: Determination of instantaneous displacements $\Delta x = x_2 - x_1$ and $\Delta y = y_2 - y_1$ of the same PS microparticle moving in 13 frames between coordinates $(x_1, y_1)$ in (a) and $(x_2, y_2)$ in (b). The short white arrow shows the direction of movement of a particle.....	112
Figure 4.3: Schematic illustration of the effect fast descending air-liquid interface on the position of the particle. A particle from point 1 after time $\Delta t$ is located at position 2 for fast descending interface and position 3 when the interface velocity is smaller than the particle velocity. ....	113
Figure 4.4: (a) A PS microparticle at the air-liquid droplet interface with coordinate $(x_1, y_1)$ from contact line of coordinate $(x_0, y_0)$ (b) Instantaneous	

displacement of the same particle in part (a) for 23 frames at  $\sim 2.0$  fps between coordinate  $(x_1, y_1)$  and  $(x_n, y_n)$  with respect contact line (the short white arrow show the direction of the particle) as the air-liquid interface moves. ....114

Figure 4.5: Illustration of particle motion (a) inward velocity (b) outward velocity and (c) vertical velocity. ....116

Figure 4.6: (a) The coordinates  $(x_1, y_1)$  of a  $5\mu\text{m}$  PS particles at higher drying rate at time  $t$  (b) After 21 frames the same particles has moved (as shown with a short white arrow) to a new coordinate  $(x_2, y_2)$ .The images were captured using a 10X magnification lens. ....117

Figure 4.7: PS microparticles as they move away from the contact line inwards form clusters as shown with an arrow from 25s to 42.5s. Below 25s image particles move individually. There are 100 frames between one image and the next (2.5s). ....118

Figure 4.8: Deposition patterns from drying 0.006% droplet of  $0.5\mu\text{m}$  PS particles drying at  $\sim 0.6\text{nL/s}$  with (a) whole droplet and (b) magnified section of the droplet close to the contact line.....120

Figure 4.9: Outward velocity for 0.006% of  $0.5\mu\text{m}$  PS particles drying at  $\sim 0.6\text{nL/s}$ . ....121

Figure 4.10: Deposition patterns from drying 0.006% droplet of  $0.5\mu\text{m}$  PS particles drying at  $>5\text{nL/s}$  with (a) whole droplet and (b) magnified section of the droplet close to the contact line.....122

Figure 4.11: Inward and outward velocities for 0.006% droplet of  $0.5\mu\text{m}$  individual PS particles drying at  $>5\text{nL/s}$  determined only from optical microscope. ....123

Figure 4.12: Cumulative particle pathline for a droplet drying at  $\sim 0.6\text{nL/s}$  containing  $2\mu\text{m}$  PS particles. ....127

Figure 4.13: Final deposits from drying 0.04% droplet of  $2\mu\text{m}$  PS particles at  $\sim 0.6\text{nL/s}$ . ....128

Figure 4.14: Velocities of 0.04% droplet containing 2 $\mu$ m PS particles drying at  $\sim$ 0.6nL/s. The filled markers are for velocities determined from OCT and hollow markers from optical microscope data. The dotted line serve as a guide for the outward velocity to show that the data for optical and OCT are consistent with each other. ....129

Figure 4.15: Cumulative particle pathline for a droplet drying at >5nL/s containing 0.04% of 2 $\mu$ m PS particles. ....130

Figure 4.16: Comparisons of cumulative particle pathline of droplet containing 0.04% of 2 $\mu$ m PS particles after 37s of droplet life time of  $\sim$ 150s using Image J and PTVlab drying at >5nL/s. ....131

Figure 4.17: A 2 $\mu$ m PS microparticle moving upward along the liquid-gas interface from frame A to D at  $\sim$ 0.2s from one frame to the next. ....131

Figure 4.18: Particle velocity vectors showing inward particle flow (Marangoni flow) near the contact line as determined by PTVlab for 2 $\mu$ m PS particles at higher drying rate.....132

Figure 4.19: Final deposits from drying 0.04% droplet of 2 $\mu$ m PS particles at >5nL/s. ....132

Figure 4.20: Cumulative particle pathline for a 0.04% droplet drying at >5nL/s containing 2 $\mu$ m PS particles using optical microscope data.....133

Figure 4.21: Velocities at high drying rate vertical, inward and outward velocities for 0.04% droplet of 2 $\mu$ m individual PS particles drying at >5L/s. The filled markers are for velocities determined from SDOCT and no fill marker from optical microscope data. The dotted line serve as a guide for the outward velocity to show that the data for optical and OCT are consistent with each other.....134

Figure 4.22: Cumulative Z-projection for 5 $\mu$ m PS particles droplet drying at  $\sim$ 0.6nL/s for the first 363s of the droplet life time of 1578s. ....136

Figure 4.23: Final deposits from drying 0.1% droplet of 5 $\mu$ m PS particles at $\sim$ 0.6nL/s. ....	137
Figure 4.24: Velocities of 0.1% droplet containing 5 $\mu$ m PS particles drying at $\sim$ 0.6nL/s. ....	138
Figure 4.25: Cumulative particle pathline for a droplet drying at >5nL/s containing 0.1% of 5 $\mu$ m PS particles. The dashed lines show the intensity of the trapped particles at the air-liquid interface. ....	139
Figure 4.26: Marangoni flow direction vectors near the contact line as determined by PTVlab for 5 $\mu$ m PS particles at higher drying rate. ....	139
Figure 4.27: Final deposits from drying 0.1% droplet of 5 $\mu$ m PS particles at >5nL/s. ....	140
Figure 4.28: Cumulative particle pathline for a 0.1% droplet drying at >5nL/s containing 2 $\mu$ m PS particles using optical microscope data.....	141
Figure 4.29: Velocities at high drying rate vertical, inward and outward velocities for 0.1% droplet of 2 $\mu$ m individual PS particles drying at $\sim$ 5nL/s. The dotted line serve as a guide for the outward velocity to show that the data for optical and OCT are consistent with each other.....	142
Figure 4.30: The montage of deposition patterns at (i) low drying rate and (ii) high drying rate with (a) and (b) for 0.5 $\mu$ m, (c) and (d) for 2 $\mu$ m, (e) and (f) for 5 $\mu$ m PS particles.....	144
Figure 5.1: Schematic illustration of a deposit from drying PEO polymer solution droplets: (a) Solid conical pillars "Mexican hat", (b) Pancake or disk-like solid "puddle" and (c) dimple in the center of the deposit.....	147
Figure 5.2: Side on image sequences as a 0.4 $\mu$ L droplet dries containing 0.5 $\mu$ m PS particles ( $c_0 = 4\%$ ) and PEO ( $c_1 = 1.6\% - 12\%$ ). ....	148
Figure 5.3: Final images captured with cross polarizer for 0.5 $\mu$ m PS particles of $c_0 = 2\% - 5\%$ mixed with $c_1 \sim 3\% - 12\%$ of PEO.....	149

Figure 5.4: Magnified final deposits of 0.5 $\mu$ m PS particles ( $c_0 = 4\%$ ) with varying PEO concentration captured with optical microscope under reflection mode..150

Figure 5.5: (a) Schematic illustration of the four drying stages of pure PEO for  $c_1 > 3\%$  [136] for comparison with our results in part (b). Thin lines indicate liquid surfaces, thick regions represent solid deposits. Progress within each stage is from solid black to dashed dark grey to dotted light grey. In (b) the schematic illustration show the drying stages of PEO with PS microparticles especially at transition concentration whose stage 2 is the most distinct with that of (a) with a formation of a dimple. In stages 1 to 4 the droplet is evaporation in a pinned mode. ....151

Figure 5.6: Side on image sequences as the 0.7 $\mu$ L droplet dries containing 5 $\mu$ m PS particles ( $c_0 = 4\%$ ) and PEO ( $c_1 = 1.6\% - 14\%$ ). ....153

Figure 5.7: Final images captured with cross polarizer for 5 $\mu$ m PS particles of  $c_0 = 2\% - 5\%$  mixed with  $c_1 \sim 3\% - 14\%$  of PEO.....154

Figure 5.8: Magnified final deposits of 0.5 $\mu$ m PS particles ( $c_0 = 4\%$ ) with varying PEO concentration captured with optical microscope under reflection mode..155

Figure 5.9: Distribution of 5 $\mu$ m PS particles inside the deposits when (a) pillar is formed at  $c_1 = 12\%$  of PEO and (b) a puddle at  $c_1 \sim 1.6\%$  of PEO.....156

Figure 5.10: Surface profiles for 1 $\mu$ L droplet of 0.5 $\mu$ m PS particles with  $c_0 = 1\% - 5\%$ .....157

Figure 5.11: The effect of PEO concentration on the deposits profiles for  $c_0 = 4\%$  of 0.5 $\mu$ m PS particles.....158

Figure 5.12: Surface profiles for 1 $\mu$ L droplet of 5 $\mu$ m PS particles with  $c_0 = 1\% - 5\%$ . ....159

Figure 5.13: The effect of PEO concentration on the deposits profiles for  $c_0 = 4\%$  of 5 $\mu$ m PS particles. ....160

Figure 5.14: Coefficient of skewness as a function of PEO concentration for a fixed $c_0 = 2\%$ of PS particles and 0% PS is included for comparison. ....	162
Figure 5.15: Coefficient of skewness as a function of PEO concentration for a fixed $c_0 = 3\%$ of PS particles and 0% PS is included for comparison. ....	162
Figure 5.16: Coefficient of skewness as a function of PEO concentration for a fixed $c_0 = 4\%$ of PS particles and 0% PS is included for comparison. ....	163
Figure 5.17: Coefficient of skewness as a function of PEO concentration for a fixed $c_0 = 5\%$ of PS particles and 0% PS is included for comparison. ....	163
Figure 5.18: Phase diagrams showing pillars, puddles and rings for $0.5\mu\text{m}$ PS particles with the purple skew line showing the cross over concentration. ....	164
Figure 5.19: Phase diagrams showing pillars, puddles and rings for $5\mu\text{m}$ PS particles with the purple skew line showing the cross over concentration. ....	165
Figure A.1: Schematic illustration of an equilibrium contact angle in terms of force balance. ....	193

## List of Tables

Table 3.1: The average value of exponent n and m for upright orientation for different PS particle sizes. ....	95
Table 3.2: The average value of exponent n and m for upside down orientation for different PS particle sizes. ....	98
Table 4.1: Zeta potential (mV) as a function of initial concentration and particles sizes as per Zetasizer instrument limits. ....	110
Table 4.2: The concentration of hydrogen ions (pH) in the suspensions corresponding to each initial concentration of PS microparticles in table 4.1. ....	110
Table 4.3: The average outward, vertical and outward PS microparticles velocities both a low and high drying rates. ....	143

## Notation

The main variables used throughout this work are listed below;

$t_F$	Droplet lifetime
$\rho$	Density
$\phi$	Packing fraction
$c_0$	Concentration of polystyrene microparticles
$c_1$	Concentration of PEO
$w_r$	Ring width
$h_r$	Ring height
$V_0$	Volume of a droplet
$M$	Mass of the microparticles
$\gamma$	Surface tension
$\gamma_{lg}$	Surface tension of the liquid-vapour interface
$\gamma_{sg}$	Surface tension of the solid-vapour interface
$\gamma_{sl}$	Surface tension of the solid-liquid interface
$\theta$	Contact angle
$B_0$	Bond number
$v_r$	Radial velocity
$\eta$	Dynamic viscosity
$g$	Acceleration due to gravity
$C_a$	Capillary number
$h_0$	Initial droplet height
$R$	Radius of the droplet
$L_c$	Capillary length

$c_s$	Interface equilibrium saturated vapour concentration
$c_\infty$	Ambient vapour concentration
RH	Relative humidity
$\Delta c$	Difference in vapour concentration
$J(r, t)$	Local evaporation flux
$D_f$	Vapour diffusion coefficient
$D_T$	Thermal diffusivity
$f(\theta)$	Contact angle function
$\theta_0$	Initial contact angle
$D_{ref}$	Vapour diffusion coefficient at reference pressure
P	Pressure
$P_{ref}$	Reference pressure (1000mbar)
$P_s$	Pressure of saturated vapour
$\Lambda$	Latent heat of vaporization
$T_\infty$	Temperature of a saturated vapour
$R_c$	Universal gas constant
T	Temperature
$\omega_s$	Ratio of particle to solvent velocities
$\vartheta$	A constant relating the ring width and particle diameter
$R_{RH}$	Radius of the droplet as a function of relative humidity
$\theta_{RH}$	Contact angle related relative humidity
$M_a$	Marangoni number
$S_T$	Soret coefficient
$\beta$	Surface tension-temperature coefficient

$T_e$	Temperature at the edge of the droplet
$T_c$	Temperature at the top center of the droplet
$V_{MA}$	Marangoni velocity
$\psi_p$	Surface potential
$\sigma_p$	surface charge density
$k_B$	Boltzmann constant
$\kappa^{-1}$	Debye length
$N_A$	Avogadro's number
$I$	Ionic strength of the solution
$e$	Electronic unit charge
$\epsilon\epsilon_0$	Total permittivity of water
$F_{vdw}$	Particle Van der Waals force
$F_{el}$	Electrostatic force
$d_p$	Diameter of a particle
$n_e$	Number concentration of the counter ions far away
$\gamma_p$	Surface potential of particle
$\gamma_s$	Surface potential of the substrate
$U_e$	Electrophoretic mobility
$f(\kappa a)$	Henry's function
$N_{pol}$	Degree of polymerization
$M_{mom}$	Molar mass of the monomer
$M_{pol}$	Molar mass of the polymer
$T_g$	Glass transition temperature
$P_e$	Péclet number

$c^*$	Overlap concentration
$R_g$	Radius of gyration
$G_p$	Pearson coefficient of skewness
$\sigma$	Standard deviation
$V_T$	Stokes velocity
$r$	Radius coordinate
$z$	Height coordinate
$r^*$	Rescaled coordinate for radius
$z^*$	Rescaled coordinate for height

## Abbreviation

DNA	Deoxyribonucleic Acid
RNA	Ribonucleic Acid
PEO	Poly(ethylene oxide)
PS	Polystyrene
RCA	Receding Contact Angle
ACA	Advancing Contact Angle
ECA	Equilibrium Contact Angle
CCR	Constant Contact Radius
CCA	Constant Contact Angle
RH	Relative Humidity
VdW	Van der Waals
DLVO	Derjaguin-Landau-Verwey-Overbeek
PEG	Polyethylene Glycol
OCT	Optical Coherence Tomography
SDOCT	Spectral Domain Optical Coherence Tomography
CCD	Charge Coupled Device
DSA	Drop Shape Analysis
LVDT	Linear Variable Differential Transformer
SLD	Super Luminescent Diode
ICCRM	Intergrated Cross-correction and Relaxation Algorithm
PTVlab	Time-resolved Digital Particle Tracking Velocimetry
PIVlab	Time-resolved Digital Particle Image Velocimetry
RHS	Right Hand Side
LHS	Left Hand Side

# **Chapter 1**

## **Introduction**

## 1.1 Motivation

When a liquid containing microparticles is removed by evaporation from the edge of a drop and replenished by a flow of liquid from the interior of the hemispherical surface, microparticles dispersed in the drop aggregate along the periphery of the droplet forming ring like deposits well known as coffee stain effect [1-8]. An example of this is when a droplet of coffee is spilled on a solid surface and allowed to dry. After sometime the deposit in figure 1.1 is observed with a dark deposit at the edges and translucent stain at the center.



Figure 1.1: The coffee stain affect formed from a spilled and dried coffee droplet on a wooden table.

To obtain the stain shown in figure 1.1 the droplets have to evaporate in constant contact radius [9-11]. The evaporation of microparticles dispersed in a liquid have found many applications in sensors [12], inkjet printing [13-15], fabrication of transistors [16], deposition and organization of biological materials such as DNA/RNA and carbohydrates [17-22] and sorting of colloids [23]. While applications involving inkjet printing [13-15] require the final deposition after evaporation to be uniform, applications involving drug discovery [24], nanowires and carbon nanotubes array production [25-27], nano and ring-dot patterning [28], utilizes the coffee ring effect and thus controlling the evaporation process of microparticles suspension is of vital important. The present thesis focuses on drying of sessile

droplets containing polystyrene microparticles and/or polymer solution of Poly(ethylene oxide) (PEO) using experimentally controlled parameters.

## 1.2 Liquid-solid interface

### 1.2.1 Surface Tension

There are common phenomena observed in daily life such as water droplets beading on a leaf, tears of wine in a glass containing alcoholic beverages and water striders walking on a surface of a pond. All of these phenomena are explained in terms of surface tension. To explain surface tension, the molecular theory in which all liquids contain molecules which are in state of random motion as shown in figure 1.2.

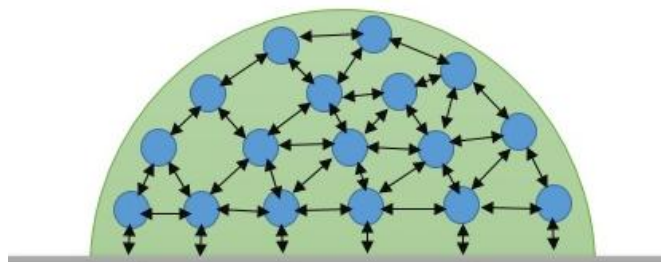


Figure 1.2: Schematic illustration of intermolecular forces between molecules in a liquid responsible for surface tension (arrows show attractive forces between the molecules).

The molecules in the bulk of the droplet experience cohesive forces from the nearby molecules in all directions leading to net zero force. The molecules close to the air-liquid interface experience unbalanced attractive forces from the neighbouring molecules beneath them as result the net force (cohesive force) pulls these molecules towards the bulk of the liquid. For a molecule in the bulk of the droplet to be brought to the surface, work has to be done against this force. The work done is stored as the potential energy of the molecules, the more the molecules at the surface the higher the potential energy. However for a stable system the potential

energy of the molecules at the surface have to be minimum as possible. The energy per unit area needed to reduce the surface area to lower the free energy arrangement is called surface tension  $\gamma$  [29].

The surface tension can be illustrated in figure 1.3 by considering a soap film in which a surface contained by a rectangular frame with one end capable of sliding along the sides exerts a force,  $F$  on the slide [30]. By moving the slide through a distance  $dx$  to extend the surface, then the surface area will increase by amount  $l dx$ . The surface tension force to resist this extension is given by  $F = \gamma l$ , where  $\gamma$  is surface tension. The energy required to create a surface is equal to area times the surface tension according to equation (1.1).

$$\text{workdone} = \int \gamma l dx \quad (1.1)$$

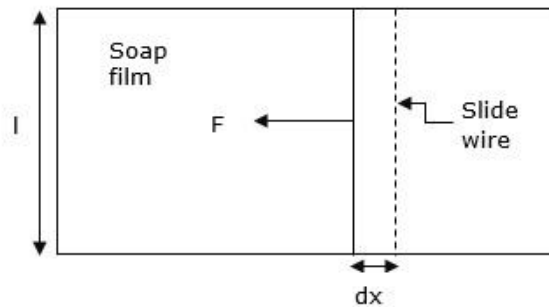


Figure 1.3: Schematic illustration of the wire frame for increasing the surface area of a soap film.

### 1.2.2 Wetting

When a drop of a liquid is deposited on a solid surface, it will attain its final shape after equilibrium is reached. This phenomenon is termed as wetting and the affinity of the surface to get wetted by a given liquid is known as wettability [31]. Wetting is governed by the balance between two competing forces (cohesive and adhesive) in a liquid and the solid surface. Cohesive forces exist between like molecules such as those in liquid and the adhesive forces exists between different molecules such as liquid and solid surface. When the cohesive forces are stronger than the

adhesive forces, the liquid does not wet the solid surface. The solid surfaces with this affinity are called hydrophobic surfaces and will form a contact angle,  $\theta > 90^\circ$  as shown in figure 1.3. The contact angle  $\theta$  is angle at which a liquid/vapour interface meets a solid surface.

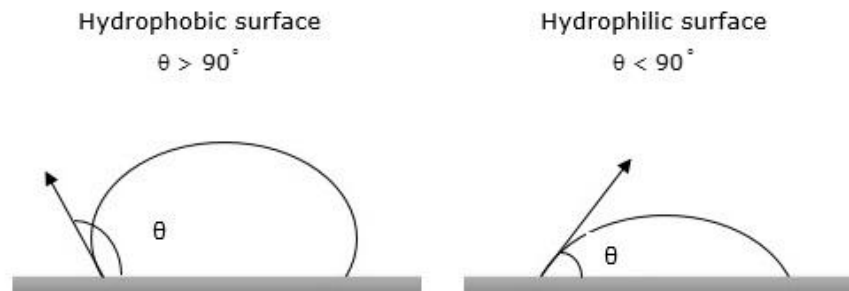


Figure 1.4: Schematic illustration of a hydrophobic and hydrophilic surface

Otherwise when the adhesive forces are stronger than the cohesive forces the liquid wets the solid surface partially or completely. These solid surfaces are termed as hydrophilic and will form a contact angle,  $\theta < 90^\circ$ .

### 1.2.3 Young's Equation

For total wetting ( $\theta \sim 0$ ), the liquid spreads completely to lower its surface energy and partial wetting ( $\theta > 0$ ), the drop does not spread but, instead, forms at equilibrium a spherical cap resting on the solid surface with an equilibrium contact angle  $\theta$  as shown in figure 1.5.



Figure 1.5: Schematic illustration of a contact angle and the mechanical equilibrium of interfacial surface tensions of a sessile drop resting on a solid surface

In equilibrium, there are three forces,  $F$  acting on the edge of a liquid droplet to keep it still. These forces are acting along the three interfaces between the solid, liquid and vapour phases, and commonly measured as corresponding surface tensions at the solid-liquid, solid-vapour, and the liquid-vapour interface. When the mechanical equilibrium has been established  $\sum F_x = 0$  and  $\sum F_y = 0$ . At mechanical equilibrium, the contact angle is related to the surface tensions of the liquid-vapour  $\gamma_{lg}$ , solid-vapour  $\gamma_{sg}$  and solid-liquid  $\gamma_{sl}$  interfaces according to equation given by [32, 33]:

$$\cos\theta = \frac{\gamma_{sg} - \gamma_{sl}}{\gamma_{lg}} \quad (1.2)$$

Equation (1.2) is called the Young equation to quantify the wetting phenomenon and holds only when the triple line (liquid-vapour-solid) is free to move without constraints. It also assumes the solid surface is flat and inert as well as the effect of gravity is negligible on the droplet. The derivation of equation (1.2) is described fully in Appendix A. The contact angle can be measured directly using video recording systems (Drop shape analyzer) or calculated using other measured parameters. The Contact angle is important in painting, cleaning, coating and printing industries. The contact angle is also useful in determining the solid-liquid surface free energies. In real experimental conditions, solid surfaces are rough containing contaminants and different functional groups making them chemically heterogeneous. This follows from the fact that it is impossible to obtain an ideal solid surface which is rigid, smooth, homogeneous and inert chemically. This results into variations in the observable contact angle giving rise to contact angle multiplicity [34, 35] and contact angle hysteresis [36-38]. The contact angle multiplicity results when there is corrugation (wrinkles) at the three phase contact line.

The contact angle hysteresis is an indicator of the imperfections which exist on solid surfaces. It is when a contact angle depends on the past history of the wetting process. For simplicity contact angle hysteresis will be expressed in terms of the advancing and receding contact angles. The difference between the advancing contact angle (ACA) and the receding contact angle (RCA) for a contact line moving in the opposite direction at the same velocity is known as contact angle hysteresis [37]. As explained one of the causes of contact angle hysteresis is solid surfaces heterogeneity, however Neumann and Good [39] point that for this to happen the dimension of the patch must be greater than  $0.1\mu\text{m}$ . Further Rodriguez-Valverde et.al, [36] point out that there must exist metastates whose number and locations is a function of the droplet's volume. Figure 1.6 shows these metastates characterized by the advancing contact angle, receding contact angle and equilibrium contact angle (ECA) of minimum energy. The receding contact angle is important when characterizing the solid-liquid interface especially during depinning of an evaporating sessile droplet [40, 41].

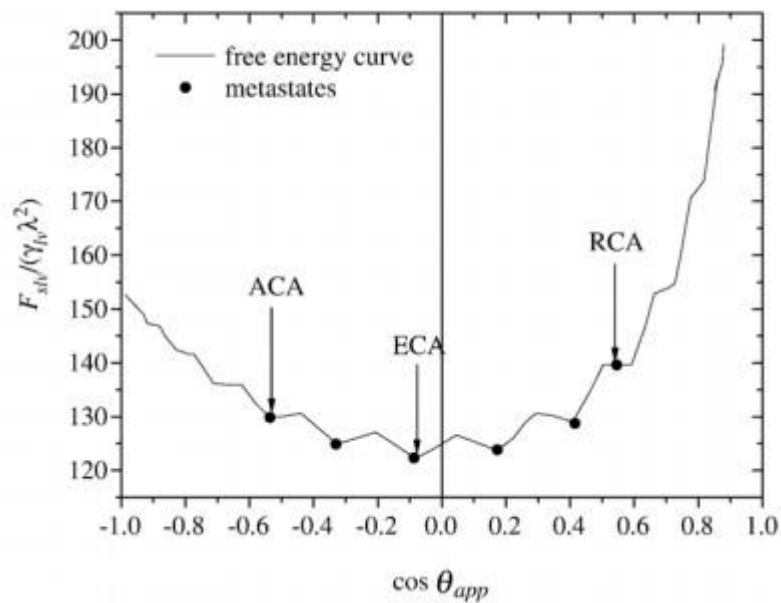


Figure 1.6: Graphical representation of contact angle hysteresis in terms of the free energy and cosine of apparent contact angle for sessile droplet [36].

### 1.3 Droplet Evaporation of Pure Liquids

This chapter describes the theory of droplet evaporation and how the evaporation rate of pure liquid droplets depends on air pressure, contact angle, temperature and thermal conductivity of a substrate.

#### 1.3.1 Theory of Droplet Evaporation

When a droplet of liquid is dispensed on a solid surface, it will adhere and become

constrained to it. Its shape will be determined by the Bond number,  $B_0 = \frac{\rho g R h_0}{\gamma}$

where  $\gamma$  is the surface tension of liquid,  $g$  is the acceleration due to gravity,  $\rho$  is the density of a liquid,  $R$  is the contact line radius of the liquid droplet and  $h_0$  is the initial height of the droplet [42]. The spreading of the droplet is determined by

capillary number  $C_a = \frac{\eta v_r}{\gamma}$  where  $v_r$  is the average radial velocity induced by

liquid droplet evaporation [43]. The value of  $C_a$  determines the movement of a contact line and hence the radius of the droplet. For a pinned droplet the capillary number,  $C_a \leq 0.1$  [44]. The Bond number compares the weight of the droplet to

the surface tension force. When the contribution of gravitational forces is negligible compared to surface tension forces, the value of,  $B_0 = 1$  then,  $h_0 = R = L_c$  where

$L_c$  is the capillary length. For  $B_0 > 1$ , the droplet flattens due to the effect of gravity leading to an increased contact radius and decrease in the height of the droplet. Similarly for  $B_0 < 1$ , the droplet will attain the spherical cap. The droplet

shape in figure 1.7 is regarded as a spherical cap [42] whose dimension is less than

the capillary length,  $L_c = \sqrt{\frac{\gamma}{g\rho}}$ . The capillary length for water droplet in this case

takes the value of  $\approx 2.70\text{mm}$  by substituting the known constants in the capillary length equation [45]. The volume of a spherical cap as a function of contact angle

and wetting radius  $R$  in figure 1.7 has been found to vary according to equation

(1.3) as the droplet evaporates [46, 47]. Equation (1.3) holds well for a droplet with a dimension less than a capillary length and has been derived from first principle assuming a spherical cap is part of a sphere.

$$V = \frac{\pi R^3 (2 - 3 \cos \theta + \cos^3 \theta)}{3 \sin^3 \theta} \quad (1.3)$$

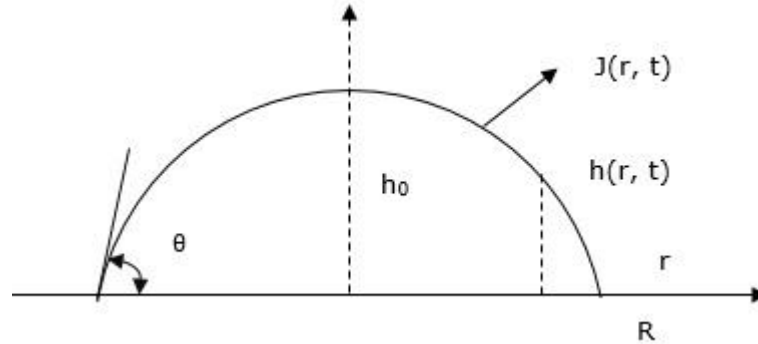


Figure 1.7: Droplet with the shape of a spherical cap rests on a flat surface. The local height and evaporation flux are  $h(r, t)$  and  $J(r, t)$  respectively.

Consider a spherical droplet evaporating free from any surface. For a pure liquid droplet to evaporate, its molecules must vibrate with enough force to break the bonds holding them together due to cohesive forces. These vibrations cannot happen without energy, thus the energy available to a liquid and the strengths of intermolecular forces will determine how fast the evaporation will take place. The resulting vapour concentration, at the interface is equal to its equilibrium saturated vapour concentration,  $c_s$ . Far above the liquid droplet surface, the concentration of liquid vapour approaches that of an ambient air,  $c_\infty$ . The molecules escaping to the gas phase at the liquid–interface are limited by diffusion.

The concentration of liquid vapour at the droplet interface, concentration of ambient vapour and relative humidity,  $R_H$  are related by,  $c_\infty = c_s R_H$ . Relative humidity is defined as the partial pressure of water vapour in air divided by the vapour

pressure of water at the given temperature [48, 49]. For a saturated atmosphere the relative humidity is 100%. The difference in vapour concentration  $\Delta c = c_s - c_\infty = c_s(1 - R_H)$  drives the evaporation of liquid droplets into air whose concentration diffuses at rate given by  $\frac{\partial c}{\partial t} = D_f \frac{\partial^2 c}{\partial r^2}$  where  $D_f$  is the vapour diffusion coefficient. The local evaporation flux,  $J(r, t)$  defined as the mass of vapour flowing into air through a given area per time interval is described by the Fick's Law.

$$J(r, t) = -D_f \frac{\partial c}{\partial r} \quad (1.4)$$

Equation 1.4 assumes the droplet evaporation is so slow that the temperature is kept constant along the liquid-vapour interface so that the vapour diffusion coefficient does not change. The vapour diffusion coefficient  $D_f$  depends on the size and velocity of diffusing molecules as well as the viscosity of the medium (the air)  $\eta$  according to well-known Stoke-Einstein equation [29] given by:

$$D_f = \frac{k_B T}{6\pi\eta r_s} \quad (1.5)$$

Where  $r_s$  is the radius of the spherical molecule,  $k_B$  is the Boltzmann's constant and  $T$  is the absolute temperature. By keeping temperature constant, the viscosity of the medium and velocity of molecules will be same leading to a constant value of vapour diffusion coefficient. Birdi and Winter [47] have shown that, the total evaporation rate,  $\frac{dM}{dt}$  over the whole droplet of radius,  $R$  free from any solid surface is given by;

$$-\frac{dM}{dt} = 4\pi R D_f c_s (1 - R_H) \quad (1.6)$$

It is clear from equation (1.6) the rate at which the droplet decreases because of evaporation is proportional to the radius and escape of molecules at the liquid-vapour interface is uniformly controlled by diffusion.

Let us consider the case of a droplet with a spherical shape resting on a solid boundary, such as a substrate shown in figure 1.7. A simple theory of droplet evaporation incorporating the contact angle function,  $f(\theta)$ , has been developed and show that the evaporation rate in equation (1.6) is given by [11, 42];

$$-\frac{dM}{dt} = \pi R D_f C_s (1 - R_H) f(\theta) \quad (1.7)$$

$f(\theta)$  describes how the evaporation rate changes with contact angle and can be approximated for small angles by  $f(\theta) = 1.3 + 0.27\theta^2$ . The evaporation model takes account of non-uniformity in evaporation flux which is small at the centre of the spherical cap and gradually increases towards the contact line. For small values of  $\theta \ll 1$  radian [50] the total drying time,  $t_F$  of the droplet is given by equation (1.8) according to Popov [51] where  $\theta_0$  the initial contact angle of the droplet.

$$t_F = \frac{\pi \rho R^2 \theta_0}{16 D_f C_s (1 - R_H)} \quad (1.8)$$

Popov also showed that the mass of a droplet as a function of time is given by equation (1.9). The mass of the drying droplet according to equation (1.9) was found to have linear relationship in the entire drying process for  $\theta \ll 1$  radian.

$$M = \frac{\pi \rho R^2 \theta_0}{4} \left( 1 - \frac{t}{t_F} \right) \quad (1.9)$$

The Popov as well as Hu and Larson models of evaporation are in good agreement with their experimental data [11, 42]. In particular, they have shown their evaporation models to predict the experimental results with an error of  $\sim 10\%$  for

droplet of radius between 0.5mm and 1mm. For smaller droplets of radius less than 0.5mm, Hu and Larson model predicts the experimental results within an error of ~25%.

### **1.3.2 Modes of Droplet Evaporation.**

Gleason and Putnam [52] point out that a water droplet on a substrate will evaporate in a constant contact angle mode (CCA), constant contact radius mode (CCR), stick-slip mode or a mixed mode where both droplet radius and contact angle decreases concurrently depending on the dynamics at the contact line. When the droplet is pinned due to asperities on the substrate surfaces and the evaporation takes the CCR mode for contact angle less than 90°. Schönfeld et.al, [53] have shown that the volume of the droplet decreases linearly with time. These findings have been shown to agree with previous studies by Hu and Larson [42] who found that for contact angles less than 90°, the droplet height, volume and contact angle decrease linearly with time.

When a contact line is not pinned in some places at the droplet edge and such that there is a movement or jump of a contact line on the substrate over time as the droplet evaporates, this mode of evaporation is called stick-slip [54]. In this mode of evaporation, the contact angle oscillates over time during stick-slip stages [55]. According to Shanahan and Sefiane [56], the stick-slip mode of evaporation exists due to surmounting chemical or potential energy barriers as a result of pinning at liquid-vapour-solid phase contact line. Figure 1.8 shows the evaporation leading to stick-slip phenomenon, in which both contact angle and droplet height decrease or increase due to pinning/depinning cycles.

The constant contact area mode of evaporation is common in patterned substrate surfaces and hydrophobic surfaces where the contact angle is greater than 90°. Chuang et.al, [57] found that when droplets of water are evaporated on the

patterned surface of pillar-like PDMS substrate, the droplet begins to evaporate with CCR mode followed by CCA mode through jumping the contact line ending up with mixed mode sequentially. Experimental results revealed that, evaporation of water droplets on superhydrophobic surfaces is dominated mainly by CCR and CCA modes [46].

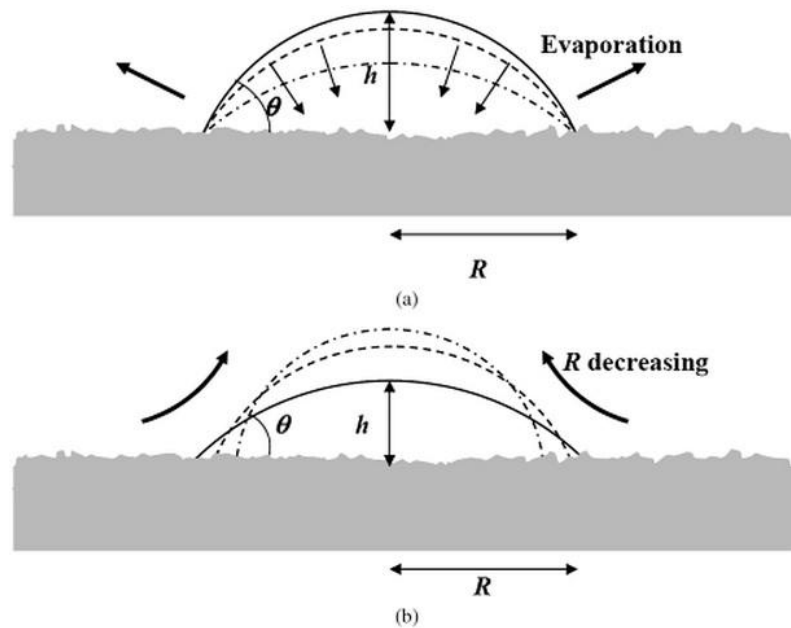


Figure 1.8: The formation of stick-slip in an evaporating droplet with (a) the droplet radius is constant with a pinned triple line while both contact angle and droplet height decreases with time (b) the triple depinns leading to an increased contact angle and droplet height while the radius decreases [56].

### 1.3.3 Temperature

In this section the effect of temperature distribution within the droplet, temperature of the substrate and surrounding air on the evaporation rates of the droplets of pure liquids will be presented. Temperature is a measure of the amount of kinetic energy the liquid molecules have and consequently the ability to diffuse through vapour. Two droplets of the same size will evaporate at different rate provided that their temperature is different since their vapour pressure is not the same. The

higher the vapour pressure the higher the evaporation rate and vice versa. The vapour pressure at the liquid surface is related to the local temperature by Clausius–Clapeyron equation [58] given by equation (1.10).

$$\ln\left(\frac{P_1}{P_2}\right) = \frac{\Delta H_{\text{vap}}}{R_c} \left( \frac{1}{T_1} - \frac{1}{T_2} \right) \quad (1.10)$$

where  $P_1$  is a known vapour pressure at given initial temperature  $T_1$ ,  $P_2$  is the value of vapour pressure after altering the temperature to  $T_2$ ,  $\Delta H_{\text{vap}}$  is the heat of vaporisation and  $R_c$  is the universal gas constant. Equation (1.10) was derived for a flat liquid or solid surface above which there are molecules in the gas phase. When extremely small droplets form in the atmosphere, the surface of the droplet is curved. As a result the molecules in the drop at the surface are not surrounded and bonded by quite as many molecules and are therefore somewhat less tightly bound than in the case of a flat surface and the surface tension is therefore smaller. This means molecules on the surface of a droplet can fly off the surface more easily than those on a flat surface. Therefore achieving saturation vapour pressure equilibrium can require substantially higher vapour pressures than over a flat surface when the droplets are very small. Let the vapour pressure of a curved surface be denoted by  $P_3$  and is related by the vapour pressure of the flat surface by Kelvin's equation [59] given by:

$$\ln\left(\frac{P_3}{P_1}\right) = \frac{\gamma K_z M_g}{\rho R_c T_1} \quad (1.11)$$

Where  $\gamma$  is the liquid–vapour interfacial tension,  $M_g$  and  $\rho$  are the molecular weight and the density of the evaporating liquid, and  $K_z$  is the curvature of the liquid–vapour interface, determined as  $K_z = (\nabla \cdot \vec{n})_\Gamma$ , where  $\vec{n}$  is the unit vector perpendicular to the liquid–gas interface ( $\Gamma$ ) and pointing into the gaseous phase.

The rate at which the droplet evaporates also depends on the temperature of the substrate. Starov and Sefiane [60] varied the temperature of the Al/PTFE substrate between 25°C to 40°C to study the evaporation behaviour of volatile droplets. The theoretical prediction of the evaporation flux as a function of droplet radius is shown in figure 1.9, with the graph in the box showing the temperature of the droplet at the surface as a function of location on droplet radius [60, 61].

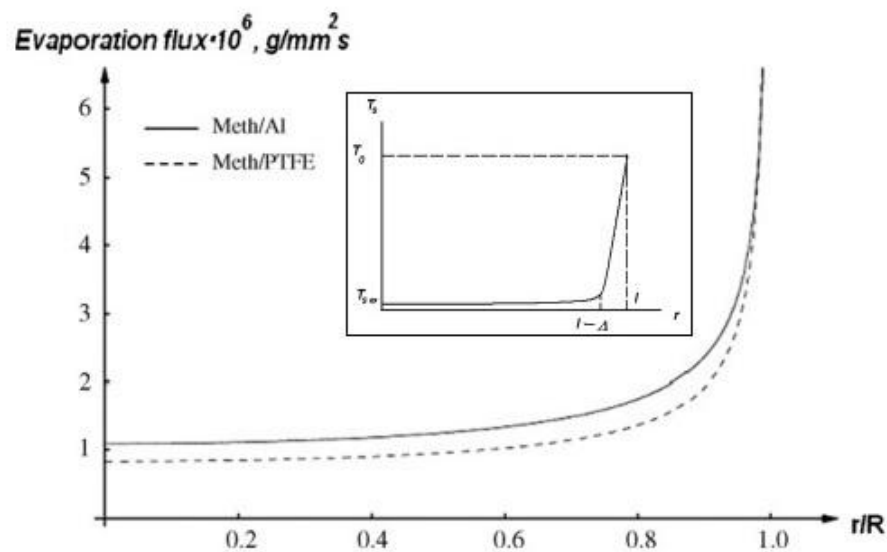


Figure 1.9: Local evaporation flux and temperature of methanol droplet as a function of location on droplet radius on Al/PTFE substrate [60, 61].

These findings indicate that the higher the temperature the higher the evaporation flux as expected. Girard et.al, [62] studied the evaporation of water droplets on a heated aluminum substrate at 40°C and extracted the temperature profiles along the surface of the droplets using infrared techniques. The authors observed a temperature difference  $\sim 0.8^{\circ}\text{C}$  between the droplets edge and apex, with the apex being cooler than the edge. However Girard and Antoni [63] analytically showed that whether the droplet apex or edge will be warmer/colder depends on the ratio of substrate thickness to droplet radius. As a result this ratio will influence the evaporation rate at a fixed temperature. Findings indicates that for a ratio greater

than one when the temperature was fixed at 50°C, evaporation time increases (slow evaporation rate) and for ratio below one, the evaporation rate is independent of it. Recently Snegirev [64] has analytically and experimentally found that temperature gradients are more pronounced for volatile liquids than water and has no effect on determining the life time of a droplet during evaporation.

### 1.3.4 Marangoni Flow

When there is a non-uniform temperature in a liquid a temperature gradient will exist. The temperature gradient will cause mass transport of the liquid from hot to cold region [65]. The phenomenon is termed as thermodiffusion or Soret effect after the person who first observed it experimentally about 150 years ago [66-72]. When a droplet of water is dispensed on a substrate it will evaporate by extracting the latent heat of evaporation from the surrounding. It is assumed that the thermal conductivity of the substrate is higher than that of the droplet; as a result the droplet edge extracts latent heat of evaporation from the substrate and the top edge losses temperature because of evaporation. During droplet evaporation, evaporative cooling reduces the droplet surface temperature non-uniformly as surface tension, typically decreases with increasing temperature and this leads to variations in surface tension. This can lead to a flow due to gradients of surface tension along the droplet interface and is termed as Marangoni effect named after Carlo Marangoni who studied it. The mass transport of the liquid is characterized by the Marangoni number,  $M_a$  [73-75] and Soret coefficient,  $S_T$  [76, 77] given by equation (1.12) and (1.13) respectively.

$$M_a = -\beta(T_e - T_c) \frac{t_F}{\eta R} \text{ or } M_a = -\beta(T_e - T_c) \frac{R}{\eta D_T} \quad (1.12)$$

$$\nabla c_0 = S_T c_0 (1 - c_0) \nabla T \quad (1.13)$$

Where  $t_F$  is the drying time for the droplet,  $R$  radius of the droplet,  $\eta$  viscosity of the suspension,  $\beta = \frac{d\gamma}{dT}$  surface tension-temperature coefficient,  $c_0$  initial concentration of the microparticles by mass,  $D_T$  is the thermal diffusivity,  $T_e$  temperature at the edge of the droplet,  $T_c$  temperature at the top center of the droplet. The sign of  $S_T$  indicates the direction in which the liquid will move, with positive sign the direction of liquid being towards the cold region. There is no Marangoni stress when  $(T_e - T_c) \approx 0$ , as  $M_a = 0$ . Diagrammatically, the Marangoni flow is presented in figure 1.10.

According to Deegan et.al, [4], the evaporation rate in a droplet is higher near the edge when contact line is pinned and the value of  $M_a$  for evaporating water droplets is weak due to the presence of small amounts of surface active molecules at liquid-vapour interface. Hu and Larson [73] have shown analytically that when the contact angle of the evaporating droplet reaches  $14^\circ$  the Marangoni number changes its sign from positive to negative, consequently there is no recirculation below this value, only radial flow. The Marangoni velocity can be determined by equation (1.20) [78].

$$V_{MA} = \frac{1}{32} \left( \frac{\beta \theta^2 \Delta T}{\eta} \right) \quad (1.14)$$

Equation (1.20) was obtained using equation (28) in reference [79] by order of magnitude analysis method. The term with Marangoni number  $M_a$  was assumed to be larger than other terms, so other terms were dropped. The maximum Marangoni velocity  $V_{MA}$  was determined at  $h \approx \frac{h_0}{2}$  where  $h_0$  is the initial droplet height. Equations (1.12) and (1.14) assumes the Marangoni flow is brought about by surface tension gradients resulting from temperature gradients, however Marangoni

flow can be induced by variation in surfactant concentration along vapour-liquid interface which also suppress coffee ring effect [80, 81]. Surfactants are chemical species (such as soaps and detergents) that acts as wetting agents to lower the surface tension at vapour-liquid interface. Also evaporation of droplets containing binary liquids such as ethanol or methanol–water solution leads to concentration variations, causing the surface tension gradients and hence Marangoni flow.

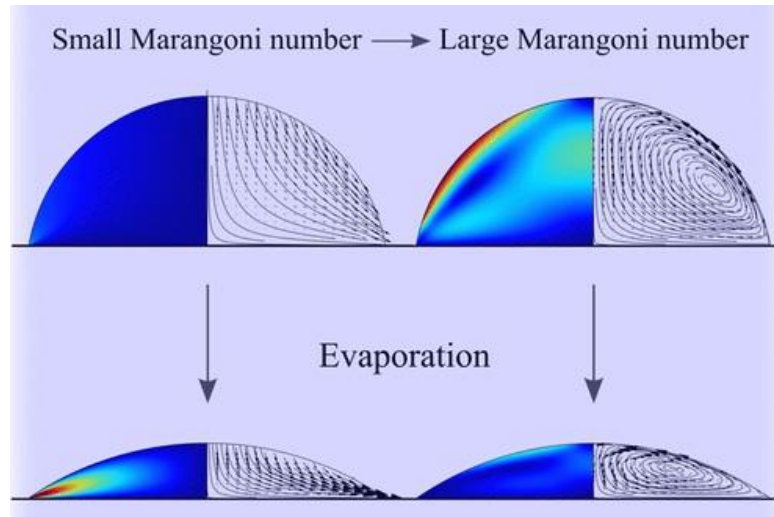


Figure 1.10: Internal convective flow in the presence of Marangoni flow. As the droplet evaporates the Marangoni flow decreases and the radial flow dominates [75].

### 1.3.5 Thermal Conductivity of the Substrate.

Thermal conductivity is the property of the solid, liquid or gas to transfer heat energy. Heat is transferred from high energy to low energy molecules, atoms, electrons and phonons by virtue of collisions and diffusion. Heat energy will be transferred at highest rate in materials with higher thermal conductivity than those with lower thermal conductivity. Heat energy flows from the region of higher temperature with molecules, atoms, electrons or phonons associated with higher internal energy to low temperature regions. When the substrate-liquid interface is maintained under isothermal condition, Ristenpart et.al, [82] have found that the

ratio of the substrate to liquid conductivities as well as contact angle determines the direction of Marangoni flow in an evaporating droplet. Marangoni flow is the one driven by surface tension gradient across the droplet. Saada and co-workers [45] analytically studied the effect of varying thermal conductivities of the substrate on the evaporation of droplets and the result is shown in figure 1.11.

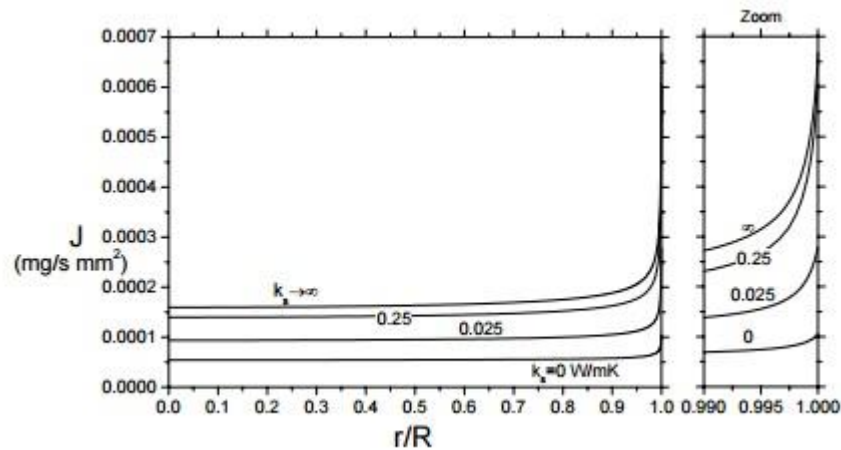


Figure 1.11: Dependence of the evaporation flux of droplet of water ( $\theta_0 = 78^\circ$ ) on various substrate thermal conductivity ( $k_s$ ) [48].

Their results indicate that the evaporation flux is uniform along the gas-liquid interface for most of the drop except for a very slight increase near the contact line (as shown in fig 1.11). The only source of energy to enable the droplet to evaporate is from the surrounding environment. For conducting substrates, the evaporation flux varies along the liquid-vapour interface with its value higher near the contact line. The evaporation of the droplet at vapour-liquid interface depends on the magnitude of heat it receives from the conducting substrate. However for conducting substrate at smaller contact angles, the effect of thermal conductivity on evaporation flux is reduced and even vanishes. The theory that incorporates thermal conductivity of the substrate and properties of the liquid in evaporative cooling beyond the isothermal diffusion model has recently been developed by

Sefiane and Bennace [83]. The experimental results agree with the predicted reduced evaporation rate (at reduced pressure) for non-isothermal condition at the solid-liquid interface due to thermal cooling and change in kinetics at the contact line.

### 1.3.6 Air Pressure

According to Hu and Larson [42] the approximate expression for total evaporation rate in terms mass of vapour,  $\frac{dM}{dt}$  leaving the surface of the droplet per unit time given by equation (1.7) with the difference in water vapor concentration  $(1 - R_H)c_s$ , being responsible for driving evaporation of water into the air. Since the water vapour diffusion constant,  $D_f$  is related to pressure by relation of the form  $D_f \approx \frac{D_{ref}P_{ref}}{P}$  [60] where  $D_{ref}$  is the value at reference pressure  $P_{ref} = 1000\text{mbar}$ , hence with all other parameters being constant equation (1.7) can written according to equation (1.15).

$$\frac{dM}{dt} \approx \frac{dM}{dt}(1000\text{mbar})\frac{P_{ref}}{P} \quad (1.15)$$

By varying the pressure between 40 to 1000mbar in an atmosphere of nitrogen, helium and carbon dioxide gases, Sefiane and co-workers [84] were able to show that the evaporation rates of the droplets increases at reduced pressure.

## 1.4 Evaporation of Droplets Containing Particles

This section reviews the recent research developments on evaporation of droplets containing colloidal particles. The section begins by reviewing the coffee ring effect, particle ring growth and how it can be suppressed. The effects of colloidal interactions and relative humidity on deposit patterns have been reviewed.

### 1.4.1 Coffee Ring Effect

As explained in section 1.1, when droplets containing colloids are left to dry, ring-like deposits are observed along the perimeter [85]. Apart from this other variety of morphologies have been observed ranging from complex deposits patterns with multiple rings [86, 87], central bumps [88] and uniform deposits [89]. There has been an extensive study on the mechanisms of microparticle depositions and the patterns formed.

The first evaporation model to explain this was proposed by Deegan and co-workers [4] who stressed that the necessary requirements are pinning of the droplets and that the evaporation is higher at the edge (figure 1.9) which drags the microparticles due to capillary flow to replenish the lost liquid. As a consequence of capillary flow, all microparticles in a droplet will be deposited at the ring. To put these two conditions into practice, consider a section of a droplet as shown in figure 1.12. At early stages when a droplet containing microparticles is dispensed on a substrate it becomes pinned and the microparticles are diffused over the entire droplet liquid phase. At later stage the liquid evaporates faster at the contact line than across the rest of the droplet surface. As a result the fraction of the microparticles remaining in the bulk of liquid droplet is lower compared to that at the perimeter due to flow towards the contact line.

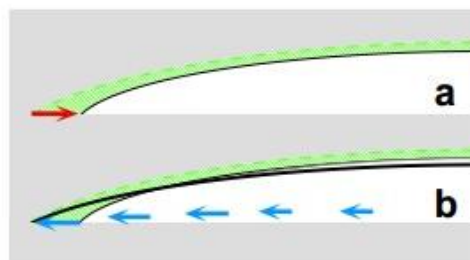


Figure 1.12: In (a) the absence of microparticles leads the droplet shrink as the it dries and (b) presence of microparticle enables pinning at the contact line [4].

Deegan et.al, [4] derived the analytical expression for the local evaporation rate from the surface of the droplet as a function of  $r$  (local radial coordinate) and  $t$  according to equation (1.16)

$$\bar{J}(r, t) = J_0(\theta)(1 - \bar{r}^2)^{-\vartheta(\theta)} \quad (1.16)$$

Where  $\vartheta(\theta) = \frac{1}{2} - \frac{\theta}{\pi}$  is a parameter reflecting the uniformity of evaporation. When the contact angle is  $90^\circ$ , one obtains  $\vartheta = 0$ , implying that the evaporation flux is uniform along the surface of the droplet, while for small contact angles,  $\vartheta$  is close to 0.5, yielding a singularity in evaporation flux at the edge of the droplet. The approximate expression for  $J(\theta)$  has been given elsewhere by Hu and Larson [73] as:

$$J(\theta) = \frac{D_f(c_s - c_\infty)}{\rho R} \frac{t_F}{h_0} (0.27\theta^2 + 0.13) \left[ 0.6381 - 0.2239 \left( \theta - \frac{\pi}{4} \right)^2 \right] \quad (1.17)$$

Equation (1.17) has been derived from the first principle to describe evaporation of droplets at any contact angle  $0^\circ \leq \theta \leq 90^\circ$ . It can be seen that at a given contact angle the evaporation rate is inversely proportional to the contact line radius and direct proportional to vapour concentration difference  $c_s - c_\infty$  as well as the diffusivity  $D_f$ . The evaporation rate is weakly dependent on the contact angle  $\theta$  which shows even at zero contact angles the evaporation can still take place.

From Deegan's Model, the mass in the ring,  $M_r$  increase with time according to power law  $M_r \propto t^{\frac{2}{1+\vartheta(\theta)}}$  [4, 90]. Since the function  $\vartheta$  depends on contact angle, one would expect that as the contact angle vanishes,  $\vartheta$  becomes constant such that the rate at which the ring grows tends to diverge. It is this divergence which is responsible for the remaining 100% of microparticles to be very quickly transferred and deposited along the perimeter. Recently Dmitriev and Makarov [91] have studied the evaporation of droplets containing  $\text{SiO}_2$  and  $\text{Fe}_2\text{O}_3$  nanoparticles in salt

solution and found a three stage drying process. The stages are namely, uniform evaporation (82-96%), formation of a thin film and evaporation of a liquid from a thin film. The presence of particles in the droplets has been found to increase the evaporation rate in comparison to a droplet of a pure liquid due to enhanced pinning [92].

#### 1.4.2 Particle Ring Growth

According to a study by Chhasatia and Sun [3], adding particles in a pure liquid drop extends the constant contact area stage of evaporation due to accumulation of particles at the contact line region that further enhances pinning. The rate at which the particle ring width grows has been described by Maenosono et.al, [93] according to the equation (1.18)

$$\frac{dw_r}{dt} = \frac{\mathbb{Z}\omega_s V_0 J(r)}{(1-\phi)\sin\theta} \frac{c_0}{1-c_0} \quad (1.18)$$

Where  $\phi$  is the packing fraction,  $\omega_s$  is the ratio of particle to solvent velocities whose value is nearly equal to a unit,  $\mathbb{Z}$  is a constant relating the ring width and particle diameter,  $\theta$  contact angle,  $c_0$  is the concentration of the particles,  $J(r)$  is local evaporation rate and  $\omega_s$  is the solvent volume. From equation (1.18) the rate at which the ring width grows is inversely proportional to  $\sin\theta$  which shows that as the contact angle of the droplet vanishes the ring attains its highest growth rate  $\frac{dw_r}{dt}$ . Deegan [94] determined theoretically and experimentally the effect of gold particle size and initial volume fraction on the ring width produced by a constant volume on silicon substrate at ambient conditions. Theoretically, the ring width  $w_r$  was determined from the experimental parameters with an assumption that all the solute was transferred to the ring as [94]:

$$w_r = \sqrt{\frac{c_0 V_0}{\phi \pi R \tan \theta}} \quad (1.19)$$

where  $V_0$  is the initial volume of the drop,  $R$  is the initial radius of the drop and  $\phi$  is the packing fraction. The deposits left after evaporation showed a densely packed ring at high concentration and a ring filled with voids at low concentration as shown in figure 1.13. The ring widths were measured directly and ring heights were inferred using assumed values of the contact angle and showed strong dependence on the initial concentration by volume of the particles.

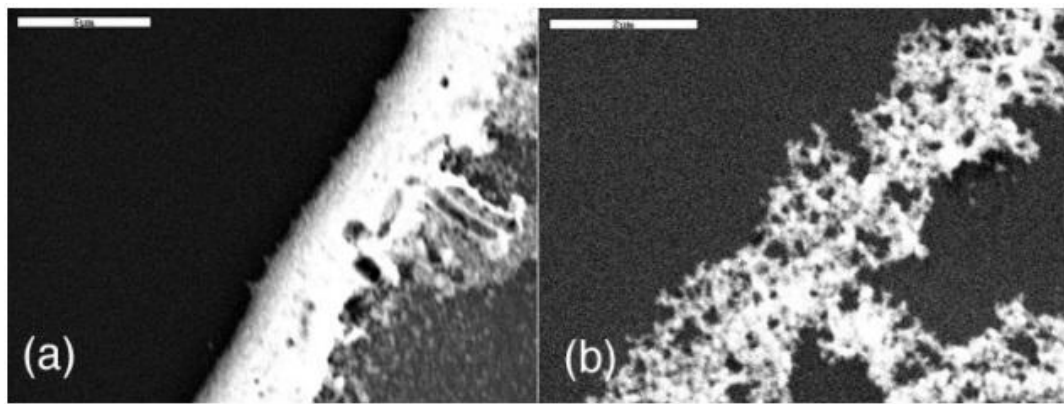


Figure 1.13: (a) Densely packed ring at  $c_0 = 3\%$  (and (b) wispy ring filled with voids at  $c_0 = 0.003\%$  of gold nanoparticles [94].

Popov [51] presented a complex analytical calculation to predict the spatial dimensions of the ring stain, which agrees with the simple argument that  $h_r$  and  $w_r$  are both proportional to the square root of the initial concentration of the particles in the droplet provided that all particles end up in the ring with.

The kinematics inside evaporating droplets and the final deposits is controlled by many factors. Conway et.al [6] in their study found that the kinematics behaviour of drying polystyrene bead suspension shifted towards that of pure water with decreasing initial suspension concentration. For droplets containing particles with diameter of  $2\mu\text{m}$ , evaporating with pinned triple line, Marín et.al, [95] showed that

the arrangement of particles in the ring stain is controlled by the speed with which they are carried to the periphery: For slow flow, dense, crystalline regions are built with either square or hexagonal packing; towards the end of the evaporation particle speeds increase above a critical speed  $u_c$  and particles do not have time to rearrange so the ring is randomly structured as shown as shown in figure 1.14.

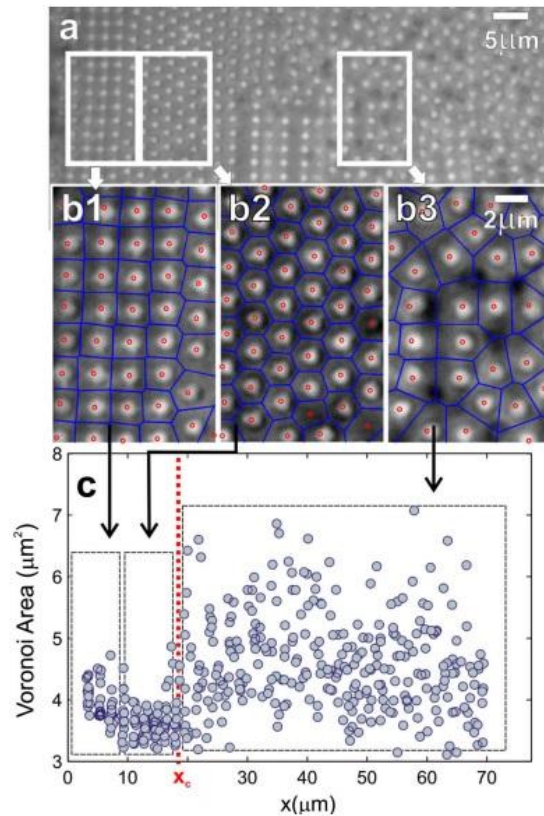


Figure 1.14: (a) Deposition patterns, (b1) square packed stain, (b2) hexagonal packed stain, (b3) disordered packed stain and (c) Voronoi cells as a function of the distance from the contact line [95].

The crystalline regions are also more densely packed than the random structure, as determined by the average Voronoi area around each particle. The critical speed is found by equating the diffusive and hydrodynamic time scales and is given by equation (1.20).

$$u_c \sim \frac{LD_f}{d_p^2} \sim \frac{1}{c_0^{1/3}} \frac{1}{d_p^3} \quad (1.20)$$

where  $L$  is the typical separation between particles, and  $D_f$  is the particle diffusion coefficient. There is a weak dependency on initial concentration but a much stronger dependency on particle size, which led the authors to comment that nanofluid droplets should always form crystalline deposits as the flow velocity will never exceed  $u_c$ .

Meanwhile Askounis et.al, [96] studied the effect of evaporation rate of monodisperse, spherical and non-porous  $\text{SiO}_2$  particles (80 nm diameter) for 0.125% weight fraction using silicon substrate. Their results reveal that increasing the drying rate led to stick-slip patterns, uniform rings and irregular shaped deposits at the periphery of the rings as shown in figure 1.15.

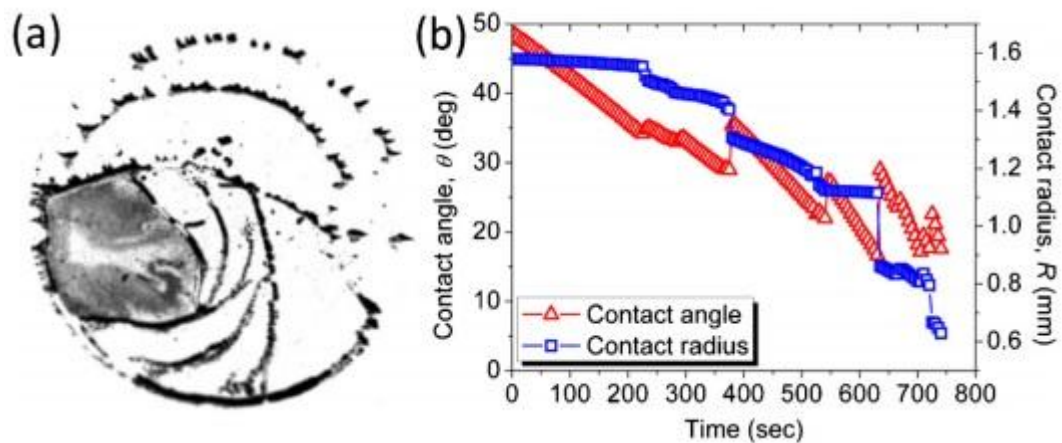


Figure 1.15: (a) Final deposit left after evaporation of 0.125%  $\text{SiO}_2$  particles at 750 mbar showing stick-slip patterns and (b) the change in contact angle and radius of the droplet with time [96].

Each circular deposit had a further structure showing four distinct regions: disordered outside, then a region with both square and hexagonal crystals, next a purely hexagonal region, and finally another disordered region. The authors proposed that as the smaller particles can approach much closer to the triple line

where the evaporative flux accelerates above the critical speed  $u_c$  and the effects of the disjoining pressure will be enhanced, these particles are frozen into position before they have time to crystallize. By reducing pressure, they increased particle flow and observed an increase in crystallinity. In contrast to Marín et.al, [95], here with much smaller particles, the flow is causing the ordering rather than disrupting it.

Most recently a study by Zhong and Duan [97] has found that by increasing the concentration of ethanol from 0% to 50% in binary mixture of graphite nanoparticle and water, the nanoparticles are carried to the droplet surface and form aggregates. The most striking feature is that the evaporation rate is not uniform over times being higher at early stages and lower stages which have not been shown before for pure water or ethanol. The final deposits patterns in figure 1.16 have been observed to depend on the concentration of ethanol, in the binary mixture.

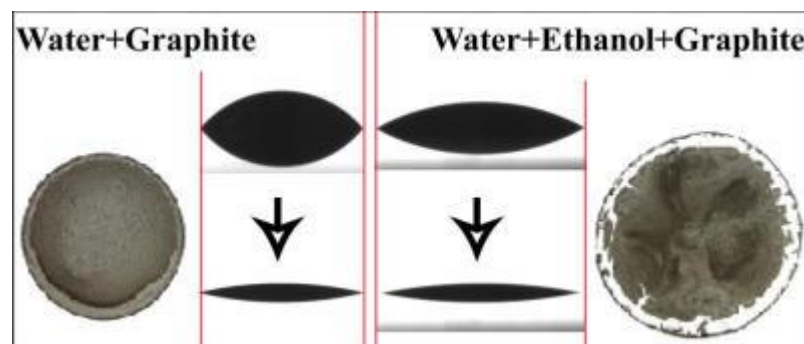


Figure 1.16: Deposits patterns dried from 0% of ethanol, 100% of water (left) and with binary mixture with 50% of ethanol and 50% of water (right) [97].

Introduction of ethanol is thought to change the surface tension at the liquid-gas interface causing recirculation. For example for pure water the deposit is uniformly distributed; for 10% ethanol microparticles, stay at the central region and detach from the ring; at 25% ethanol, the deposit approaches uniformity again; and at 50% ethanol there is detachment from the ring and most deposits stay at the center. There are three stages in the evaporation for water-ethanol mixture starting

with ethanol controlled evaporation; chaotic flows and vortices; followed by Marangoni dominated evaporation and ending with water dominated evaporation.

Yunker et.al, [98] have recently investigated the effect of varying the aspect ratio of prolate spheroidal particles on the structure and growth mechanisms of the particle deposits at the edge of a droplet. The width of the deposit was seen in all cases to increase linearly in time, but the roughness depended very sensitively on the eccentricity of the particles. Spherically-shaped particles created a compact, smooth deposit, whereas rodlike particles formed a rough, sparse, dendritic deposit. Interestingly, these suspension droplets are one of the first systems whose growth dynamics can be easily switched experimentally from one universality class to another according to Yunker et.al, [99]. The coffee ring effect can be suppressed by applying capillary forces [100]; inducing surface tension gradients to create Marangoni flow [101]; electrowetting (modification of the wetting properties of a hydrophobic with an applied electric field) [102]; and droplets smaller than a critical size [103].

### **1.4.3 Relative Humidity and Ring Stain Formation**

Chhasatia et.al, [104] observed variation in deposits patterns when relative humidity was varied during evaporation of droplets containing 1.1  $\mu\text{m}$  diameter carboxylate-modified polystyrene fluorescent beads. As the relative humidity was increased from 30% to 60%, the evaporation rates and contact angle decreased accordingly leading to a deterioration of circularity of the final deposits with increasing relative humidity as shown in figure 1.17. Recently Zeid and Brutin [105] have studied the evaporation of droplets containing blood and found that varying the relative humidity has a strong influence on the deposit patterns left after the drying process (figure 1.18). Results show that for a fixed blood droplet volume of  $\sim 14.2 \mu\text{L}$  while varying the relative humidity between 13.5% and 78.0%, the

contact angle of the droplets on the substrates varied from  $17.2^\circ$  to  $5.1^\circ$  respectively.

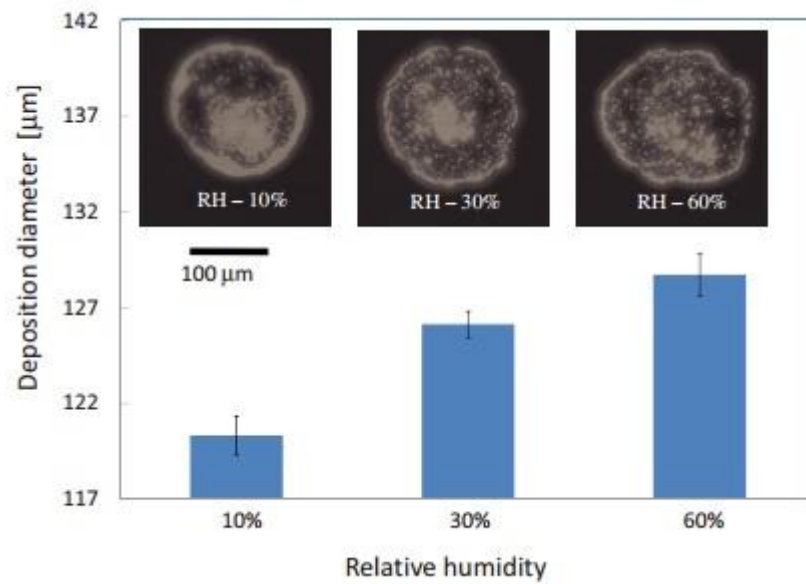


Figure 1.17: Relationship between final deposit diameter and the relative humidity [104].

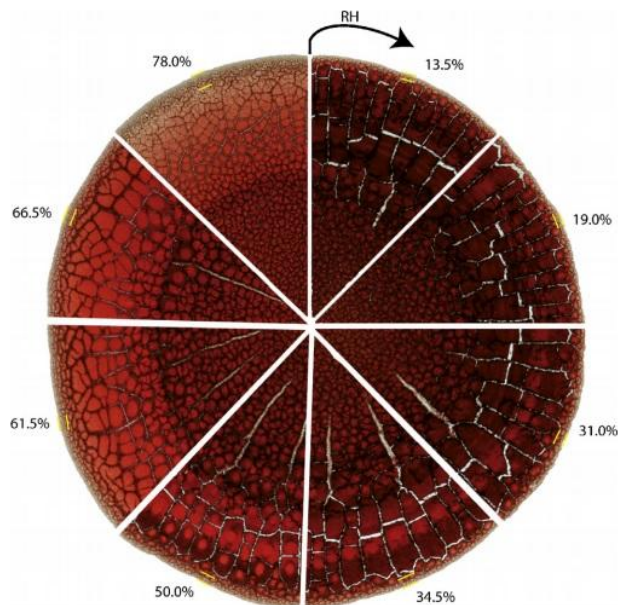


Figure 1.18: Final blood deposits patterns as a function of relative humidity [105]

Consequently the diameter of the final deposits also increases with an increase in relative humidity for a given initial concentration of blood. The authors have explained this in connection to how variation in relative humidity changes the contact angle of the droplets and evaporation rates. The relative humidity  $R_H$ , volume of the droplet  $V_0$ , radius of the droplet as a function of relative humidity  $R(R_H)$  and the contact angle  $\theta_{R_H} = 21(1 - R_H)$  are related by equation given as [104, 105]:

$$R(R_H) = \left( \frac{3V_0}{\pi} \frac{\sin^3[21(1 - R_H)]}{(2 + \cos\theta_{R_H})(1 - \cos\theta_{R_H})} \right)^{\frac{1}{3}} \quad (1.21)$$

Equation (1.21) has been obtained by substituting the expression for the variation of contact angle with relative humidity,  $\theta_{R_H} = 21(1 - R_H)$  in equation (1.3) and rearranging accordingly. Brutin [106] studied the evaporation of droplets containing 24nm diameter PS particles on aluminium substrate at atmospheric conditions while varying the relative humidity between 13% and 85%. It was observed that increasing the relative humidity had no effect on the pattern formation of the deposits.

#### **1.4.4 Forces between the particles in solution and the substrate**

In this section, the effect of surface electrostatic forces on the evaporating droplets and hence on the final deposits pattern is presented. Emphasis is put on van der Waals and double layer forces. Van der Waal forces are weaker, short range forces of attraction between molecules, atoms and surfaces due to fluctuating polarizations. Van der Waal forces are not sensitive to variations in electrolyte concentration as well as to the pH [107]. Meanwhile double layers forces are long range force between charged objects in liquid whose strength increase with the magnitude of electric surface potential. Van der Waal forces and double layer forces

are both explained by Derjaguin-Landau-Verwey-Overbeek (DLVO) theory [108, 109].

When particles are in a solution, dissolution of ionic groups or preferential adsorption of ions both induce surface charges on their solid surface, whose surface potential,  $\psi_p$  and surface charge density,  $\sigma_p$  are related by Gouy-Chapman relation [103, 110, 111].

$$\sigma_p = \frac{2\varepsilon\varepsilon_0k_B T}{e\kappa^{-1}} \sinh\left(\frac{e\psi_p}{2k_B T}\right) \quad (1.22)$$

Where  $\varepsilon\varepsilon_0$  is the total permittivity of the water,  $k_B$  the Boltzmann constant,  $T$  the temperature,  $e$  the electronic unit charge, and  $\kappa^{-1}$  the Debye length defined by;

$$\kappa^{-1} = \sqrt{\frac{\varepsilon\varepsilon_0k_B T}{2N_A e^2 I}} \quad (1.23)$$

Where  $N_A$  and  $I$  are the Avogadro's number and ionic strength of the solution respectively. When in solution, microparticle interactions are explained by DLVO theory of colloidal stability [108, 109]. According to this theory colloidal particles in an evaporating drop experience van der Waals and electrostatic interactions with other particles, as well as with the substrate. The particle Van der Waals force,  $F_{vdw}$  and electrostatic force,  $F_{el}$  is given in equation (1.24) and (1.25) respectively [103].

$$F_{vdw} = \frac{1}{12} Ad_p^3 \frac{\alpha_{rtd}}{z^2(y + d_p)^2} \quad (1.24)$$

$$F_{el} = -\frac{128\pi d_p \gamma_s \gamma_p n_e k_B T \kappa^{-1}}{2} \exp\left(-\frac{y}{\kappa^{-1}}\right) \quad (1.25)$$

Where  $d_p$  is the diameter of the particle,  $n_e$  the number concentration of the counter ions far away,  $y$  the distance between the particle and the substrate,  $\gamma_p$  and  $\gamma_s$  are functions of the surface potential of particle and substrate respectively.

The total DLVO force is the sum of forces in equation (1.24) and (1.25). The zeta potential of microparticles is determined experimentally by measuring their electrophoretic mobility,  $U_e$  of particles using the M3-PALS technique. The electrophoretic mobility is governed by the strength of the electric field, the dielectric constant of the electrolyte,  $\epsilon$  viscosity of the electrolyte,  $\eta$  and  $\gamma_p$  the zeta potential of the particles. The combination of these factors form the well-known Henry's equation [112] given by equation (1.26).

$$U_e = \frac{2\epsilon\gamma_p f(\kappa a)}{3\eta} \quad (1.26)$$

Where  $f(\kappa a)$  is the Henry's function, and  $(\kappa a)$  is the measure of the ratio of the particle hydrodynamic radius to the Debye length. The Henry's function has two values, 1.0 and 1.5 depending on the media used. For aqueous and moderate electrolyte media concentration,  $f(\kappa a) = 1.5$  and  $f(\kappa a) = 1.0$  for non-aqueous media. The forces between the particles in solution and the substrate in an evaporation droplets have previously been studied [3, 113-114].

Figure 1.19 shows the relationship between the interaction energy,  $W$  against the profiles of the DLVO interaction. The following are the basic features from figure 1.19:

- Strong long range repulsion peaking between 1 and 5nm at energy barrier which is common for highly charged surfaces in dilute electrolytes.
- For more concentrated electrolytic solutions, there exist a significant secondary minimum beyond 3nm before the energy barrier. The minimum potential energy at contact is called primary minimum. The magnitude of the energy barrier determines the kinetic stability of the colloidal system. Particles will remain dispersed in a solution or undergo coagulation/flocculation depending on the energy barrier.

- As the surface charge,  $\sigma$  approaches zero the net interaction curve approaches that of Van der Waal curve which will lead to strong attraction between two surfaces.

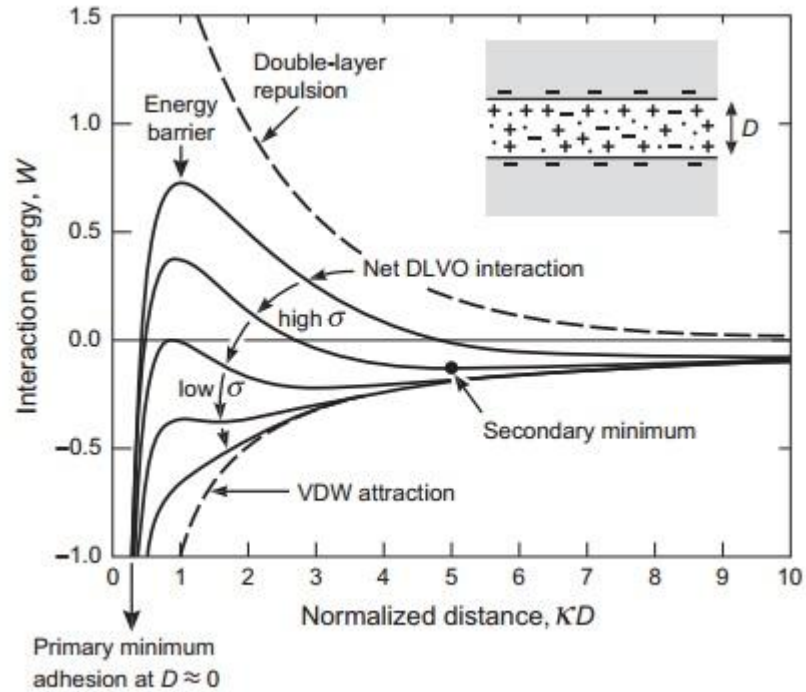


Figure 1.19: Schematic interaction energy versus distance profiles of the DLVO interaction. The actual magnitude of the energy  $W$  is proportional to the particle size or interaction area [107].

Yan et.al, [115] have observed the evaporation of droplets to study the self-assembly of charged 860nm monodisperse polystyrene microparticles with a non-ionic amphiphilic surfactant on positive and negative substrates whose deposit is shown in figure 1.20.

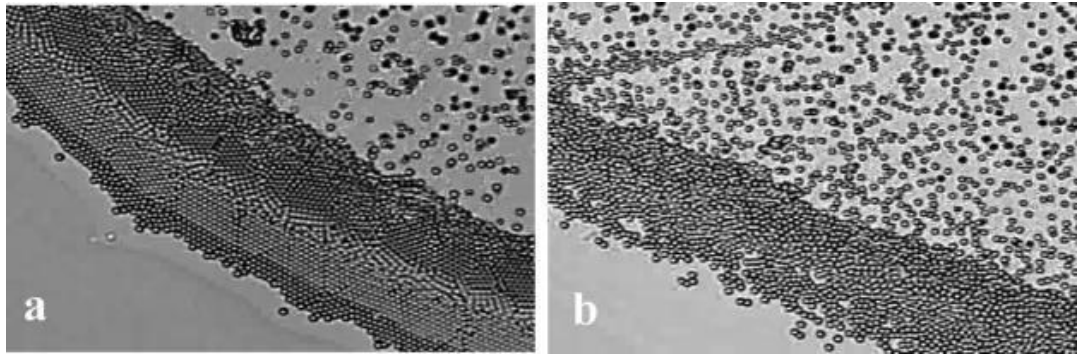


Figure 1.20: Deposit patterns from a suspension of 0.005% volume fraction of negatively charged PS microparticles and surfactant on (a) negatively charged glass substrate and (b) a positively charged glass substrate [115].

Results reveal that negatively charged microparticles are highly mobile and assemble into ordered structures on negative charged substrate in contrast to disordered structures on positive substrate due to strong adhesion on the surface and low mobility as in figure 1.20.

## **1.5 Evaporation of Droplets Containing Polymers**

In the previous section 1.3 and 1.4 the evaporation of droplets of pure liquids and those containing microparticles have been reviewed. In this section the evaporation of droplets of pure polymer solution and of binary mixtures with microparticles are considered. The behaviour of PEO polymer solution and subsequent evaporation mixed with microparticles will be described.

### **1.5.1 What is a polymer?**

A polymer is a large molecule constructed from many smaller structural units called monomers, covalently bonded together in any conceivable pattern [116]. Polymers are very often linear, so each monomer is bonded only 2 others. There are branched polymers too but we do not consider them in this thesis. The essential requirement for a small molecule to qualify as a monomer is the possession of two or more bonding sites through which each monomer can be linked to others to form

a polymer chain. Figure 1.21 shows sample examples of polymers, monomers and their repeating units building the polymer. The entire polymer structures of examples in figure 1.21 are generated during polymerization, a process in which the repeating units are covalently bonded together [117].

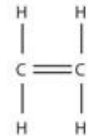
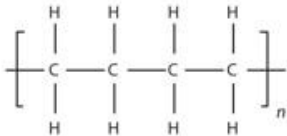
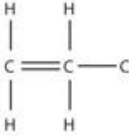
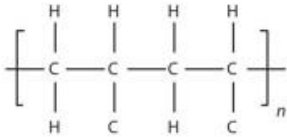
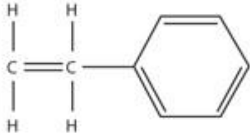
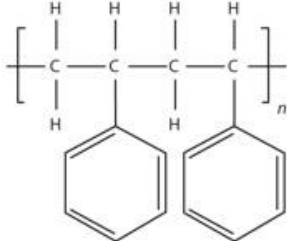
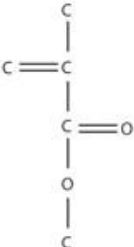
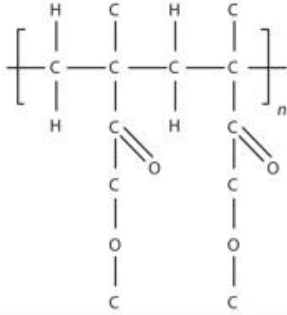
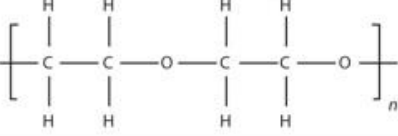
Monomer	Monomer Name	Polymer	Polymer Name
	ethylene		poly(ethylene)
	propylene		poly(propylene)
	styrene		poly(styrene)
	methyl methacrylate		poly(methyl methacrylate)
	ethylene oxide		poly(ethylene oxide)

Figure 1.21: Examples of polymer molecule with their monomers as well as the repeating units.

The molar mass of these polymers are determined by the so called degree of polymerization, which is the number of monomers in one polymer molecule. If the

molar mass of the monomer is denoted by  $M_{\text{mom}}$  and the degree of polymerization by  $N_{\text{pol}}$ , then the molar mass of a given polymer,  $M_{\text{pol}} = N_{\text{pol}} M_{\text{mom}}$ . For example polyethylene molecule consisting of  $N_{\text{pol}} = 800$  monomer each with  $M_{\text{mom}} = 28 \text{g mol}^{-1}$  has a molar mass of  $M_{\text{pol}} = 22400 \text{g mol}^{-1}$ . Polymers are classified depending on their origin (natural, semi-synthetic and synthetic), thermal response (thermoplastic and thermosetting), physical properties (such as low density and tensile strength) and for their applications (rubber, fibers and plastics), polymer structure (homochain or heterochain) and mechanism of polymerization (addition or condensation) [116-119].

Natural polymers such as cellulose and proteins form the basis of plant and animal life. Thermoplastic polymers are polymers when heated soften and can be processed in any desired form. Polystyrene, polyethylene, polypropylene and polyvinyl chloride are examples of thermoplastic polymers.

Thermosets are polymers which harden when two components are heated together due to crosslinking. Thermoset polymers such as epoxy, phenol-formaldehyde resins, and unsaturated polyesters are suitable for material applications involving coatings, adhesives and composites because they can resist mechanical deformation and solvent attack. The physical properties of polymers such as plastic flow, elasticity, softening point, resistance to plastic flow and tensile strengths are determined by the strengths of the intermolecular forces between the chains and temperature and also polymer molecular weight, branched/linear. At low temperatures, many polymers are hard and behave like glass due to the fact that the movements of polymer segments relative to each other are very slow. The particular value of temperature below which the polymer behaves like a glass is called glass transition temperature,  $T_g$  [117].

In the absence of solvent, polymers are in liquid state above the glass transition temperature called polymer melts. Polymer melts are characterized by heavily overlapping chains and elastic networks due to temporary entanglement of the chains. In semi-crystalline polymer chains fold together and form ordered regions called lamellae, which themselves aggregate to form spheroidal structures called spherulites [120]. Between these lamellae there exists a region of an amorphous solid as shown in figure 1.22. The spherulites form coloured patterns due to birefringence when viewed between crossed polarizers (maltese cross) in an optical microscope. In the present study we use a polymer PEO whose properties in powder and solution form are detailed explained in section 1.5.2.

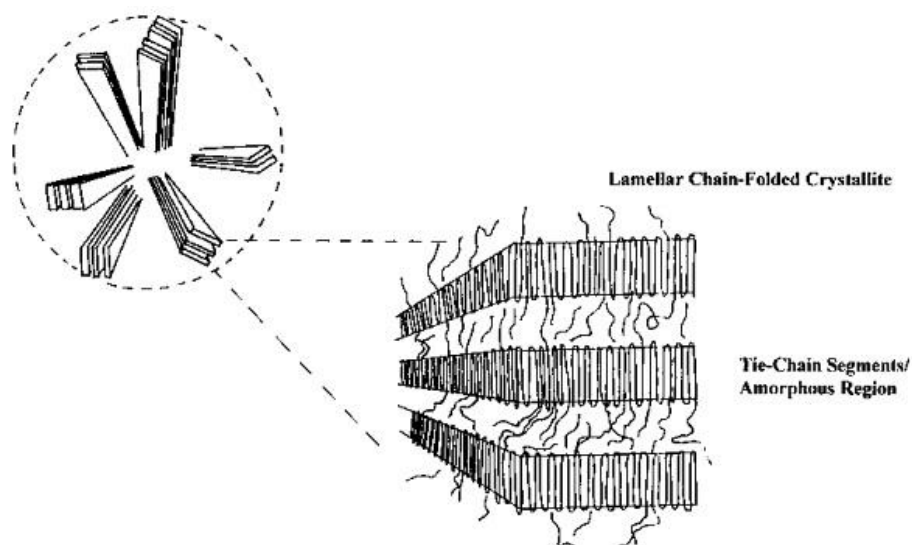


Figure 1.22: Spherulites showing lamella chain folded platelets [120].

### 1.5.2 Behaviour of PEO solutions

Poly(ethylene oxide) is a semi-crystalline polymer, a unique member of reactive epoxy resins (polyepoxides) with a general molecular formula of  $X-(OCH_2H_2)_j-Y$  [121, 122]. The end groups X and Y are hydroxyl one for lower molar mass. For value of j up to 150, polymers with lower molar masses are known as polyethylene glycol (PEG) and those with higher molar mass are called Poly(ethylene oxide). For

the sake of avoiding confusion between PEG and PEO in the entire document "PEO" will be used. PEO with molar mass between 100,000 g/mol and 1,200,000 g/mol (which I will abbreviate to 100K and 1200K) are white powders with melting point of 65°C and glass transition temperature of -67°C [123].

PEO is soluble in water and organic solvents such as chloroform and dimethylformamide and insoluble in aliphatic hydrocarbons [122]. The solubility of PEO however depends on the chain length which is proportional to molar mass [124, 125]. As a result for high concentrated PEO solution, solvent such as water acts as a plasticiser making PEO tough. For dilute solutions PEO dissolves, but small undissolved clusters often remain when water is used as solvent which upon filtration reappears and are found to be time dependent [126, 127]. Another important property of PEO is the viscosity. Yu et.al, [128] carried out an experiment to investigate the viscoelastic properties of PEO using the mixture of water, propylene glycol and glycerol formal (glyform) as solvent while varying the molar masses of PEO and sodium chloride salt concentration. Experimental results reveals that viscoelastic properties (viscosity and dynamic moduli) is a function of molar masses of PEO, showing liquid like behaviour for low molar mass PEO (600K) and elasticity for higher molar mass PEO (5000K) due to entanglement. In another study by Torres et.al, [129] addition of anionic surfactants in a PEO solution above the critical aggregation concentration have been found to increase the shear viscosity due to coil expansion of PEO and strengthening of interchain interactions. Critical aggregation concentration is the concentration corresponding to the appearance of polyelectrolyte/surfactant complexes in the bulk. Above the critical aggregates concentration the micellar aggregates attach to the polymer chain.

The dependence of viscosity on shear rate of PEO solutions have previously been studied by Kalashnikov [130] as a function of PEO concentration, molar mass and temperature of the solution. Shear rate for dilute concentration was found to agree

with theoretical predictions (by molecular dispersion) while it deviates for higher molar mass PEO due to shear-thinning viscosity. The intrinsic viscosity and viscoelastic properties of PEO solution depends also on the mechanical history of preparing the solutions [131]. By mechanical history here is referred to where the PEO solutions were prepared by shaking or stirring. The rheological properties are independent of mechanical history provided the concentrations and molar masses of PEO are kept low (<300K). Stirring or shaking influences PEO chain scission and aggregations. Other studies have also found PEO solutions to undergo mechanical degradations in laminar and turbulent flows and degradation increases when the temperature increases accordingly [132-134]. Care has to be taken especially in mixing and filtration so that the shear rate value chosen is less than that required to damage PEO [135].

### **1.5.3 PEO droplets**

In this section the evaporation of droplets of PEO solution are considered. Unlike evaporation of droplets containing colloidal suspension where coffee ring stain is common, evaporation of droplets of PEO is quite different. The experimental studies indicates that evaporation of droplets of PEO involves pinned drying followed by de-wetting of the droplet then lift up (bootstrap deposition) before shrinking to attain final drying stage as shown in figure 1.23.

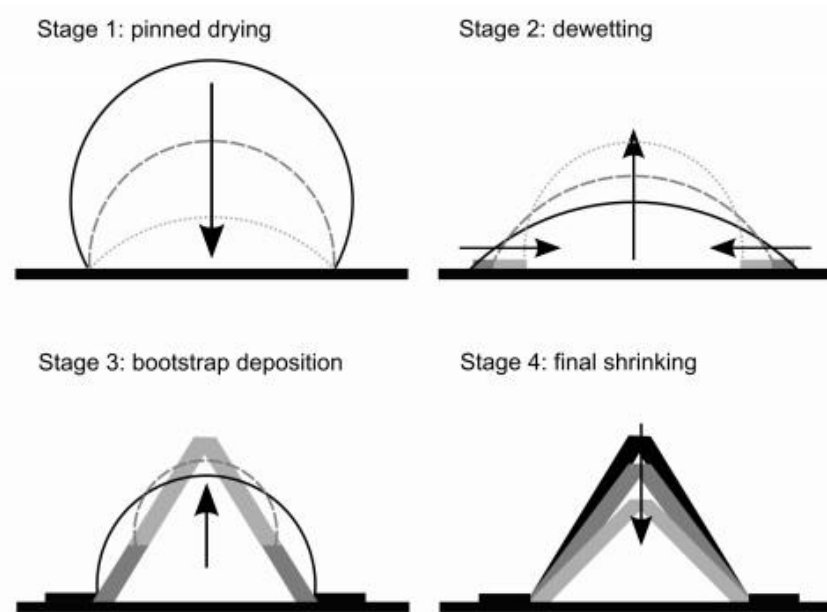


Figure 1.23: Drying stages of PEO solutions and phase separation. Thin lines indicate liquid surfaces, thick regions represent solid deposits. Progress within each stage is from solid black to dashed dark grey to dotted light grey. Image from [136].

Phase separation may be induced chemically or physically from initially homogeneous system by the process known as nucleation and growth [29]. In another study, Baldwin et.al, [137] systematically varied relative humidity, temperature, pressure droplet volume and initial contact angle of evaporating PEO droplets. The results for these parameters were all represented by a Péclet number, which is a dimensionless number which compares relative effects of evaporation and diffusion as observed previous in reference [136].

Experimental results shows that the behaviour of drying PEO droplets and final deposits strongly depends on the initial concentration of PEO solution and the value of Péclet number forming either puddle or pillar as shown on the phase diagram figure 1.24.

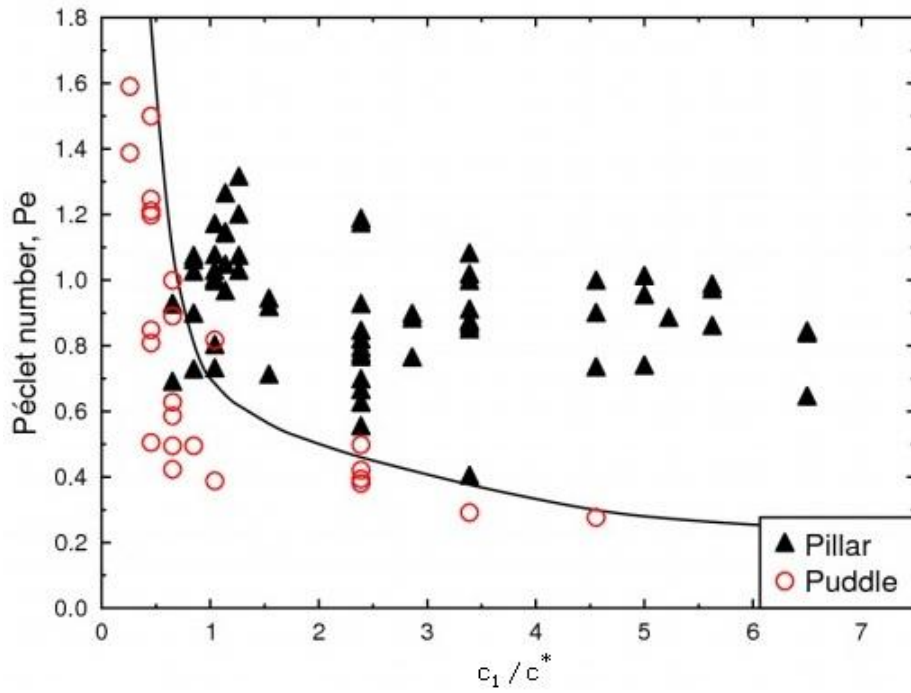


Figure 1.24: The relationship between Péclet number,  $Pe$  and the initial concentration,  $c_1$  normalized to overlap concentration,  $c^*$ . Puddles and pillars are formed with a line roughly between them showing the transition region [137].

The initial concentration,  $c_1$  in figure 1.24 was normalized to overlap concentration,  $c^*$  which is defined as the concentration at which the neighbouring polymer coils start to overlap with each other and is determined according to equation (1.27) [138], where,  $R_g$  is the radius of gyration,  $N_A$  is the Avogadro's number and,  $M_{pol}$  is the molar mass of the polymer. The value of  $R_g$  is also related to  $M_{pol}$  by equation (1.28).

$$c^* = \frac{3M_{pol}}{4N_A \pi R_g^3} \quad (1.27)$$

$$R_g = 0.215 M_{pol}^{0.583 \pm 0.031} \text{ \AA} \quad (1.28)$$

Hu et.al, [139] carried out a study to investigate the effect of substrate temperature between 30°C to 80°C on the evaporation of PEO droplets. It was found that at 30°C the PEO droplets were pinned and crystalline spherulites were observed to form beginning from the edge towards the center leaving ring-like deposits. Beyond 50°C the droplets were first pinned and later receded towards the center and at 80°C the deposits were all found at the central region of the droplets due to Marangoni flow. Receding of the droplets was explained in terms of decrease in viscosity of PEO solution with increasing temperature.

#### **1.5.4 PEO and particle droplets**

In section 1.3, 1.4 and 1.5.3 we have looked at the evaporation of droplets of pure liquid, liquid with particles and PEO solutions respectively. This section deals with mixing of pure liquid with particles and PEO to obtain a mixture. There are few previous studies reported on the evaporation of droplets containing PEO solution mixed with particles. Choi et.al, [140] studied the effect of adding 1 $\mu$ m, 6 $\mu$ m polystyrene microparticles and positively charged 9-13 glass beads on the evaporation of droplets containing 200K and 900K PEO on microscope glass slide substrate and the final deposits are shown in figure 1.25. A control experiment was also performed with droplets of water containing polystyrene microparticles and glass beads. Results shows that the deposit pattern varied depending on the particle size as well as the viscosity of the fluid due to the competition between the outward flow (Deegan flow ) and inward flow due to capillary and/ or buoyant force acting on the particles trapped at the liquid interface.

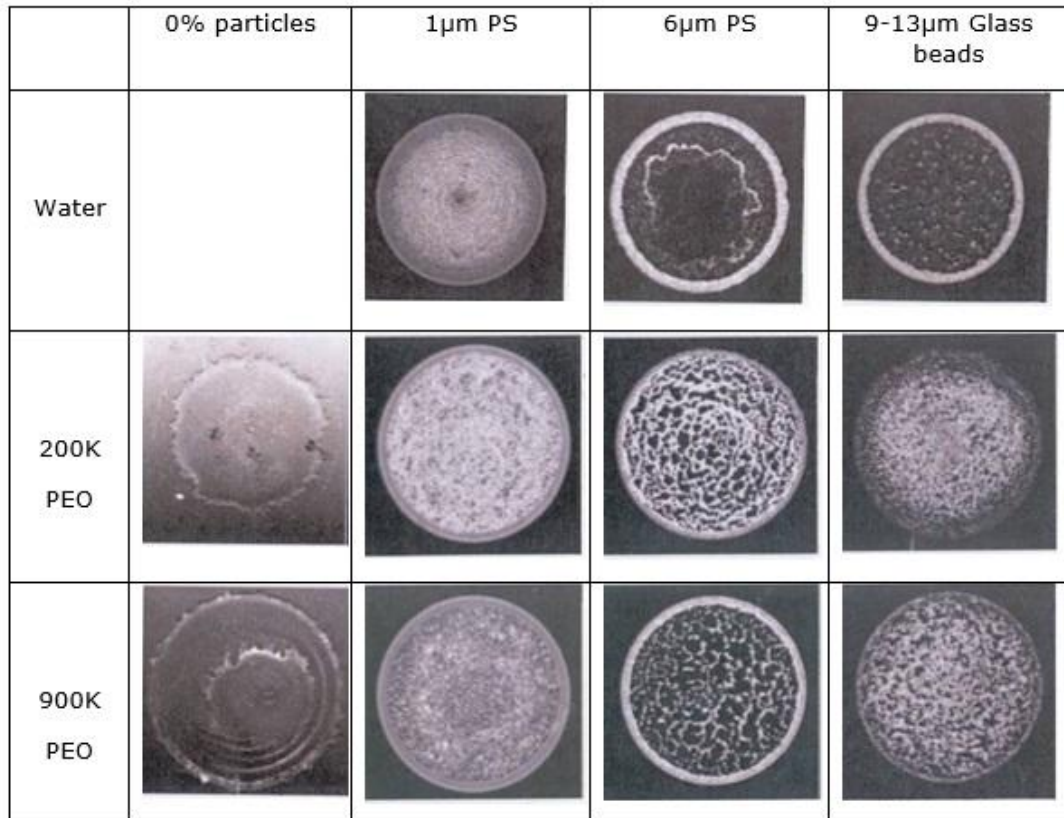


Figure 1.25: Final deposits from drying polystyrene particles, glass bead in water and when are mixed with 200K and 900K of PEO [140].

## 1.6 The Present Work

Drying droplets of liquid containing a suspension of microparticles leaves a coffee-ring stain [1-8]. Popov [51] presented a complex analytical calculation to predict the spatial dimensions of the ring stain, which agrees with the simple argument that the ring height  $h_r$  and ring width  $w_r$  are both proportional to the square root of the initial concentration  $c_0$  of the particles in the droplet provided that all particles end up in the ring. The simple argument predicts that the ring height  $h_r$  and ring width  $w_r$  as shown in figure 1.26 scales according to equations (1.29) and (1.30) whose derivations are shown in Appendix B.

$$w_r \propto c_0^{0.5} \tag{1.29}$$

$$h_r \propto c_0^{0.5} \quad (1.30)$$

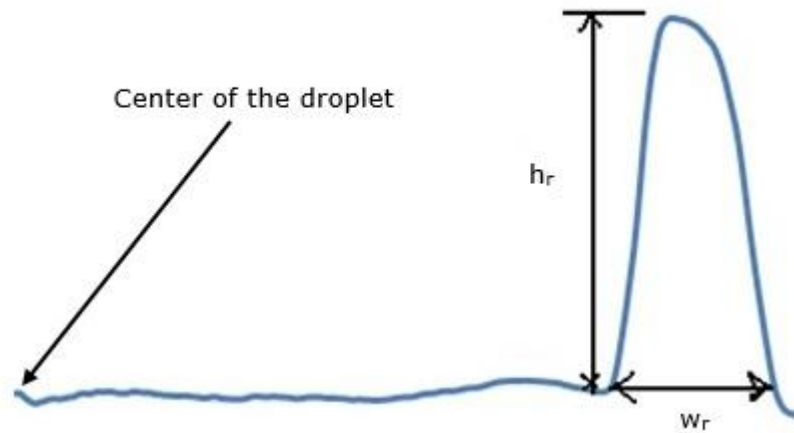


Figure 1.26: A radial profile of a deposit of a dried droplet showing the ring width,  $w_r$  and its height,  $h_r$ .

Equations (1.29) and (1.30) hold assuming that (i) all the particles end up in the ring, (ii) the cross-sectional shape of the deposit does not depend on the initial concentration  $c_0$  of the particles in the droplet and (iii) the packing fraction  $\phi$  of the final deposit is constant. Packing fraction is the fraction of volume in a crystal structure that is occupied by constituent particles. It is dimensionless and always less than unity. For the best of my knowledge there has been one attempt to experimentally verify equation (1.29) and not equation (1.30) by Deegan [141] using gold nanoparticles. It is also worth noting that experiments were carried out at atmospheric conditions without varying other parameters such as initial contact angle and evaporation rate to account on the ring stain scaling prediction. The purpose of the present study was therefore to:

- a) Investigate how robust the ring-stain scaling predictions are by varying experimentally controlled parameters, including particle size, concentration, evaporation rate, contact angle and orientations of the droplets.

- b) Investigate the evaporation kinematics of droplets drying containing PS microparticles

Meanwhile drying droplets of liquid containing a suspension of microparticles leaves a coffee-ring stain [1-8], drying of droplets of aqueous solutions of PEO form a flat deposit or a tall "central pillar" depending on the concentration of the polymer, its molecular weight, relative humidity and drying rate [137] as shown in figure 1.27.



Figure 1.27: (a) The tall central deposit called pillar forms from drying  $c_1 = 10\%$  of PEO and (b) Puddle like deposits when  $c_1 = 2\%$  of PEO is dried at atmospheric conditions.

Choi et.al, [140] studied the drying of PS microparticles dispersed in a PEO polymer solution. Two molecular weight solutions were considered (200 and 900kg/mole) at very low concentration. However, there were several experimental parameters not systematically investigated such as higher concentrations, microparticles sizes and drying rate. The purpose of the present study was therefore:

- a) To investigate the effect of PEO concentration on ring stain formation and evaporation mechanisms of the droplets containing PS microparticles
- b) To investigate the effect of the size of the PS microparticles and their concentration on the unusual drying mechanisms of PEO droplet.

## **Chapter 2**

### **Experimental Techniques and Methods**

## **2.1 Introduction**

This chapter is divided into three sections that describe the experimental techniques and methods used to acquire and analyze experimental data. The first section deals with the evaporation of polystyrene microparticles droplets to investigate the effects of droplets orientation, microparticle sizes, relative humidity, contact angle, concentration of the microparticles and evaporation rates on the ring dimensions of the final deposits. The preparation of samples through mixing with deionized water and experiments at atmospheric conditions and high evaporation rates using low pressure chamber are described. The experimental techniques includes contact profilometry for assessing the surface depth profiles of the deposits, scanning electron microscope for surface morphology characterization, sputter coater for sample preparation, dynamic light scattering for zeta potential measurements, CCD and microscopy imaging and drop shape analyzer for characterizing the contact angles of the droplet.

In the second section the kinematics of the droplet drying is described using conventional microscope imaging technique, and Spectral domain optical coherence tomography (OCT) combined with a pressure chamber. The section intends to give more detailed explanations of the findings in section one especially at low pressure by imaging and tracking the individual microparticles of the entire droplets and at the edge using time resolved particle tracking velocimetry technique and Image J software. In section three, the effect of polystyrene (PS) microparticles on the unusual drying of PEO is studied. The preparation of PEO through mixing with deionized water and filtration followed by mixing with polystyrene microparticles suspension is described. The experimental drying of the droplets through varying concentration and particle sizes are described.

## **2.2 Sample Preparation**

### **2.2.1 PS Microparticle Suspensions**

The colloidal suspensions used in this study were commercial microparticles based on monodisperse PS microparticles with density of  $1.050 \text{ gcm}^{-3}$  at  $20^\circ\text{C}$  (Sigma-Aldrich Corporation., UK). The microparticle sizes were  $0.1\mu\text{m}$  ( $\sigma \leq 0.01\mu\text{m}$ ),  $0.2\mu\text{m}$  ( $\sigma < 0.05\mu\text{m}$ ),  $0.5\mu\text{m}$  ( $\sigma \leq 0.05\mu\text{m}$ ),  $2\mu\text{m}$  ( $\sigma \leq 0.05\mu\text{m}$ ) and  $5\mu\text{m}$  ( $\sigma \leq 0.1\mu\text{m}$ ) where  $\sigma$  is the standard deviation. In order to simplify the dilution process and make solution over a wide range of concentration of polystyrene microparticles between 10% and 0.001% calculations were first made. Calculations were limited to a total mass of 1g after dilution, the limit posed by the volume of 1 mL Cryotube vials used to store the solutions. A known mass of the original concentration of solids was carefully measured into a Cryotube vial using a Kern mass balance (ALJ160-4NM, UK) to within 0.1 milligram, then deionized water was added according to the ratio by mass calculated before. The diluted solution resulted in a colloidal suspension with a concentration of 0.009%, 0.002%, 0.02%, 0.1%, 0.25%, 0.5%, 1% and 2% by mass. The colloidal suspension in the Cryotube vial were then left in a roller mixer (T6-Stuart., UK) for a minimum of 12 hours to minimize the agglomeration of particles.

### **2.2.2 PS-PEO Solution**

In this section PS microparticle suspensions were mixed with PEO (100K) polymer solution in order to investigate the effect of added particles and their sizes on the unusual drying of PEO. In the second part of this section the effect of PEO on the ring stain formation were also investigated through varying the concentration of PEO to a fixed number density of polystyrene microparticles. To make the PEO solutions, the PEO powder (Sigma-Aldrich., UK) of mass of 1g, 2g, and 3g were weighed in 14 mL vials with a Kern mass balance, then 9g, 8g and 7g of deionized

water were added respectively. The mixtures resulted into 10%, 20% and 30% respectively of PEO by mass.

The vial lids were sealed with Nescofilm to prevent a change in the concentration of PEO due to evaporation. The mixtures were left on the roller mixer for at least 24 hours before they were filtered to remove any clusters. The filtration process was performed using an adjustable speed filtration pump (11Plus, Harvard Apparatus., UK) and Minisart single use filters (NML, Sartorius., UK) of pore diameter  $\sim 0.45\mu\text{m}$ . To retain the physical properties of PEO, filtration was performed at 0.1mL per hour according to available reported literature. To obtain desired PS-PEO solution, first the mass ratio between PEO, PS and deionized water had to be calculated. The  $C_0$  of  $0.5\mu\text{m}$  and  $5\mu\text{m}$  polystyrene microparticles were chosen to given 1%, 2%, 3% 4% and 5% in PS-PEO solution while PEO was in the range between 2% to 18%. The total mass of the PS-PEO solution was limited to 1g due to the size of Cryotube vial used. The PEO and PS solution were then weighed on the Kern mass balance, and placed in the roller mixer for at least 48 hours to mix thoroughly before use.

### **2.2.3 Substrates**

In order to study the effect of the substrate surface on the ring dimensions, different substrates were used such as microscope glass slides and cover slips. Microscope glass slides were purchased from Sail Lab Co. Ltd (China) with dimensions of (1.0-1.2)x25.4x76.2 mm. Another type of microscope glass slide with dimension of (1.0-1.2)x26x76 mm was purchased from Thermo Scientific (Menzel-Glaser). Microscope glass cover slips with dimension of (0.13-0.17)x22x22 mm and (0.13-0.17) x24x50mm were purchased from Fischer Scientific and Chance Proper Ltd respectively. The substrates were cleaned to alter wetting properties of the surface with 2% of Decon 90 followed by rinsing with iso-propanol and finally blowing with stream of nitrogen gas at high pressure. For the substrates which

were not cleaned with the procedure above, stream of nitrogen gas was blown to remove any dust. The wetting properties of these substrate were determined by measuring the contact angle of the water droplets deposited there as described below.

The initial static and dynamic contact angles of the droplets on the substrates used were determined by optical tensiometry using drop shape analysis (DSA) contact angle meter ( DSA 10-MK2, KRÜSS, Germany). The basic elements of DSA contact angle meter are shown in figure 2.1.

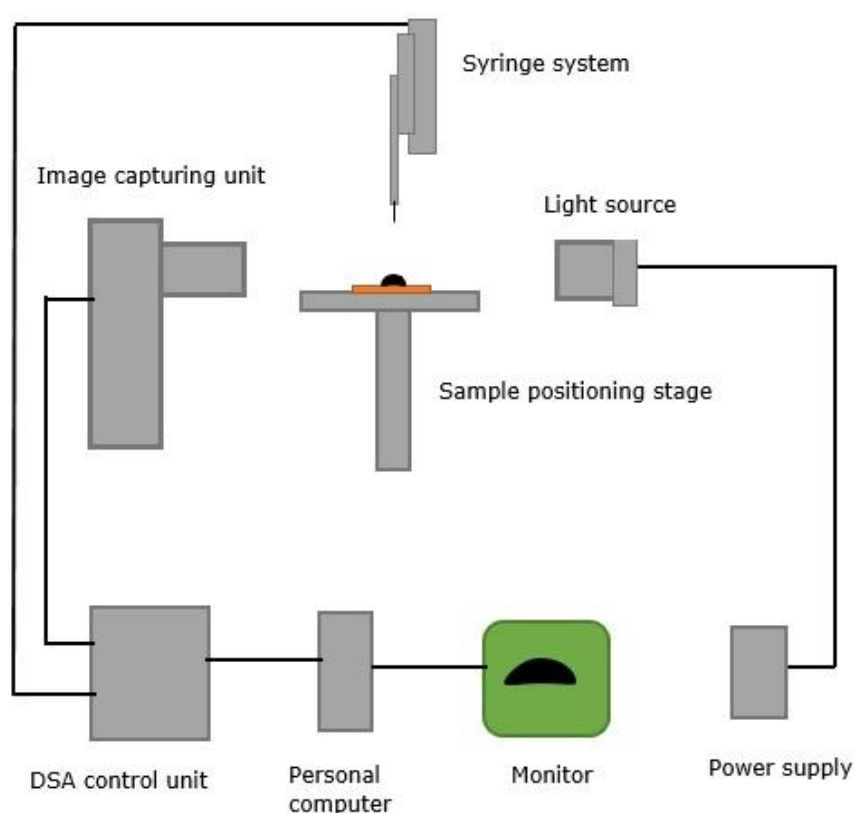


Figure 2.1: Schematic presentation of drop shape analysis system experimental setup.

It comprises of a light source, sample positioning stage, personal computer, monitor, syringe system, DSA control unit, power supply and image capturing unit comprising of lenses, zoom and camera to enable the side view of the droplet. The light source was powered by a stabilized power supply (Model E30/2, Farnell

Instruments Ltd., UK). During data acquisition, the syringe and imaging units were controlled by DSA software in the personal computer integrated with syringe and video camera drivers in the DSA 10-MK2 control unit.

To measure the initial static contact angle, 20  $\mu\text{L}$  of water droplet was deposited on the microscope glass slides or cover glass slips using a 1mL syringe controlled by DSA software. The dynamic contact angles were determined by adding and removing volume of the liquid method. The droplet, as viewed on the grabber window on the monitor was adjusted to obtain maximum resolution through zooming and focusing knobs on the image capturing unit. The images to be analyzed were captured by a camera integrated with DSA software at a resolution of 780X580 pixel. The contact angle was obtained in the DSA software by measuring the angle made between the tangent to the profile and the solid surface at the point of contact through fitting the droplet by variety of methods as described below.

Our experiments used some substrates whose contact angles were less than  $30^\circ$  and smaller volume droplets with dimensions smaller than the capillary length to maintain the spherical cap. Due to limitations of some methods, the contact angles reported in this thesis were determined using height/width and circle fitting method.

#### **2.2.4 pH Measurement**

The concentration of hydrogen ions in the PS microparticles suspension was measured using Ag/AgCl glass electrode (pHG311, Denmark) and ion meter (PHM250 Ion Analyzer, Denmark). The electrodes were calibrated before taking the measurements using technical buffer solutions of pH 4.0, 7.0 and 10.0 at a temperature of  $\sim 22.0^\circ\text{C}$ . The actual pH values were automatically computed according to the temperature measured in auto mode. To ensure the accuracy of the pH value measured between two consecutive experiments, the electrode was

thoroughly rinsed with distilled water followed by wiping with medical wipes (Kimberly-Clark professionals). Each experiment was repeated three times check the reproducibility of the results. The experiments were carried out for 0.1, 0.2, 0.5, 2 and 5 $\mu$ m polystyrene microparticles in the concentrations by mass between 0.001% and 0.1%.

### **2.2.5 Zeta and Surface Potential Measurement**

The zeta potentials of polystyrene microparticles were measured using Zetasizer Nano S (Malvern Instruments Ltd., Malvern, UK) employing M3-PALS technique. The Zetasizer software (Malvern Instruments Ltd) was used to control the system during all measurements and process data to produce zeta potentials using Standard Operating Procedures (SOP). The solutions prepared in section 2.2.1 were used in this section for the purpose of determining the zeta potentials of the microparticles. To measure the surface zeta potential a cover slip glass of dimensions 1.5x4x7 mm was prepared using diamond scribe. The surface zeta potential of the substrates used was measured using the same instrument used to zeta potential.

### **2.3 Evaporation of Sessile Droplets**

This section explains the experimental methods and technique used to study the effect of evaporation rate, droplet orientation, particle sizes, concentration and contact angle on the ring stain formation using PS microparticles droplets. It also give details on how the acquired data were analyzed to assess the extent to which each factor affects the ring dimensions both at atmospheric conditions and reduced pressures.

#### **2.3.1 Experimental Set-up**

In order to vary the evaporation rate of the sessile droplets, experiments were carried out in a low pressure chamber. The droplets were placed in upright and

downside orientation in order to test the effect of gravity on PS particles as the evaporation progresses. The low pressure chamber and related accessories are shown in the schematic diagram in figure 2.2.

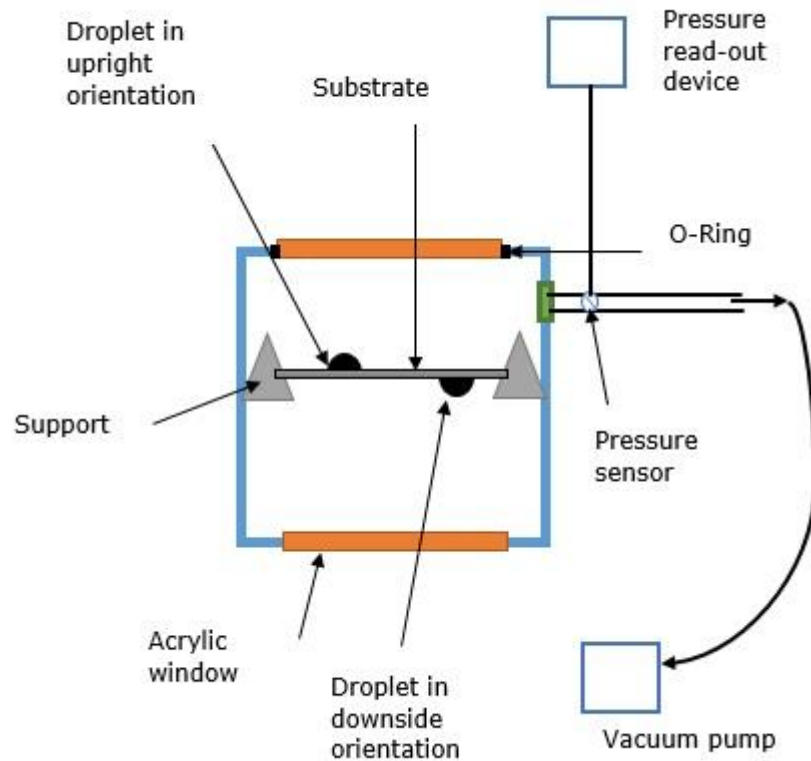


Figure 2.2: Schematic presentation of evaporation of sessile droplet experimental setup in a low pressure chamber.

It consists of a small steel cylindrical chamber with dimensions of 90 mm, 40mm and 20 mm for radius, length and thickness respectively. The imaging and visualization of the droplets was made possible through the use of a 5mm thick transparent window (Perspex Cast Acrylic CLEAR, ASD Ltd., UK) which can withstand the low pressure pumping down of up to 2.5 mbar. The chamber was connected to diaphragm vacuum pump (MD 4 NT, Vacuubrand Ltd., UK).

The Piezo Transducer (KJLC 902, Kurt J. Lesker Ltd., UK ) interfaced with controller Piezo readout (KPDR 900, Kurt J. Lesker Ltd., UK) was attached along the tube to measure the chamber pressure. During the experiments, the low pressure chamber

was placed on a linear translation stage to adjust the height of the samples. Experiments at atmospheric conditions were performed inside the pressure chamber with the two acrylic windows closed with vacuum pump on or off. The droplets in the pressure chamber are placed in both orientations to assess the effect of sedimentation of particles on the ring stain formation.

### **2.3.2 Experimental Procedures**

On a prepared microscope glass cover slip, 1 $\mu$ l droplets of polystyrene microparticles suspension of concentration by mass between 0.009% and 2% were gently deposited using a Microman positive displacement pipette (Gilson Inc., UK). The Gilson capillaries and piston has an ability to dispense a minimum of 0.01 $\mu$ L and maximum of 10 $\mu$ L of volume droplets.

A microscope glass slide was made to rest along the wall of the chamber to provide support to the substrates containing the droplets. While starting the lap split stopwatch, the substrates containing the droplets was transferred quickly to the pressure chamber and slotted on the upper and bottom part of the microscope slide, herein referred as upright and down side orientation.

The process took less than 20 seconds. The vacuum pump was started and the release knob was adjusted to attain the desired pressure. The drying of the droplets was monitored from the top and side view with an aid of Stocker Yale diffuse back light (ML-0405) and Led-clip-on lamp (Dilloytron Mode<sup>®</sup> L804SV 4.5V, 200mA). The deposits changed to milky colour, the drying process was assumed to have completed and the corresponding evaporation time,  $t_F$  was noted. In this study, experiments at reduced pressure were carried at  $\sim$ 13, 67, 269, 534, 800 and 1007mbar in both droplet orientations. The substrate used had a static contact angle of 5°, 18° and 35°. The surrounding temperature and relative humidity were measured using Omegaette meter (HH311 RS-232, UK). The average evaporation

rate,  $\frac{V_0}{t_F}$  was then determined from the initial volume of the droplet,  $V_0$  and the total time,  $t_F$  taken for the drop to dry completely.

### **2.3.3 Analysis of the Final Deposits**

In order to quantify the effect of evaporation rates, contact angle, droplet orientation, particle sizes and their concentration variance on the ring dimensions, the surface profile of the final deposits resulted from drying droplets from these parameters had to be assessed. The surface morphology and depth profiles were determined using a scanning electron microscope, surface contact profilometry technique and Image J software as described in section 2.3.3.1, 2.3.3.2 and 2.3.3.3 respectively.

#### **2.3.3.1 Surface Morphology Characterization**

The aims of characterizing the morphology of the deposits left after drying the droplets containing polystyrene microparticles were:

- i. To establish and confirm the number of microparticle layers in the interior which did not form part of the ring and hence determine their percentages as a function of initial concentration.
- ii. To confirm the presence of stick-slip phenomenon at low polystyrene microparticles concentration as well as low pressure (high evaporation rates).
- iii. To determine the surface morphology of the deposits at micro level near the ring area and other features formed in the interior of the droplets.

The morphology of the final deposit was characterized using scanning electronic microscope. To achieve this, the droplets containing polystyrene microparticles with initial concentration between 0.002% and 2% were first evaporated on 22x25 mm microscope cover slips. These samples were then coated with 10nm layer of gold

using Turbo pumped high resolution Chromium Sputter Coater (EMITECH K575X, Quorum Technologies Ltd., UK) backed up by a rotary vacuum pump using standard operating procedures. The gold pre-coated samples in cover slips were characterized by a scanning electron microscope (JEOL JSM 840A, Oxford Instruments., UK) using standard operating procedures.

The scanning electron microscope with tungsten filament operated at an accelerating voltage of between 0.2 and 40 kV. The equipment was equipped with secondary electron imaging system for capturing surface topography with magnification of between 25 and 300000. The digital images were captured to personal computer for analysis via INCA software (Oxford Instruments., UK). Figure 2.3 shows sample of these digital images captured.

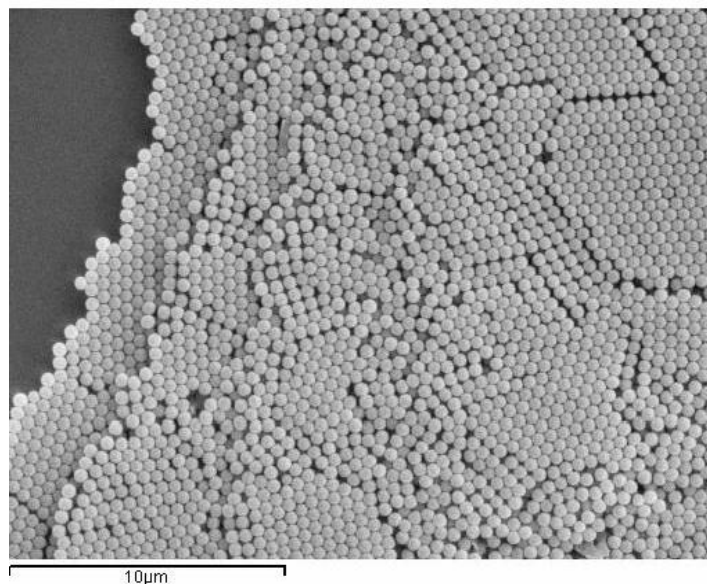


Figure 2.3: The image shows a surface morphology of 0.5μm polystyrene microparticles with  $c_0 = 0.25\%$ .

### **2.3.3.2 Surface Depth Profile Characterization**

The surface profiles of the deposits left after evaporation were measured by stylus profilometry technique (Dektak 6M Surface Profiler, Veeco., UK) and are described in section 2.3.3.2.1 and 2.3.3.2.2. The data obtained from analyzing these profiles

were used to determine the ring dimensions in terms of height and width as well as an estimate of the percentage of polystyrene microparticles in the ring and those at the interior of the droplets.

#### **2.3.3.2.1 Principle of Operation**

The measuring system operates by diamond-tipped stylus (12.5 $\mu\text{m}$  radius) physically making contact with deposits surfaces and moving the stage front and back to measure changes in deposits step heights. The slide containing the dried deposit was placed on a movable stage which moves according to a pre-programmed scan length, speed and scanning stylus force. The stylus is mechanically coupled to the core of a Linear Variable Differential Transformer (LVDT). As the stage moves the slide, the stylus rides over the sample surface. Surface variations cause the stylus to be translated vertically. Electrical signals induced by stylus movement are produced as the core position of the LVDT changes. The LVDT scales an alternating current reference signal proportional to the position change, which in turn is conditioned and converted to a digital format through multiplexers. The varying signal is then digitized and stored to represent the surface profile of the dried deposits on the slide.

The Dektak 6M Surface Profiler has the capability to accurately measure step heights of the deposits on the substrates, with a programmable stylus scanning force down to 1 milligram and a Z-height up to 1mm. In addition, it delivers horizontal resolution of up to 0.067 $\mu\text{m}/\text{sample}$ , with 300 data point per second and up to 30,000 data points per scan. The equipment measures a vertical range of up to 262 $\mu\text{m}$ .

#### **2.3.3.2.2 Measuring Procedures**

The Dektak stylus was used to acquire data in order to determine the ring width and height. The scan force was set to 1mg (minimum force possible) scan to

minimize the point pressure on the sample. With this minimum force on the sample, the final deposit was not disturbed as observed with optical microscope. The vertical range was set to  $262\mu\text{m}$  with Scan length varied up to from  $1900\mu\text{m}$  to  $6000\mu\text{m}$  depending on the size of the deposits. The cover slip glass samples with final deposits were loaded manually onto a 150mm diameter sample-positioning stage and aligned with the help of X and Y manual stage position translation as shown in figure 2.4.

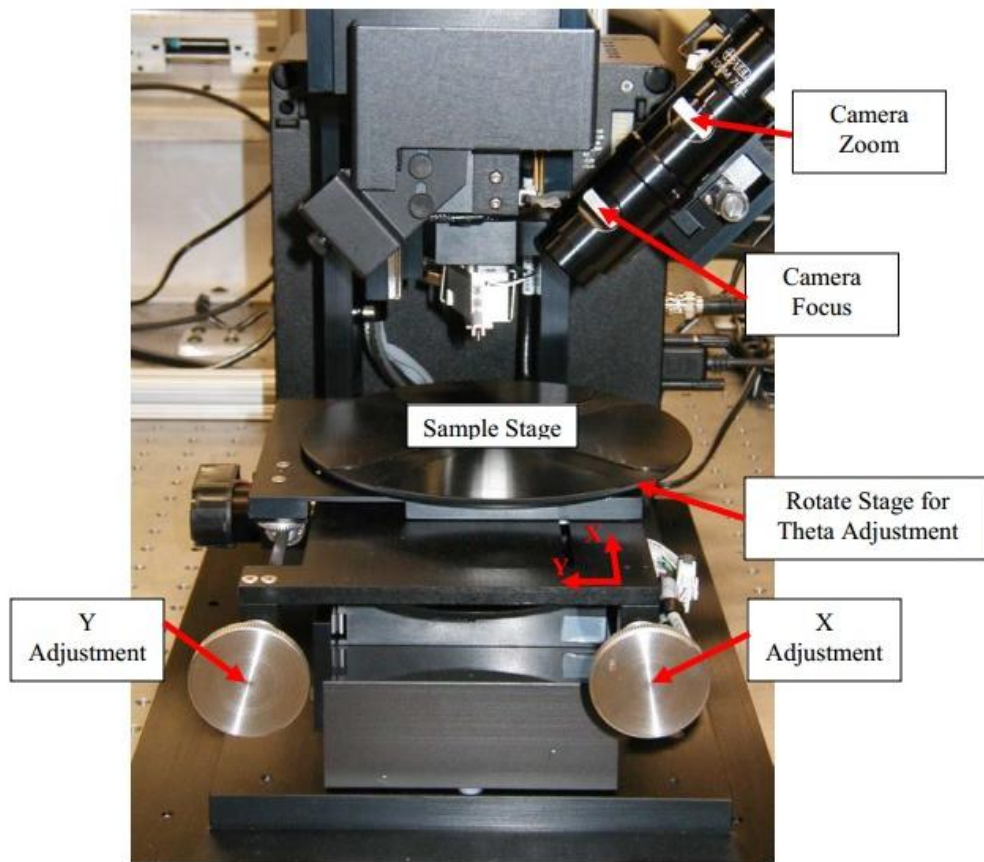


Figure 2.4: Programmable Dektak 6M Stylus Profiler used to study the surface profile of final deposits after drying droplets.

The image of the sample on the stage was acquired using high-resolution colour video camera attached to the scan head with 2.6 mm horizontal field of view and  $45^\circ$  side view. Standard operating procedures were used to run the six scans for

very droplet deposits at different positions of the deposits and export the raw data into excel sheets for further analysis. Figure 2.5 show an example of image scanned and its corresponding stylus surface profile is shown in figure 2.6

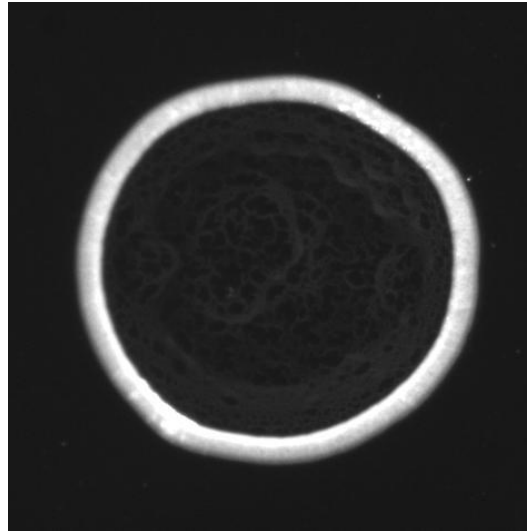


Figure 2.5: Final deposits of 1% polystyrene microparticles suspension dried at 0.6 n/s in upright orientation captured with CCD camera reflection mode.

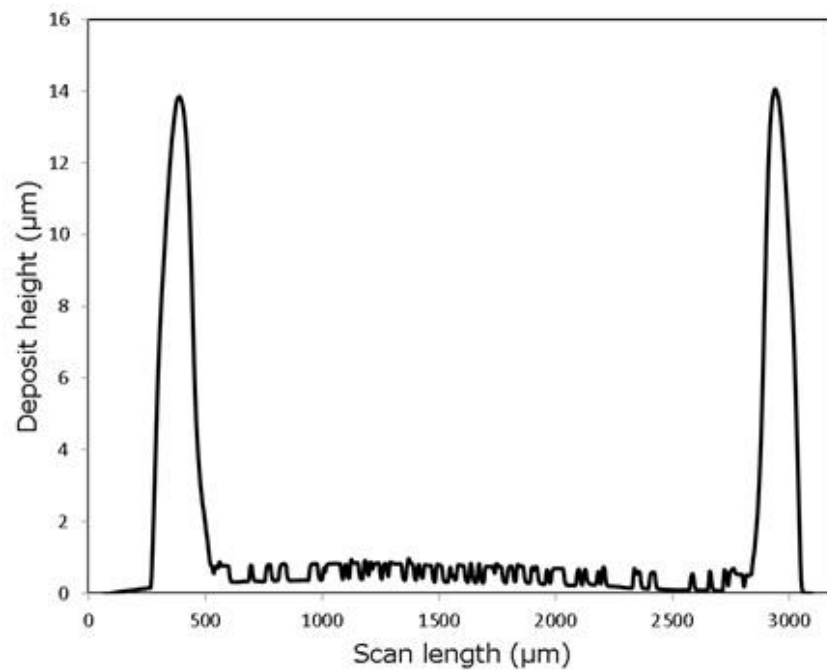


Figure 2.6: Sample of Dektak 6M surface profiles used to extract the ring height, width and diameter.

### 2.3.3.3 Image J Profile Characterization

In this method a black and white image of the deposit were first captured with CCD camera (DMK 41BU02H) in reflection mode maintained by Led-clip-on lamp (Dlloytron Mode<sup>®</sup> L804SV 4.5V, 200mA). The images captured were not post processed in order to retain the original brightness and contrast. The radial profile plug in embedded in Image J software was then used to analyse the images as described in Appendix B. The radial profile plug determines the center of the deposit profile as the radius of the circle. The deposit profile x-axis can be plotted as pixel values or as values according to the spatial calibration of input image while the y-axis as integrated normalized intensity. The accuracy of this method depends on how perfect the circle encloses the deposit as described in Appendix B. Figure 2.7 show an example of the radial profile obtained using Image J.

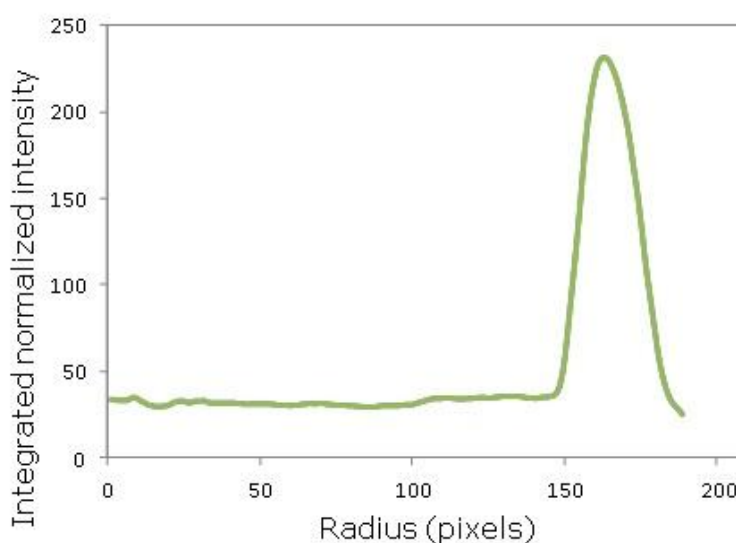


Figure 2.7: Radial profile plot versus radius for 0.5 $\mu$ m particles dried at 0.6 nL/s in upright orientation.

## 2.4 Kinematics of Droplets Drying

In this section the kinematics of droplets drying at atmospheric and low pressure conditions was investigated to understand the drying process of the droplets. Two

methods were employed using conventional optical microscope imaging and optical coherence tomography as described in section 2.4.1 and 2.4.2.

## **2.4.1 Optical Coherence Tomography (OCT)**

### **2.4.1.1 Introduction**

Optical coherence tomography is a non-invasive cross-sectional imaging method that uses low coherence interferometry to produce a two dimensional image of optical scattering from internal structures of biological systems [142]. OCT is an imaging modality analogous to ultrasound, but instead of using the difference in the flight times of acoustic waves (as in ultrasound), it uses light to achieve micrometer axial resolution. OCT has been used as a powerful tool for medical diagnostics [143] and neuroimaging applications [144]. For example the principle of ocular imaging with OCT is based upon measuring the time delay of the light reflected from each optical interface (A-scan) when a beam of light enters the eye. A series of A-scans across the structure permits a cross sectional reconstruction of a plane through the anterior or posterior segment of the eye. This is known as a B-scan. Because the velocity of light is so high, and the distance between layers is so short (in micrometer), it is not possible to measure the flight time change directly.

Instead, OCT uses low coherence interferometry in which the light source is split between that entering the eye and a reference path. The light reflected back from the two paths forms an interference pattern when the distance in the two paths matches to within the coherence length of the light source. A number of different types of OCT imaging have been developed including time domain and Fourier domain techniques. The time domain takes into account the position of a reference mirror or optical delay line in the reference channel. The Fourier-domain uses a spectrometer or sweeping the light source wavelength and calculating the inverse Fourier transform (FT) as a function of wavelength. An example of a Fourier domain

OCT is the spectral domain optical coherence tomography (SDOCT) whose experimental set up is shown in figure 2.8 (A). In figure 2.8 (A), the spectrometer measures the interference signal as a function of wavelength,  $\lambda$  to give an output shown in figure 2.8 (B). The spectral data is rescaled (figure 2.8 (C)) and resampled evenly in  $k$ -space, before it is Fourier transformed (FT) to get the sample depth profile or A-scan (figure 2.8 (D)).

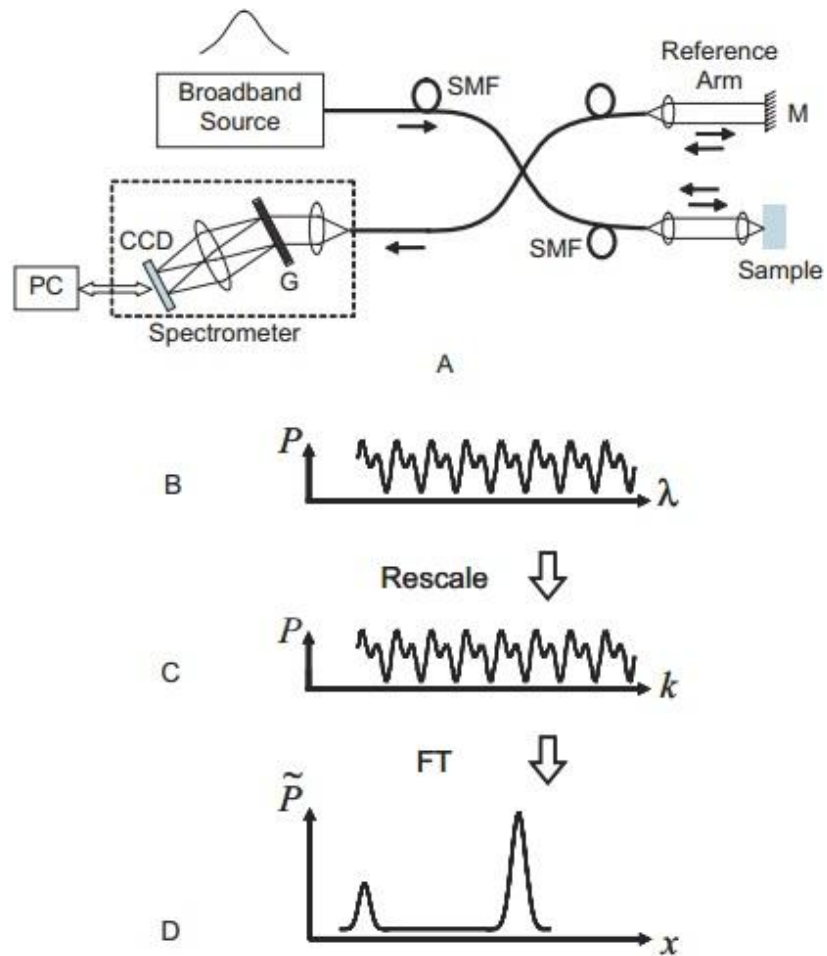


Figure 2.8: (A) Spectral domain Spectral domain optical coherence tomography (SDOCT) system comprising of broadband laser source such as superluminescent diode (SLD), single mode fiber (SMF), diffraction grating (G), personal computer (PC), charged-coupled device (CCD) and  $P$  represents intensity of power recorded by a photodetector. Also B is the interference signal, C is the rescaled signal and D is the sample depth profile or A-scan [147].

Recently OCT has emerged as a powerful tool for tracking particles in evaporating droplets [145] and tracking biological species in microfluidics [146]. To study the kinematics of droplets drying containing PS particles, commercial SDOCT (OCP930, Thorlabs Inc., UK) operating at 930 nm central wavelength combined with low pressure chamber was used. The spectral SDOCT has a 6.2  $\mu\text{m}$  axial resolution in air, 2mW peak output optical power and maximum optical depth range of 1.6mm. The important advantage of using SDOCT over time domain OCT is that, SDOCT is faster because the depth profile of droplet is obtained all at once. The time domain OCT has high scanning times due to the requirement of mechanical translation of the reference mirror.

#### **2.4.1.2 Experimental Setup and Measurement**

Figure 2.9 show schematic illustration of the OCT coupled with a low pressure chamber which is the basis of the present experiment to study the kinematics of droplet drying at atmospheric and low pressure conditions. To do this a 2mm diameter hole was drilled at the center of the acrylic window using 40W laser cutter (LM.VLS350, Hobart Laser Ltd., USA). A translucent silicone high vacuum pressure grease (Dow Corning, Belgium) was applied to one side around this hole to act as a seat then followed by placing gently 1.2x25.4x76.2mm microscope glass slide. 1 $\mu\text{L}$  droplet containing 5 $\mu\text{m}$  polystyrene microparticles was deposited on a glass slip and quickly transferred to the low pressure chamber. The low pressure chamber was run to attain a pressure of about 13mbar while simultaneously running the software. The x-range was varied depending on the section of the droplet to be scanned. The droplet was manually positioned in X-Y direction using micrometer screw gauges in the linear translation stages so that the SDOCT laser became aligned with the diameter of the droplet. The procedures outlined above were also used to obtain scan of droplet at atmospheric conditions inside a low pressure chamber. Experiments were carried out more than five times to check the

reproducibility of the results. The the ambient temperature and relative humidity were recorded in each experiment.

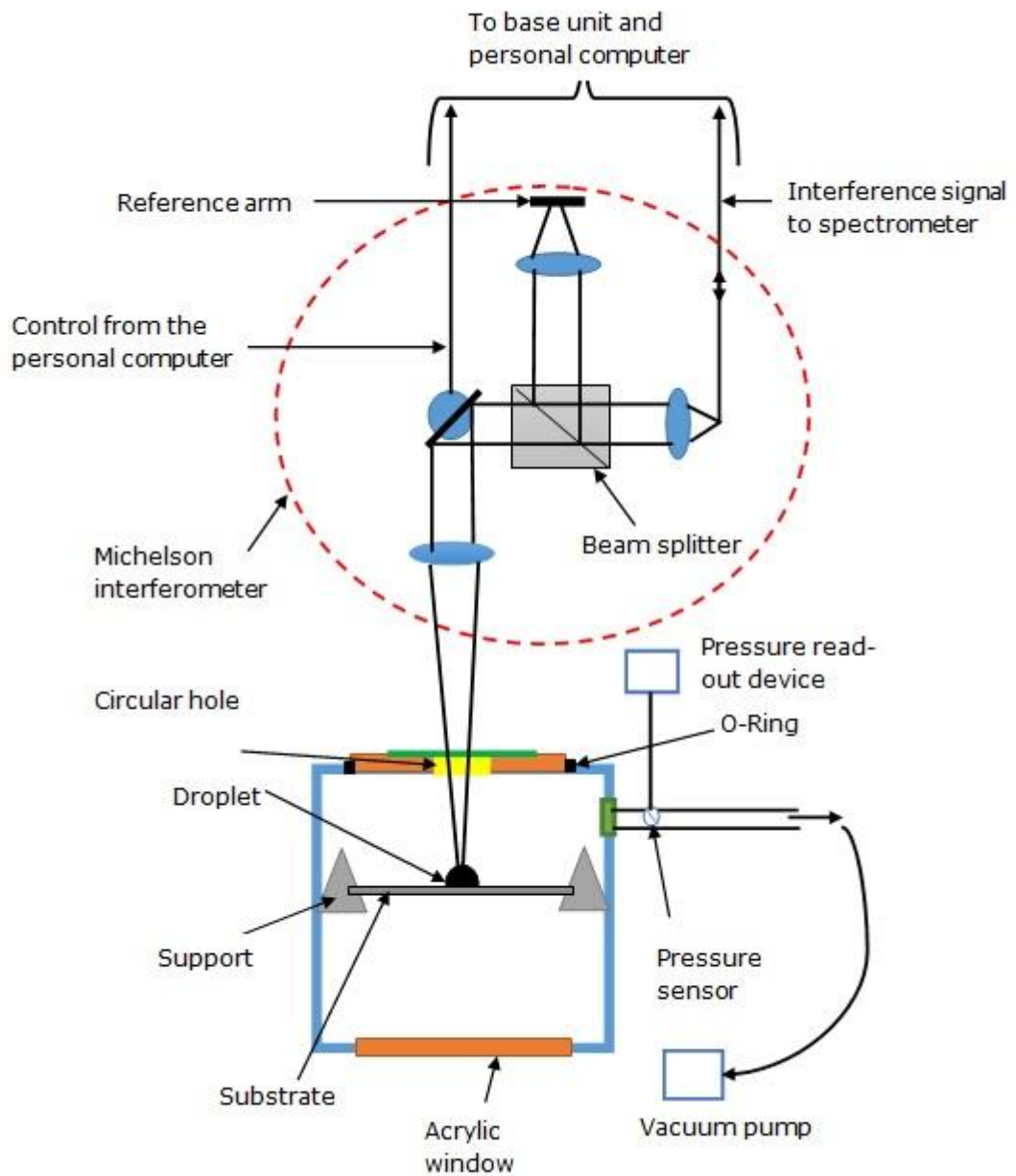


Figure 2.9: The schematic diagram a part (scanning probe/ Michelson interferometer) of commercial OCT combined with pressure chamber

The corresponding experimental set-up is shown in figure 2.10. In this experimental set-up, one of the transparent acrylic window was modified to obtain the desired working distance of the scanning probe.

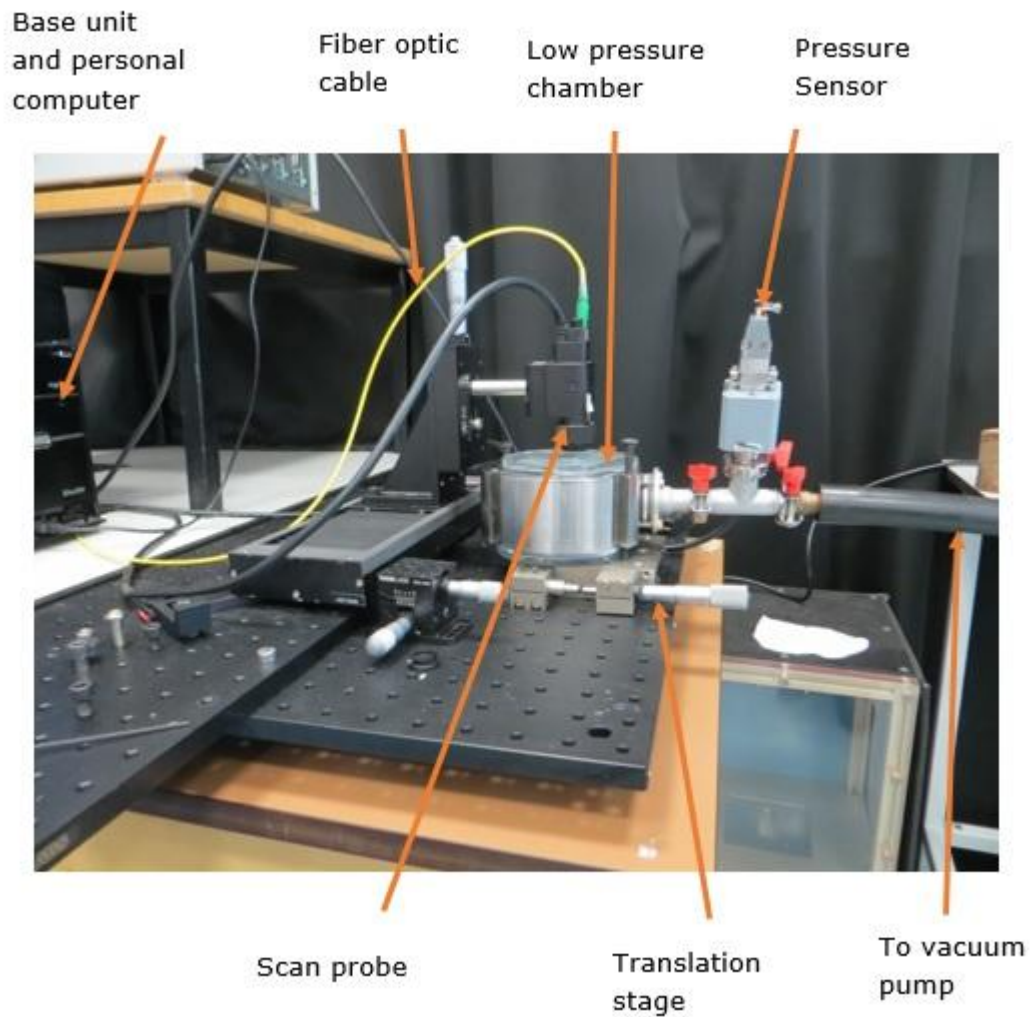


Figure 2.10: Experimental set-up to study the kinematics of the droplets drying employing SDOCT and low pressure chamber.

Figure 2.11 show an an example of a raw 2D image of a droplet containing  $5\mu\text{m}$  PS microparticles constructed using SDOCT. To obtain the 2D image in figure 2.11, a Fourier domain measurements to each subsurface axial profile of a droplet was collected at the same time without time delay between the top and the bottom interface of a profile [148]. The back scattered light from variuos depths of the droplet which interfered with the light reflected from the reference arm produced an inteferece fringe and measured by a spectrometer (figure 2.8). Fourier tranform of

the interference fringe as a function of wave number gave a droplet depth profile. Using a plugin embedded in Image J software a 2D image in figure 2.11 was obtained.

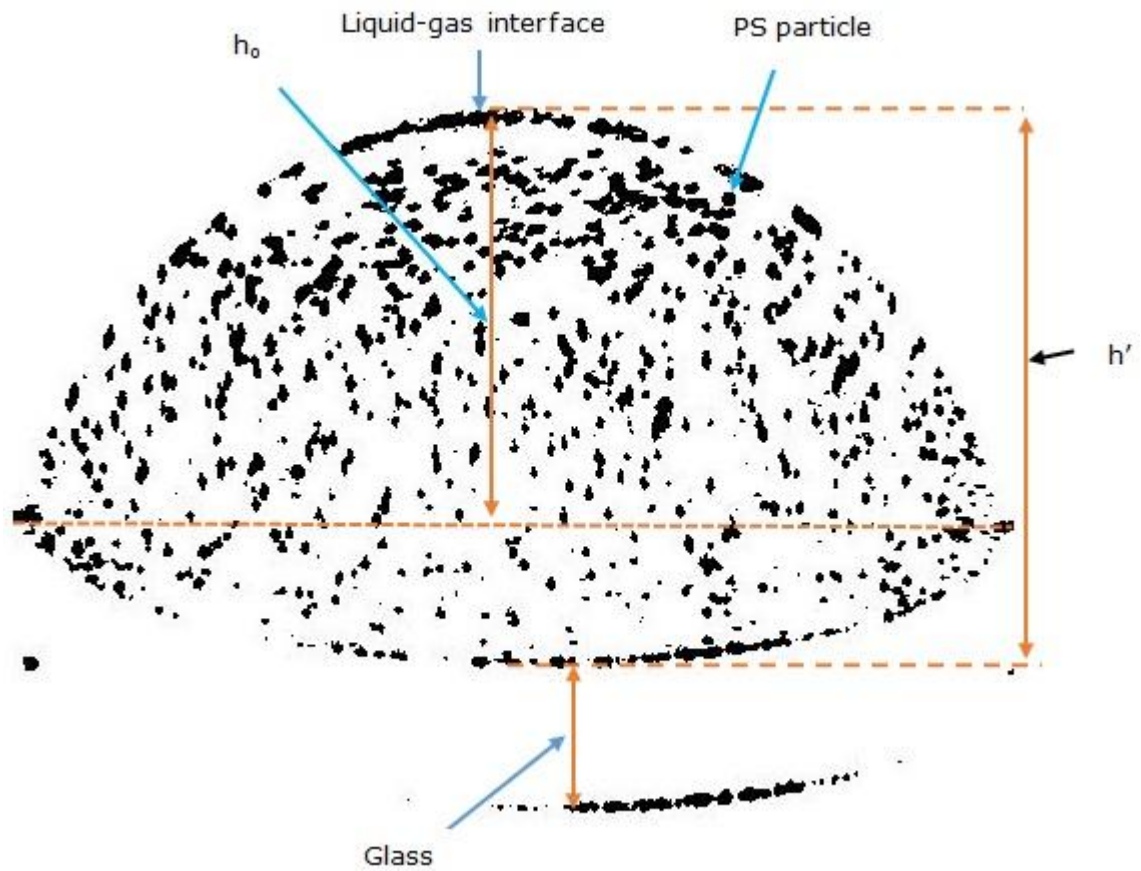


Figure 2.11: A raw 2D image of a droplet containing 5µm polystyrene microparticles constructed using SDOCT where  $h_0$  and  $h'$  are real and optical droplet heights respectively.

The bulge of the droplets downward is caused by light travelling in two media of different refractive indices in this case water of refractive index 1.33 and air with refractive index 1. It is worth noting that, SDOCT software outputs an image as a function of the time it has taken for light to travel between the emitter and the sensor, and makes the assumption that the light has travelled through air only, with a refractive index 1. When light travels through a water of refractive index 1.33, the corresponding distance travelled will be  $h'$  which is a greater from the

detector than it is causing bulging of the droplet. The ratio  $\frac{h'}{h_0}$  give the refractive index of the water ( $\sim 1.35$  from figure 2.11).

### **2.4.1.3 Particle Tracking**

In order to determine the mechanisms of ringstain formation, the instantaneous position of the individual PS microparticles during droplet drying process had to be tracked to establish their corresponding trajectories. From these trajectories, the associated directional vectors, velocities and vorticities could be determined. To achieve this a time-resolved digital particle tracking velocimetry (PTVlab) tool for Matlab was used to study the kinematics of the droplets drying at atmospheric and low pressure conditions [149] and Image J software. PTVlab is an open source software whose graphical user interface (GUI) is adapted from time-resolved digital particle image velocimetry (PIVlab version 1.2) project [150, 151].

### **2.4.2 Optical Microscope Imaging Technique**

In this technique, kinematics of the droplets drying was conducted at atmospheric conditions and low pressure of about 13mbar by conventional microscope imaging technique. The experiments were performed using CCD camera integrated with microscope and/or personal computer to acquire a sequence of images. PS microparticles with 0.5 $\mu\text{m}$  , 2 $\mu\text{m}$  and 5 $\mu\text{m}$  diameter were used with concentration by mass ranging between 0.002 to 2%. To this set-up, a USB Monochrome ICX205AL Sony CCD camera (DMK 41BU02.H, The Imaging Source., UK) was added and integrated with the personal computer to capture video images from the using IC capture software.

The Sony CCD camera had a resolution of 1280X960 pixels capable of capturing 15fps. Also USB Monochrome Micron CMOS camera (DMK 22AUC03, The Imaging Source., UK ) able to capture videos images of up to 744x480 pixel at 76fps was

used at 10torr. Thorlabs lens tubes and washers were added between the CCD camera and the LINOS lens (QIOPTIQ Germany) to adjust the size of the drop to nearly fit the IC capture screen. To ensure a uniform light illumination of the droplets, a low pressure chamber was placed on top of Stocker Yale diffuse back light (ML-045) initially placed on the height translation stage. To a prepared substrate 1 $\mu$ L of polystyrene microparticles droplet was deposited and transferred to a low pressure chamber. In order to study the dynamics near the droplet edge with high resolution at micron level, an inverted microscope (TE2000-S , Nikon Instruments., UK) attached with lenses capable of magnifying the droplets by factor of 2, 10, 60 and 100 was used.

The low pressure chamber and its accessories were integrated with this microscope. Sequence of images was captured at 1fps at atmospheric conditions and up to 50fps at 10torr using similar CCD cameras. For color images, FireWire 400 color Camera (DFK 41BF02.H, The Imaging Source., UK) able to capture 1280X960 pixels of video images of up to 15fps was used. With this set-up it was possible to capture video images able to visualize 0.5  $\mu$ m polystyrene microparticles and hence track their movements as the droplets dries using X10 lens both at atmospheric and low pressure conditions. To enhance the resolution at X60 and X100 magnification, refractive index matching immersion oil (Panscan Xtra) with refractive index 1.518 was smeared between the lower part of the substrate and the lens. However at X60 and X100 magnification was limited at atmospheric conditions only with the substrate not placed inside the low pressure chamber.

### **2.4.3 Measurements of Temperature Variations Across the Drops**

In order to account for the shape of the deposits at low pressures (section 4.2), we have tried to measure the droplet temperature at the edge and apex both for low and high drying rates using a variety of methods such as 100  $\mu$ m thermocouples and a thermal imaging camera. Observations show that using the relatively thick

thermocouple, the kinematics inside the droplets changed leading to different deposits patterns compared to control experiments droplets. The reason for this may be due to energy loss from the drop through the thermocouple. However, the Thermocouple enables a measurement of the average temperature of the droplet which was found to be  $\sim 5^{\circ}\text{C}$ . In addition, at high drying rate in a low pressure chamber it was difficult to firmly position the thermocouples in the droplets edge and apex. The type K thermocouples used had a sensitivity of  $\pm 0.1^{\circ}\text{C}$  and the digital multimeter used to measure the temperature had a sensitivity of  $\pm 0.1^{\circ}\text{C}$ . The infrared thermal imaging camera with a sensitivity of approximately  $\pm 0.1^{\circ}\text{C}$  was only useful at atmospheric conditions when the droplets were placed on the substrates in open air. Inside a low pressure chamber, it was not possible to image the droplet as Perspex is not transparent to infrared wavelengths. In order to address this, we have attempted to use a silicon window to solve this problem and conduct experiments in environmental chamber at low pressures. However, we were unable to measure temperature difference ( $1\text{-}15^{\circ}\text{C}$ ) across the droplets due to low intensity of transmitted signal and emissivity. Given the expected temperature difference across the droplet and the sensitivity of the measuring instrument we can say that temperature measurements were not limited by the sensitivity of the instrument.

## **2.5 Evaporation of PS-PEO Droplets.**

In this section drying droplet containing PS particles and PEO polymer solution were studied. The aim was to investigate the effect of PS microparticle (size and concentration) on the four stages drying of pure PEO and also the effect of PEO on the drying of PS particles.

### **2.5.1 Experimental Procedures**

Experiments for PS-PEO solution was studied at atmospheric conditions with

droplets of  $V_1 = 0.4\mu\text{L}$  and  $V_1 = 0.7\mu\text{L}$ . The concentration by mass of  $0.5\mu\text{m}$  and  $5\mu\text{m}$  PS microparticles were kept in the range  $1\% \leq c_0 \leq 5\%$  while those of PEO were kept in the range  $1.6\% \leq c_1 \leq 18\%$ . The procedures of preparing PS-PEO sample has been explained in section 2.1.2. The sequence of images at 1fps were captured using a monochrome ICX205AL Sony CCD camera controlled by IC capture software integrated in a personal computer. The Olympus Plan N lens (X10, NA=0.25) was attached to the monochrome Sony CCD camera for magnification purposes. The image sequences were taken for at least 3 droplets in each PS-PEO concentration used.

### **2.5.2 Analysis of Final Deposit**

The images of the final deposits were captured by CCD camera using inverted Nikon Eclipse TE2000-S microscope in transmission mode (Nikon Plan Apo lens, X2, NA=0.1) employing cross polarizer. In reflection mode the images of the final deposits were captured by CCD camera using Olympus B50 microscope attached with M Plan FLN lens (X10, NA=0.25 and X50, NA=0.50). Deposit obtained from drying the PS-PEO droplets of varying concentration by mass and particle sizes were characterized by stylus profiler and Image J software. Analysed data from the stylus surface profiler and Image J were used to determine the deposit profiles and their corresponding coefficient of skewness. Image J was used only to obtain deposit profiles for tall conical structures beyond the resolution of the Dektak 6M Stylus Profiler (vertical range  $>262\mu\text{m}$ ).

The coefficient of skewness quantifies how symmetrical the deposit distribution is [152]. A deposit with perfect symmetrical distribution will bear a zero coefficient of skewness. Meanwhile an asymmetrical deposits distribution with a long tail to the right and characterized with higher coefficient of skewness values ( $>0$ ) will be positively skewed. A negative skew curve is characterized by higher negative

coefficient of skewness values ( $>0$ ) with deposits of long tail asymmetrical distributed to the left. For univariate data  $X_1, X_2, \dots, X_N$  the Pearson coefficient of skewness,  $G_p$  is given by equation (2.1) where  $\sigma$  is the standard deviation and  $\bar{x}$  is the mean.

$$G_p = \frac{\sum_{i=1}^N (X_i - \bar{X})^3 / N}{\sigma^{3/2}} \quad (2.1)$$

The step for determining the coefficients are illustrated below;

(a) Plot the final deposit profiles using Stylus or Image J data as per figure 2.12 and 2.13 for  $0.5\mu\text{m}$  and  $5\mu\text{m}$  PS particles respectively.

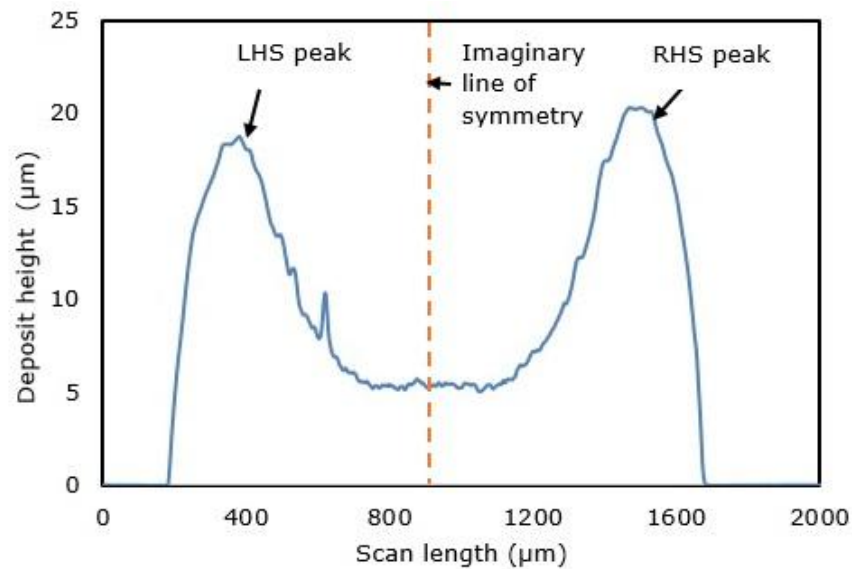


Figure 2.12: The final stylus deposit profile containing  $c_1 = 1.6\%$  (PEO) and  $c_0 = 4\%$  ( $0.5\mu\text{m}$  PS particles). The left hand side (LHS) peak and right hand side (RHS) peak are well demarcated by an imaginary line of symmetry. The imaginary line of symmetry divides a central peak into two halves of left hand side (LHS) peak and right hand side (RHS) peak.

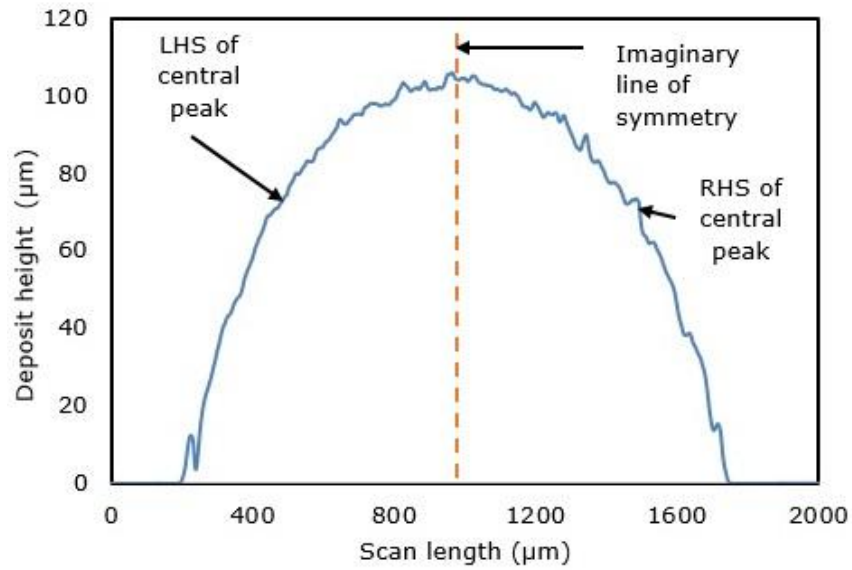


Figure 2.13: The final stylus deposit profile containing  $c_1 = 9.6\%$  (PEO) and  $c_0 = 4\%$  ( $5\mu\text{m}$  PS particles).

(b) Determining the center of the deposit (line of symmetry) using Stylus or Image J data and reploting figure 2.12 and 2.13 as folded one in figure 2.14 and 2.15 for  $0.5\mu\text{m}$  and  $5\mu\text{m}$  PS particles respectively.

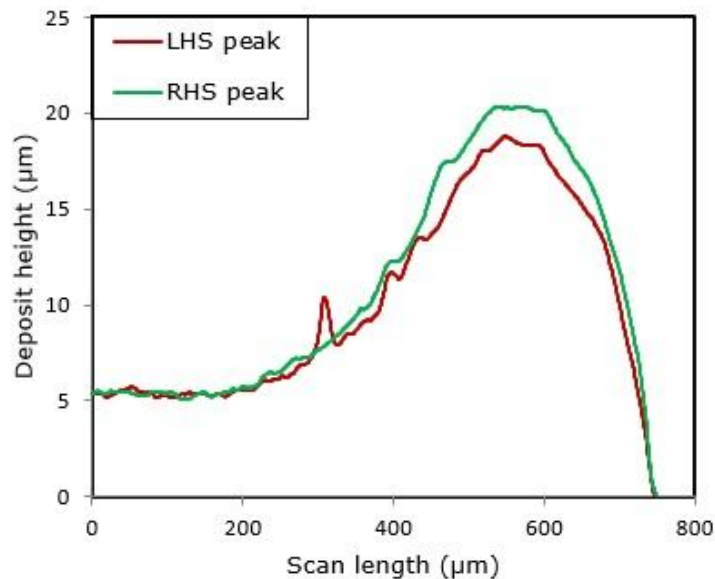


Figure 2.14: The final stylus deposit profile (folded) containing  $c_1 = 1.6\%$  (PEO) and  $c_0 = 4\%$  ( $0.5\mu\text{m}$  PS particles).

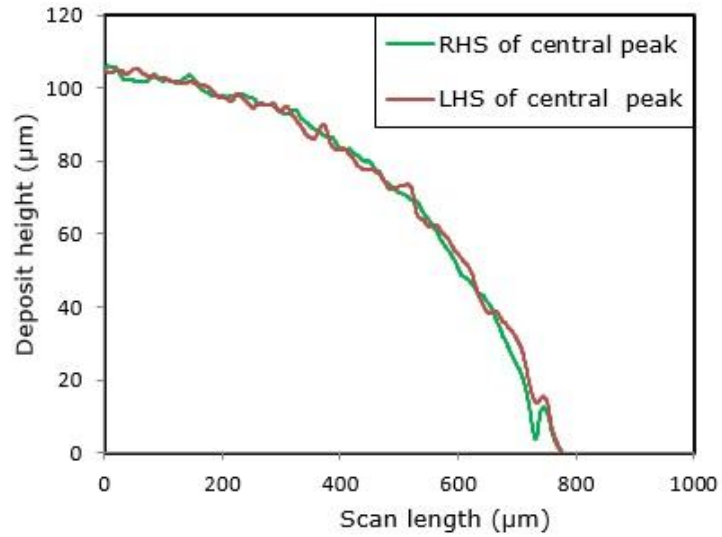


Figure 2.15: The final stylus deposit profile containing  $c_1 = 9.6\%$  (PEO) and  $c_0 = 4\%$  ( $5\mu\text{m}$  PS particles).

(c) The data in part (b) used to plot the folded deposit profile are then utilized to determine the mean, mode, standard deviation and the coefficient of skewness. Computer programming codes were written and embedded in Microsoft excel to automate the process of determining the coefficient of skewness using equation (2.1).

## **Chapter 3**

### **How Robust is the ring Stain**

### **3.1 Introduction**

As stated in Chapter 1, evaporating droplets containing particles will leave behind solid deposits in the form of a ring. A simple argument states that the ring height ( $h_r \propto c_0^{0.5}$ ) and width ( $w_r \propto c_0^{0.5}$ ) of these deposits will scale to the square root of their initial concentration provided that all the particles end up in the ring (derivation in appendix C). It also requires that the cross-sectional shape of the deposit to be independent of initial concentration, and that the packing fraction to be kept constant. In section 2.3 a number of experimental parameters were varied to assess the ring growth and to the dimensions. In this chapter we present the results of varying the evaporation rates, initial contact angle, orientation of the droplets, particles size and initial concentration of particles to determine their contribution in determining the deposits scaling power laws.

### **3.2 Experimental Results and Discussions**

#### **3.2.1 Images of the Final Deposits**

The drying of droplets containing polystyrene microparticles involved varying experimental parameters including surface wettability of the substrates, particle sizes and orientations of the droplets. The volume of the droplet containing polystyrene microparticles in the entire experiments were kept at 1 $\mu$ L whilst the corresponding initial concentration,  $c_0$  by mass were kept between 0.002% and 2%, and all particle sizes used. The variations in drying rates were achieved by varying the pressure in the working chamber. The average evaporation rate of the whole droplet is inversely proportional to pressure inside the chamber according to equation (1.15). The experiments in every parameter tested were repeated more than five times to check for reproducibility of the results. Images of the final deposits were captured using conventional microscopes in reflection and transmission mode as well as a scanning electron microscope with high resolution

to assess the deposit morphology. This section will present sample sequences of images as the representative and discussion of the general observations.

### 3.2.1.1 Effect of Droplet Orientation

#### (a) Upright Orientation: Atmospheric Conditions ( $\sim 0.6 \text{ nL/s}$ )

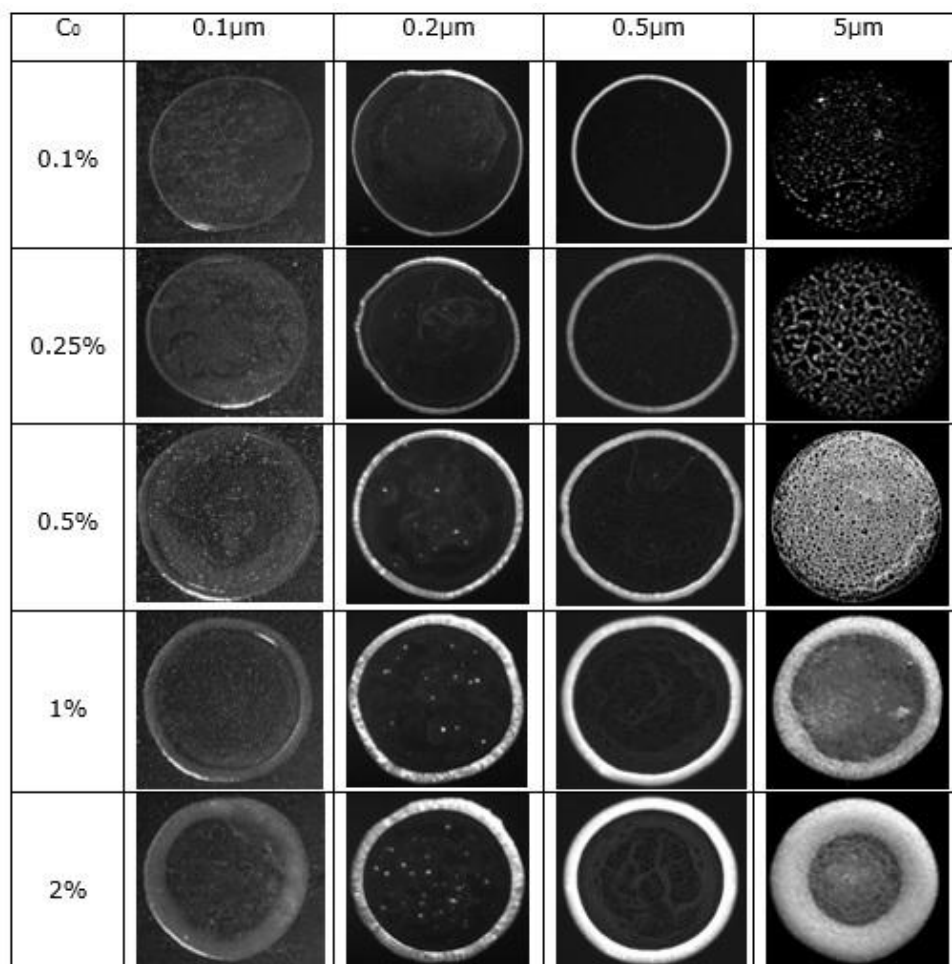


Figure 3.1: The final images as a function of initial concentration of polystyrene microparticles and particle sizes dried at  $\sim 0.6 \text{ nL/s}$  with substrate for  $\theta = 35^\circ$

It is clear in figure 3.1, that the patterns formed from drying these droplets depends on the size of the particles as well as the initial concentration of the particles. For 0.1  $\mu\text{m}$ , 0.2  $\mu\text{m}$  and 0.5 $\mu\text{m}$  particles robust rings are formed with a small fraction of particles at the interior of these rings. It is anticipated that at later stages of droplet drying small fraction of PS particles will still be present in bulk of

the liquid and following detachment of the liquid part from the ring these particles will no longer be part of the ring and thus remain at the interior of the droplet.

Since the droplets are drying at very low rates particles have enough time to move to the contact line due to capillary flow and form a robust ring. These results are consistent with Deegan et.al, [74] pointing that contact line pinning strengthens the formation of ring like deposit at the perimeter of the droplet due to roughness or chemical heterogeneity of the substrate. However for 5 $\mu\text{m}$  particles, ring like deposits are observed for 1% and 2% only. Particles are also distributed at the interior of these rings like deposits we attribute this to sedimentation (kinematics to be presented in chapter 4). Between 0.5% and 0.02%, particles are observed to be distributed in the entire droplet evenly in a monolayer without any formation of ring like deposits. There are few particles to pin and thus form ring like deposits as observed in 1% and 2%.

**(b) Upside down orientation: Atmospheric Conditions ( $\sim 0.6\text{nL/s}$ )**

In this scenario the droplets on the substrates were placed in upside down position to test the effect of gravity on particles during droplet evaporation. General observation reveals that for 0.1  $\mu\text{m}$ , 0.2  $\mu\text{m}$  and 0.5 $\mu\text{m}$  particles, robust rings are observed with smaller fraction of particles at the interior of the ring as shown in figure 3.2. The deposit patterns are seemingly similar to those in section 3.2.1.1 (a) above for upright orientation. Despite of the fact that a study by Deegan et.al, [74] concluded that, rings produced from drying droplet in upright and upside down orientations are indistinguishable from the one another, there is no enough information to prove this. No images for the final deposit (upright and upside down orientations) and the particles sizes used have been provided to justify their claim. For 5 $\mu\text{m}$  particles, no ring like deposits are formed in the entire concentration ranges used. However for lower concentration <2% most of the particles are left closer to the interior of the droplet.

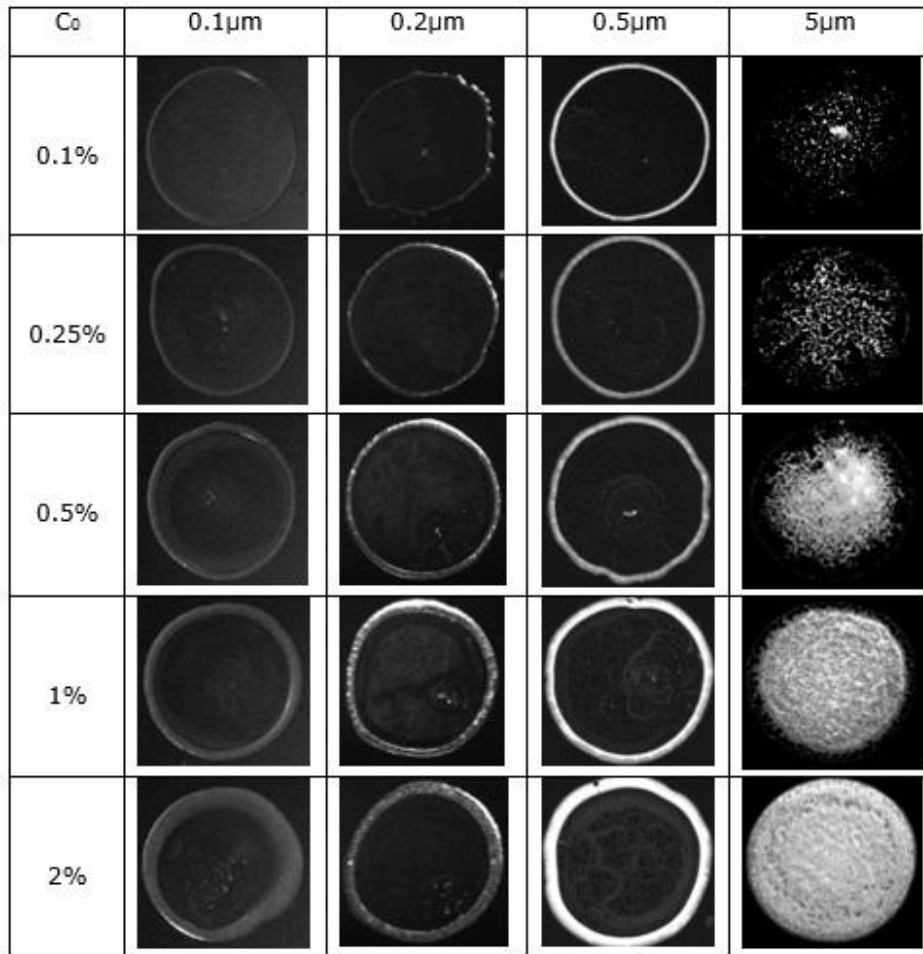


Figure 3.2: The final images as a function of initial concentration of polystyrene microparticles and particle sizes dried at  $\sim 0.6 \text{ nL/s}$  with substrate for  $\theta = 35^\circ$

As described in section 3.2.1.1 (a) 5 $\mu\text{m}$  are believed to sediment quickly even before the droplet completely dries. When the droplets are placed upside down these particles will sediment closer to liquid-vapour interface of the spherical cap and as the droplet dries, these particles are dragged by the descending spherical cap resulting into the observed deposits patterns. However few particles appear at the contact line, this may be attributed to early pinning at the surface of the substrate.

**(c) Upright Orientation: High Drying Rates (>5nL/s)**

When the drying rates increases dramatically, the particles will arrive at the ring very quickly and one would expect the ring to grow in the same manner as described in section 3.2.1.1 (a) and consequently the same deposit patterns formed. However when the drying rates exceed 5nL/s deposits patterns were observed to be different of those observed at low drying rates of  $\sim 0.6$ nl/s. Sample images as a function of initial concentration and particles sizes are shown in figure 3.3.

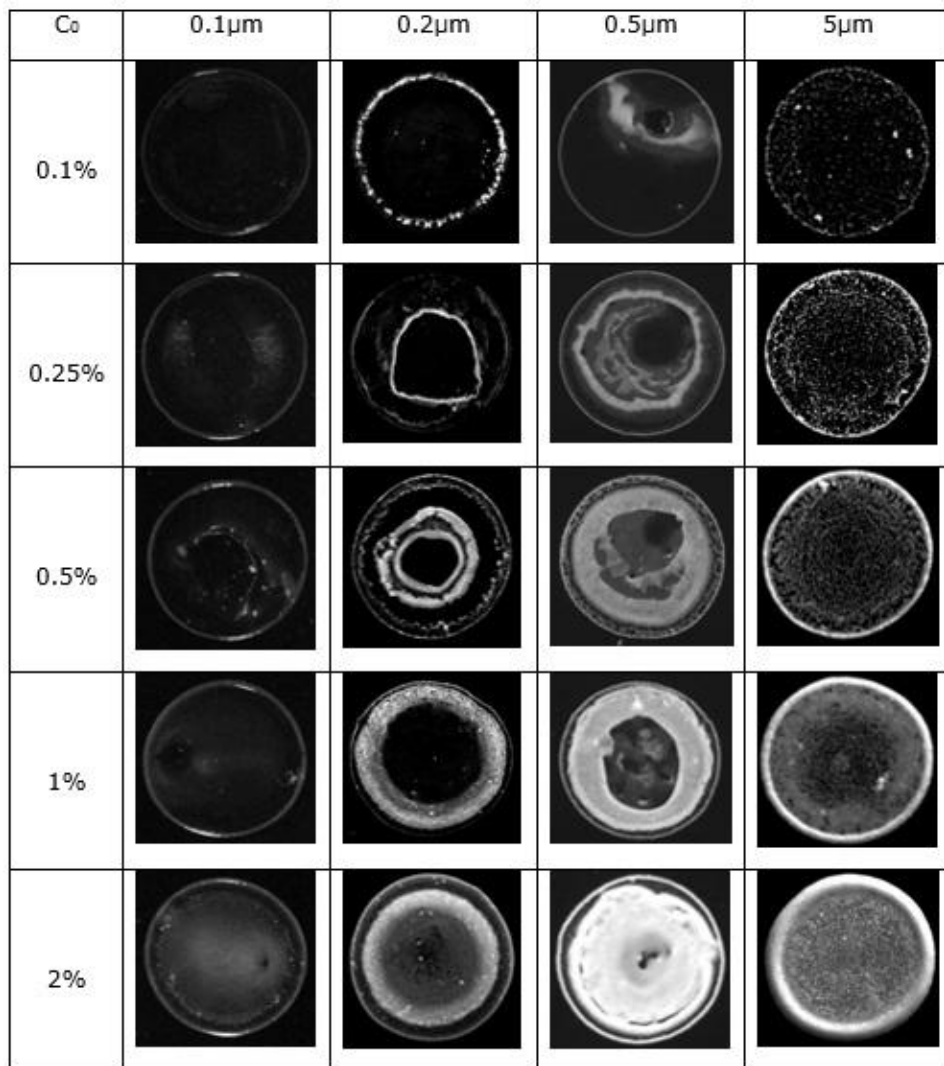


Figure 3.3: The final images as a function of initial concentration of polystyrene microparticles and particle sizes dried at >5nL/s with substrate of contact angle 35° in upright orientation.

For 0.1, 0.2 and 0.5 $\mu\text{m}$  thinner rings were observed compared to low drying rates with larger fraction of particles left at the interior of these rings. For 0.2 and 0.5 $\mu\text{m}$  at 0.25% deposits at the interior of the thin rings are seen as other multiple rings. It is suggested that, temperature-induced effect, flow effect and "Bulldozer effect" (microparticles trapped at the vapour-liquid interface and move with it as the droplets dries) may be responsible for the observed patterns but fully details on the kinematics is provided in chapter 4. For 5 $\mu\text{m}$  particles, a larger fraction of the particles are observed at the perimeter of the droplet forming ring like deposits. For the rings formed for 1% and 2% are narrow compared to those formed at low drying rates in figure 3.1. Below 0.5% monolayer of ring like deposits are also formed with fraction or other particles at the interior of these rings. Since the evaporation rate is higher, the rate at which the particles sediments competes with advection flow. The advection flow of liquid toward the droplet edge is stronger enough to drag 5 $\mu\text{m}$  particles leading to a ring like deposit observed.

**(d) Upside Down Orientation: High Drying Rates**

The effect of drying rates was also studied by placing the droplets in an upside down orientation. Figure 3.4 presents sample of images showing their deposit patterns. For 5 $\mu\text{m}$  particles at 1% and 2% concentration, particles are observed in the entire droplets with wider ring like deposits at the perimeter. Below these initial concentrations deposits patterns are a function of number of particles in the droplets. At 0.5% despite forming ring like deposits at the perimeter, a second ring like deposit is observed at the interior of the first ring. For 0.1% and 0.25% thin rings, are observed with larger fraction of particles distributed at the interior of these rings.

For smaller particles, the deposits patterns are almost seemingly similar to those in upright orientation. Larger fractions of the particles are located at the interior of the thin rings than at the perimeter. Wider multiple rings are clearly observed for

0.2 $\mu\text{m}$  and 0.5 $\mu\text{m}$  particles in the middle ranges of the initial concentrations. For 0.1 $\mu\text{m}$  thin rings are observed as well with larger fraction of particles deposited at the interior of the rings. The effect of orientation is not pronounced for smaller particle sizes of 0.1 $\mu\text{m}$ , 0.2 $\mu\text{m}$  and 0.5 $\mu\text{m}$  compared to 5 $\mu\text{m}$  particles where the deposits patterns show differences with those in upright orientation of seemingly similar drying rates.

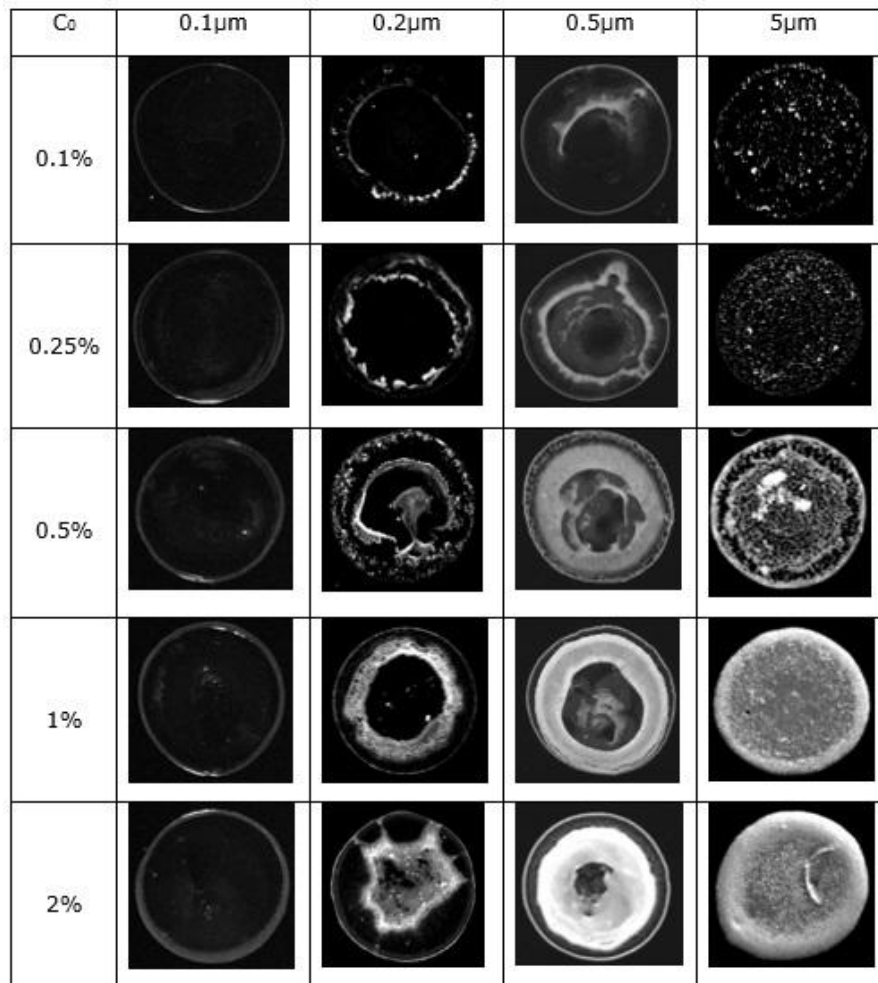


Figure 3.4: The final images as a function of initial concentration of polystyrene microparticles and particle sizes dried at  $>5\text{nl/s}$

### 3.2.1.2 Effect of Contact Angle

The effect of contact angle is known to determine the diameter of the droplet on the substrate. The contact angle will also affect the evaporation flux patterns at the

droplets interface. When the contact angle is less than  $90^\circ$  the evaporation rate according to Deegan's model will be non-uniform with higher values at the contact line and decreases towards the apex of the droplet along the liquid-vapour interface. However when the contact angle is greater than  $90^\circ$  for hydrophobic substrates, the evaporation is higher at the apex than near the contact line. Experiments were performed by varying the contact angles ( $\theta < 90^\circ$ ) of the substrate to assess their contribution in ring stain formation. Figure 3.5 shows sample images of  $0.2\mu\text{m}$  particles as a function of initial concentration for contact angle of  $5^\circ$ ,  $18^\circ$  and  $35^\circ$ .

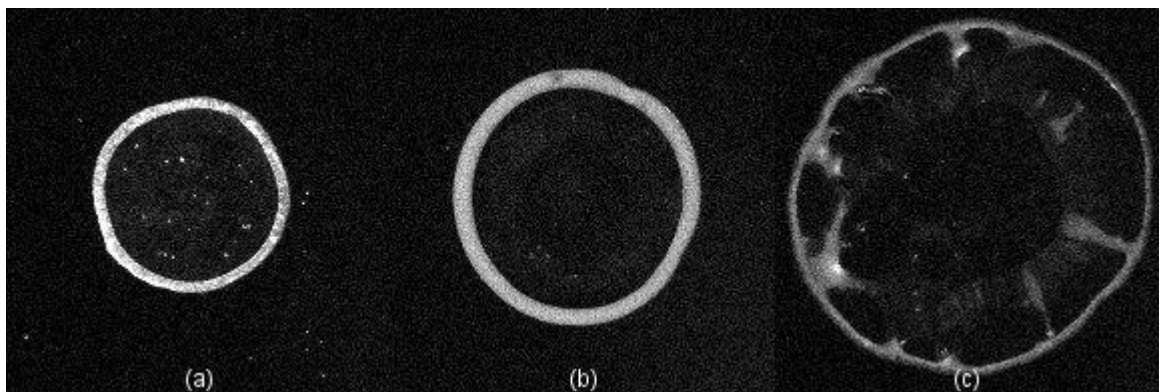


Figure 3.5: Final deposit left after drying droplets of  $0.2\mu\text{m}$  PS particles ( $c_0 = 1\%$ ) at ambient conditions with substrates of contact angle (a)  $\theta = 35^\circ$  ( $0.4 \text{ nL/s}$ ) (b)  $\theta = 18^\circ$  ( $2.6 \text{ nL/s}$ ) and (c)  $\theta = 5^\circ$  ( $3.4 \text{ nL/s}$ ).

All droplets containing 1% of  $0.2\mu\text{m}$  polystyrene particles were dried at ambient conditions. When the contact angle was increased from  $5^\circ$  to  $35^\circ$ , the drying rate decreases by a factor of  $\sim 9$  and the corresponding radius of the final deposits shown in figure 3.5 was observed to decrease by a factor of  $\sim 2$ . Since the droplets were pinned during all time when evaporation was taking place, then the outer radius of the final deposits should be similar to the initial radius of the droplets, then it follows that the evaporation rate is proportional to initial radius as reported previously by Rowan et.al, [153]. Despite forming robust rings in both contact angles, rings flattens as the contact angles decreases due to competition between

the number of particles and the increased radius as well as the droplet area at the wedge. Recently Askounis et.al, [154] have demonstrated that wedge constraints play an important role in determining the deposition patterns at a contact line and hence the nature of the ring formed.

### **3.2.1.3 Reproducibility**

The deposit patterns shown in figure 3.1 to 3.5 were repeated at least five times each in order to check for reproducibility of the results. As a representative in upright orientation for droplets drying at lower rates and upright orientation at higher drying rates at various concentrations and particle sizes, sample images are presented

#### **(a) Upright Orientation (Low Drying Rates)**

The initial concentrations were 0.02%, 1% and 0.25% for 0.1  $\mu\text{m}$ , 0.2  $\mu\text{m}$  and 0.5 $\mu\text{m}$  PS microparticles respectively with sample deposit images shown in figure 3.6. From figure 3.6, the deposits patterns are reproducible within all five images with robust rings and small fraction of particles at the interior of the rings as observed before in figure 3.1.

#### **(b) Upright Orientation (High Drying Rates)**

The initial concentrations were 0.02%, 1% and 0.25% for 0.1  $\mu\text{m}$ , 0.2  $\mu\text{m}$  and 0.5 $\mu\text{m}$  polystyrene particles respectively as in part (a) above. The images show different features especially at the interior of the ring compared to those in figure 3.6 dried at low rate of about  $\sim 0.6\text{nL/s}$ . Meanwhile in figure 3.7 thin rings are observed for droplets dried at higher rates of  $\sim 8\text{nL/s}$  compared to bigger rings in figure 3.6 of similar initial concentrations dried at  $\sim 0.6\text{nL/s}$ . The ring width and height are reproducible; there are variations in the patterns inside the drop at high drying rates. The fraction of the microparticles at the interior of the ring is the

function of both the initial concentration and the rate at which the droplets are drying.

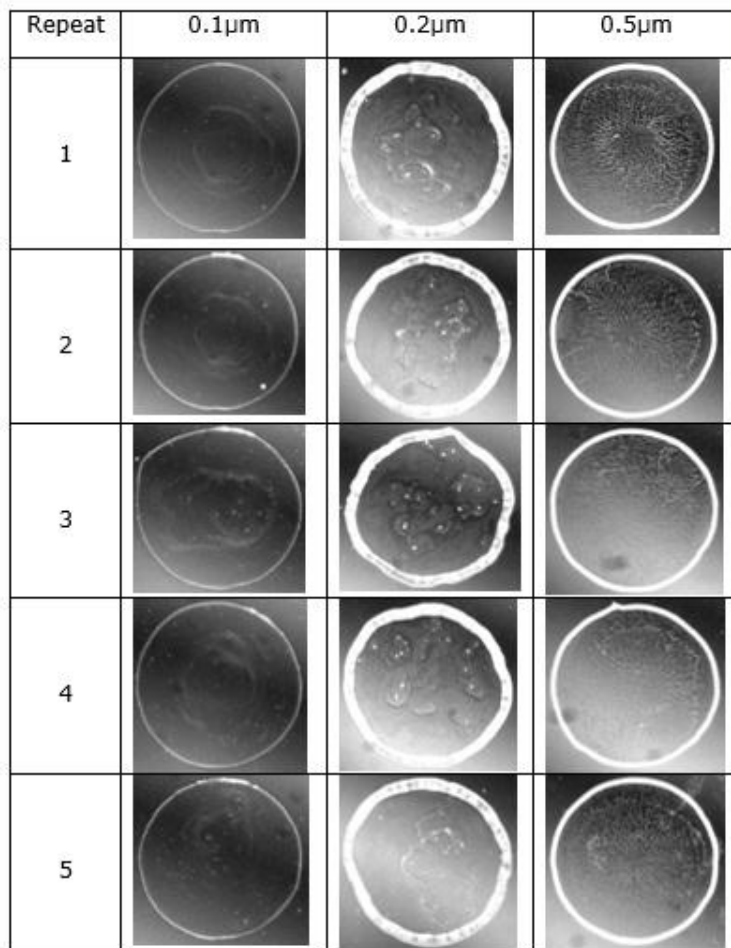


Figure 3.6: The five final images showing their reproducibility when dried at  $\sim 0.6$ nL/s with substrate of contact angle  $35^\circ$  in upright orientation.

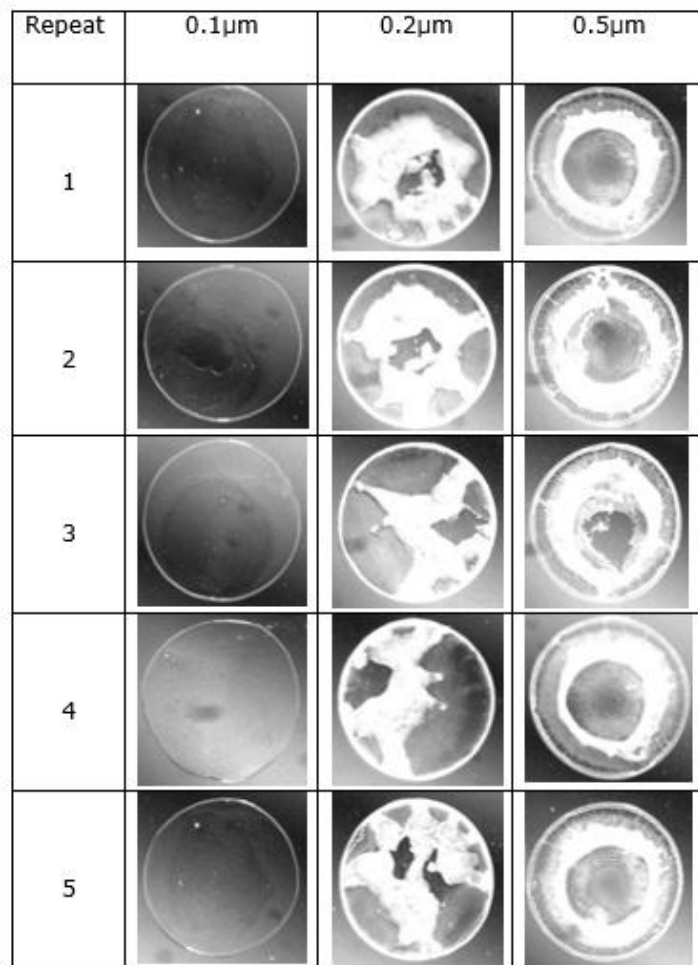


Figure 3.7: The five final images showing their reproducibility when dried at  $\sim 8$ nL/s with substrate of contact angle  $35^\circ$  in upright orientation.

### 3.2.2 Analysis of the Images/Patterns

Having observed the patterns deposited using conventional CCD/microscopes, the next stage was to quantify the dimensions of these deposits in terms of their height, width and radii. The final deposits from the dried droplets were analyzed by surface stylus profiler and Image J software techniques. As described in section 2.3.3, the stylus surface profiling involved the physical contact of the scanning stylus tip with the deposits when determining their respective depths (hills and valleys). The image J method is a non-invasive method which relied on the integrated light intensity of the images from the areas with and without deposits. The two methods

were implemented to extract the important parameters of interest from the deposits and results compared. Figure 3.8 show sample of these deposits and their corresponding profiles using surface stylus profiler and Image J software with droplets dried in upright orientation.

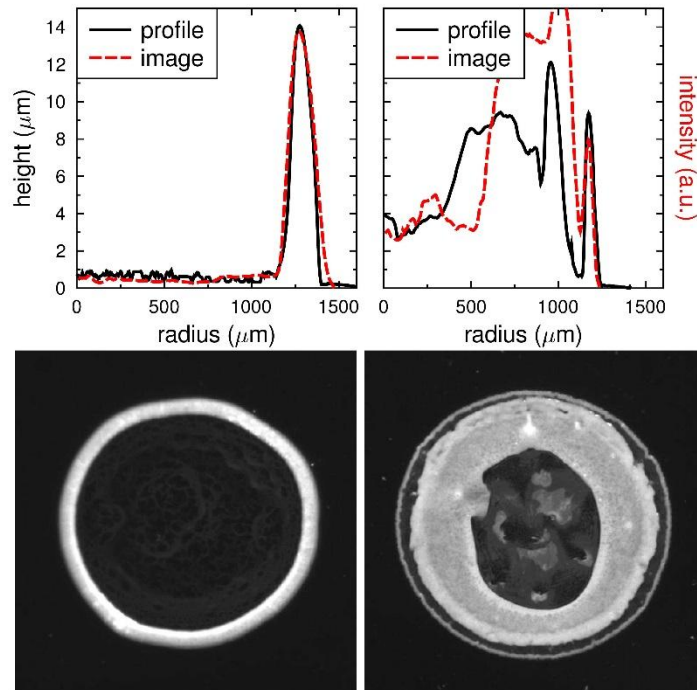


Figure 3.8: Comparison of deposit profiles showing the height of the deposits in  $\mu\text{m}$  using the stylus profilometer (solid black lines) and normalised integrated intensity (in arbitrary units) obtained from ImageJ (red dashed lines). The scale of the latter was adjusted for easy comparison with the profilometry data. The two images are shown underneath. Both droplets contained  $0.5\mu\text{m}$  polystyrene particles at initial concentration,  $c_0 = 1\%$  at two different drying rates,  $0.6\text{nL/s}$  (left) and  $5.3\text{nL/s}$  (right)

Usually the deposit height using Image J software is expressed as integrated normalized intensity in arbitrary units (see figure 2.7). The radius of the deposit was calibrated using a glass graticule. In order to check whether the deposit profile shape using the two methods does indeed give comparable results, the Image J

data was scaled in the deposit height (in arbitrary units) to give the same amplitude as the height for easy comparison. From figure 3.8 the two methods of analysing the final deposits worked better when the droplets were dried at  $\sim 0.6 \text{ nL/s}$ . When the droplets were dried at higher rates, much of the final deposits were located at the interior of the droplets as a result the imaging method became limited.

Also there was a variation within deposits so cannot really compare inside the ring. The other limitation of the imaging method was its inability to give the final deposits height rather than intensity in arbitrary units. However Image J software analysis could provide ring width which compares well to that determined from stylus profiler to within 5%. The only results of ring height and width reported in this section are those extracted using data analysed with stylus surface profiler.

The stylus surface profiler methods was also used to confirm the presence or absence of rings across the particles sizes used in the experiments. Results show that  $5 \mu\text{m}$  particles had deposit patterns varying greatly depending on the experimental parameter such as drying rate, orientation and initial concentration. This was confirmed by data analysed using stylus surface profiler as shown in figures 3.9 and 3.10. In figure 3.9 for initial concentration of 0.1% and 0.25% only monolayers of deposited particles of  $\sim 5 \mu\text{m}$  are observed. For 0.5% and 1% the deposit height is between  $\sim 5 \mu\text{m}$  and  $\sim 15 \mu\text{m}$  whereas for 2% the deposit heights are between  $\sim 10 \mu\text{m}$  and  $\sim 25 \mu\text{m}$ . There is no clear robust ring observed apart for the highest concentration as consequences its scaling power law prediction would not be easy to determine.

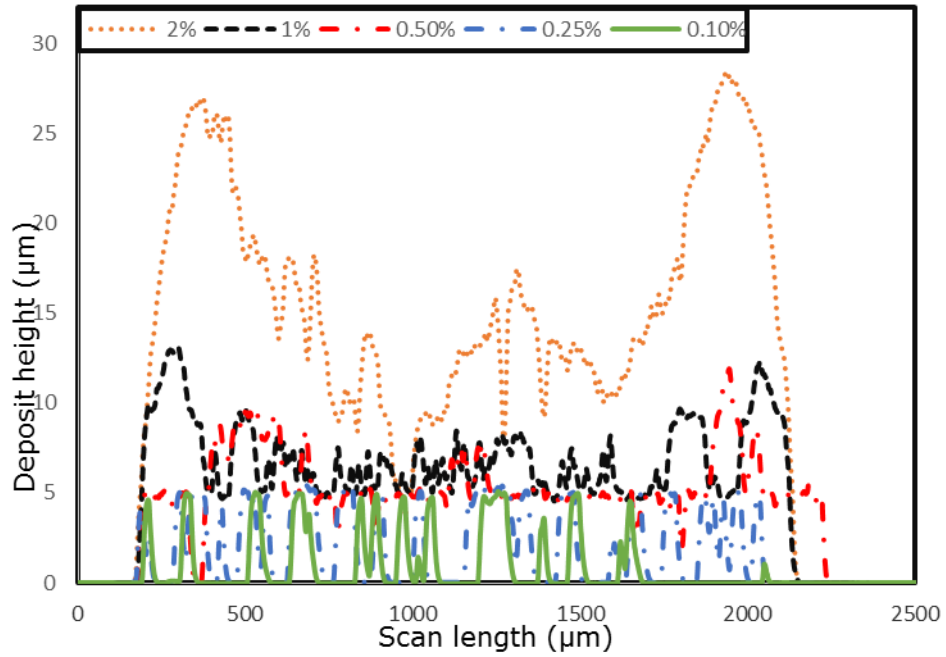


Figure 3.9: Deposit profiles obtained with stylus profilimeter of 5µm particles dried at ~0.6nL/s.

However in figure 3.10 there is a clear deposit patterns at the perimeter and at the interior. For 2% the deposit at the perimeter are as higher as 30µm and around ~10µm at the interior. Meanwhile for 0.5% and 1% the deposit height at the perimeter is in between ~13µm and ~21µm with a monolayer of 5µm in the interior. For 0.25% and 0.1% a 5µm monolayer of deposited particle is observed. Despite forming rings in some concentration ranges both at low and high drying the scaling power law prediction for 5µm particle will not be considered in this thesis except its dynamics of droplets drying.

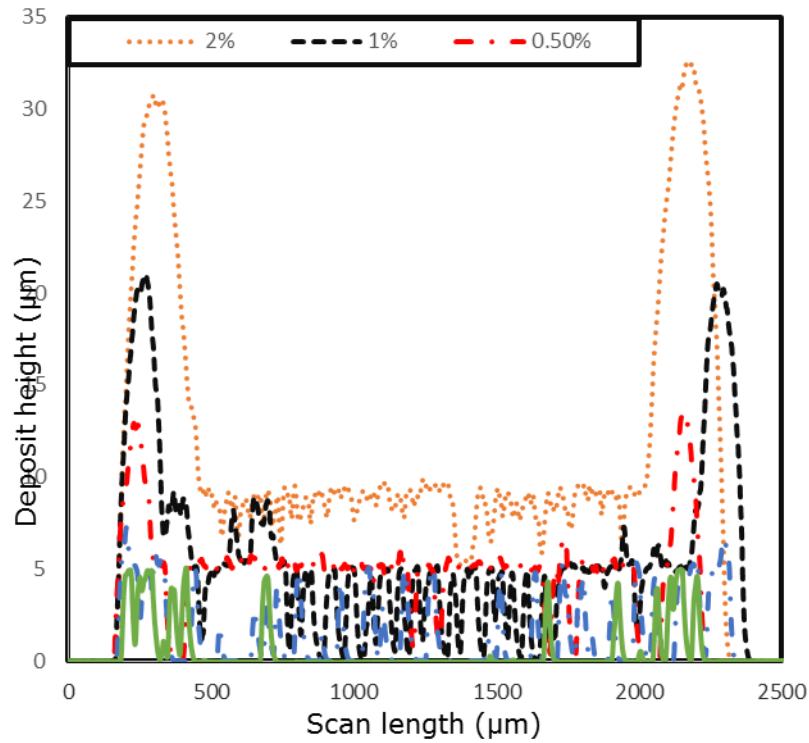


Figure 3.10: Deposit profiles of 5µm particles dried at >5nl/s.

### 3.2.3 The Scaling Laws

In the following section, we aim to study the effect of particle concentrations  $c_0$  on the width  $w_r$  and height  $h_r$  of the deposit. Earlier investigations and theory found a power dependence of the form  $w_r \propto c_0^{0.5}$  and  $h_r \propto c_0^{0.5}$ . The effect of contact angle, evaporation rate, orientation of the droplet and particles sizes will be investigated to assess their effect on power law as a function of particle concentration.

#### 3.2.3.1 The Effect of Contact Angle

In this section the initial contact angle was varied using substrates of various wettability as measured by drop shape analysis contact angle meter. The glass cover slips substrates bought from Chance Proper, Ltd., (UK) had a value of  $\theta = 35.3 \pm 0.5^\circ$ , advancing contact angle,  $\theta_a = 38.4 \pm 0.4^\circ$  and receding contact angle,  $\theta_r = 34.0 \pm 0.5^\circ$ . On the other hand, the microscope glass slides substrates

bought from Sail Lab Co. Ltd., (China) had  $\theta = 18.3 \pm 3.3^\circ$ ,  $\theta_a = 19.1 \pm 0.3^\circ$  and  $\theta_r = 16.3 \pm 0.7^\circ$ . Meanwhile microscope glass slides substrates bought from Thermo Fischer Scientific Inc., (Menzel-Glaser) had  $\theta = 5^\circ$ . The advancing and receding contact angle for Menzel-Glaser microscope glass slides was not possible due to small droplet height on it. To investigate the effect of contact angle only 0.2 $\mu$ m PS particles was used. To assess the effect of contact angle on the power law exponent the deposit profiles were analyzed by surface stylus profiler to extract the deposit radius  $R$ , ring height,  $h_r$  and width,  $w_r$ . The line running through the data of ring height,  $h_r$  and width,  $w_r$  against initial concentration,  $c_0$  were fitted with function of the form  $h_r = Q_1 c_0^n$  and  $w_r = Q_2 c_0^m$ . By taking log to these function we find that  $\log(h_r) = n \log(c_0) + \log Q_1$  and  $\log(w_r) = m \log(c_0) + \log Q_2$  respectively where,  $n$  and  $m$  are exponents. It is worth noting that  $Q_1$  and  $Q_2$  are intercepts for which  $\log(c_0) = 0$ . The error in the gradient of the line running through the data were determined by excel LINEST function.

Figure 3.11 shows sample plot of a ring height as a function of initial concentration of the PS microparticles in the droplets for different substrates (having each a different contact angle value). The value of intercepts  $Q_1$  in figure 3.11 represent the ring height for which  $c_0 = 1\%$ . The values of  $Q_1$  are reproducible for the same value of contact angle. Overall the ring height is a strong function of the contact angle. The average value  $n = 0.51 \pm 0.07$  concluding that the initial contact angle has much effect on the ring height and the scaling power law compares well with the theoretical predictions  $h_r \propto c_0^{0.5}$  within a limit of experimental error.

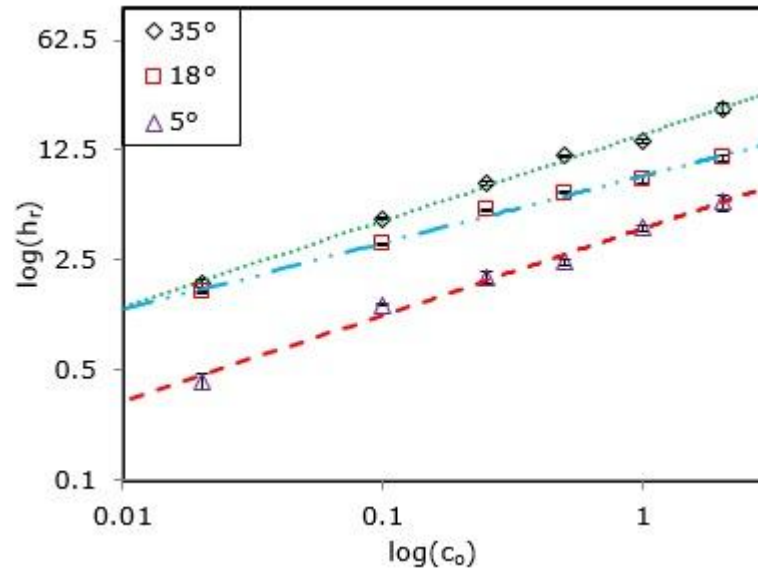


Figure 3.11: The effect of contact angle on ring height  $h_r$  for varying concentration,  $c_0$  on three different substrates with contact angle values  $\theta=5^\circ$ ,  $18^\circ$  and  $35^\circ$ . The lines are linear best fit,  $\log(h_r) = n\log(c_0) + \log Q_1$  indicating a power law with an exponent given by the slope of the fits with  $n(5^\circ) = 0.55 \pm 0.05$ ,  $n(18^\circ) = 0.43 \pm 0.03$ , and  $n(35^\circ) = 0.55 \pm 0.03$ .

Figure 3.12 show sample plot of a ring width respectively as a function of initial concentration of the PS microparticles in the droplets for different substrates (having each a different contact angle value). The value of intercept,  $Q_2$  in figure 3.12 represents the ring width respectively for which  $c_0 = 1\%$ . The values of  $Q_2$  are reproducible for the same value of contact angle. The average value  $m = 0.35 \pm 0.04$  and shows that the initial contact angle has less effect on the ring width. The scaling power law for ring is less than the theoretical predictions  $w_r \propto c_0^{0.5}$  within a limit of experimental error. The discrepancy may be attributed to fact the the packing fraction is not the same across the deposit and that the ring width is not of the same order as the ring height as described in deriving the equation  $w_r \propto c_0^{0.5}$  in appendix C.

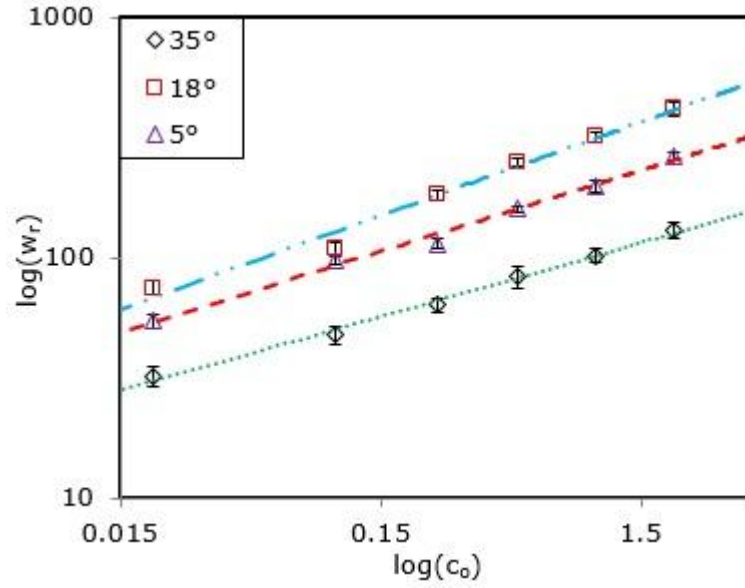


Figure 3.12: The effect of contact angle on ring width  $w_r$  for varying concentration,  $c_0$  on three different substrates with contact angle values  $\theta=5^\circ$ ,  $18^\circ$  and  $35^\circ$ . The straight lines are best fits indicating a power law dependence with an exponent given by the slope  $m(5^\circ) = 0.34 \pm 0.03$ ,  $m(18^\circ) = 0.39 \pm 0.06$ , and  $m(35^\circ) = 0.31 \pm 0.02$ . For  $\theta = 35^\circ$ . The three data sets coincide and, therefore, for clarity they are offset from each other by multiplying  $\theta = 35^\circ$  data by 0.6 and  $\theta = 18^\circ$  data set by 1.4.

Also we investigate the effect of deposit radius and its contribution to the exponent for ring width. To do that the ring widths,  $w_r$  data used to plot figure 3.12 was normalized to their respective deposit radius,  $R$  for each contact angle and the results re-plotted as a function of  $c_0$  as shown in figure 3.13. The normalization was performed to assess the effect of increased deposits radius with decreasing contact angle and its consequences on the scaling power law for ring width. The lines running through the data in figure 3.13 were fitted with function of form

$$\log\left(\frac{w_r}{R}\right) = s \log(c_0) + \log Q_3$$

where  $s$  is the slope.

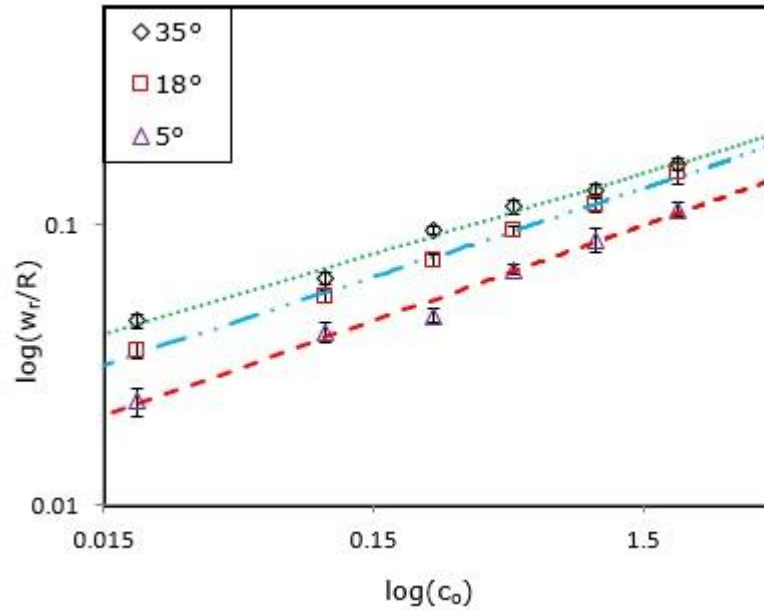


Figure 3.13: The width of the ring normalized by the droplet radius for varying concentration,  $c_0$  on three different substrates with contact angle values  $\theta=5^\circ$ ,  $18^\circ$  and  $35^\circ$ . The straight lines are best fits indicating a power law dependence with an exponent given by the slope  $s(5^\circ) = 0.34 \pm 0.03$ ,  $s(18^\circ) = 0.32 \pm 0.02$ , and  $s(35^\circ) = 0.29 \pm 0.02$ .

From figure 3.13 it is observed there is slightly increase in the value of exponents as the contact angle decreases. This may be due the competition between the increased radius and the number of PS particles in the droplet for similar initial concentration and particle size. Using PS microparticles, Deegan et.al, [1] found the relationships between the ring width at the moment the liquid depins (the process of detachment of the liquid phase from the deposit ring) in terms of radius of droplet contact area  $\left(\frac{W_r}{R}\right)$  and initial concentration  $c_0$  of the particles in the droplet.

From the experiments it was concluded that the exponents were  $s = 0.78 \pm 0.10$  for  $0.1\mu\text{m}$  PS microparticles and  $s = 0.86 \pm 0.10$  for  $1\mu\text{m}$  PS microparticles. The ring height was not measured directly but inferred using values off contact angle and

not available for comparison. However these values by Deegan et.al, [1] are larger than our observed values. Popov [51] presented a complex calculation to predict (a power of 0.5 for both ring height and width) the spatial dimensions of the ring stain which agrees with the simple physical argument presented in section 1.6, but not the measurements of Deegan. His resolution to this discrepancy was that as the depinning time is also a function of initial concentration, scaling as  $\sim c_0^{0.26}$ , more concentrated solutions will remain pinned for longer and more of the particles will end up deposited in the ring. By addition of the exponents, he recovers Deegan's  $s = 0.78$  exponent for ring width. The difference in the exponents between the present study and those in reference [1] may be attributed to the shape dependency of the deposit on the concentration (details presented in section 3.2.3.3). Our results is based on a full reproducible and controllable ring while result from Deegan et.al, [1] is based on a small section of a ring where the liquid has been detached forming a hole. The portion of the ring next to the hole remains wet throughout the period before the droplet dries completely allowing accumulation of some particles. Thus the ring width determined at the moment of depinning is always less than that determined in the next portion after the droplet has completely dried. This may result in a different exponent as we have observed due to the fact that some particles are still in the bulk of the droplet contradicting with the assumption that all particles end up in the ring.

### **3.2.3.2 The Effect of Particle sizes and droplet orientation**

#### **(a) Upright Orientation**

This section presents the results of the scaling power exponents as function of particles sizes in upright orientation of the droplets during drying as shown in figure 3.14 and 3.15 for ring height and width respectively.

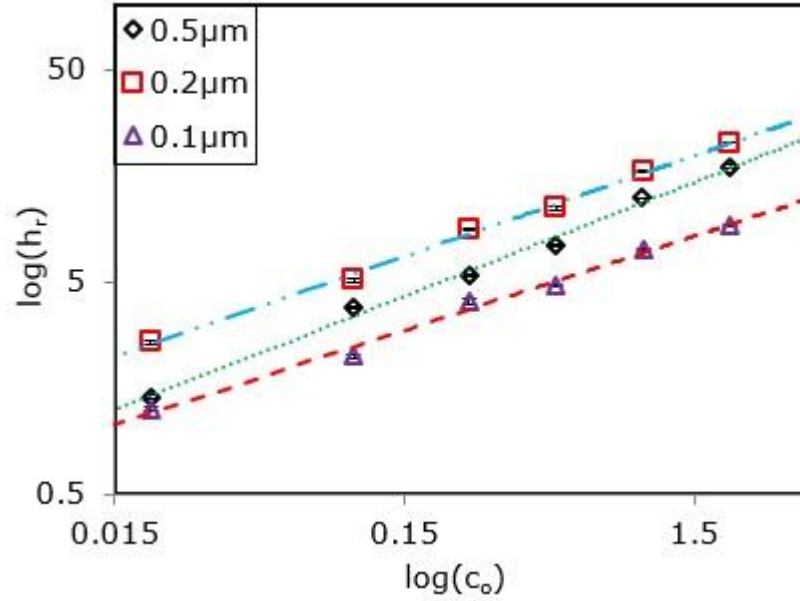


Figure 3.14: The effect of particle size on ring height for varying concentration,  $c_o$  for upright orientation on three PS microparticles sizes  $0.1\mu\text{m}$ ,  $0.2\mu\text{m}$  and  $0.5\mu\text{m}$ . The straight lines are best fits indicating a power law dependence with an exponent given by the slope  $n(0.1\mu\text{m}) = 0.49 \pm 0.09$ ,  $n(0.2\mu\text{m}) = 0.46 \pm 0.07$ , and  $n(0.5\mu\text{m}) = 0.51 \pm 0.07$ . The three data sets coincide and, therefore, for clarity they are offset from each other by multiplying  $0.2\mu\text{m}$  data set by 1.4 and  $0.1\mu\text{m}$  data set by 0.6.

By averaging these values of exponents in table 3.1 for all PS microparticles gives  $m = 0.30 \pm 0.04$  and  $n = 0.49 \pm 0.03$ .

Particle size	m	n
$0.1\mu\text{m}$	$0.35 \pm 0.02$	$0.47 \pm 0.02$
$0.2\mu\text{m}$	$0.31 \pm 0.04$	$0.50 \pm 0.04$
$0.5\mu\text{m}$	$0.28 \pm 0.02$	$0.53 \pm 0.02$

Table 3.1: The average value of exponent  $n$  and  $m$  for upright orientation for different PS particle sizes.

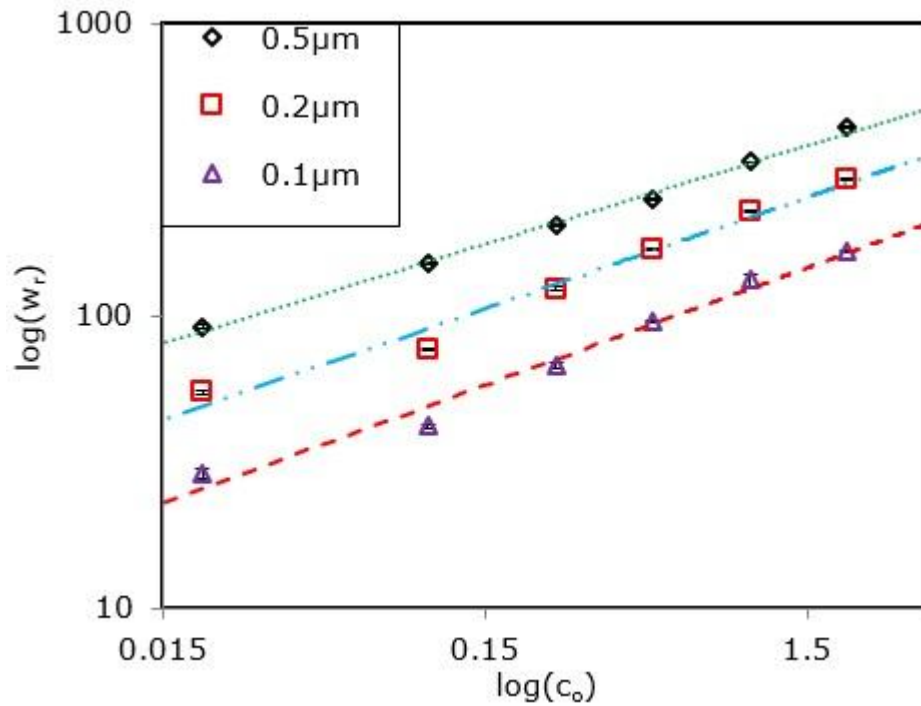


Figure 3.15: The effect of particle size on ring width for varying concentration,  $c_o$  for upright orientation on three PS microparticles sizes 0.1 $\mu\text{m}$ , 0.2 $\mu\text{m}$  and 0.5 $\mu\text{m}$ . The straight lines are best fits indicating a power law dependence with an exponent given by the slope  $m(0.1\mu\text{m}) = 0.35 \pm 0.09$ ,  $m(0.2\mu\text{m}) = 0.31 \pm 0.10$ , and  $m(0.5\mu\text{m}) = 0.34 \pm 0.02$ . The three data sets coincide and, therefore, for clarity they are offset from each other by multiplying 0.5 $\mu\text{m}$  data set by 1.4 and 0.1 $\mu\text{m}$  data set by 0.6.

In general within the limit of experimental errors the values of  $m$  or  $n$  for all particles sizes in upright orientations are seemingly similar. Deegan [78] had reported a value of  $m = 0.25$  for 15 and 40 nm gold nanoparticles evaporating at ambient conditions in a silicon substrate with initial contact angle of 49°. The values of  $m$  for PS microparticles in the present study are slightly greater than those found by Deegan [78] using gold nanoparticles. The difference between these values may be attributed to effect of concentration on the shape of the deposit. For Deegan [78] the deposits showed a densely packed ring at high concentration (3%)

which is comparable to 2% in our experiments. However at low concentration (0.003%) the ring was filled with voids while in our experiments the lowest concentration in figure 3.15 was 0.02% with the deposit showing packed rings. This lead to a misleading dimension of a ring filled with voids as well as the packing fraction and hence the scaling power law. No data for ring height by Deegan [78] was provided and thus a direct comparison to the present study is not possible.

**(b) Upside Down Orientation**

The same procedure in 3.3.2 (a) was employed for droplets dried from the upside down orientation. Sample graphs are shown in figure 3.16 and 3.17 for ring height and width respectively.

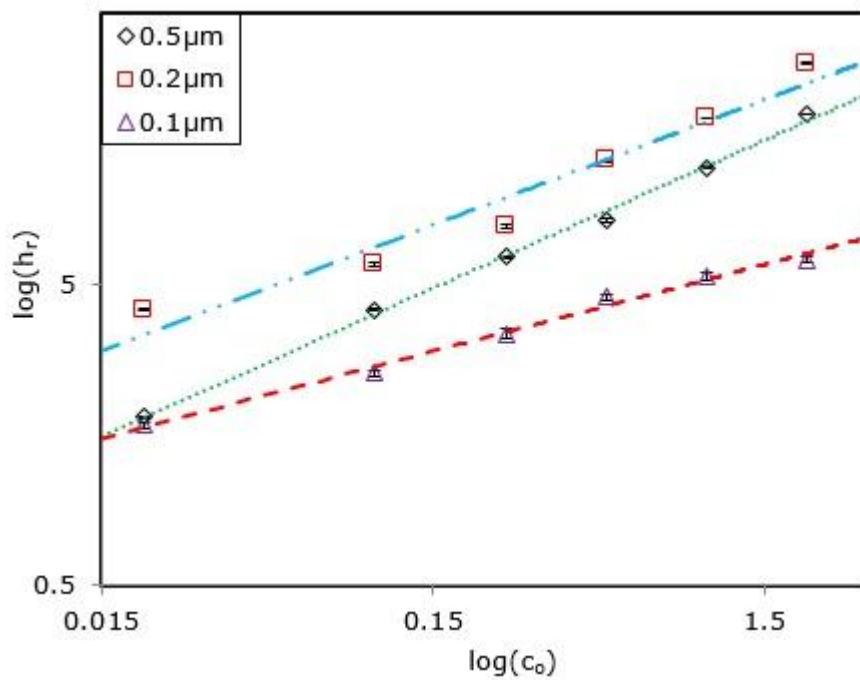


Figure 3.16: The effect of particle size on ring height for varying concentration  $c_0$  for upside down orientation on three PS microparticles sizes  $0.1\mu\text{m}$ ,  $0.2\mu\text{m}$  and  $0.5\mu\text{m}$ . The straight lines are best fits indicating a power law dependence with an exponent given by the slope  $n(0.1\mu\text{m}) = 0.47 \pm 0.09$ ,  $n(0.2\mu\text{m}) = 0.51 \pm 0.07$ , and  $n(0.5\mu\text{m}) = 0.53 \pm 0.06$ . The  $0.2\mu\text{m}$  data set multiplied by 1.4 and  $0.1\mu\text{m}$  by 0.6).

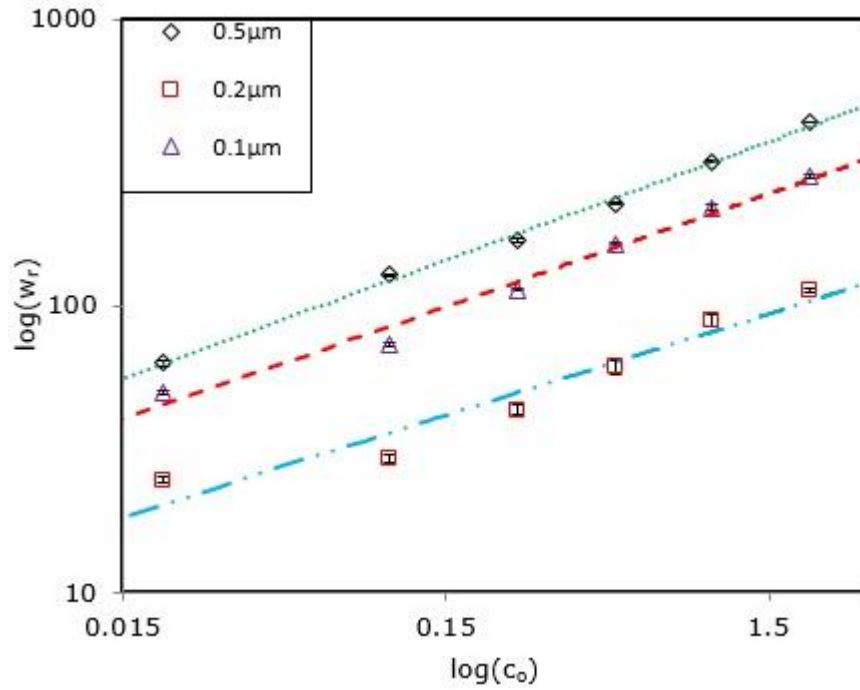


Figure 3.17: The effect of particle size on ring width for varying concentration,  $c_o$  for upside down orientation on three PS microparticles sizes  $0.1\mu\text{m}$ ,  $0.2\mu\text{m}$  and  $0.5\mu\text{m}$ . The straight lines are best fits indicating a power law dependence with an exponent given by the slope  $m(0.1\mu\text{m}) = 0.33 \pm 0.04$ ,  $m(0.2\mu\text{m}) = 0.31 \pm 0.05$ , and  $m(0.5\mu\text{m}) = 0.32 \pm 0.03$ . The  $0.5\mu\text{m}$  data set was multiplied by 1.4 and  $0.1\mu\text{m}$  data set by 0.6 for clarity.

The overall average for all PS microparticles in table 3.2 yields  $m = 0.30 \pm 0.03$  and  $n = 0.50 \pm 0.03$ . Regardless of the particles sizes the exponent power law are seemingly similar with the limit of experimental error.

	m	n
$0.1\mu\text{m}$	$0.33 \pm 0.02$	$0.48 \pm 0.02$
$0.2\mu\text{m}$	$0.31 \pm 0.02$	$0.50 \pm 0.02$
$0.5\mu\text{m}$	$0.27 \pm 0.04$	$0.53 \pm 0.04$

Table 3.2: The average value of exponent  $n$  and  $m$  for upside down orientation for different PS particle sizes.

By considering the mean value of exponent power laws for both upright and upside down orientations it is fair to say the orientation plays no role in determining these exponents for the PS microparticles considered in this thesis. This suggests that gravity does not play a role in PS particles present in the droplets and has been confirmed with OCT measurements (results presented in chapter 4). The PS microparticles sizes were chosen such that the effect of gravity is negligible to avoid sedimentation for larger particles such as 5 $\mu\text{m}$ .

### **3.2.3.3 The Effect of Evaporation Rate**

The rate at which the ring dimensions grows at the perimeter of the droplets were studied by reducing the pressure of the working chamber from atmospheric conditions to low pressure of about 13 mbar. Despite the fact that the low pressure chamber could be evacuated to as low as 3.5 mbar, the limit of 13 mbar was not exceeded to avoid freezing of the droplets. Experiments evaporated 1 $\mu\text{L}$  droplets containing polystyrene microparticles with diameter of 0.1, 0.2 and 0.5 $\mu\text{m}$  were conducted at 13, 67, 269, 534, 800 and 1007 mbar. As described in section 2.3.2 the effect of evaporation on the ring growth was conducted when the droplets were deposited both in upright and upside down orientations inside the low pressure chamber. The radius of the droplet,  $R$  which is the same as the radius of the ring was plotted (not shown) as a function of initial concentration for different evaporation rates and the line running through the data fitted with a function of the form  $\log(R) = p\log(c_0) + \log Q_4$ . The volume  $V_{\text{ring}}$  of the deposit in the ring at the perimeter of the droplet is expected to be equal to the product of ring height ( $h_r$ ), ring width ( $w_r$ ) and droplet radius ( $R$ ) given as  $[V_{\text{ring}} = (w_r \times 2\pi R)(h_r)]$ . As a result the summation of their corresponding exponents to their initial concentration should then be equal to one,  $m+n+p=1$ . The experimental results for values of

exponents  $m$ ,  $n$ ,  $p$  and  $m+n+p$  are presented in figure 3.18 as a function of evaporation rates for different particle sizes.

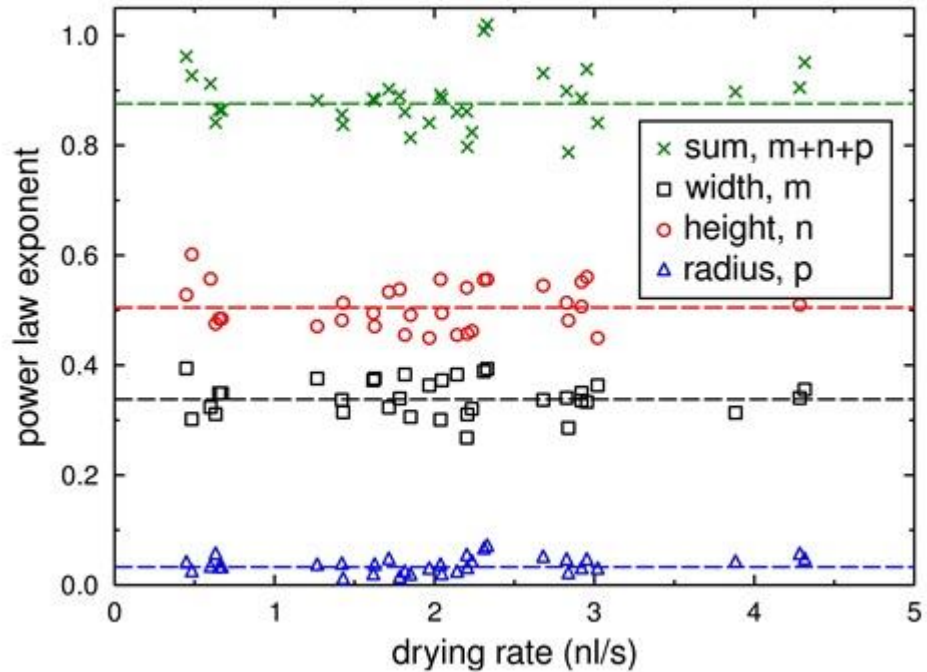


Figure 3.18: Data points show the fitted values for the power law exponents describing how the ring width ( $m$ , black squares), ring height ( $n$ , red circles) and initial droplet radius ( $p$ , blue triangles) vary with drying rate. Also shown is the sum of all three exponents  $m+n+p$ . Exponents were determined for a range of PS microparticle sizes, initial contact angles, and droplet orientations.

It is worth noting that results presented in this section does not include power law exponent whose evaporation rates corresponds to a pressure of 13 mbar. At this particular value of pressure the final deposits were characterized by thin rings with most of the deposits located at the interior of the droplets and sometime there was no clear ring from the rest of the ring stain (figure 3.8 page 86). From figure 3.18 the average values of exponents are  $m = 0.33 \pm 0.05$ ,  $n = 0.50 \pm 0.04$ ,  $p = 0.03 \pm 0.01$  and  $m+n+p = 0.86 \pm 0.07$ . If all the polystyrene microparticles were deposited at the ring then,  $m+n+p = 1$ , however it turns out to be less than

one. The experimental results presented agree on the arguments presented section 1.6 only for exponent power law for ring height of 0.5 as theory predicts. There is discrepancy on the exponent power law for ring width from the predicted value. One possible reason for this discrepancy is attributed to the fact that the small fraction of the PS microparticles are deposited at the interior of the ring and hence not involved in calculating its volume in equation (3.1). For a droplet evaporating with constant radius, by conservation of particles, the theoretical predictions requires that, the final mass,  $M(t = t_F)$  of the deposit in the ring should be proportional to the initial volume  $V_0$  multiplied by their initial concentration by mass of the particles  $c_0$  according to equation (3.1).

$$M(t = t_F) = \rho V_0 c_0 \phi \quad (3.1)$$

where  $\rho$  is the density of a particle,  $t_F$  is the droplet life time and  $\phi$  is the average packing fraction in the deposit. An example of the deposit at the interior of the droplet is shown in figure 3.19.

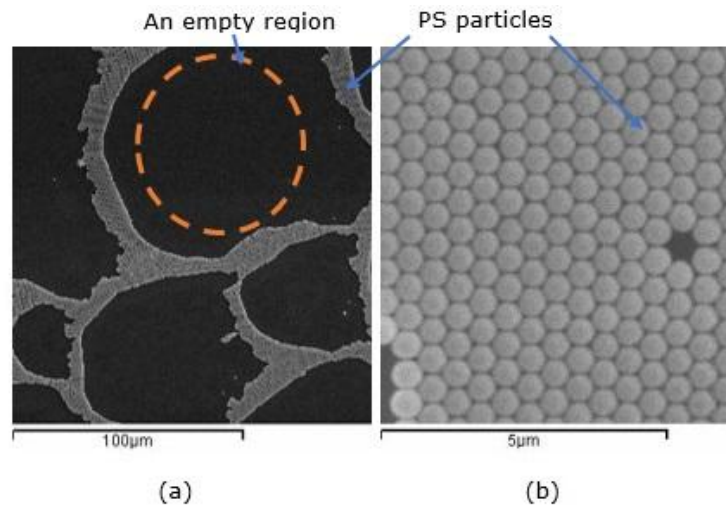


Figure 3.19: Scanning electron microscope of deposit left at the interior of the ring from drying (a) 0.25% of 0.5µm of PS microparticles at 0.6nL/s and (b) 2% of 0.5µm of PS microparticles at 0.6nL/s. The image in (b) was obtained at higher magnification compared to (a).

The patterns of the deposit at the interior of the droplet are determined by dramatic temporal speed up of the particles motion near the end of the evaporation (“rush hour effect”) and the direction of liquid detachment from the ring as well as the substrate. Further these deposits at the interior of the ring were quantified in terms of percentage of the total volume of the initial concentration by using imaging methods (assuming monolayer) and data from surface stylus profiler to determine percentage in the ring. Determining percentage using imaging method was limited by the resolution of the images and the number layer of microparticles at the interior of the ring. For more than one layer of microparticles it was impossible to determine the actual surface area occupied by the microparticles. We anticipate that the absence of the microparticles to form part of the ring contributes to the discrepancy in the exponent power law observed. Sample of the result is shown in figure 3.20 and it is clear that percentage of the deposits in the ring is also a strong function of the rate at which the droplets were drying.

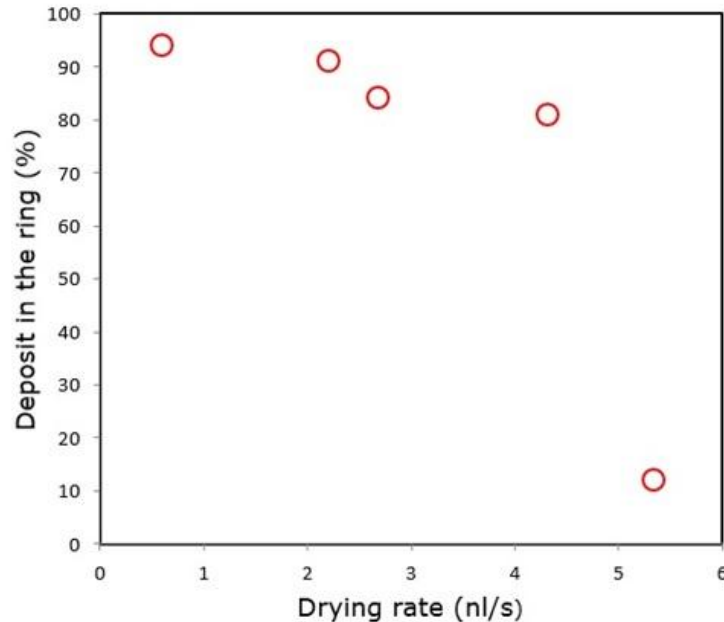


Figure 3.20: Percentage of the deposit in the ring from drying 2% of 0.5 $\mu$ m PS particles in upright orientation using data from surface stylus profiler.

From figure 3.20 the percentage of the deposit in the ring at  $\sim 0.6 \text{ nL/s}$  is about 94% and decreases to about 81% at  $\sim 4 \text{ nL/s}$ . By counting  $10 \mu\text{m}$  particles (with concentration 0.004% by volume) arriving at the contact line as the droplet evaporates, Deegan et.al, [4] found that  $\sim 10\%$  did not reach the contact line and hence form part of the ring. This is in agreement with our results that not all PS particles reach the contact line. However when the drying rate is increased at greater than  $5 \text{ nL/s}$ , only less than 12% of the deposit is found in the ring. At higher drying rates, a high fraction of the polystyrene microparticles move to the interior of the droplet as a result only a thin ring is observed. Except for higher drying rates, the percentage of the deposits in the ring is higher and almost constant in both orientations and is consistent to the observed exponent power laws. The percentage of deposit in the ring as a function of initial concentration  $c_0$  of the particles is shown in figure 3.21.

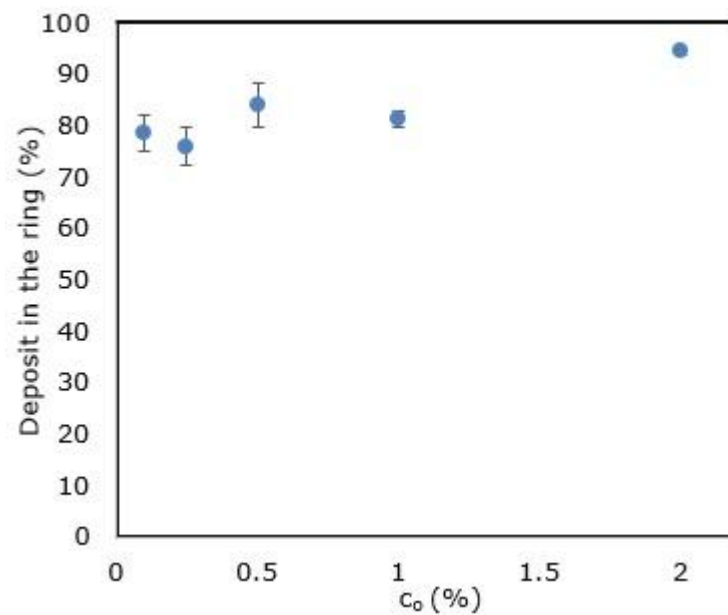


Figure 3.21: Percentage of the deposit in the ring as a function of initial concentration  $c_0$  for  $0.5 \mu\text{m}$  PS particles in upright orientation (atmospheric conditions)

There is a slightly decrease in percentage of particles in the ring as the initial concentration of the PS particles decreases attributed to competition between the capillary and diffusion flow. For a droplet initially with particles  $>10^{10}$ , there is strong pinning at the contact line controlled by diffusion and hence the formation of coffee ring stain [103]. When the droplet contains particles  $<10^{10}$ , few particles pin at the contact line and capillary flow is responsible for it. For  $0.5\mu\text{m}$  PS particles with the concentration range  $0.002\% \leq c_0 \leq 2\%$ , the droplets contained between  $3 \times 10^8$  and  $3 \times 10^{11}$  number of particles. This shows that at low initial concentration below the threshold ( $<10^{10}$  particles) there is less pinning and one would expect fewer particles in the ring compared to those above the threshold where there is strong pinning.

To further investigate the validity of the scaling laws, we centered the stylus profilometer data on the peak of the deposit and rescale in the horizontal and vertical coordinates using the 2% data as the unscaled values by applying equation (3.2).

$$r^* = r \left( \frac{0.02}{c_0} \right)^g, \quad z^* = z \left( \frac{0.02}{c_0} \right)^n \quad (3.2)$$

where  $r$  and  $z$  is radius and height coordinates respectively. The rescaled coordinates for radius and height are  $r^*$  and  $z^*$  respectively. The aim of rescaling was to assess whether the assumption in section 1.6 which says for the simple argument to hold, the cross-sectional shape of the deposit should not depend on the initial concentration  $c_0$  of the particles in the droplet. In figure 3.22, using values of  $g=0.42$  and  $n=0.55$ , the scaled profiles are similar, although the detailed shape of the deposit shows some variation with concentration. These might contribute to the discrepancy in the power law for ring width.

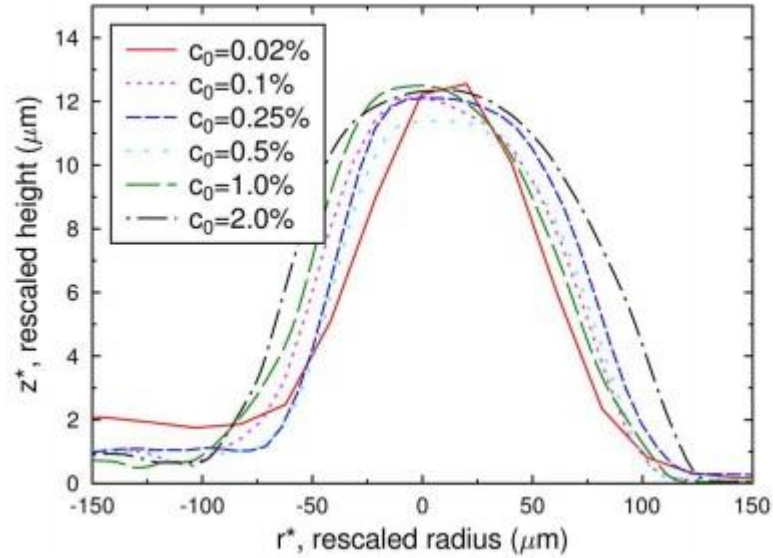


Figure 3.22: Ring profile data for droplets containing 500 nm particles drying at a pressure of 800 mbar for a range of initial concentrations. Radius and height coordinates are rescaled with concentration using exponents  $g = 0.42$  and  $n = 0.55$  respectively. The outside of the droplet is in the positive  $r^*$  direction.

Another reason that may have contributed to the discrepancy observed exponent power law is that there is an increase in microparticles packing fraction,  $\phi$  at higher initial concentrations such that the ring deposit have misleadingly small dimension [95]. For example figure 3.23 show the scanning electron microscope image of inner and outer section of a ring for 0.25% initial concentration with a droplet dried at atmospheric conditions. From figure 3.23 the deposit pattern show ordered (hexagonal close packed) to disordered pattern and is consistent with previous study by Marín et.al, [95]. This show the packing fraction within the deposit is not the same as for hexagonal closed packed of  $\sim 0.74$  and for disordered the packing fraction of  $\sim 0.66$ . Since the ring width is inversely proportional to the square root of the packing fraction,  $w_r \propto \sqrt{\frac{1}{\phi}}$  one would expect a misleading dimension. The

smaller the packing fraction for disordered particles the wider the ring, compared to the same initial concentration for ordered particles with a thin ring.

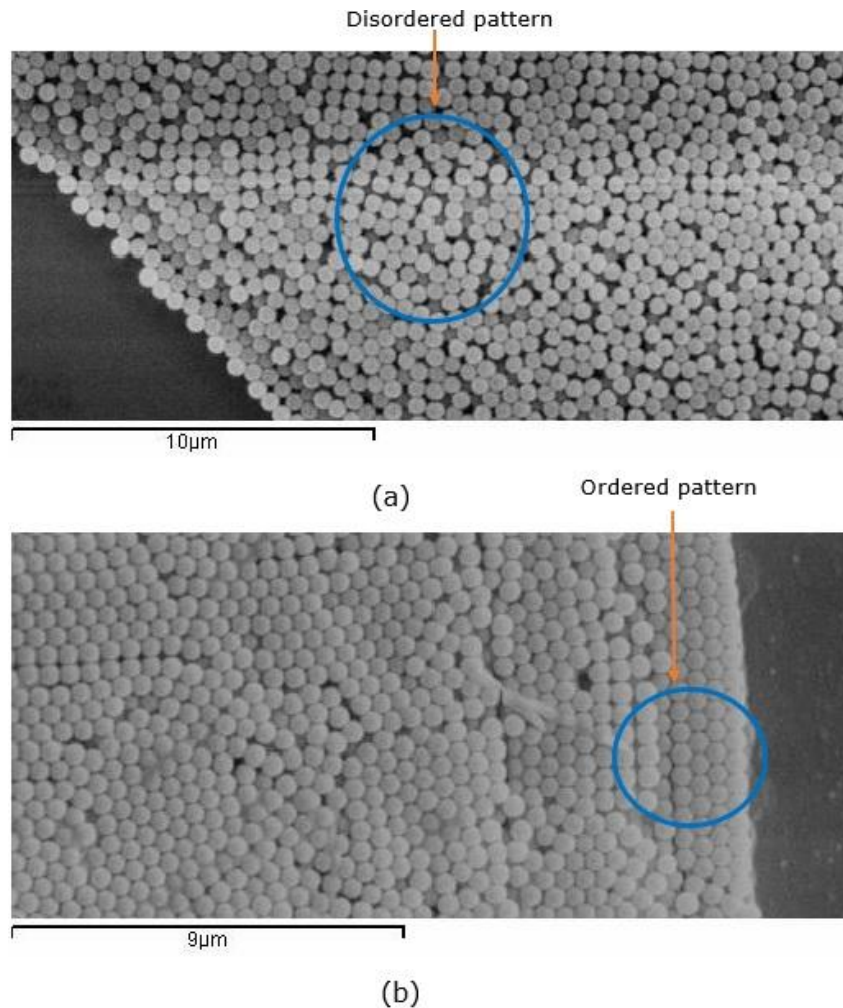


Figure 3.23: Scanning electron microscope section of a ring with 0.25% of 0.5 μm PS microparticles with (a) inner most ring and (b) outer most ring.

### 3.3 Conclusions

The evaporation of droplet containing PS microparticles have been studied by varying initial contact angle, concentration of the particles, size of the particles, evaporation rate and orientation of the droplet. Robust rings have been observed for drying rate  $<5\text{nL/s}$  and thin ring for  $>5\text{nL/s}$ . However the ring stain is particle size dependent when evaporation rate and concentration are varied. Experimental

results on scaling power law show that, ring height has strong dependence on the contact angle, particle sizes and droplet orientation for drying rate  $< 5 \text{ nL/s}$  and agree well with theoretical prediction. However there is a discrepancy in the power law for ring with from the theoretical prediction.

## **Chapter 4**

### **Kinematics of Droplet Drying**

## **4.1 Introduction**

In an experimental investigation, Abramchuk et.al, [155] and Jing et.al, [156] observed internal circulation flow in evaporating droplets to determine the patterns of DNA stretching without modifying their biochemical properties. In chapter 3 a number of experimental parameters were varied to investigate their effects on ring stain formation including evaporation rate, contact angle, orientation of the droplets, particles sizes and their initial concentrations. Varieties of deposition patterns were observed, however the kinematics behind these observations were not quantified at low ( $\sim 0.6\text{nL/s}$ ) and high ( $> 5\text{nL/s}$ ) drying rates. A robust ring and small fractions of PS microparticles at the interior of the ring at  $\sim 0.6\text{nL/s}$  was observed while for  $> 5\text{nL/s}$  a thin ring and large fraction of PS microparticles at the interior of the ring was observed. A better way of finding the mechanisms behind the observed deposition patterns was to visualize the flow of the individual PS microparticles to describe fully the droplet evaporation mechanism. As described in experimental techniques (section 2.4) we utilized optical microscope and Spectral domain optical coherence tomography (SDOCT) to visualize the PS microparticles flow inside the drying sessile droplets to describe the convection flow to explain the deposition patterns observed as in chapter three. The aim of this chapter is to understand the dynamics of droplet drying and the reasons behind the behaviours observed and the effects of particle sizes.

## **4.2 Experimental Methods**

### **4.2.1 Material Preparation**

To study the kinematics of droplet drying, surfactant free  $0.5\mu\text{m}$ ,  $2\mu\text{m}$  and  $5\mu\text{m}$  PS microparticles were used. The PS microparticles suspension and substrates were prepared as described in sections 2.2.1, 2.2.3, 2.2.4 and 2.2.5. The optimum initial

concentration used in the present experiments were chosen to satisfy two conditions; firstly to ensure pinning at the contact line and secondly to enable ease of visualisation and tracking them accordingly. The initial concentrations used were 0.06%, 0.04% and 0.1% for 0.5 $\mu$ m, 2 $\mu$ m and 5 $\mu$ m PS particles respectively. Only microscope cover slip glasses substrate of initial static contact angle of 35° was used. The surface zeta potential of the microscope cover slip glasses substrate was measured by Zetasizer to be  $-49.4\pm 4.2$ mV. The average zeta potential of PS microparticles is shown in table 4.1 and their corresponding concentrations of hydrogen ions (pH) in table 4.2.

	0.001%	0.01%	0.1%	1%
0.1 $\mu$ m	$-15.1\pm 2.8$	$-32.9\pm 0.2$	$-43.4\pm 0.2$	-
0.2 $\mu$ m	$-25.9\pm 0.6$	$-38.5\pm 0.7$	$-45.4\pm 0.5$	-
0.5 $\mu$ m	$-36.7\pm 1.4$	$-37.3\pm 0.3$	$-38.2\pm 0.4$	-
2 $\mu$ m	-	$-30.1\pm 0.0$	$-32.3\pm 0.2$	$-50.8\pm 0.3$
5 $\mu$ m	-	$-12.7\pm 2.1$	$-31.7\pm 0.8$	$-35.7\pm 0.1$

Table 4.1: Zeta potential (mV) as a function of initial concentration and particles sizes as per Zetasizer instrument limits.

	0.001%	0.01%	0.1%	1%
0.1 $\mu$ m	$6.2\pm 0.1$	$5.8\pm 0.0$	$5.8\pm 0.0$	-
0.2 $\mu$ m	$5.6\pm 0.2$	$5.7\pm 0.1$	$5.7\pm 0.1$	-
0.5 $\mu$ m	$5.6\pm 0.0$	$5.6\pm 0.0$	$5.6\pm 0.2$	-
2 $\mu$ m	-	$5.7\pm 0.1$	$5.6\pm 0.0$	$5.7\pm 0.1$
5 $\mu$ m	-	$5.9\pm 0.0$	$5.8\pm 0.0$	$5.6\pm 0.0$

Table 4.2: The concentration of hydrogen ions (pH) in the suspensions corresponding to each initial concentration of PS microparticles in table 4.1.

The zeta potential of the PS microparticles in Table 4.1 show stability from moderate to good toward the flocculation depending on the concentration of the

microparticles and in table 4.2 the suspension is slightly acid using deionized water of pH  $5.7 \pm 0.1$ .

#### **4.2.2 Kinematics of Droplets Drying by SDOCT**

The SDOCT method enables the 2D cross-sectional visualization of PS microparticles flow inside the drying droplets. The experimental set-up and principle behind the operation of SDOCT coupled with low pressure chamber has been described fully in section 2.4.1. The room temperature was maintained at about  $22.2 \pm 0.2^\circ\text{C}$  (the variations seem to be quite small due good air conditioning in the laboratory) while the relative humidity at  $57.4 \pm 4.6\%$ . The SDOCT x-spacing (pixel size) is determined by the scanning length and the number of columns. The number of columns was varied from 200 to 1000 while the scanning length of up to 2.4mm producing a scanning rates between  $\sim 1.0$  to 4.6 fps. For example for  $1\mu\text{L}$  droplet with horizontal scan length of 1.8mm, depth range of 1.6mm and 500 columns produces horizontal x-spacing of  $3.6\mu\text{m}/\text{pixel}$  at a scanning rate of  $\sim 2.0\text{fps}$ . SDOCT axial resolution is determined by the coherence length of the source, while SDOCT transverse resolution depends not only on the wavelength, but also the focal length and the diameter of the laser beam. Depending on the experiment such as the whole droplet, half a droplet or a small section of a droplet near the contact line, the parameter above was combined accordingly. The sequence of images was saved as video after processing them with Image J software.

To determine the PS microparticles velocities, two methods were employed one using the PIV/PTVlab tracking algorithm and manually using Image J software. To determine the PS microparticles velocity by Image J, displacements in a given number of frames were determined by tracking particle through their center-of-mass to determine the Cartesian coordinates [145, 146] as illustrated in figure 4.1 and 4.2.

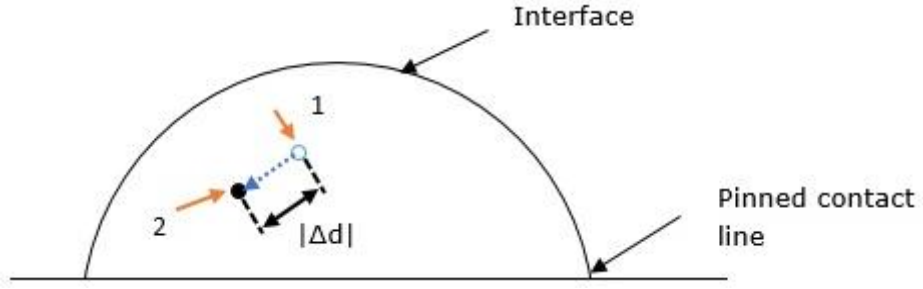


Figure 4.1: Schematic illustration of a PS microparticle movement from position 1 to 2 through an instantaneous displacement  $\Delta \vec{d}$ .

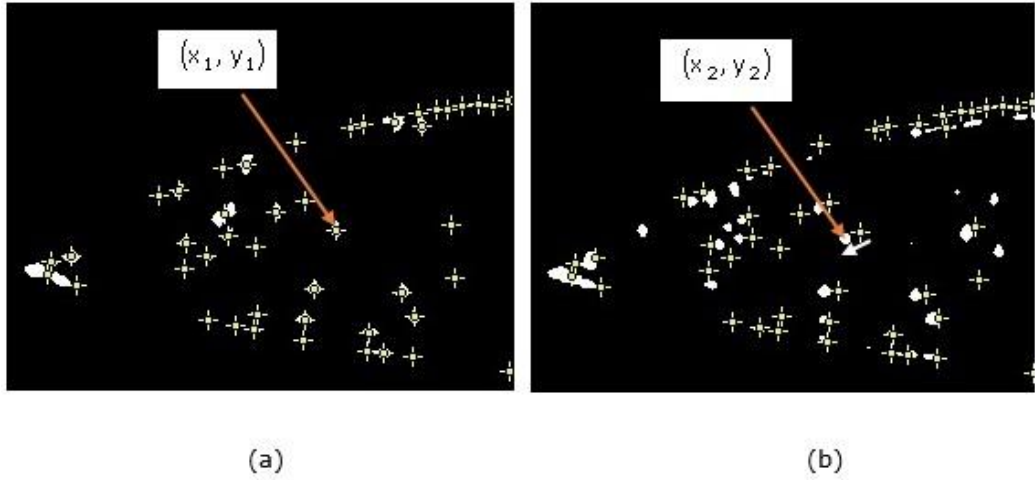


Figure 4.2: Determination of instantaneous displacements  $\Delta x = x_2 - x_1$  and  $\Delta y = y_2 - y_1$  of the same PS microparticle moving in 13 frames between coordinates  $(x_1, y_1)$  in (a) and  $(x_2, y_2)$  in (b). The short white arrow shows the direction of movement of a particle.

In figure 4.2, the actual PS microparticles are shown in an evaporating droplet between 13 frames. The PS microparticle considered in this case was tracked between coordinate  $(x_1, y_1)$  to  $(x_2, y_2)$  in order to determine the magnitude Instantaneous displacement  $|\Delta d| = \sqrt{(\Delta x)^2 + (\Delta y)^2}$ . The magnitude of velocity for each particle at time interval  $\Delta t$  was determined according to equation (4.1).

$$|V_i| = \frac{\sqrt{(\Delta x)^2 + (\Delta y)^2}}{\Delta t} \quad (4.1)$$

The calibration factors for x and y coordinates were represented by the value of x-spacing and y-spacing respectively for a given experiment. The vertical component of velocity of the PS microparticles was determined by measuring the optical path length [145] rather than the physical path length due to the difference in refractive index between air ( $n=1$ ) and water ( $n=1.33$ ). Therefore the vertical component of the PS microparticles displacement was divided by the refractive index of water ( $n=1.33$ ). For particles recirculating and/or moving through an air-liquid interface, their velocities has to be corrected as illustrated in figure 4.3 to include the effect of air-liquid interface displacement.

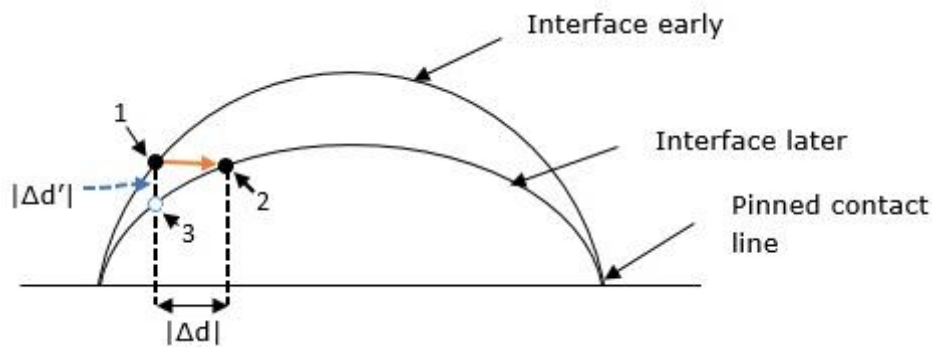


Figure 4.3: Schematic illustration of the effect fast descending air-liquid interface on the position of the particle. A particle from point 1 after time  $\Delta t$  is located at position 2 for fast descending interface and position 3 when the interface velocity is smaller than the particle velocity.

Form figure 4.3, initially a particle is located at position marked 1 and there are two possibilities this particle will be located later as the air-liquid interface descend.

One possibility is the particle to be located at position marked 3 when interface velocity is very small then the particle velocity and the corresponding displacement from point marked 1 will be  $\Delta \bar{d}'$ . However for high drying rate the air-liquid interface descends faster such that the particle is no longer located at position marked 3. The second possibility a particle will be located at position marked 2 and corresponding displacement from point marked 1 will be  $\Delta \bar{d}$ . In figure 4.4 a droplet containing PS microparticles is considered similar to illustration in figure 4.3.

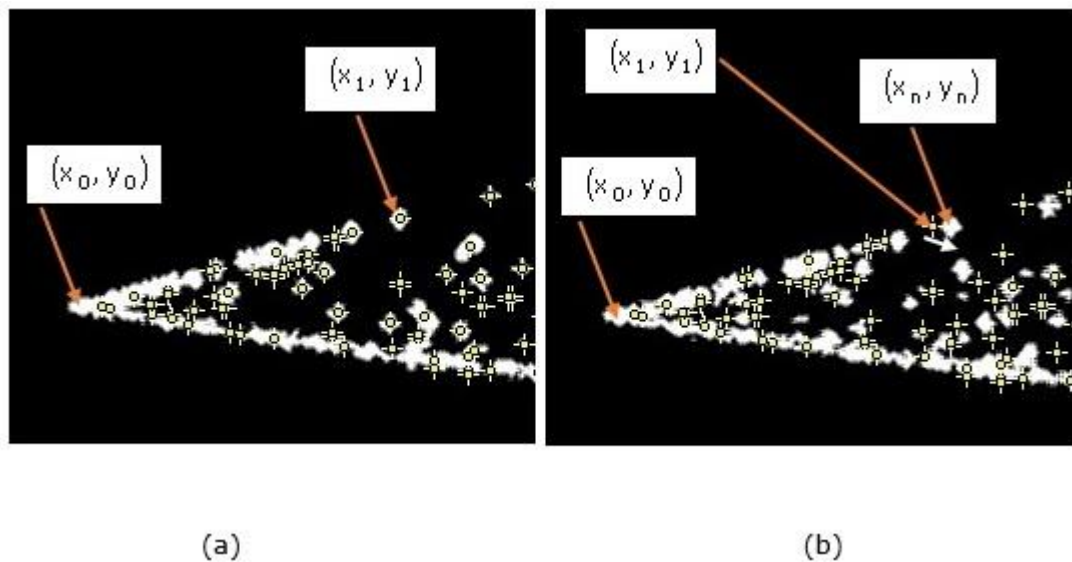


Figure 4.4: (a) A PS microparticle at the air-liquid droplet interface with coordinate  $(x_1, y_1)$  from contact line of coordinate  $(x_0, y_0)$  (b) Instantaneous displacement of the same particle in part (a) for 23 frames at  $\sim 2.0$  fps between coordinate  $(x_1, y_1)$  and  $(x_n, y_n)$  with respect contact line (the short white arrow show the direction of the particle) as the air-liquid interface moves.

The contact line is considered to be pinned at all-time whose coordinates are  $(x_0, y_0)$  and a PS microparticle at air-liquid interface with coordinates  $(x_1, y_1)$  at

time  $t_1$  in the frame  $f_1$  as shown in figure 4.4(a). Then the approximate magnitude of the distance  $|d_1|$  of this particle from the contact will be given according to equation (4.2).

$$|d_1| = \sqrt{[(x_1 - x_0)]^2 + [(y_1 - y_0)]^2} \quad (4.2)$$

For a given number frames the same PS microparticle will have displaced from coordinate  $(x_1, y_1)$  to a new coordinate  $(x_n, y_n)$  as described in figure 4.3(b) and the corresponding distance from the contact line will be given by equation (4.3).

$$|d_n| = \sqrt{[(x_n - x_0)]^2 + [(y_n - y_0)]^2} \quad (4.3)$$

The PS microparticle displacement  $\Delta \vec{d}$  for a given number frames taking into account of air-liquid droplet interface will be given as  $\Delta \vec{d} = \vec{d}_n - \vec{d}_1$  and the instantaneous velocity  $\vec{V}_i = \frac{\Delta \vec{d}}{\Delta t}$ . An equation (4.2) and (4.3) holds only for small change in contact angle and applies only for small number of frames. Then similar PS microparticle was tracked for a number of frames until it disappeared to determine the instantaneous velocities and average them. Similar procedures were repeated for at least 8 PS microparticles in a droplet and other two droplets making a total of 24 instantaneous measurements for inward velocity. The calculations above allowed the outward flow, vertical and inward velocities to be determined as illustrated in figure 4.5. Another important image processing tool was the Z-projection using Image J software. The Z-Projection is the one in which an image stack is projected along an axis perpendicular to the plane of the image (Z-axis) [157]. The preferred projection output method was to use average intensity where each pixel stored

average intensity over all images in a given stack at corresponding pixel location. Using PIV/PTVlab tracking algorithm Z-projection was automatically generated at the end of each session for the number of frames considered.

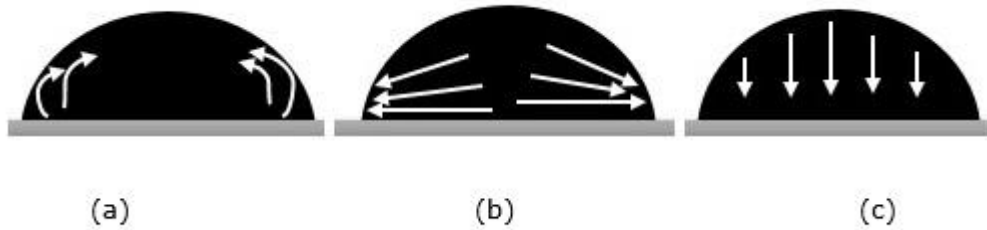


Figure 4.5: Illustration of particle motion (a) inward velocity (b) outward velocity and (c) vertical velocity.

### **4.2.3 Kinematics of Droplets Drying by Optical Imaging Microscope**

To study the kinematics of these particles an inverted optical microscope was used to capture images from underneath the droplet and reflection optical microscope from the top. With this experimental set-up it is only possible to determine the inward and outward PS microparticles velocity not the vertical velocity. The experimental details using an inverted optical microscope to image the movement of individual PS microparticles in an evaporating droplet is described in section 2.4.2. The PS microparticles velocities were determined by the method described in section 4.2.2 above using equation (4.1). The calibration factor (vertical and horizontal) of approximately  $0.59\mu\text{m}/\text{pixel}$ ,  $0.44\mu\text{m}/\text{pixel}$ ,  $0.067\mu\text{m}/\text{pixel}$  using a 10X, 50X and 100X magnifying lens respectively was applied. Figure 4.6 shows a sample of image sequences used to determine the instantaneous velocity of  $5\mu\text{m}$  particles at higher drying rates for those reaching the contact line captured inside a low pressure chamber

using 10X lens. Initially a PS microparticle is located at coordinate  $(x_1, y_1)$  as shown in figure 4.6(a) and after 21 frames at scan rate of 40fps this particle is located at coordinate  $(x_2, y_2)$  as shown in figure 4.6(b).

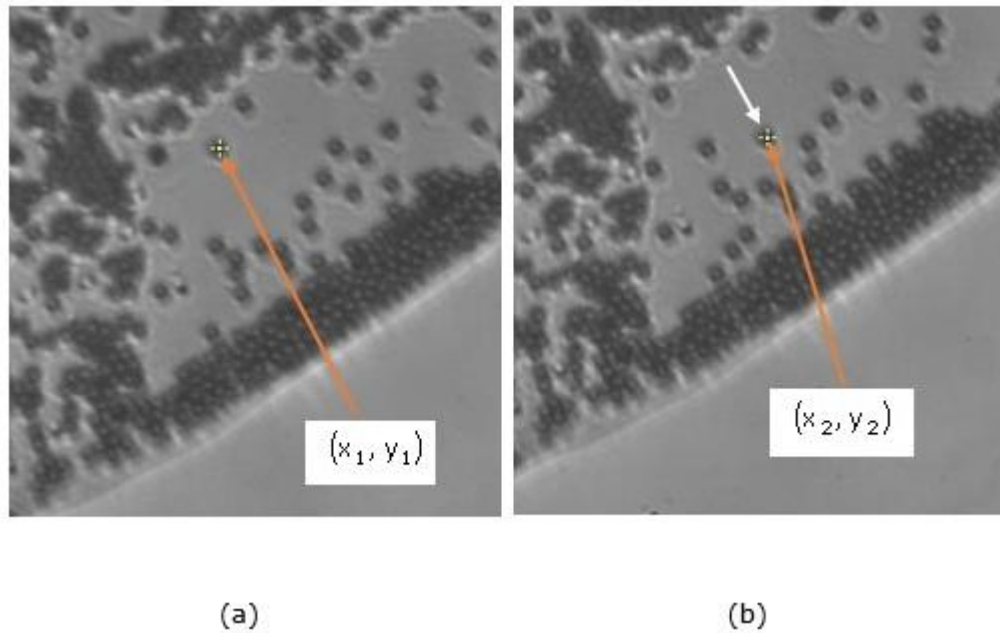


Figure 4.6: (a) The coordinates  $(x_1, y_1)$  of a  $5\mu\text{m}$  PS particles at higher drying rate at time  $t$  (b) After 21 frames the same particles has moved (as shown with a short white arrow) to a new coordinate  $(x_2, y_2)$ . The images were captured using a 10X magnification lens.

There are challenges in using optical imaging microscope in studying the kinematics of droplet drying. Firstly it is not possible to perform optical imaging of the individual PS microparticles in the bulk of the droplets in early stages of the droplets life time due to opaqueness. As a result the velocities determined in this section represent the later stage of the droplet life-time. Where there is vertical PS microparticles movement inside the droplet during evaporation, determining the actual coordinates of the particles is not possible resulting in larger errors of the instantaneous velocities. Secondly is the formation of

clusters making difficulty in determining individual particles velocities as shown in figure 4.7 for 5 $\mu$ m PS particles using 10X lens.

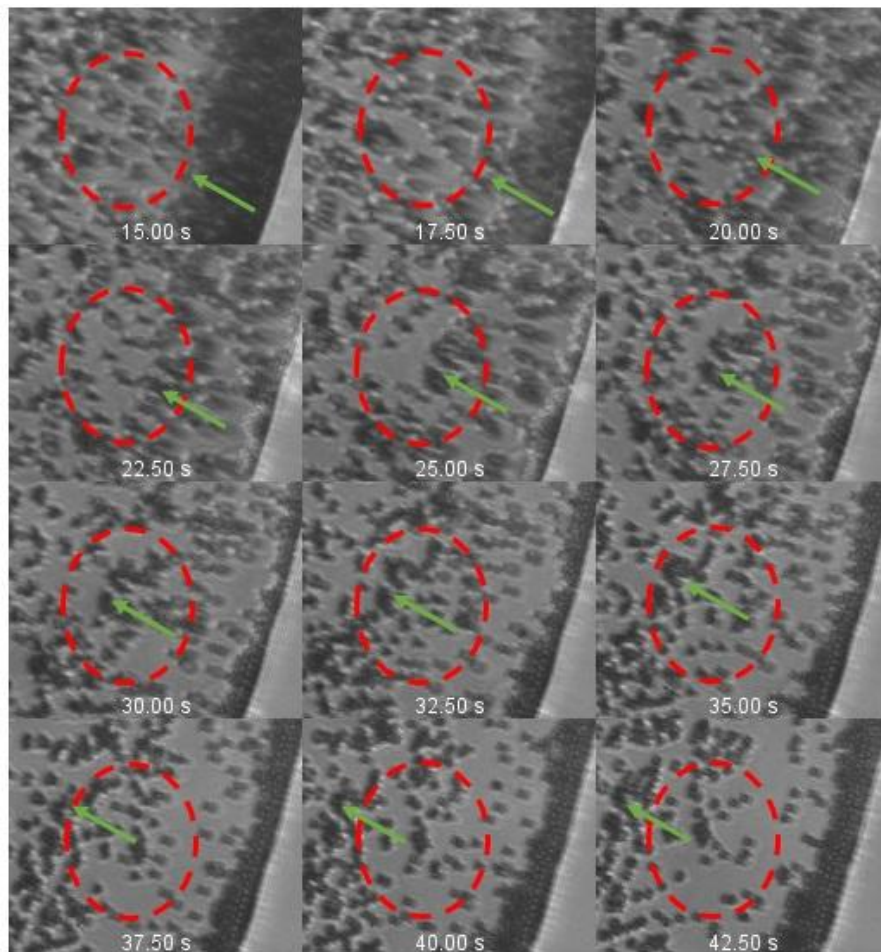


Figure 4.7: PS microparticles as they move away from the contact line inwards form clusters as shown with an arrow from 25s to 42.5s. Below 25s image particles move individually. There are 100 frames between one image and the next (2.5s).

### 4.3 Experimental Results and Discussions

In this section the experimental results are presented according to the particle sizes and for each particle size the data from the SDOCT and optical imaging microscope are combined. In each particle size further subsections low ( $\sim 0.6$ nL/s) and high ( $> 5$ nL/s) drying rates are considered accordingly.

### **4.3.1: 0.5 $\mu$ m PS Microparticles**

#### **4.3.1.1 Low Drying rate**

The results presented in this section to study the kinematics on droplet drying for 0.5 $\mu$ m PS particles were obtained by the optical imaging microscope method only. In order to easily track the microparticles to determine their velocities, the corresponding initial concentration had to be low but high enough to enable pinning at the contact line. Using an initial concentration of 0.006% was enough to achieve this. At the low drying rate ( $\sim$ 0.6nL/s), a robust ring is formed with a small fraction of the microparticles scattered at the interior of the ring as described in chapter 3. A sample deposition pattern is shown in figure 4.8 for initial concentration of 0.006%. In figure 4.8(a) the entire droplet final deposit patterns is presented imaged using a 2X magnifying lens and in figure 4.8(b) a 50X magnifying lens was used to image a small section close to the contact line. The robust ring and small fractions of microparticles at the interior of the ring can easily being seen in figure 4.8(b). Observations from the series of videos show that microparticles were indeed moving outward toward the contact line with no inward or vertical movement. Their corresponding outward velocities were determined within a distance  $\sim$ 190 $\mu$ m from the contact line.

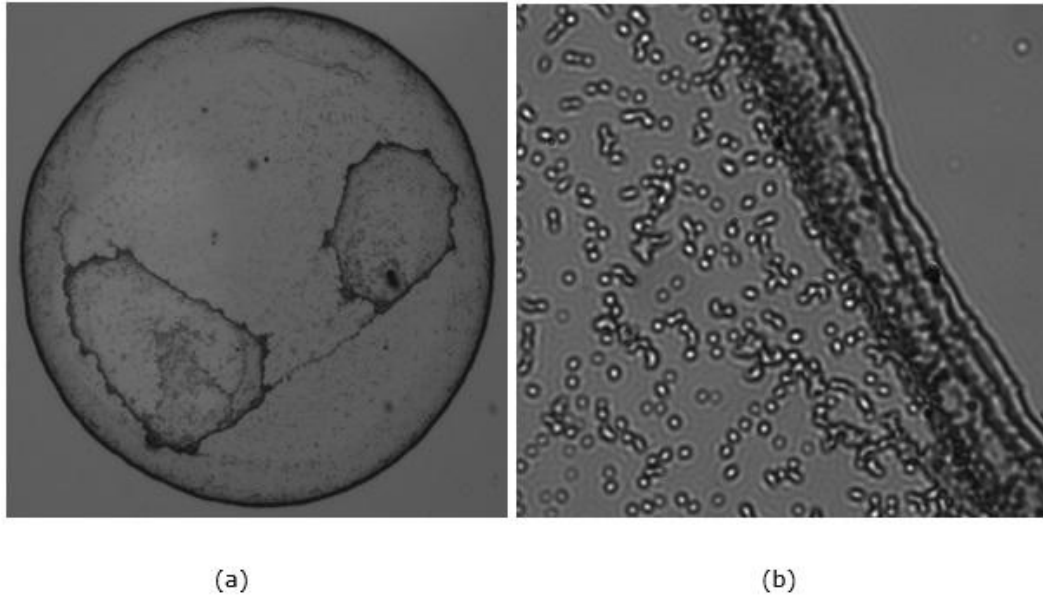


Figure 4.8: Deposition patterns from drying 0.006% droplet of 0.5µm PS particles drying at ~0.6nL/s with (a) whole droplet and (b) magnified section of the droplet close to the contact line

Figure 4.9 show a graph of the outward velocity against time ( $t$ ) normalized to the droplet life time ( $t_F$ ). Only velocity data above 40% of the droplet life time are shown due to the limitation of the method used. The magnitude of capillary velocities ranges from ~2µm/s at 40% to ~16µm/s at ~80% of the droplet life time ( $t_F$ ). The abrupt increase in capillary velocity near the end of droplet drying is responsible for carrying microparticle in the ring. This result is in agreement with Marín et.al, [95] who observed that, particles (0.5-2µm diameter) velocity increases dramatically in the last moments of the droplet's life which they referred as "rush hour." With an average drying rate of ~0.6nL/s, the microparticles average velocity is  $\sim 8.2 \pm 2.6 \mu\text{m/s}$ . The theoretical vertical velocity  $v_T$  for 0.5µm PS particles in stationary water at atmospheric conditions is  $\sim 0.006 \mu\text{m/s}$  estimated using Stokes

$$\text{equation } v_T = \frac{2}{9} \frac{gr^2(\rho_p - \rho_l)}{\eta} \quad [146].$$

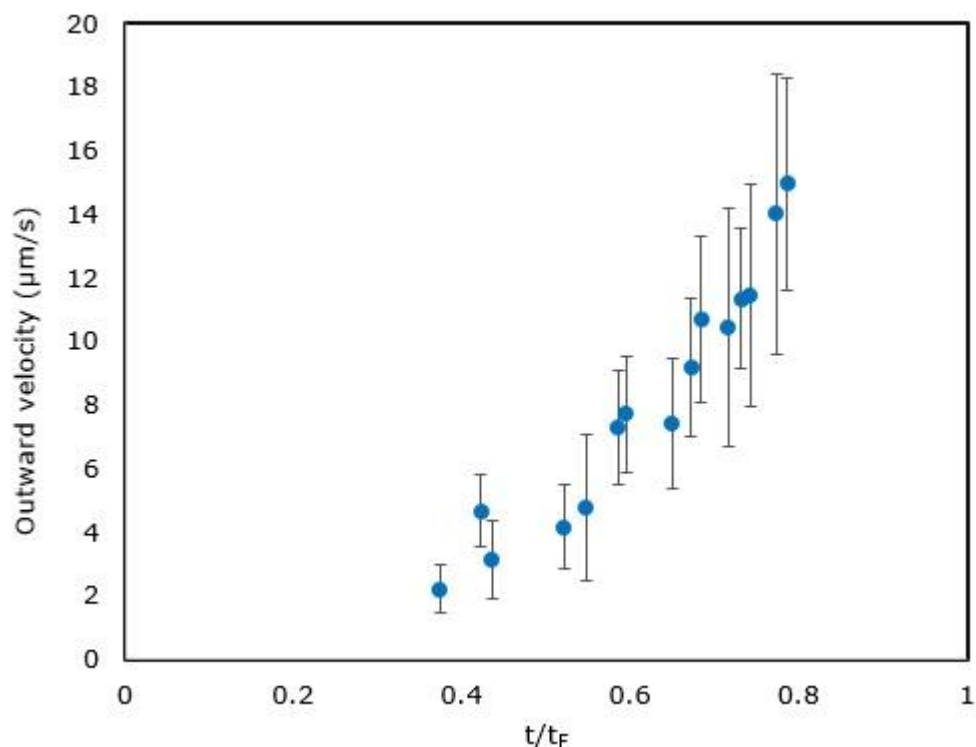


Figure 4.9: Outward velocity for 0.006% of 0.5 $\mu\text{m}$  PS particles drying at  $\sim 0.6\text{nL/s}$ .

#### 4.3.2.2 High Drying rate

Figure 4.10 shows a sample image of 0.006% of 0.5 $\mu\text{m}$  PS particles dried at high evaporation rate of  $>5\text{nL/s}$ . As described in chapter 3 a thin ring is seen with large fraction of the particles at the interior of the ring. Observations from a series of videos during drying of these droplets show particles going toward the contact line but a number of them back inwards to the interior of the droplet. Focusing in and out, it can be concluded that these particles are at the air-liquid droplet interface. While at the air-liquid interface, these particles move in clusters and there exists a depleted zone of mobile individual particles between the contact line and the clustered microparticles. Studies have shown that when there is deformation of an interface caused by the presence of particles at the interface will lead to mutual attraction between particles and eventually to the formation of large clusters [158, 159]. This phenomenon could be due to the so-called Cheerios effect caused by

surface tension and it occurs when floating objects that don't normally float attract one another.

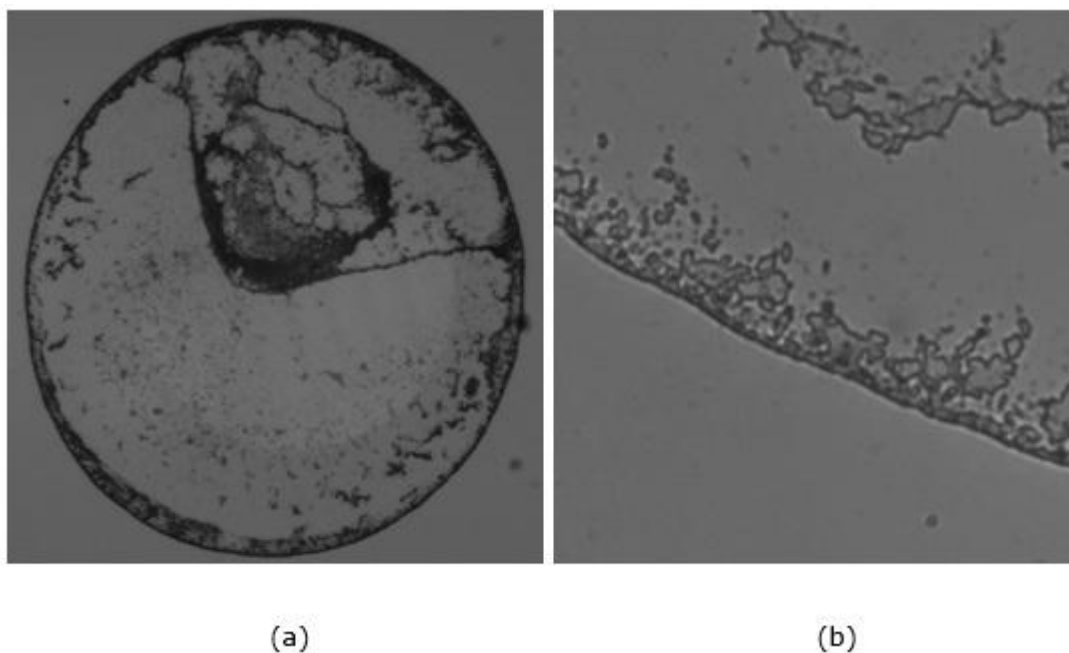


Figure 4.10: Deposition patterns from drying 0.006% droplet of 0.5 $\mu$ m PS particles drying at  $>5$ nL/s with (a) whole droplet and (b) magnified section of the droplet close to the contact line.

Similarly to our work, the inward motion of particles has also been recently observed for 0.1 $\mu$ m surfactant free PS particles when the temperature of microscope glass slides substrate were varied between 30°C and 80°C [160] and was attributed to an "enhanced Marangoni flow". Similar findings have been recently published utilizing  $<0.05$   $\mu$ m copper (II) oxide particles when the temperature of silicon wafers substrate were varied between 47°C and 99°C [161]. The two recent studies however used enhanced temperature but in the present study evaporative cooling was used to change the temperature of the microscope glass cover slips between  $\sim 5^\circ\text{C}$  and  $22^\circ\text{C}$ . PS microparticles at the air-liquid droplet interface have been observed for temperature of  $\sim 5^\circ\text{C}$ . This study utilized surfactant free PS microparticles and likely reasons for our observation are caused

by a gradient in temperature induced by high drying rate. Using equation (1.12) this should lead to gradients in surface tension between the droplet edge and the apex according Hu and Larson [42, 73]. This temperature gradient would cause an inward flow of the particles from the edge to the inside of the drop (Marangoni flow), in agreement with our observations. At the lower drying rates, the temperature gradient is not expected to exceed 1°C for our structures with contact angle 35°C and so the Marangoni flow would be negligible as observed experimentally.

Both inward and outward velocities increase with time and are shown in figure 4.11.

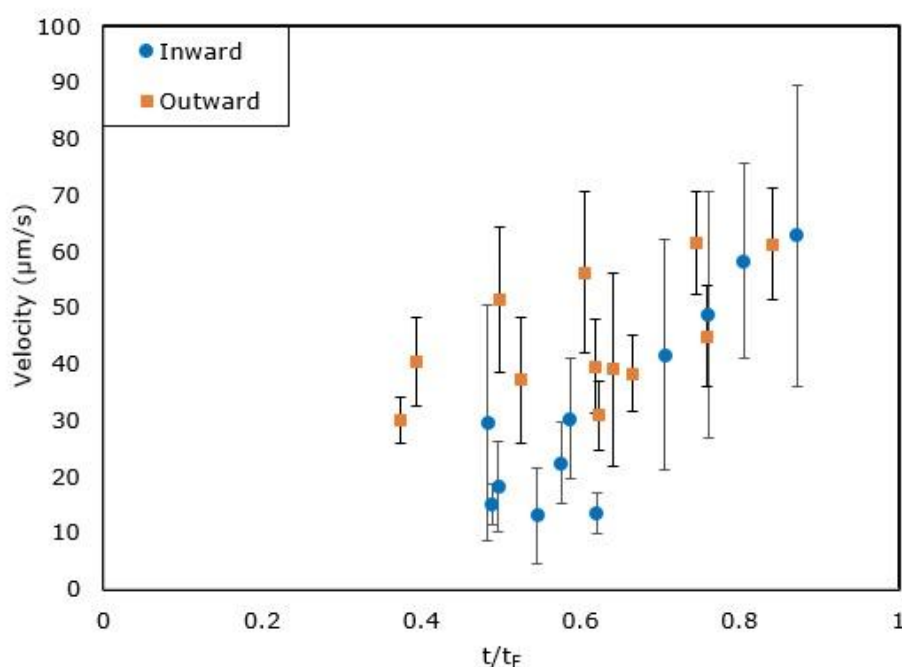


Figure 4.11: Inward and outward velocities for 0.006% droplet of 0.5 $\mu\text{m}$  individual PS particles drying at  $>5\text{nL/s}$  determined only from optical microscope.

The velocity data are scattered and within the limit of experimental errors, inward and outward velocities are similar. Only few microparticles form part of the ring, perhaps in the early stages of droplet drying, but in the later stages velocities indicate that as they approach the contact line they recirculate and move as

clusters inwards. The average inward and outward microparticle velocity is  $\sim 32.2 \pm 15.7 \mu\text{m/s}$  and  $\sim 44.3 \pm 10.0 \mu\text{m/s}$  respectively. Using equation (1.24), the Marangoni velocity,  $V_{MA}$  of liquid flow induced by a gradient in temperature  $\Delta T = T_e - T_c$  ( $T_e$  and  $T_c$  are the temperature at the edge and centre of the drop respectively) is given by  $V_{MA} = \frac{1}{32} \left( \frac{\beta \theta^2 \Delta T}{\eta} \right)$  [78] where  $\eta$  viscosity of the suspension and  $\beta$  surface tension-temperature coefficient. It is of note that this expression does not include microparticles. As discussed in 2.4.3, attempts to measure  $\Delta T$  experimentally were inconclusive at low pressures. To get an estimate of the velocities, we consider that the value to be  $1^\circ\text{C} \leq \Delta T \leq 15^\circ\text{C}$  upon substituting  $\eta = 1 \times 10^{-3} \text{kg/ms}$ ,  $\beta = -1.61 \times 10^{-4} \text{kg/ms}^2$  [162],  $\theta \approx 20^\circ$  (at  $h \approx \frac{h_0}{2}$ ), would give a maximum liquid inward velocity,  $600 \leq V_{MA} \leq 9000 \mu\text{ms}^{-1}$ .

These values of inward experimental velocity for  $0.5 \mu\text{m}$  particles do not compare with the experimental values given in figure 4.11. It should be noted that theoretical velocity assumes the inward flow is brought by temperature gradient only. Also consider equation (1.12) for Marangoni number  $M_a$  given as  $M_a = -\beta(T_e - T_c) \frac{R}{\eta D_T}$ , where  $R$  the radius of the droplet,  $\eta$  viscosity of the suspension,  $\beta$  surface tension-temperature coefficient, and  $D_T$  the thermal diffusivity. At low drying rate  $D_T \approx 1.4 \times 10^{-7} \text{m}^2/\text{s}$  and  $T_e - T_c \approx 1^\circ\text{C}$  while at high drying rate  $D_T \approx 1.3 \times 10^{-7} \text{m}^2/\text{s}$  and at the most  $T_e - T_c \approx 15^\circ\text{C}$ . Upon substituting in equation (1.12) for  $R=1\text{mm}$ , value of  $M_a \approx 1158$  at low drying rate ( $\sim 0.6 \text{nL/s}$ ) and  $M_a \approx 18000$  at high drying rate ( $>5 \text{nL/s}$ ) were derived. Hu and Larson [101] point out that that in water, calculation show that the Marangoni number needs to be  $\sim 100$  times lower than calculated to get agreement with theory due to

surfactant contaminations. If the same reduction in effective Marangoni number applies to the velocity calculations, then our experimental values calculated above should be  $\sim 100$  times small, improves agreement. This follows from the fact that the PS suspension used in this study contained small amounts of surfactant (0.1-0.5%) as well as inorganic salts (0.2%) according to manufacturer specifications [163] and is responsible for the reduction in PS microparticles velocity. Our theoretical Marangoni number thus become  $M_a \approx 11.6$  at low drying rate ( $\sim 0.6 \text{ nL/s}$ ) and  $M_a \approx 180$  at high drying rate ( $> 5 \text{ nL/s}$ ). The Marangoni number for a droplet drying at low rate is less than the critical Marangoni number,  $M_{ac} = 84$  required for the onset of the inward flow [164].

For high drying rate the Marangoni number is greater than the critical value and inward flow of particles as observed experimentally. This also may account for the presence of inward flow of particles in our results at high drying rate is consistent the theoretical prediction with  $M_a \approx 180$ . Since  $M_a$  is directly proportional to  $V_{MA}$  then our theoretical Marangoni velocities are within the range  $6 \leq V_{MA} \leq 90 \mu\text{ms}^{-1}$  and are consistent with our experimental results in figure 4.11. The inward flow of particles disappears in later stages of droplet drying. This is expected since for thin droplets the temperature profile will be more influenced by the evaporation flux [165]. The conduction path length would be nearly the same for every point on the gas-liquid interface, and therefore the substrate will have less influence on the temperature profile. The presence of inward flow in this case suggests the existence of a surface tension gradient [42, 73] between the apex and droplet edge controlling the internal flow of PS microparticles. According to Barmi and Meinhart [75] when the inward (Marangoni) velocity is much smaller than the outward velocity the particles in droplet will be carried to the perimeter to form a ring. Further Askounis et al [166] point out that reducing pressure increases the

evaporation rate which amplifies the outward velocity taking with it particles at the perimeter forming disordered patterns. When the inward velocity is comparable or higher than the outward velocity recirculation of particles near the contact line occurs limiting the formation of a robust ring.

### **4.3.2: 2 $\mu$ m PS Microparticles**

#### **4.3.2.1 Low Drying rate**

To determine the PS microparticle flow inside the droplet drying at atmospheric conditions, a Z-projection was performed to obtain the cumulative particle pathline of a group of 300 consecutive sequences (150s) of images as a sample shown figure 4.12. The cumulative particle pathline is shown in figure 4.12 is for the first 1023s with a droplet life time of  $\sim$ 1440s. After 140, 419, 698 and 1023s, the maximum droplet height has fallen from 0.86mm to 0.78, 0.64, 0.47, and 0.27mm respectively. Between 419s ( $\sim$ 29%) and 698s (49%), there is a substantial outward flow of PS microparticles and no inward flow is observed. Since the air-liquid interface is moving vertically down and inwards some of the PS microparticles are trapped and move with it as indicated in figure 4.12 with arrows. The cumulative particle pathline of the trapped particles leaves a trail of white band at the air-liquid interface. This adsorption at low drying rate may be attributed to Brownian motion of the particles near the proximity of the air-liquid interface as the droplet dries [145]. At about 70% (1023s) of the droplet life time the PS microparticles are still distributed in the bulk of the droplet and the outward flow is observed to be dominating vertical flow as observed for 0.5 $\mu$ m PS particles in section 4.3.1.1.

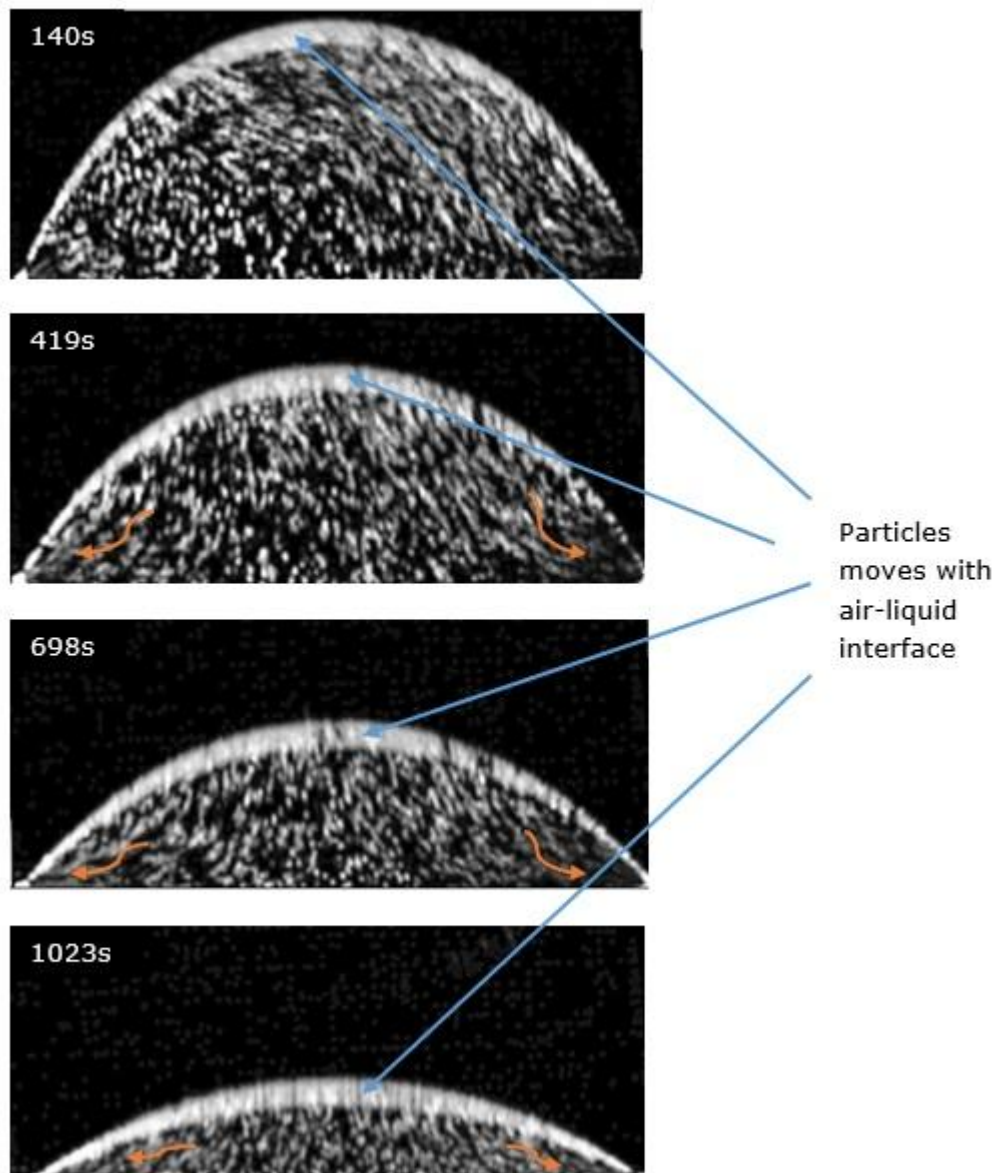


Figure 4.12: Cumulative particle pathline for a droplet drying at  $\sim 0.6 \text{ nL/s}$  containing  $2 \mu\text{m}$  PS particles.

The corresponding final deposit is shown in figure 4.13 is characterized by a robust ring and small fractions of the microparticles at the interior of the ring.

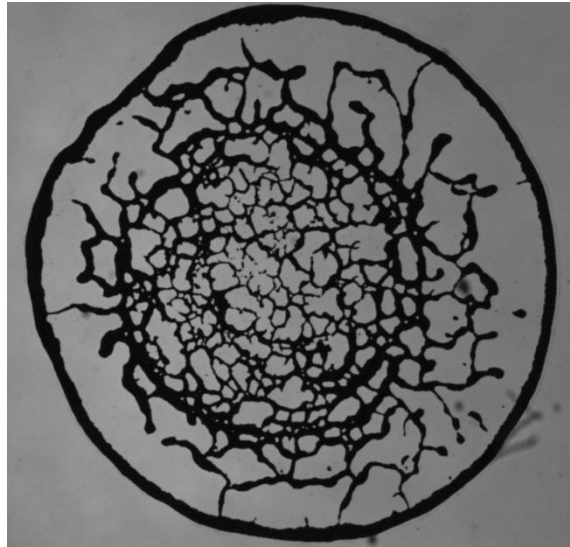


Figure 4.13: Final deposits from drying 0.04% droplet of 2µm PS particles at ~0.6nL/s.

In figure 4.14, the PS microparticles velocities are presented, determined both, from image sequences from SDOCT in early stages and optical microscope at later stages. The outward velocities increase from  $\sim 1.0\mu\text{m/s}$  at  $\sim 2\%$  of the droplet life time to  $\sim 7\mu\text{m/s}$  at  $\sim 86\%$  of the droplet life time. The vertical velocity is fairly constant at  $\sim 1.0\pm 0.1\mu\text{m/s}$  which is ten times greater than the theoretical Stokes velocity of  $\sim 0.1\mu\text{m/s}$  for 2µm PS particles in stationary water at atmospheric conditions. In the first 60% of the droplet life time the vertical and outward velocity are fairly similar, however near the end of the droplet drying, the outward velocity increases abruptly as seen for 0.5µm PS particles at low drying rate in section 4.3.1.1. The increasing outward velocity is responsible for carrying PS microparticles to the droplet edge forming a ring in a similar way to 0.5µm particles and the remaining are randomly distributed at the interior during the rush-hour and consistent with other observations by Marín et.al, [95].

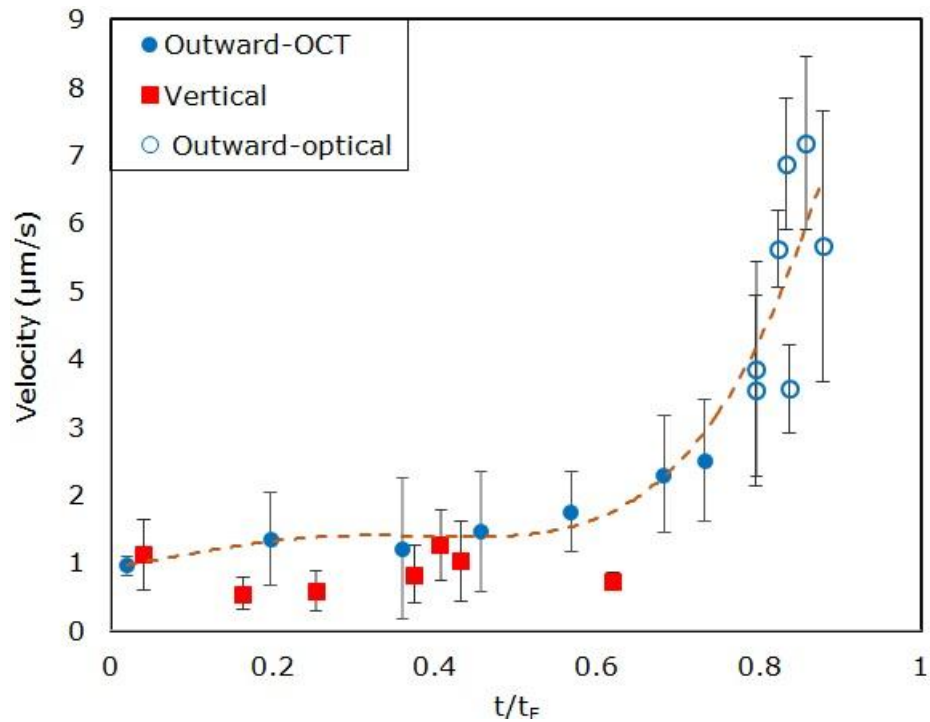


Figure 4.14: Velocities of 0.04% droplet containing 2µm PS particles drying at ~0.6nL/s. The filled markers are for velocities determined from OCT and hollow markers from optical microscope data. The dotted line serve as a guide for the outward velocity to show that the data for optical and OCT are consistent with each other.

#### 4.3.2.2 High Drying rate

For the high drying rate (>5nL/s), the cumulative particle pathline is shown in figure 4.15 obtained from a group of 20 consecutive image sequences in each composite. The cumulative particle pathline have been obtained after 14s, 37s, 56s and 76s for a droplet lifetime of ~150s during which the maximum droplet height of ~0.86 mm fell to 0.53, 0.47, 0.35, and 0.21 mm respectively. At 14s, the cumulative particle pathline show outward flow and less of vertical movement of PS microparticles near the apex of the droplet. At about 56s and 76s the PS microparticle movement is dominated by outward flow. Observation of sequence of

videos shows recirculation of particles near the contact line and thereafter moves at air-liquid droplet interface as observed for  $0.5\mu\text{m}$  particles in section 4.3.1.2.

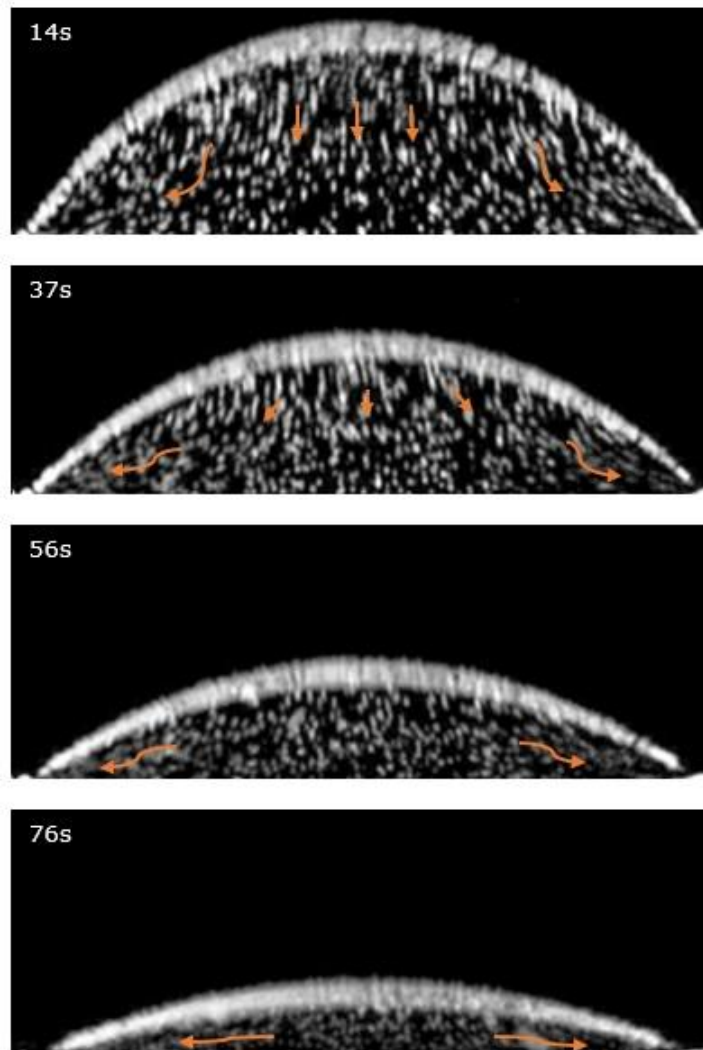


Figure 4.15: Cumulative particle pathline for a droplet drying at  $>5\text{nL/s}$  containing 0.04% of  $2\mu\text{m}$  PS particles.

We also tracked the PS microparticles using the time-resolved digital particle tracking velocimetry (PTVlab) and time-resolved digital particle image velocimetry (PIVlab ) in order to obtain the cumulative particle pathline for a given number of frames for comparison purposes. The sample cumulative particle pathline is shown

in figure 4.16 and compares well in terms of pathlines. In figure 4.17 a PS microparticle moving along the liquid-gas interface is shown.

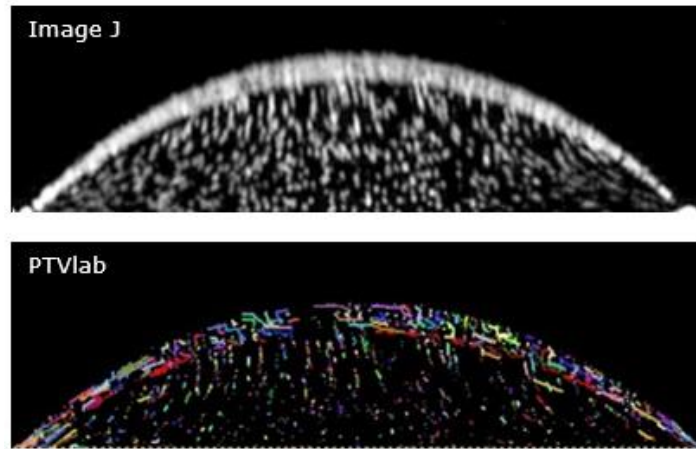


Figure 4.16: Comparisons of cumulative particle pathline of droplet containing 0.04% of  $2\mu\text{m}$  PS particles after 37s of droplet life time of  $\sim 150\text{s}$  using Image J and PTVlab drying at  $>5\text{nL/s}$ .

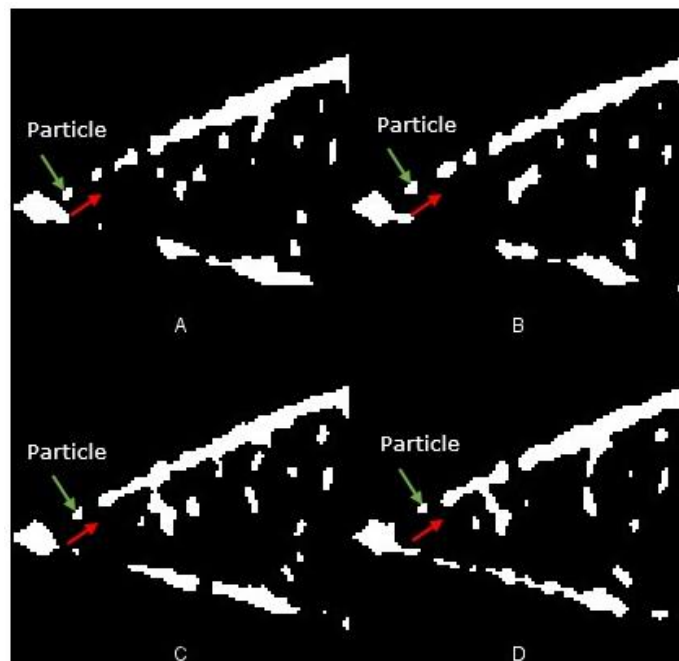


Figure 4.17: A  $2\mu\text{m}$  PS microparticle moving upward along the liquid-gas interface from frame A to D at  $\sim 0.2\text{s}$  from one frame to the next.

In figure 4.17 a PS microparticle initially moves from the bulk of the droplet to the contact line and then reverses its direction along the liquid-gas interface. Images in the stack have been scaled by a factor of 2 to make it visible. To further quantify this, PTVlab tool was used to track PS microparticles to a small region near the contact line and obtain the average direction vectors for 20 consecutive frames scanned at  $\sim 5$ fps using SDOCT (figure 4.18).



Figure 4.18: Particle velocity vectors showing inward particle flow (Marangoni flow) near the contact line as determined by PTVlab for  $2\mu\text{m}$  PS particles at higher drying rate.

Figure 4.18 show an example of the directional vectors and are consistent with PS microparticles movement in figure 4.17. The final deposition patterns is shown in figure 4.19 characterized by thinner robust ring compared to low drying rate in figure 4.13.

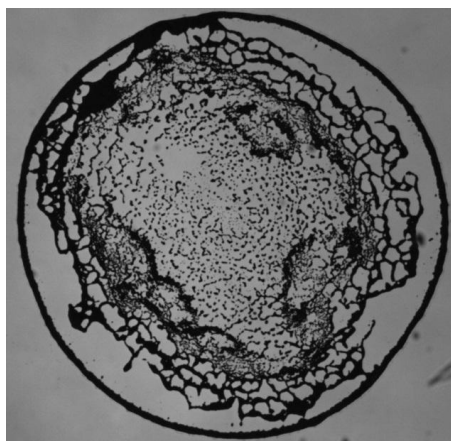


Figure 4.19: Final deposits from drying 0.04% droplet of  $2\mu\text{m}$  PS particles at  $>5\text{nL/s}$ .

The patterns of the deposits at the interior are also slightly different in comparison with that at low drying rate ( $\sim 0.6 \text{ nL/s}$ ). To get more details the kinematics behind the observed depositions patterns optical imaging using optical microscope from below the droplet was used. Figure 4.20 shows cumulative particle pathline of microscope data obtained over a sequence of 100 images at a scan rate of 14fps. The sequence of images was taken when the droplet was drying between  $0.69t_f$  and  $0.79t_f$  of the droplet life time. Most PS microparticles are observed moving radially outward and back again along the liquid-gas interface and there is a depletion zone as observed for  $0.5 \mu\text{m}$  particles in section 4.3.1.2.

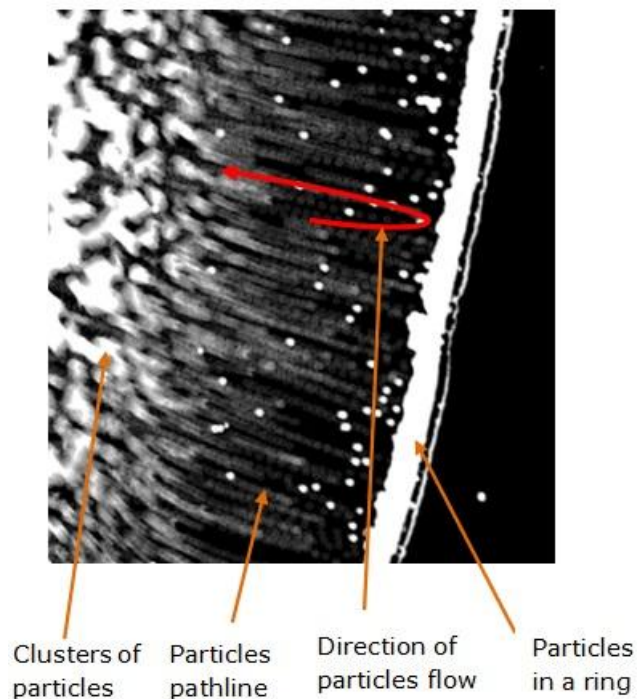


Figure 4.20: Cumulative particle pathline for a 0.04% droplet drying at  $>5 \text{ nL/s}$  containing  $2 \mu\text{m}$  PS particles using optical microscope data.

Despite the fact that there is recirculation some of the particles manage to reach the contact line and form part of the ring. The ring width is much narrower than that at  $\sim 0.6 \text{ nL/s}$ . In figure 4.21 the particle velocities are shown combining both obtained from OCT and optical microscope data. The vertical velocity is fairly

constant at  $\sim 4.1 \pm 0.2 \mu\text{m/s}$ . The inward velocity increases from  $\sim 7 \mu\text{m/s}$  to  $\sim 50 \mu\text{m/s}$  at 65% of the droplet life time. The outward velocity is similar to the inward velocities below 65% and increases sharply to  $\sim 92 \mu\text{m/s}$  at about 80% of the droplet life time. The inward velocity has reached as high as  $\sim 50 \mu\text{m/s}$  and is with the range of the theoretical predictions  $6 \leq V_{MA} \leq 90 \mu\text{m/s}^{-1}$  according equation (1.14) as calculated in section 4.3.2.2. As pointed in section 4.3.2.2 the inward movement of PS particles along the liquid-gas interface is caused by surface tension gradient between the apex and edge of the droplet.

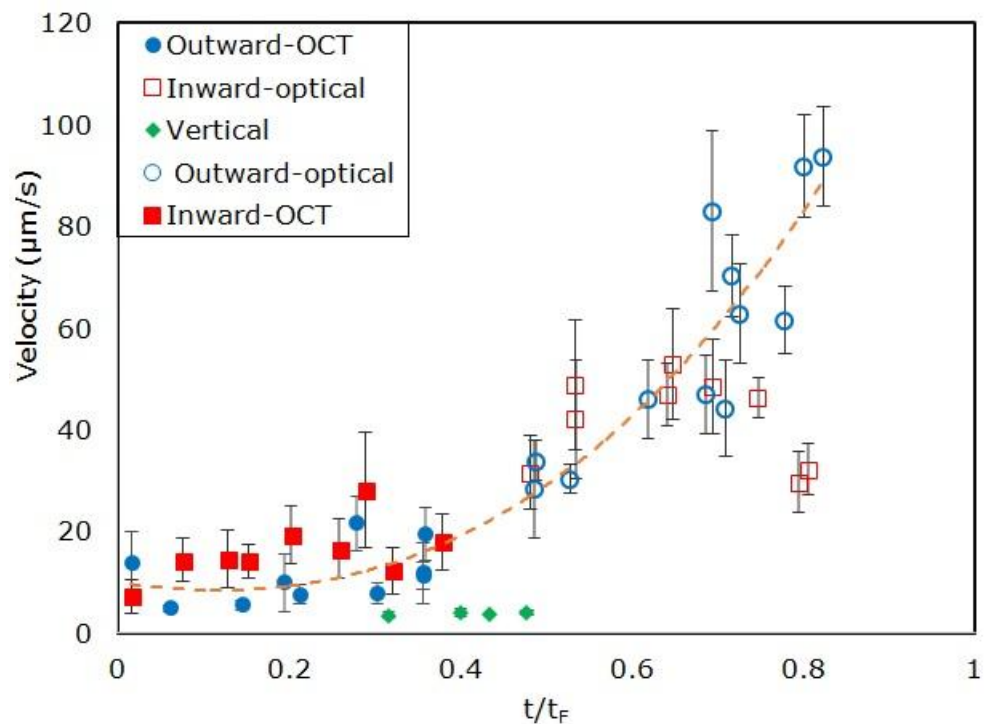


Figure 4.21: Velocities at high drying rate vertical, inward and outward velocities for 0.04% droplet of  $2 \mu\text{m}$  individual PS particles drying at  $>5 \text{L/s}$ . The filled markers are for velocities determined from SDOCT and no fill marker from optical microscope data. The dotted line serve as a guide for the outward velocity to show that the data for optical and OCT are consistent with each other.

### 4.3.3: 5 $\mu$ m PS Microparticles

#### 4.3.3.1 Low Drying rate

Figure 4.22 shows cumulative particle pathline of OCT B-scan of 1 $\mu$ L droplet at atmospheric conditions ( $\sim 0.6$ nL/s). The cumulative particle pathline were obtained for a sequence of 200 images taken after 93s, 185s, 280s and 363s of droplet drying in which the droplet lifetime  $t_f$  was  $\sim 1578$ s. At  $\sim 465$ s (30%) of the droplet life time, the PS particles have completely disappeared from the bulk of the droplet as depicted by the blue dashed oval lines in figure 4.22. At this moment the droplet is still assuming a spherical cap with the interface visible due to either few trapped particles or reflection of incident laser on the droplet surface.

The maximum droplet height after every 200 sequences of images captured at  $\sim 2$ fps has fallen from 0.85 mm to 0.80 mm, 0.77 mm, 0.72 mm and 0.69 mm corresponding to 93, 185, 280 and 363s respectively. In the first 93s the particles movement are only seen pronounced near the central region of the droplet than closer to the contact line as shown with the cumulative particle pathline length (little outward flow). After 185s, the PS microparticles outward particle pathlines are visible near the contact line but vertical flow seems to be dominant. The region depleted with particles between the air-liquid droplet interface and the rest of other particles in the bulk of the droplet is clearly seen at this moment when maximum droplet height has just decreased by  $\sim 9\%$  of the initial maximum height of 0.64mm. At 280s with maximum droplet height decreased by 16%, the particles pathline are characterized by largely vertical flow. At 363s short path lines are observed with larger part of the droplet bulk depleted with particles. At this moment only about  $\sim 23\%$  of the droplet had dried and the PS microparticles are deposited on the substrate and one would expect the deposition patterns to be determined solely by vertical velocity rather than outward velocity.

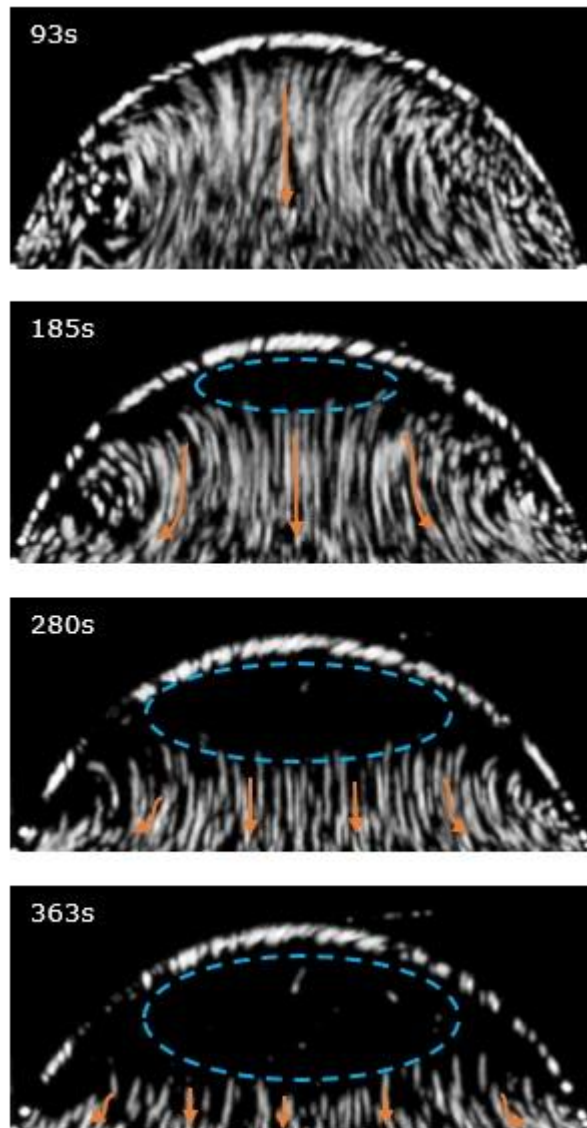


Figure 4.22: Cumulative Z-projection for 5 $\mu$ m PS particles droplet drying at  $\sim$ 0.6nL/s for the first 363s of the droplet life time of 1578s.

Since the SDOCT does not allow the visualization of particles kinematics after the 30% of the droplet drying it was necessary to use optical microscope to study this. No robust ring formed, instead PS microparticles are scattered at the interior of the droplet with small amount of the PS microparticles at the contact line as shown in figure 4.23 indicating that sedimentation play the important role compared to capillary flow right to the end of the drying (as confirmed by optical microscope).

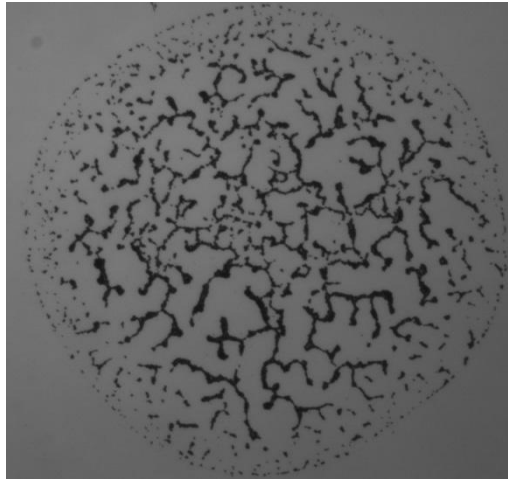


Figure 4.23: Final deposits from drying 0.1% droplet of 5µm PS particles at  $\sim 0.6\text{nL/s}$ .

This was further confirmed by measuring PS microparticles outward and vertical velocity as shown in figure 4.24. The vertical velocity is fairly constant at  $\sim 2.1 \pm 0.6 \mu\text{m/s}$  while the particles radially velocity of  $\sim 1.0 \pm 0.2 \mu\text{m/s}$  was determined near the contact line. The outward velocity is about the same order as the theoretical Stokes velocity for 5µm of  $\sim 0.7 \mu\text{m/s}$  whereas the measure vertical velocity in the present experiment is three times the theoretical value. Given the initial maximum height of 0.85mm and the vertical velocity of  $\sim 2.1 \mu\text{m/s}$  it will take  $\sim 400\text{s}$  to have completely settled on the substrate and for those particles moving with outward velocity of  $\sim 1.0 \mu\text{m/s}$  it will take  $\sim 850\text{s}$  to reach the contact line. Since the vertical velocity is greater than outward velocity, only few particles will arrive at the contact line to form the ring. It should be noted that the droplets life time is longer by a factor of  $\sim 8$  compared to the time for almost all microparticles to settle on the substrate as a result the deposit pattern will be determined by sedimentation.

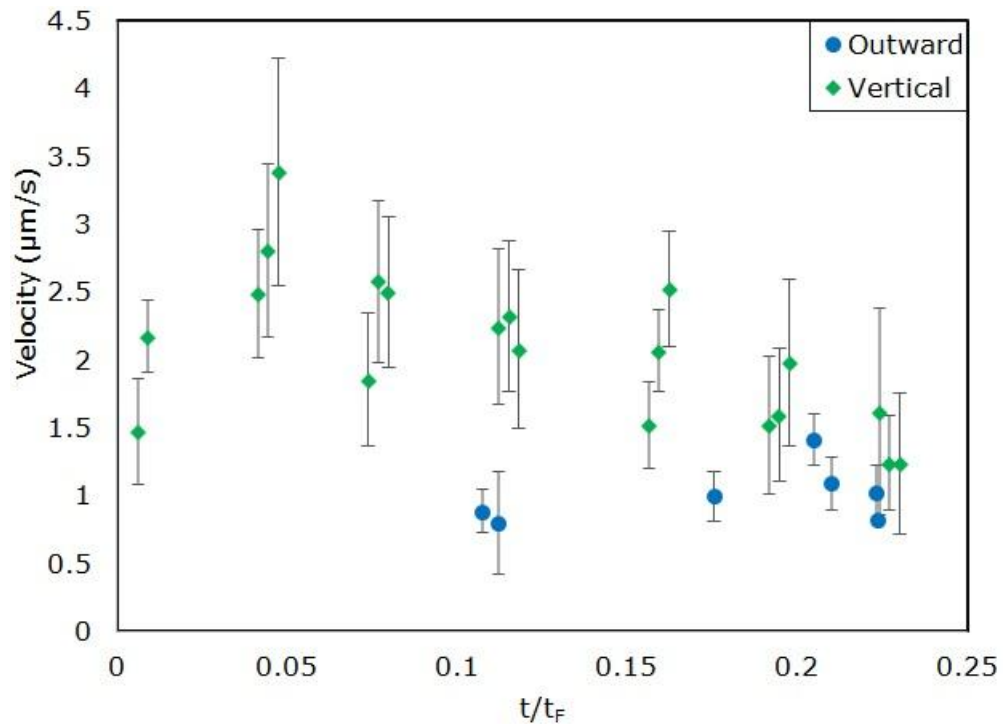


Figure 4.24: Velocities of 0.1% droplet containing 5µm PS particles drying at  $\sim 0.6\text{nL/s}$ .

#### 4.3.3.2 High Drying rate

For high drying rate it took about two minutes ( $>5\text{nL/s}$ ) for the droplets to completely dry. The corresponding cumulative particle pathline for a group of 20 consecutive frames scanned at a rate of 2.15 fps is shown in figure 4.25. After 28s, 42s, 65s, and 77s, the droplet initial maximum height of 0.85 mm has decreased to 0.47, 0.37, 0.21, and 0.13 mm respectively. The particles pathlines in figure 4.25 show that movement of individual PS microparticles are dominated by outward as well as vertical flow. The vertical flow of PS particles is pronounced at early stages of droplet drying and only visible near apex region of the droplet. Near the contact line PTVlab tool was used to determine the direction vectors and show that there is reverse of microparticles inward as shown in figure 4.26.

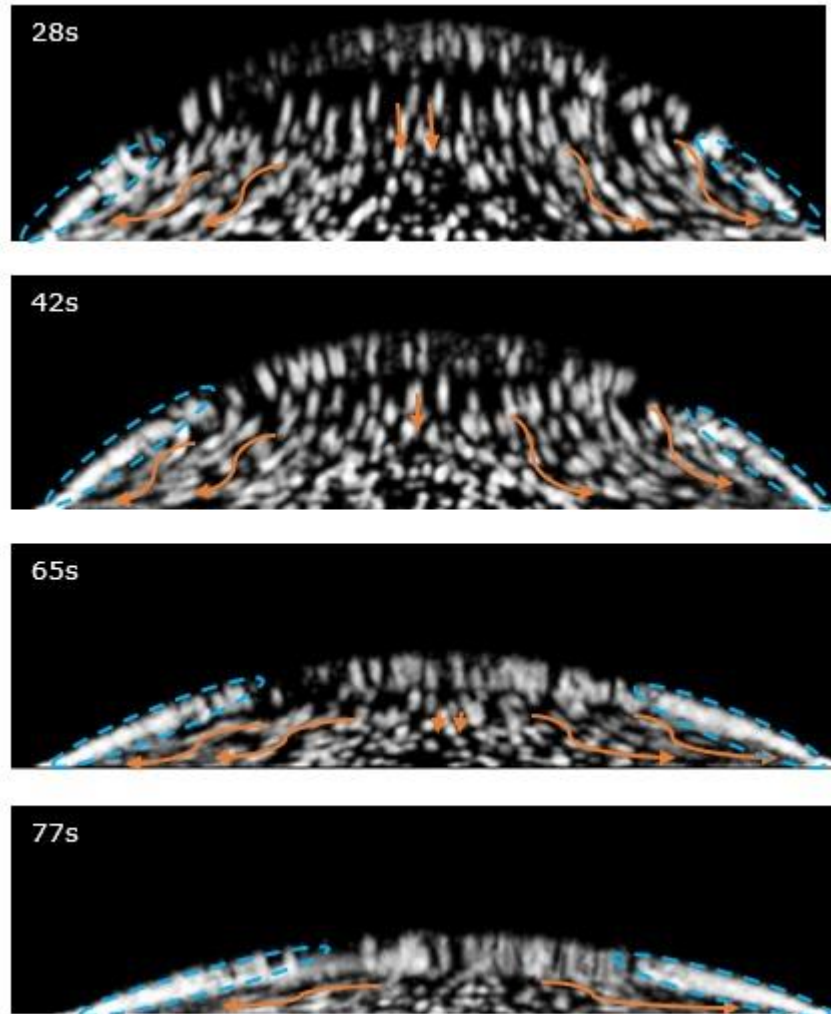


Figure 4.25: Cumulative particle pathline for a droplet drying at  $>5\text{nL/s}$  containing 0.1% of  $5\mu\text{m}$  PS particles. The dashed lines show the intensity of the trapped particles at the air-liquid interface.

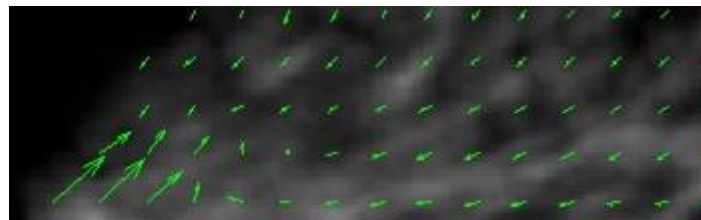


Figure 4.26: Marangoni flow direction vectors near the contact line as determined by PTVlab for  $5\mu\text{m}$  PS particles at higher drying rate.

Figure 4.27 show the deposits left from drying droplets containing 0.1% of  $5\mu\text{m}$  PS particles at  $>5\text{nL/s}$ . Particles are observed at the contact line forming a monolayer of a ring and the rest scattered at the interior of the ring.

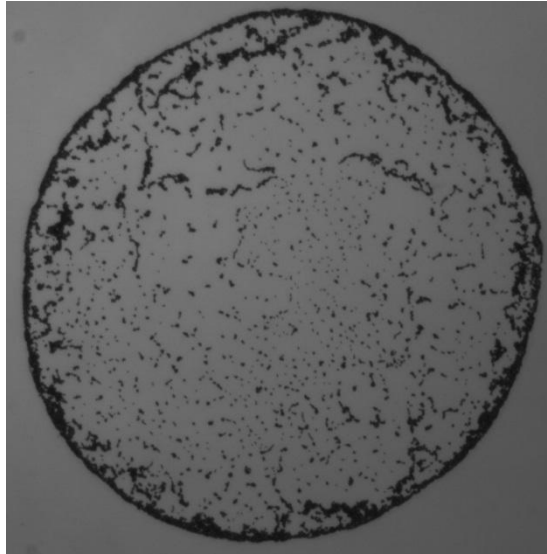


Figure 4.27: Final deposits from drying 0.1% droplet of  $5\mu\text{m}$  PS particles at  $>5\text{nL/s}$ .

To explain the deposit patterns in figure 4.27 an optical imaging using microscope was performed to capture the kinematics of particles inside the droplet in later stages of drying. Figure 4.28, show the cumulative particle pathline obtained for a time frame of 2.5s within 100 image sequences taken at  $\sim 80$  of the droplet life time. Clusters of particles are observed moving away from the contact line toward the interior of the droplet at the air-liquid interface by zooming in and out. The outward, inward and vertical velocities were determined to account their contribution in the deposition patterns.

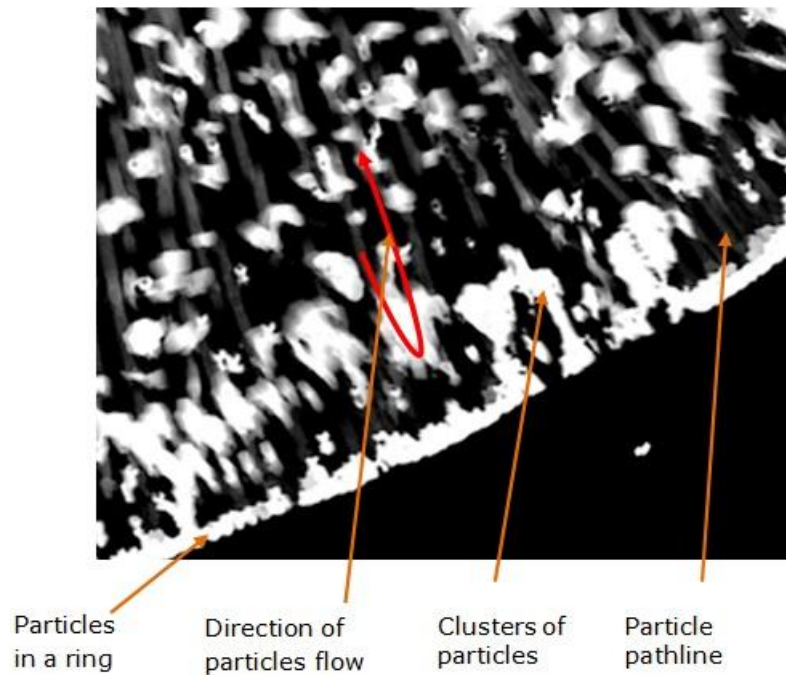


Figure 4.28: Cumulative particle pathline for a 0.1% droplet drying at  $>5\text{nL/s}$  containing  $2\mu\text{m}$  PS particles using optical microscope data.

The velocities obtained from SDOCT (at early stages) are combined with those obtained from the optical microscope at the later stages and shown in figure 4.29. The inward velocity increases from  $\sim 8\mu\text{m/s}$  at  $\sim 2.5\%$  of the droplet life time to  $\sim 180\mu\text{m/s}$  at  $\sim 80\%$  of the droplet life time. The inward velocity as determined by SDOCT is more or less constant at  $\sim 5.6 \pm 1.3 \mu\text{m/s}$  while the vertical velocity is also fairly constant  $\sim 5.5 \pm 0.4 \mu\text{m/s}$ . The measured vertical velocity is greater than the theoretical value of  $\sim 0.7\mu\text{m/s}$ . The reason is the movement of interface due to high drying rate ( $\sim 5\text{nL/s}$ ) and so the measured value is not purely sedimentation. To summarize at early stages the outward and vertical velocity are approximately the same because of the large drying rate such that particles do not have time to sediment. Toward the end of the droplet drying as seen in figure 4.29 the outward velocity increases sharply while the outward velocity is small giving a ring.

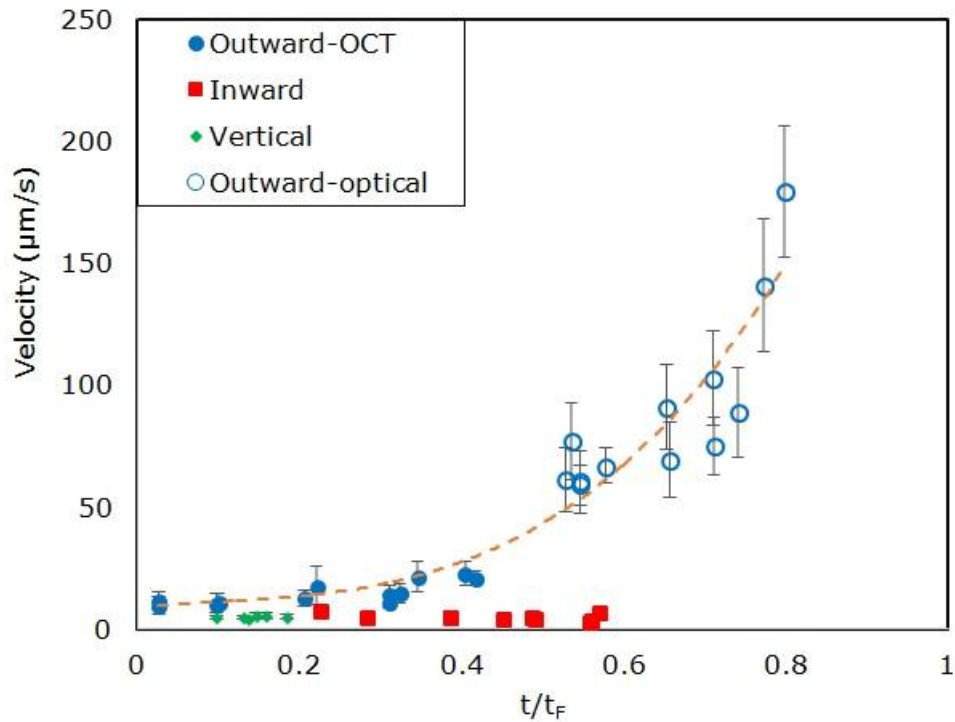


Figure 4.29: Velocities at high drying rate vertical, inward and outward velocities for 0.1% droplet of 2µm individual PS particles drying at ~5nL/s. The dotted line serve as a guide for the outward velocity to show that the data for optical and OCT are consistent with each other.

### 4.3 Conclusions

The quantitative microscale imaging using SDOCT and optical microscope to study the kinematics of droplet drying containing PS microparticles both at low and high drying rates have been demonstrated. No observable inward flow to particles was observed at atmospheric conditions of low drying rates for all particle sizes. At high drying rates, however recirculation were observed as demonstrated by the outward velocities whose magnitude increases with decrease in particle sizes. The presence of inward flow in this case suggests the existence of a surface tension gradient between the apex and droplet edge controlling the internal flow of PS microparticles. At high drying rates the vertical velocities are higher than those at low drying rates attributed to the fast moving air-liquid droplet interface. At high drying rate, 0.5µm,

2 $\mu\text{m}$  and 5 $\mu\text{m}$  PS particles show high outward velocities but there is no clear dependence on particle sizes as demonstrated for vertical velocity as shown in Table 4.3.

	Outward ( $\mu\text{m/s}$ )		Vertical ( $\mu\text{m/s}$ )		Inward( $\mu\text{m/s}$ )	
	Low	High	Low	High	Low	High
0.5 $\mu\text{m}$	8.2 $\pm$ 2.6	44.3 $\pm$ 10.0	None	None	None	32.2 $\pm$ 15.7
2 $\mu\text{m}$	3.4 $\pm$ 2.2	36.8 $\pm$ 29.3	0.8 $\pm$ 0.3	4.1 $\pm$ 0.2	None	29.2 $\pm$ 15.2
5 $\mu\text{m}$	1.0 $\pm$ 0.2	52.5 $\pm$ 45.8	2.1 $\pm$ 0.6	5.5 $\pm$ 0.4	None	5.0 $\pm$ 1.5

Table 4.3: The average outward, vertical and outward PS microparticles velocities both a low and high drying rates.

In the previous study by Hu and Larson [73], evaporation of droplets of pure water at atmospheric conditions with similar contact line radius as ours has shown to have an average radial flow of  $\sim 1\mu\text{m/s}$ . By comparing with our results in Table 4.3 for outward velocity, only average velocity value for 5 $\mu\text{m}$  PS particles is consistent with Hu and Larson experimental average radial flow velocity of pure water. For 0.5 $\mu\text{m}$  and 2 $\mu\text{m}$  PS particles (outward velocity at low drying rates) in Table 4.3, there is no consistency with Hu and Larson experimental results for pure water droplets. We anticipate high average outward velocity due to onset of rush hour prior the end of droplet evaporation. For 5 $\mu\text{m}$  PS particles most of the particles are already deposited at the substrate prior to the onset of the rush hour. The competitions between outward, inward and vertical velocities have a strong influence to the pattern of final deposit as shown in Figure 4.30. When the vertical velocity is higher than outward and inward velocities, no ring is formed and the PS are distributed at the interior of the droplet as observed for 5 $\mu\text{m}$  particles at low drying rates (Figure 4.30 (e)). When there is competition between the inward and outward flow, thin ring is formed with larger fraction of the particles distributed at the interior of the ring as is the case for 0.5 $\mu\text{m}$  and 2 $\mu\text{m}$  at high drying rates(Figure 4.30 (b) and (d)).

When the inward (Marangoni) velocity is much smaller than the outward velocity the particles in droplet will be carried to the perimeter to form a ring.

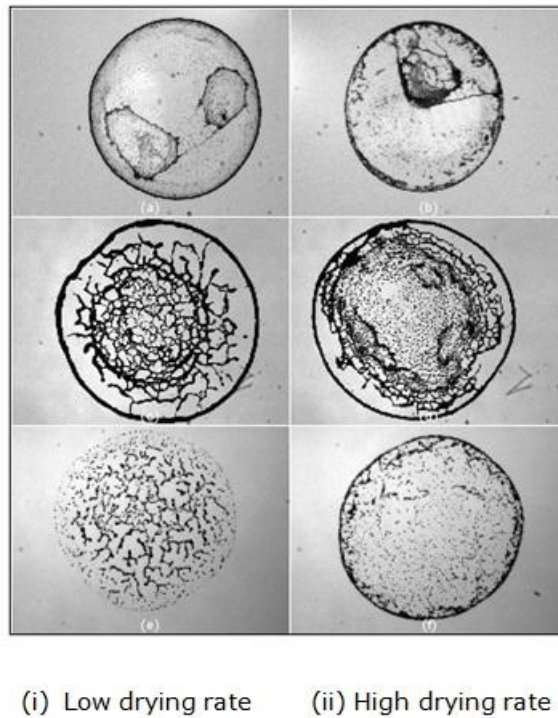


Figure 4.30: The montage of deposition patterns at (i) low drying rate and (ii) high drying rate with (a) and (b) for  $0.5\mu\text{m}$ , (c) and (d) for  $2\mu\text{m}$ , (e) and (f) for  $5\mu\text{m}$  PS particles.

We believe that this is the first observations of the effect of drying rate on the capillary flow in an evaporating droplet and hence on the shape of the final deposit and would have implication in the understanding of the complex kinematics of evaporating droplets. More work would be required to fully quantify the different flow mechanics using OCT.

## **Chapter 5**

### **PS-PEO Droplet Drying**

## 5.1 Introduction

In chapter 3 it has been found that drying droplets containing polystyrene (PS) particles results into final deposit with varieties of patterns. By varying the evaporation rates, contact angles, droplet orientation, particles sizes and initial concentrations, ring-like deposits were observed. The patterns were deduced to be influenced by competition between the inward, outward and vertical flow velocities of PS microparticles as the droplets dried. However for concentration,  $c_1 > 3\%$  of PEO (100K) polymer solution droplets upon drying forms solid conical pillars "Mexican hat" through a four stage drying and pancake or disk-like solid "puddle" for  $c_1 < 3\%$  as shown in figure 5.1 (a) and (b) respectively [136, 137]. In the physics context puddles may refer to where a liquid forms into patches on top of a surface of a solid material. For instance gravitational effects cause the droplet to flatten at the peak thus losing their spherical cap shape and can no longer be satisfactorily described as droplets at all, but rather small puddles. Li [167] has also observed that for intermediate concentration of Toluene polymer solution when their droplets are evaporated on a polystyrene polymer substrate a Mexican hat or dimple in the center of the deposit (figure 5.1(c)) is formed. A dimple is a slight depression or indentation in a surface.

In this chapter drying droplets containing PS-PEO are considered specifically to investigate the effect of PS particles sizes and their initial concentration on the drying of PEO and the effect of initial concentration of PEO on the drying of PS particle droplets. The experimental procedures for drying PS-PEO droplets, acquiring image sequences and analysis of experimental data are described in section 2.5. The image sequences in the drying of PS-PEO droplets were acquired using optical imaging method and data were analysed by surface stylus profiler and Image J software. From the analysed data, the coefficient of skewness was

determined. The coefficient of skewness is the degree of asymmetry, or departure from symmetry, of a distribution.

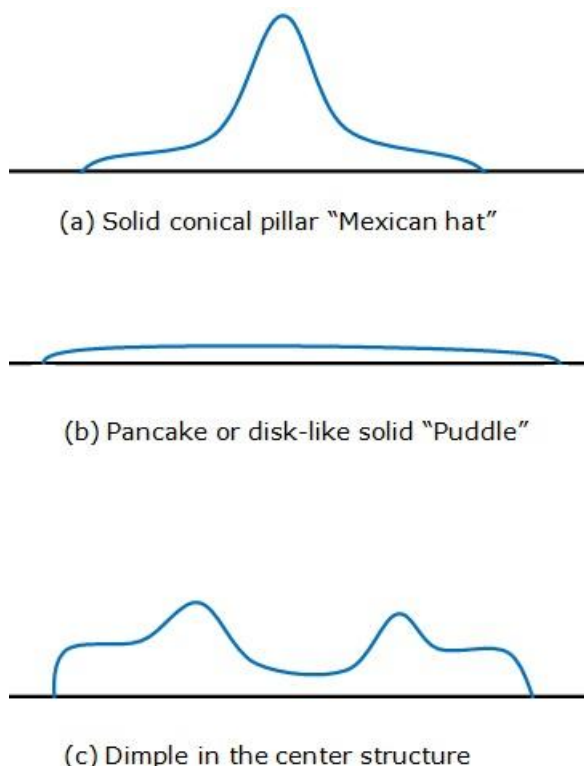


Figure 5.1: Schematic illustration of a deposit from drying PEO polymer solution droplets: (a) Solid conical pillars "Mexican hat", (b) Pancake or disk-like solid "puddle" and (c) dimple in the center of the deposit.

## 5.2 Experimental Results and Discussions

The section will present the detailed experimental results and corresponding discussions. The experimental results include the images, surface profiles and final deposits shapes inform of phase diagrams and coefficient of skewness from varying experimental parameters. The representative images (side on, polarized and reflection mode) are reported in terms PS particles sizes with varying initial concentration of PEO polymer solution.

## 5.2.1 Images of the Final Deposits

### 5.2.1.1 : 0.5 $\mu$ m PS Particles in PEO Solution

In figure 5.2 sample side on image sequences are presented showing time steps as the droplets containing a fixed PS particles concentration ( $c_0 = 4\%$ ) mixed with varying concentration of PEO ( $c_1 = 1.6\% - 12\%$ ) dries.

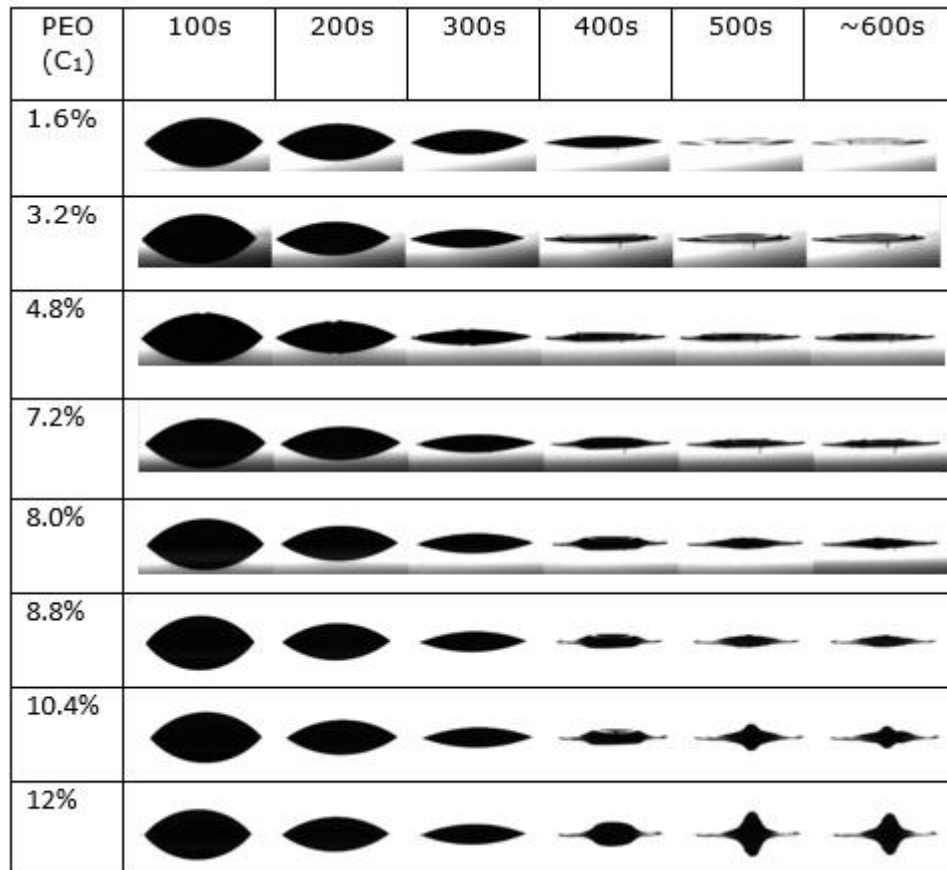


Figure 5.2: Side on image sequences as a 0.4 $\mu$ L droplet dries containing 0.5 $\mu$ m PS particles ( $c_0 = 4\%$ ) and PEO ( $c_1 = 1.6\% - 12\%$ ).

From figure 5.2, the following can be deduced; In the first 300s droplets volume decreases linearly with time regardless of their initial concentrations. However at 400s the droplets shapes are not similar in particular for  $c_1 > 7.2\%$  the dewetting to the droplets is clearly observed. At ~600s pancake or disk-like solid "puddle" are

observed for droplets with PEO concentration  $c_1 \leq 8.8\%$ . A small pillar is observed at  $c_1 = 10.4\%$  and a taller one for  $c_1 = 12\%$ . As explained in section 5.1 for droplets of PEO (100K) polymer solution with concentration,  $c_1 > 3\%$  upon drying forms solid conical pillars through a four stage drying. In the present study by adding PS particles to PEO polymer solution, the minimum concentration  $c_1 \approx 3\%$  according to Willmer et. al, [136] for forming pillars has shifted to  $\sim 10\%$ . The four stages drying of PEO has been disrupted upon adding PS microparticles leading to the formation of puddles. Figure 5.3 show the images of the final deposits of varying  $0.5\mu\text{m}$  PS particles concentration as well as varying PEO concentration in a polarized mode.

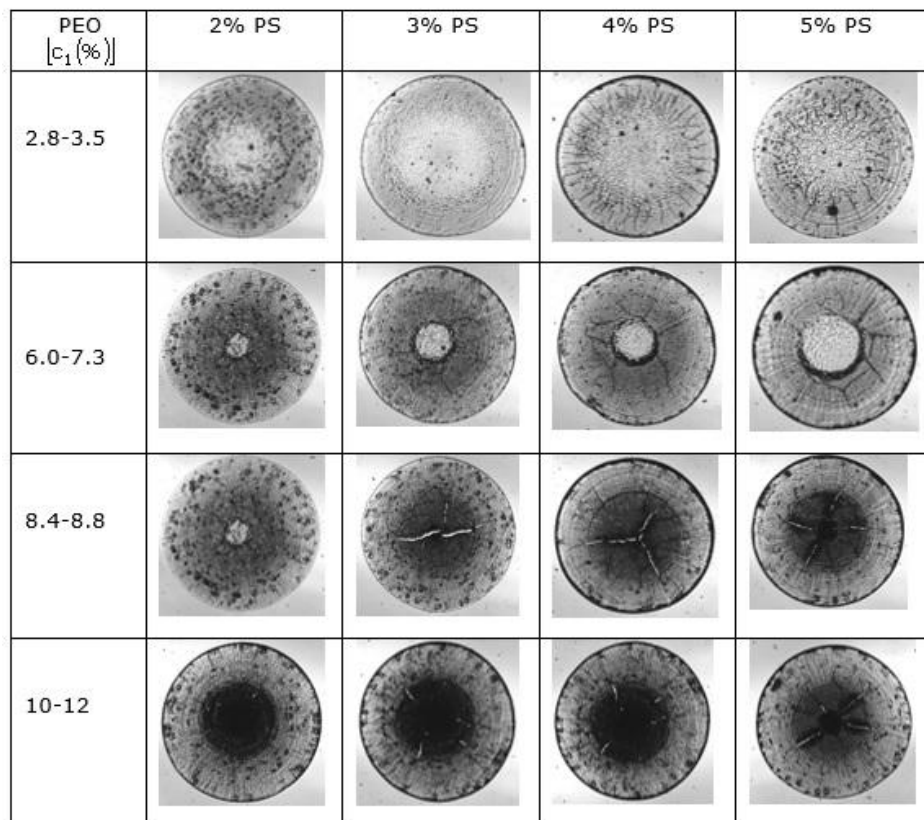


Figure 5.3: Final images captured with cross polarizer for  $0.5\mu\text{m}$  PS particles of  $c_0 = 2\% - 5\%$  mixed with  $c_1 \sim 3\% - 12\%$  of PEO.

The images in each column represent a fixed PS microparticles concentration and varying PEO concentration. There are observable distinct features in all images at fixed PS concentration. For higher PEO initial concentration (10-12%) there is a dark circular region at the interior of the droplet corresponding to conical like deposit. As the concentration of PE decreases in the mixture at fixed PS concentration, puddles appear as shown in figure 5.4. The overall winner (puddle or pillar) for PEO with  $c_1 > 3\%$  in the mixture depends on the concentration of PEO/PS.

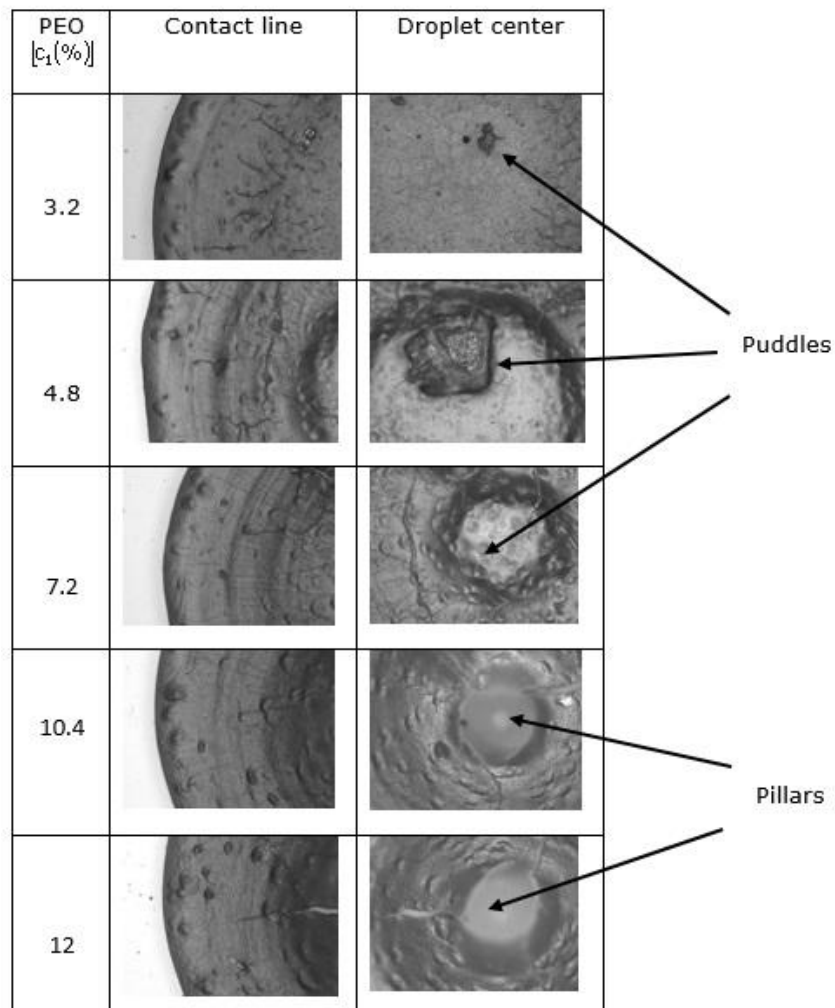


Figure 5.4: Magnified final deposits of  $0.5\mu\text{m}$  PS particles ( $c_0 = 4\%$ ) with varying PEO concentration captured with optical microscope under reflection mode.

In order to interpret the results it is reasonable to consider both mechanisms described for PEO or PS alone responsible to forming the observed final deposit operating concurrently as illustrated in figure 5.5.

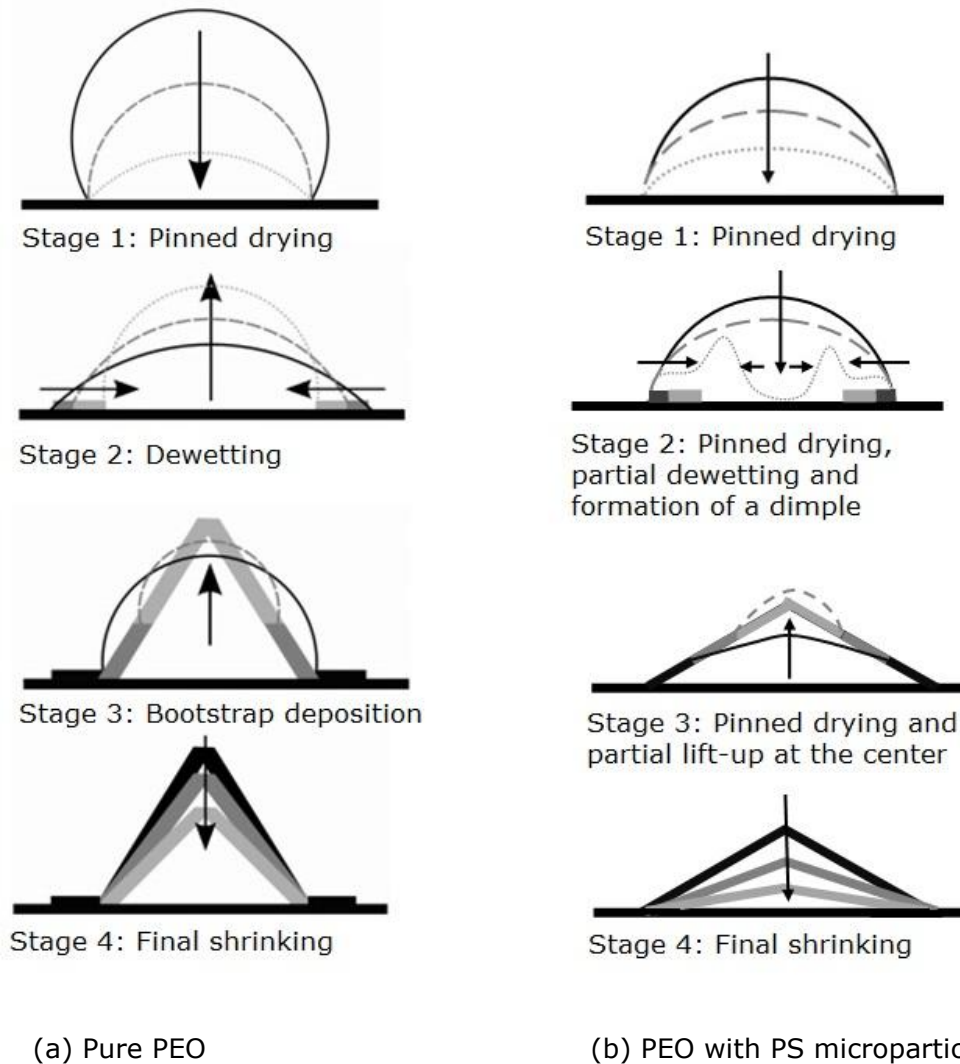


Figure 5.5: (a) Schematic illustration of the four drying stages of pure PEO for  $c_1 > 3\%$  [136] for comparison with our results in part (b). Thin lines indicate liquid surfaces, thick regions represent solid deposits. Progress within each stage is from solid black to dashed dark grey to dotted light grey. In (b) the schematic illustration show the drying stages of PEO with PS microparticles especially at transition concentration whose stage 2 is the most distinct with that of (a) with a formation of a dimple. In stages 1 to 4 the droplet is evaporation in a pinned mode.

It has been shown that when pinned droplets with contact angle  $<90^\circ$  containing PS particles alone evaporates; ring like deposits are observed at the perimeter. The ring like deposit is formed due capillary flow to replenish lost water at the contact line [4]. For droplets containing PEO (100K), conical deposits at the central part of the droplets are formed determined by the saturation concentration of the PEO as shown in figure 5.5 (a). In other study using PEO, Choi et al [140] have suggested that the conical deposit at the central part of the droplet is formed due to contact angle of the droplets dropping below the receding contact angle.

Sequence of images have confirmed that in the transition concentration region there exists two competing movement of the PS-PEO mixture as illustrated in figure 5.5 (b) stage 2. One movement like dewetting stage for PEO alone is observed and the second movement away from the central region creating a "dimple like structure" and this dimple expands in the direction towards the contact line. When the dewetting movement is stronger than the radially outward movement the dimple is raised leading to a flat puddle. It is worth noting that for pure PEO drying in the dewetting stage is followed by bootstrap deposition leading to an increase in central droplet height. As the concentration of the PEO decreases far from the transition region the outward movement becomes stronger to overcome the inward movement of PEO due to dewetting stage. As a result the ring like deposits and flat puddles are formed. Our results are consistent with a recently study by Mamalis et. al, [168] that puddles are formed when the droplets are pinned longer in which the accumulation of PEO crystals and dewetting stage at the contact line occur at later stages of droplet drying. Above the transition region pillars are formed by four stages as illustrated in figure 5.5 (a). The coffee ring stain of  $\text{SiO}_2$  microsphere has also been seen to be destroyed by adding PEO [169, 170] which is consistent with our results. The authors attribute the destruction to an increased velocity due to PEO which decreases capillary flow, and an increased Marangoni flow.

### 5.2.1.2 : 5 $\mu$ m PS Particles in PEO solution

The same procedures described in section 5.2.1.1 were performed for final deposits comprising of 5 $\mu$ m PS particles ( $c_0 = 4\%$ ) and PEO ( $c_1 = 1.6\% - 14\%$ ). The sequence of images as the droplets dries are shown in figure 5.6.

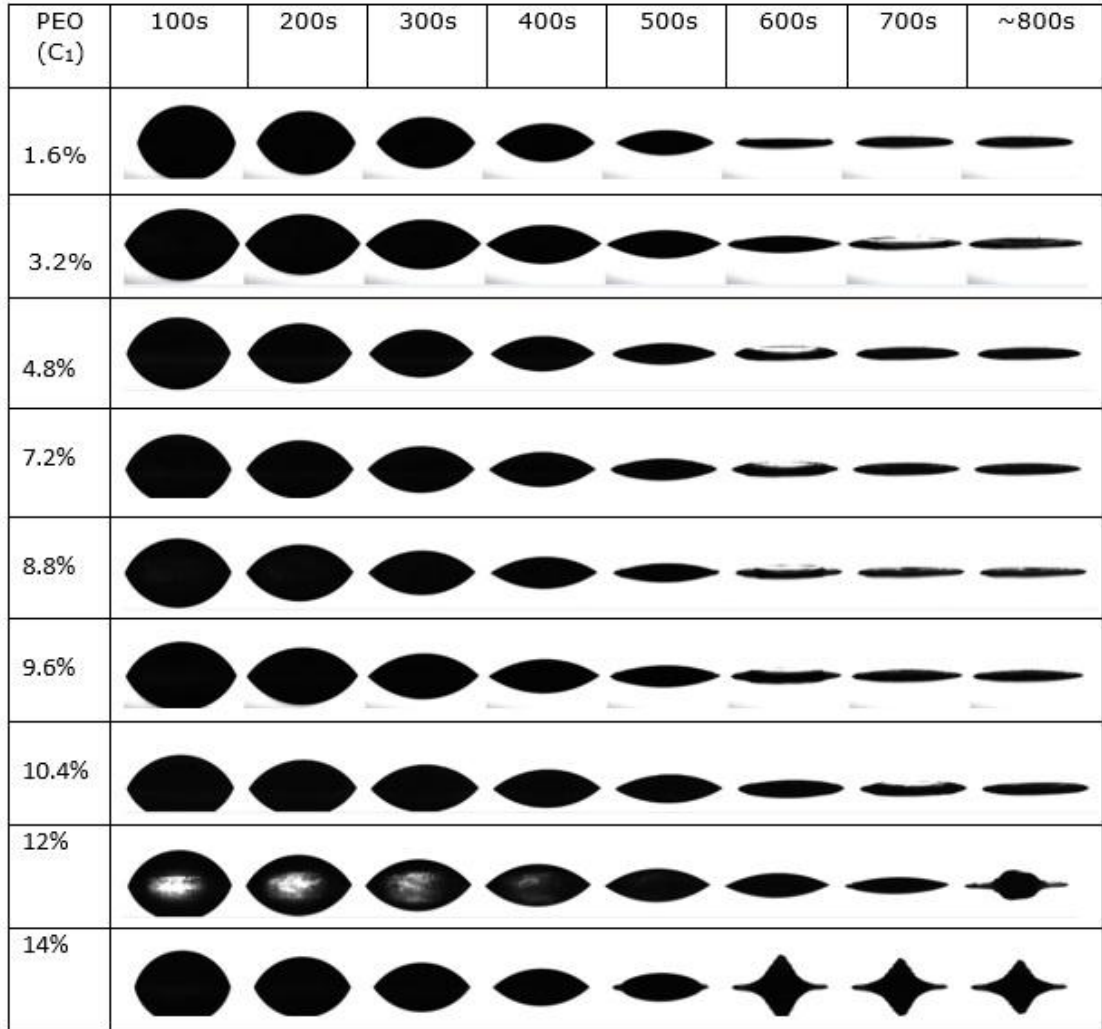


Figure 5.6: Side on image sequences as the 0.7 $\mu$ L droplet dries containing 5 $\mu$ m PS particles ( $c_0 = 4\%$ ) and PEO ( $c_1 = 1.6\% - 14\%$ ).

From figure 5.6 it has been observed that up to 400s of droplets drying, their corresponding profiles are similar for all PEO concentration. The dewetting step is observed for  $c_1 = 12\%$  at  $\sim 800$ s while for  $c_1 = 14\%$  is observed at  $\sim 500$ s. Below

$c_1 = 12\%$ , four stages of PEO drying are disrupted due to the presence of PS particles. The droplets are pinned all the droplet lifetime and the dewetting stage is destroyed. Figure 5.7 show the final deposits under cross polarizers.

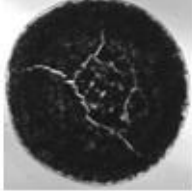
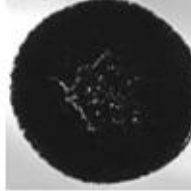
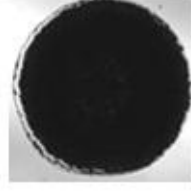
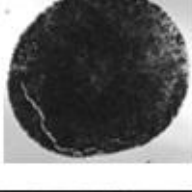
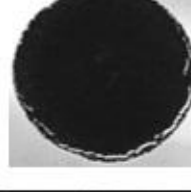
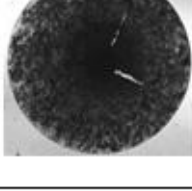
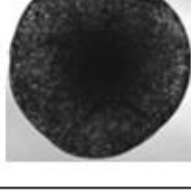
PEO [ $c_1$ (%)]	2% PS	3% PS	4% PS	5% PS
3.2-4.0				
7.2-7.5				
8.4-8.8				
10-14				

Figure 5.7: Final images captured with cross polarizer for  $5\mu\text{m}$  PS particles of  $c_0 = 2\% - 5\%$  mixed with  $c_1 \sim 3\% - 14\%$  of PEO.

One of the distinct features in figure 5.6 is a white band near the contact line or central part of the deposits. Videos from the side on and top view have confirmed this stage to happen when all liquid above is completely gone. It might be caused by some liquid trapped inside the deposits as it dries causing the deposit contract toward the interior at the same time the contact line failing to retreat to de-pinning process or vice versa. Closer inspection shows that this region does not contain

trapped PS particles. The pillar, puddle or discs like structures are clearly seen under magnified reflection mode as shown in figure 5.8.

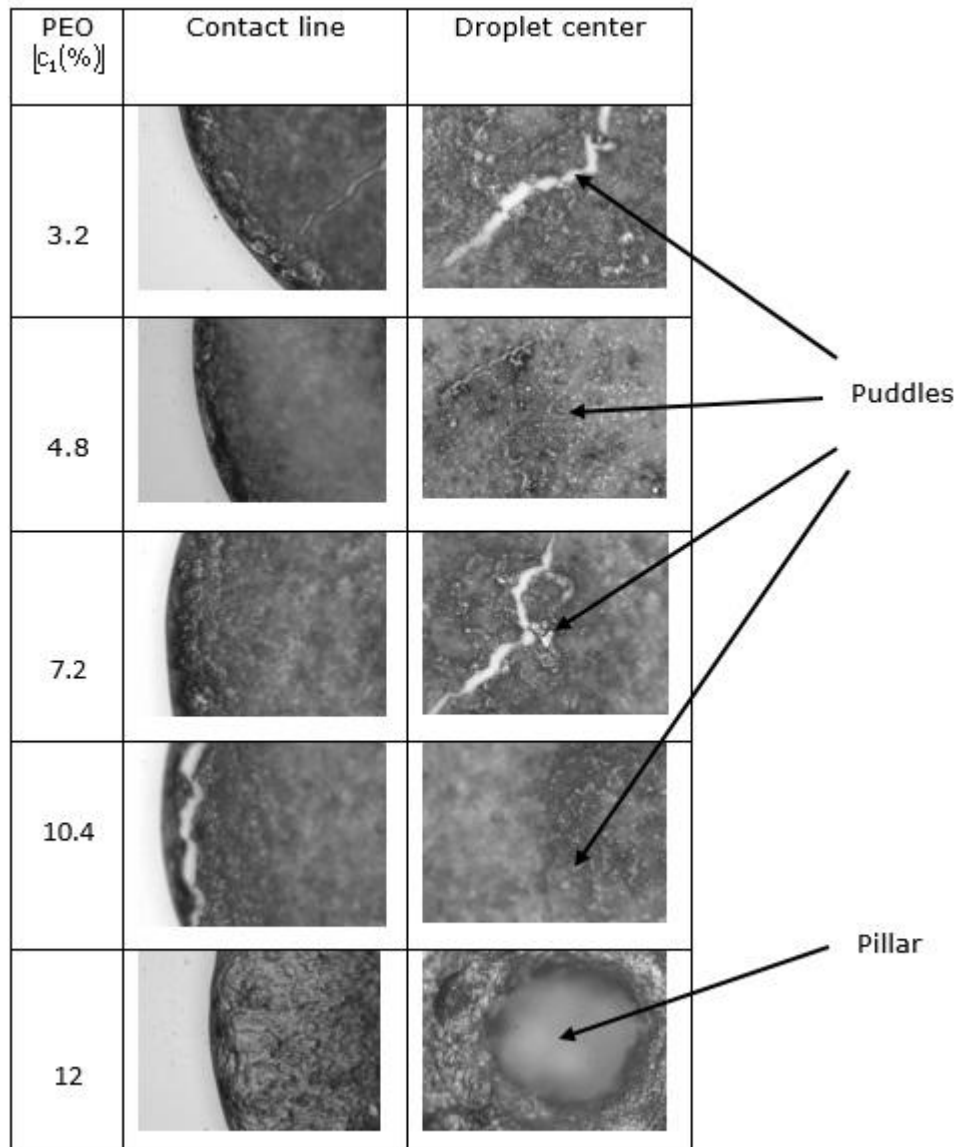


Figure 5.8: Magnified final deposits of  $0.5\mu\text{m}$  PS particles ( $c_0 = 4\%$ ) with varying PEO concentration captured with optical microscope under reflection mode.

In figure 5.9 the distribution of PS microparticles inside the deposits are shown especially when a pillar or puddle is formed. For  $c_1 \sim 1.6\%$  of PEO, particles are observed ordered in coffee ring like deposits and amorphous region of PEO covering

them is some areas. For  $c_1 \sim 12\%$  of PEO single particles and in clusters are randomly observed near the surface of the crystalline solid PEO. The random deposition of the PS particles takes place during dewetting stage of the pillar formation. The mechanism for the observed deposit is similar as illustrated if figure 5.5 in section 5.2.1.1.

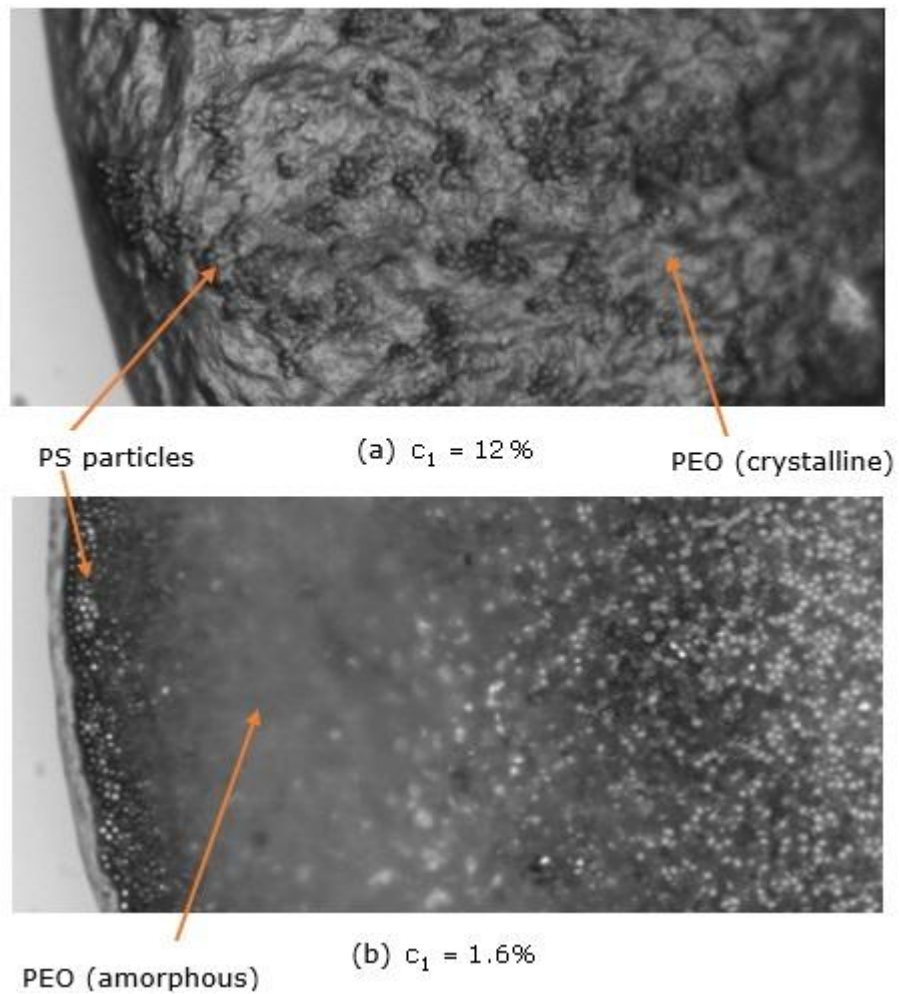


Figure 5.9: Distribution of 5µm PS particles inside the deposits when (a) pillar is formed at  $c_1 = 12\%$  of PEO and (b) a puddle at  $c_1 \sim 1.6\%$  of PEO.

### 5.2.2 Surface Profiles

To further quantify the images presented in section 5.2.1, the surface morphology of the final deposit was assessed by Stylus surface profiler both for PS particles

alone and those mixed with PEO polymer solution. The representative sample surface profiles are presented in section 5.2.2.1 and 5.2.2.2 for 0.5 $\mu\text{m}$  and 5 $\mu\text{m}$  PS particles respectively.

### 5.2.2.1 : 0.5 $\mu\text{m}$ PS Particles in PEO Solution

Figure 5.10 shows representative samples of surface profiles for 1 $\mu\text{L}$  droplet volume of 0.5 $\mu\text{m}$  PS particles alone.

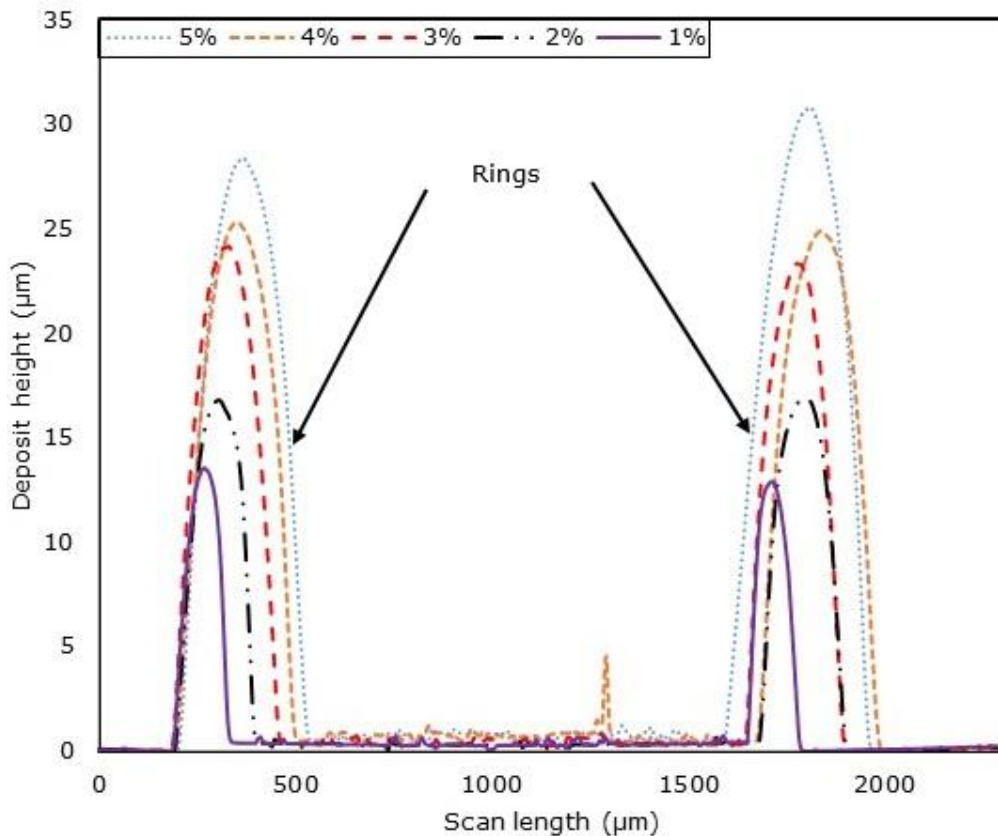


Figure 5.10: Surface profiles for 1 $\mu\text{L}$  droplet of 0.5 $\mu\text{m}$  PS particles with  $c_0 = 1\% - 5\%$ .

Robust rings are formed for  $c_0 = 1\% - 5\%$  of PS particles used. For  $c_0 = 5\%$  the ring height is about 30 $\mu\text{m}$  and decreases with the concentration of PS particles in the droplet to  $\sim 13\mu\text{m}$  for  $c_0 = 1\%$ . The ring width also decreases from  $\sim 340\mu\text{m}$  for  $c_0 = 5\%$  to  $\sim 146\mu\text{m}$  for  $c_0 = 1\%$ . At the interior of deposit the fraction of the

particles left are as high as  $1\mu\text{m}$  for  $c_0 = 5\%$  and  $0.5\mu\text{m}$  for  $c_0 = 1\%$ . When a droplet with initial volume of  $0.4\mu\text{L}$  containing PS particles of fixed  $c_0 = 4\%$  and varying PEO concentration ( $c_1 = 1.6\% - 12\%$ ) is dried, the corresponding surface stylus profiles of the final deposits are presented in figure 5.11. The curve for  $c_1 = 0\%$  of PEO is also included for comparison purposes. The deposit diameter for  $c_1 = 0\%$  of PEO is slightly greater than those with varying PEO concentration ( $c_1 = 1.6\% - 12\%$ ) which may be attributed to the differences in viscosities [171].

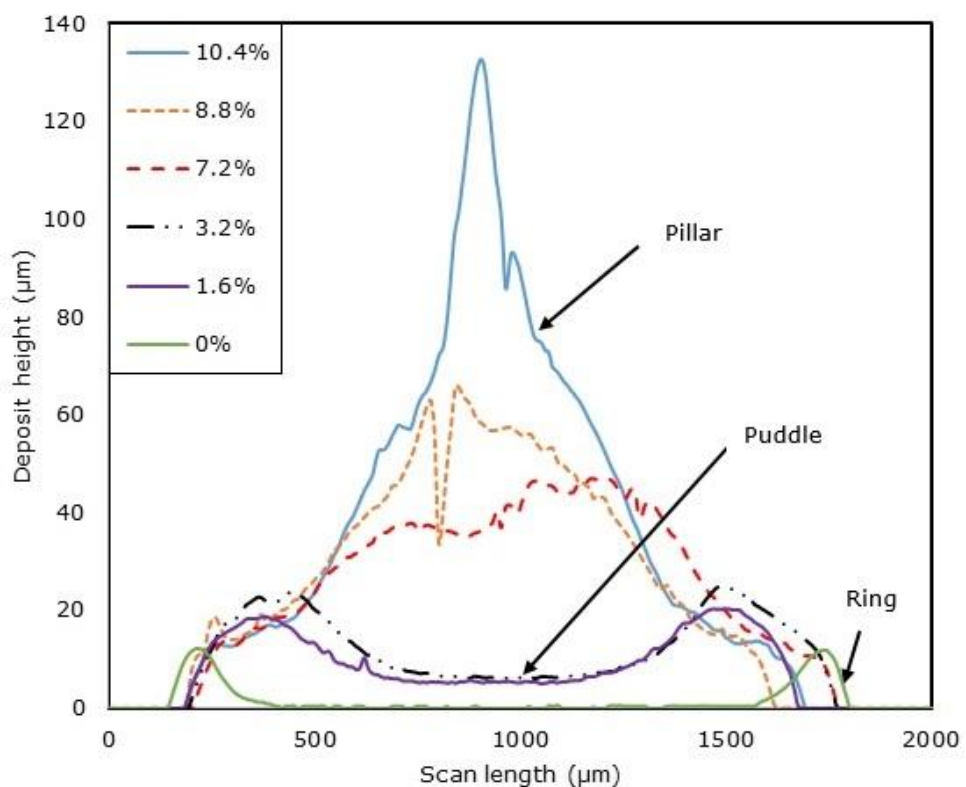


Figure 5.11: The effect of PEO concentration on the deposits profiles for  $c_0 = 4\%$  of  $0.5\mu\text{m}$  PS particles.

For  $c_1 < 3\%$  of PEO ( $c_1 = 1.6\%$ ) a puddle as high as  $\sim 20\mu\text{m}$  at the perimeter and  $\sim 5\mu\text{m}$  at the interior of the deposit is formed. Just above  $c_1 = 3\%$  of PEO ( $c_1 = 3.2\%$ ) a puddle is also formed with  $\sim 25\mu\text{m}$  high at the perimeter and  $\sim 6\mu\text{m}$  at the interior of the deposit. As the concentration of PEO increases to  $8.8\%$  the

deposit shape takes a conical like structure with the central region as high as  $\sim 60\mu\text{m}$ . The conical like structure is brought about by dewetting and bootstrap deposition stages in PEO drying [140]. For  $c_1 = 10.4\%$  of PEO the pillar is  $\sim 130\mu\text{m}$  high.

### 5.2.2.2 : 5 $\mu\text{m}$ PS Particles in PEO Solution

In figure 5.12, the final deposit profiles for 5 $\mu\text{m}$  PS particles alone of varying concentrations ( $c_0 = 1\% - 5\%$ ) are shown. For  $c_0 = 1\%$  only a single layer  $\sim 5\mu\text{m}$  of deposited particles are observed. At  $c_0 = 5\%$  about eight layers of particles are deposited leading to  $\sim 40\mu\text{m}$  high of coffee like deposits. At the interior of the ring for  $c_0 = 5\%$ , The ring is rather wide as observed in chapter 4 due to sedimentation. When a droplet containing  $c_1 = 1.6\%$  of PEO mixed with  $c_0 = 4\%$  of PS particles is dried, the deposit profile is seemingly similar to that for PS particles alone corresponding to  $c_0 = 4\%$  as presented in figure 5.13.

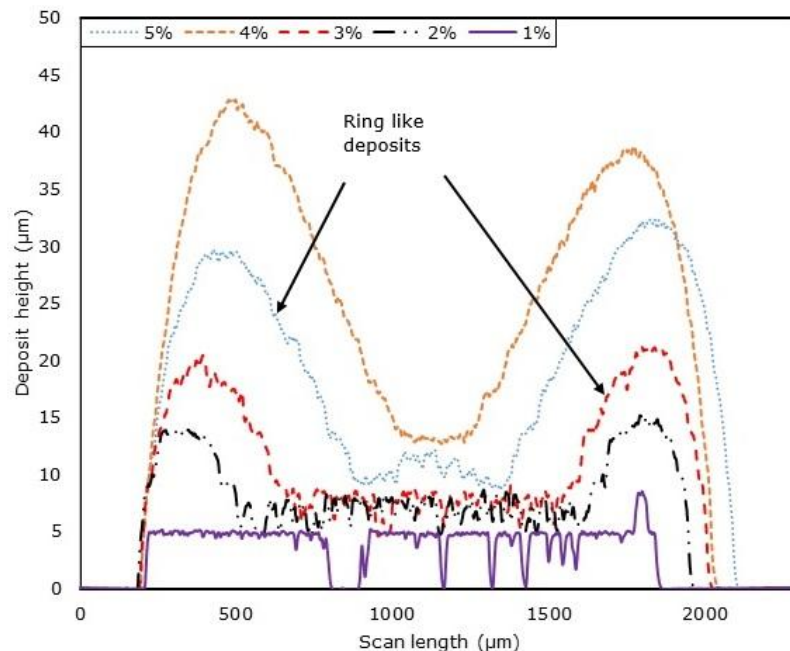


Figure 5.12: Surface profiles for 1 $\mu\text{L}$  droplet of 5 $\mu\text{m}$  PS particles with  $c_0 = 1\% - 5\%$ .

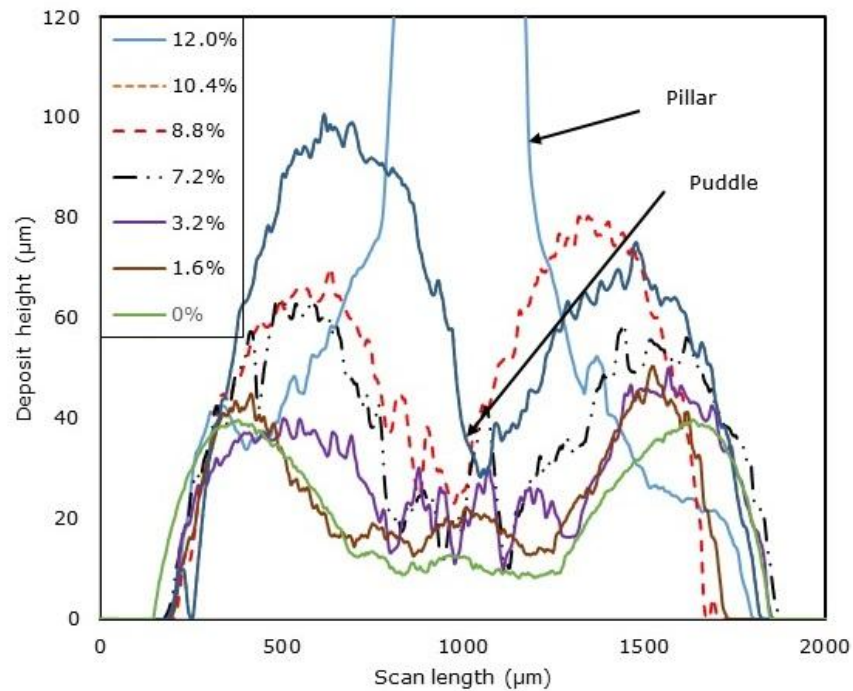


Figure 5.13: The effect of PEO concentration on the deposits profiles for  $c_0 = 4\%$  of  $5\mu\text{m}$  PS particles.

The deposit height is slightly high compared to that of PS particles alone due to added PEO. For PEO of  $c_1 > 3\%$ , deposits height at the perimeter of the droplet increases slightly slower compared to that at the interior as observed for  $0.5\mu\text{m}$  PS particles of similar PEO concentration. In figure 5.13, the increase in PEO concentration has great effect on the ring width of the ring-like deposits than their corresponding heights before the pillars are formed. For  $c_1 > 3\%$  and less than concentration for which pillars are formed, their corresponding deposits profiles contain spikes. This has not been observed for  $0.5\mu\text{m}$  PS particles when similar PEO concentration was used suggesting the effect of PS particles size on the deposits morphology. When a Pillar is formed in this case  $c_1 = 12\%$ , the spikes disappear.

### 5.2.3 Effect of PS-PEO concentration and Particle Sizes

In section 5.2.1 and 5.2.2 the deposit patterns have been described by considering their images both in the top view and side on as well as to their surface morphology.

It has been observed that rings like deposits appear for PS alone as previously described in chapter three, however when PEO is introduced the patterns changes accordingly determined by concentration of the two components as well as the PS particle sizes. As a result, the deposits shapes vary from puddles to pillars. The effects of these parameters on the final deposit are combined into single quantity called coefficient of skewness. The procedures for determining the coefficient of skewness are described in section 2.5 and appendix D. The relationship between the coefficient of skewness and varying PS-PEO concentrations as well as particles sizes are presented in figure 5.14 to 5.17.

As the concentration of PS particles decreases from 5% to 2%, concentration of PEO at which the coefficient of skewness is zero, changes accordingly. For  $c_0 = 5\%$  of PS in figure 5.17, the crossover PEO concentrations are  $\sim 10\%$  and  $\sim 6\%$  for  $5\mu\text{m}$  and  $0.5\mu\text{m}$  diameter particles respectively. When the PS particles drop to  $c_0 = 2\%$  in figure 5.14, the PEO crossover concentration is  $\sim 8\%$  and  $\sim 5\%$  for  $5\mu\text{m}$  and  $0.5\mu\text{m}$  diameter particles respectively. The coefficient of skewness curves for  $5\mu\text{m}$  PS particles are very unique compared to the other two curves for pure PEO and  $0.5\mu\text{m}$  PS particles which are seemingly similar in their shapes. The coefficient of skewness is little affected by adding  $0.5\mu\text{m}$  PS diameter particles compared to  $5\mu\text{m}$  PS diameter particles. This shows the effect of particle sizes in disrupting the four stage drying of PEO (the larger the particles the bigger the effect).

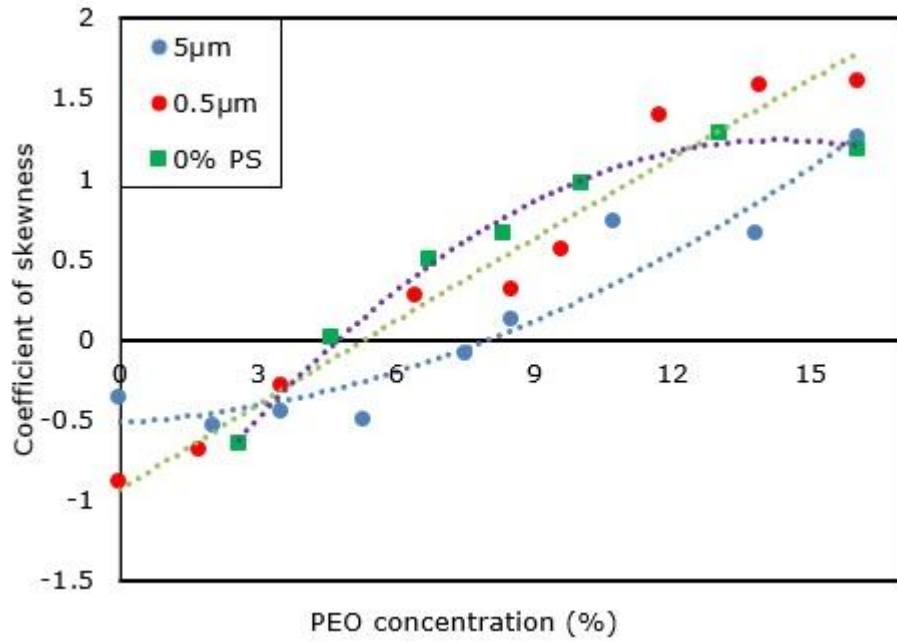


Figure 5.14: Coefficient of skewness as a function of PEO concentration for a fixed  $c_0 = 2\%$  of PS particles and 0% PS is included for comparison.

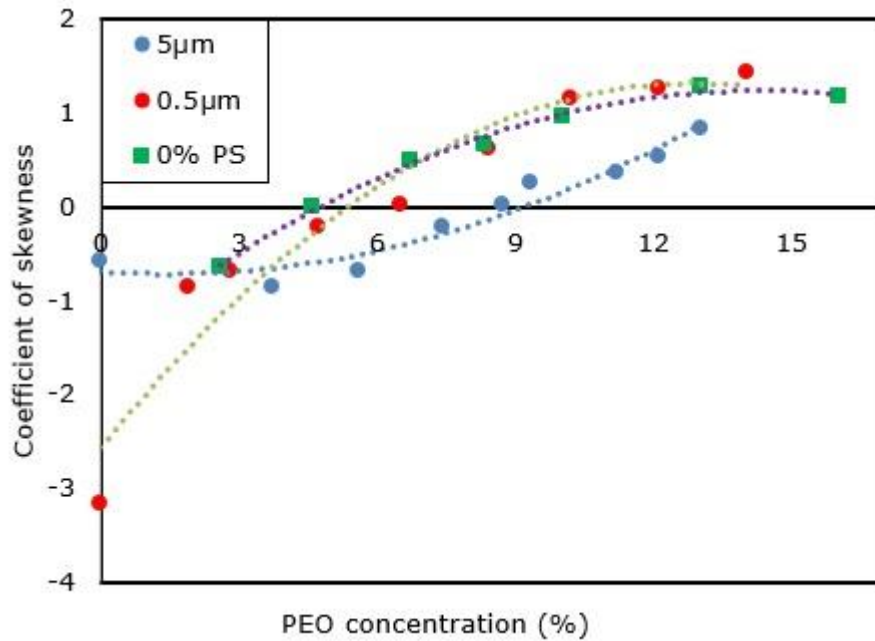


Figure 5.15: Coefficient of skewness as a function of PEO concentration for a fixed  $c_0 = 3\%$  of PS particles and 0% PS is included for comparison.

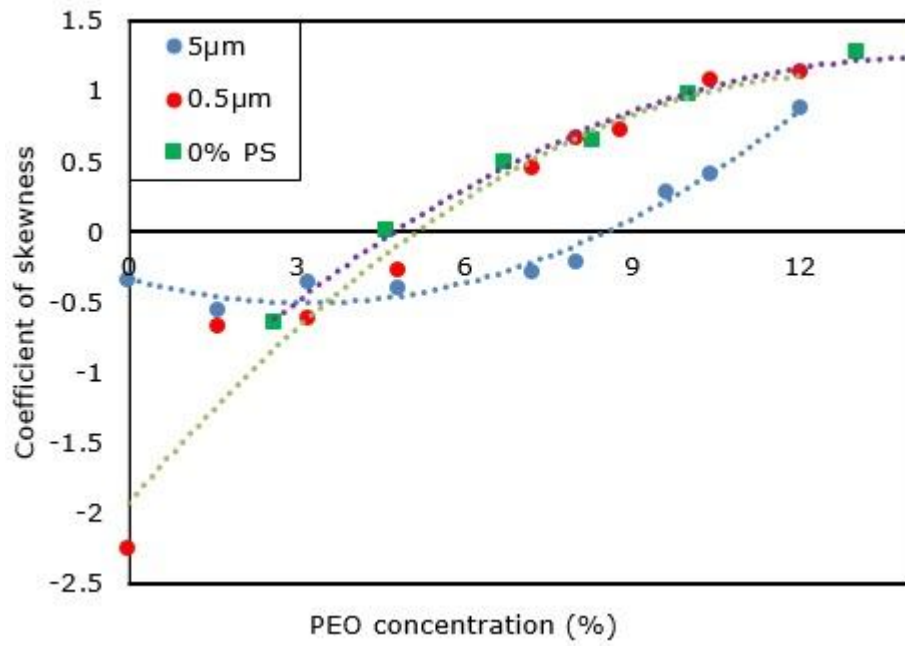


Figure 5.16: Coefficient of skewness as a function of PEO concentration for a fixed  $c_0 = 4\%$  of PS particles and 0% PS is included for comparison.

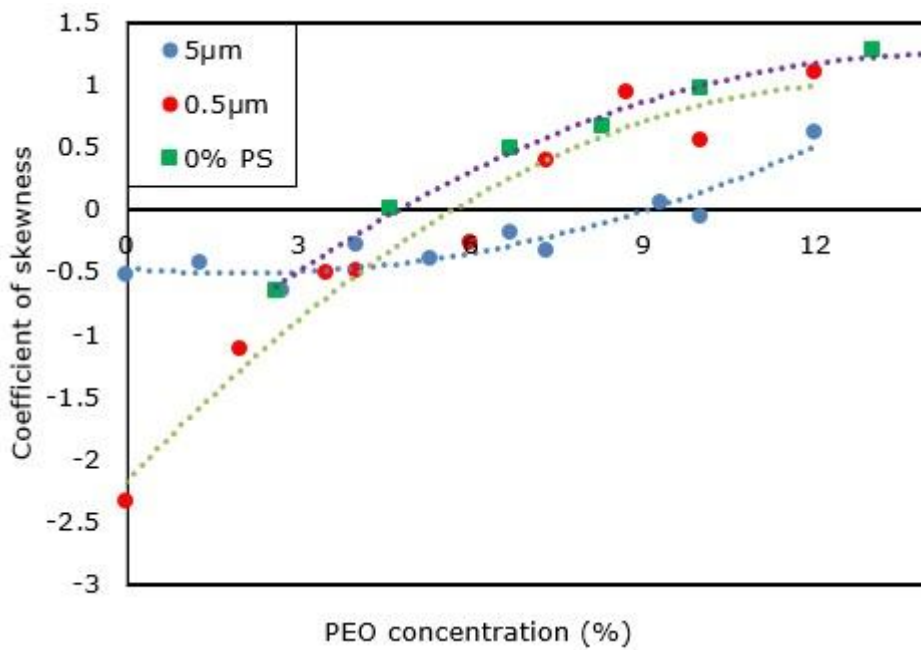


Figure 5.17: Coefficient of skewness as a function of PEO concentration for a fixed  $c_0 = 5\%$  of PS particles and 0% PS is included for comparison.

In figure 5.18 and 5.19 the crossover concentration at which the coefficient of skewness is zero is incorporated show the transition from puddle to pillars. Also the transition from puddle to pillar increases to higher PEO concentration with increasing PS particles concentration as presented in figure 5.18 and 5.19.

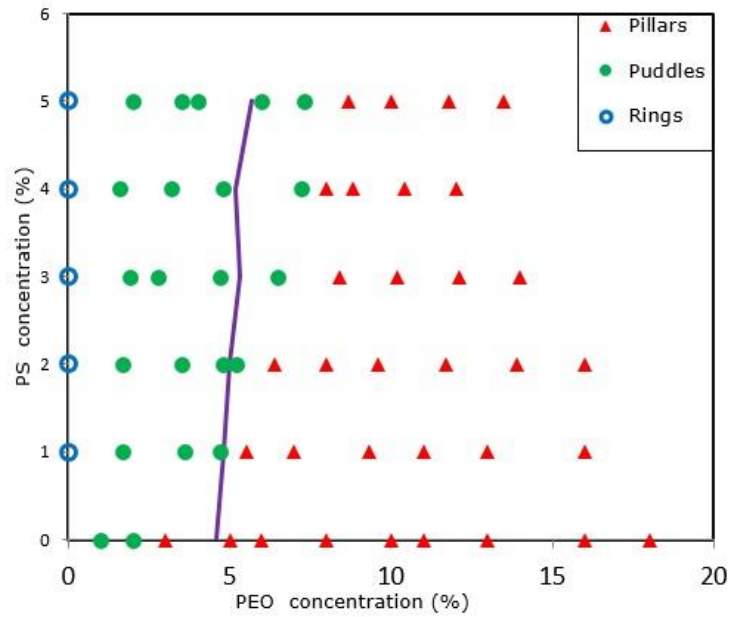


Figure 5.18: Phase diagrams showing pillars, puddles and rings for 0.5µm PS particles with the purple skew line showing the cross over concentration.

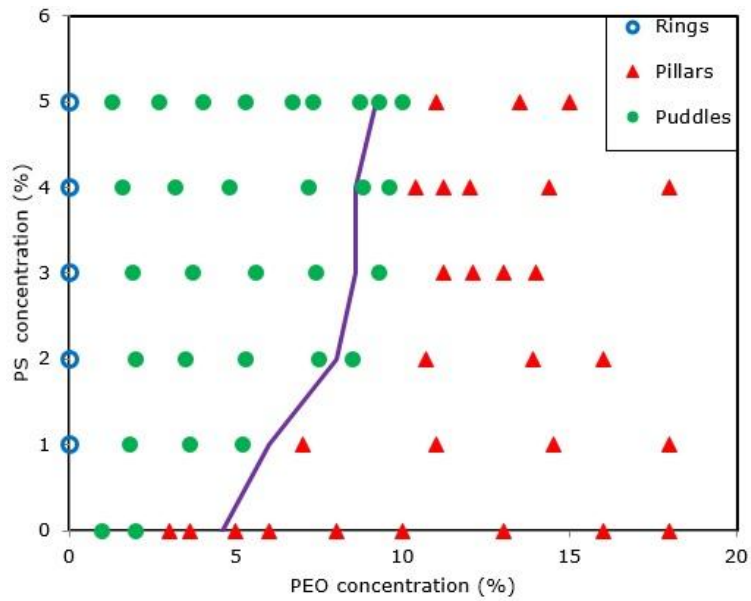


Figure 5.19: Phase diagrams showing pillars, puddles and rings for 5µm PS particles with the purple skew line showing the cross over concentration.

### 5.3 Conclusions

The present study has investigated the effect of adding PS microparticles of different sizes to evaporating droplets of PEO. In pure solutions, PEO forms tall pillars above around 3% concentration and PS microparticles typically leave ring stain deposits. We have shown that particles disrupt pillar formation and polymer disrupts ring stain formation. Pillar formation is shifted to slightly higher polymer concentrations when large 5µm PS particles are added, but is less affected by the addition of 0.5µm PS particles. We have characterized the topologies of the deposit using skewness of the profile as a simple analytic method for quantifying the shapes: pillars produce positive, flat deposits have zero skew and ring stain have a negative skew. The skewness factor has the future potential to be very useful for characterization of deposits in a wide variety of systems.

# Chapter 6

## Conclusions

### 6.1 How Robust is the Ring Stain

In this chapter the coffee ring stain was studied by varying contact angle ( $5^\circ$ ,  $18^\circ$  and  $35^\circ$ ), concentration of the particles, size of the particles ( $0.1\mu\text{m}$ ,  $0.2\mu\text{m}$ ,  $0.5\mu\text{m}$  and  $5\mu\text{m}$ ), evaporation rate and orientation of the droplet (upright and upside down). Varying evaporation rate was achieved by reducing the pressure from atmospheric condition to  $\sim 13\text{mbar}$  using low pressure chamber. Robust rings have been observed for drying rate  $< 5\text{nL/s}$  and thin ring for  $> 5\text{nL/s}$ . However the ring stain is particle size dependent when evaporation rate and concentration are varied due to the wedge effect. This is consistent with available literature [172] for larger particles in an evaporating droplet in which the droplet diameter is slightly larger than the diameter of the final dried deposit leading to wedge effect. The final deposit were analysed to determine the scaling power law of ring height and width. Experimental results on scaling power law show that, ring height has strong dependence on the contact angle, particle sizes and droplet orientation for drying rate  $< 5\text{nL/s}$  and agree well with theoretical prediction than ring width.

#### 6.1.1 Evaporation Rate

The evaporation rate has been found to affect the deposition pattern for drying rate  $> 5\text{nL/s}$ . Above this value a thin ring was observed with larger percent of microparticles being deposited at the interior of the ring for  $0.1$ ,  $0.2$ ,  $0.5$  and  $5\mu\text{m}$  particles. Below evaporation rate of  $5\text{nL/s}$ , robust ring was observed with a smaller fraction of deposits at the interior of the ring for  $0.1$ ,  $0.2$ ,  $0.5$  and  $5\mu\text{m}$  particles sizes. For  $5\mu\text{m}$  particles at low drying rates  $\sim 0.6\text{nL/s}$ , the deposition patterns is

concentration dependent, however, for  $>5\text{nL/s}$  rings are formed even at lower initial concentrations. For robust rings observed especially 0.1, 0.2 and  $0.5\mu\text{m}$  particles the average values of exponents are  $m = 0.33 \pm 0.05$ ,  $n = 0.50 \pm 0.04$  and  $p = 0.03 \pm 0.01$  for ring width, height and radius with their corresponding summation  $m+n+p = 0.86 \pm 0.07$ . Theoretically the summation  $m+n+p$  should give a value of a unity, however based on our findings there is a discrepancy. The value of exponent for ring height is consistent with theoretical prediction. The major discrepancy comes from ring width whose exponent is less than the predicted one. This discrepancy may be contributed by an increase in microparticles packing fraction at higher initial concentrations such that the ring deposit have misleadingly small dimension and that some PS microparticles are deposited at the interior of the ring and hence not involved in calculating the volume of the ring. In conclusion, our study showed, for the first time, that the drying rate is important in determining the shape of the final deposit, which may contribute to a better understanding of the coffee ring effect.

### **6.1.2 Contact Angle**

For the contact angles used in the present study of  $5^\circ$ ,  $18^\circ$  and  $35^\circ$ , the deposit patterns at low drying rates are characterized by robust rings. However, as the contact angle decreases, the rings flatten due to the competition between the increased droplet radius and the number of particles present. The ring height has a stronger dependence on the contact angle than ring width.

### **6.1.3 Droplet Orientation and Particle Sizes**

The effect of droplet orientation has very much been found to depend both on evaporation rate as well as the particles sizes. For drying rates  $<5\text{nL/s}$  the scaling power laws for 0.1, 0.2 and  $0.5\mu\text{m}$  particles sizes, both in upright and upside down orientations the values are seemingly similar. The depositions patterns in both

orientations for these particles sizes are also similar and those for  $>5\text{nL/s}$  drying rate characterized by thin rings. For  $5\mu\text{m}$  particles sizes, the deposition patterns are determined by sedimentation at low drying rate in upright orientation and evaporation rates in the same orientation. For upside down orientation at low drying, particles sediment at the cap of the droplet resulting in deposit patterns which gather at the interior of the droplet as the air-liquid interface recedes with them.

## **6.2 Kinematics of Droplet Drying**

In this chapter we studied the kinematics of evaporation using three particle sizes ( $0.5\mu\text{m}$ ,  $2\mu\text{m}$  and  $5\mu\text{m}$ ) and, low ( $\sim 0.6\text{nL/s}$ ) and high drying rate ( $>5\text{nL/s}$ ) using SDOCT and optical microscope. We found that deposition patterns varied, including the ring stains, and the central deposit. By measuring the inward, outward and vertical velocity, we suggest that rings form when the outward velocity dominates over the Marangoni flow. More work is needed to confirm this. When there is a competition between vertical, outward and inward velocity, either thin/wider rings or no rings are formed.

### **6.2.1: 0.5 $\mu\text{m}$ PS Microparticles**

One way to describe the kinematics of PS microparticles inside the drying droplet was to determine vertical, outward and inward velocity corresponding to sedimentation, capillary flow and gradient in surface tension forces respectively. For  $0.5\mu\text{m}$  PS particles both at low and high droplet drying the sedimentation of individual particles have not been observed and thus play no role in determining the final deposition patterns. At low drying rates capillary and diffusion dominate while at high drying rate there is a competition between Marangoni flow and capillary flow as confirmed with average velocities determined. The capillary flow is responsible for robust rings observed at low drying rates. When this is coupled with

Marangoni flow taking the microparticles at the air-liquid droplet interface few microparticles remain pinned and accumulate at the contact line resulting in a thin ring at high drying rate.

### **6.2.2: 2 $\mu$ m PS Microparticles**

For 2 $\mu$ m PS particles at low drying rate both sedimentation and capillary flow are present with no Marangoni flow. The outward velocities are far larger in comparison to vertical velocities, so the final deposit patterns are characterized by robust ring and smaller fractions of microparticles scattered at the interior of the ring. The deposition patterns at the interior of the ring are largely determined by the final stages of drying. For high drying rates, sedimentation, capillary and Marangoni flow are all present. The intensity of vertical velocity is quite small compared to outward and inward velocity. There is a competition between inward and outward velocity with an exception near the end of the droplet drying when the inward flow ceases and the outward flow is maximum, as in the rush hour effect. The Marangoni flow is responsible for the thin ring observed at high drying rate compared to that at low drying rate given the same initial concentration of PS microparticles. The re-circulated microparticles are carried at the air-liquid interface as the droplet recedes as observed for 0.5 $\mu$ m PS particles at high drying rate.

### **6.2.3: 5 $\mu$ m PS Microparticles**

The 5 $\mu$ m PS particles had distinctive kinematics which depends both on drying rate and the concentration of particles in the droplets. At low drying rate sedimentation, was dominant to capillary with no Marangoni flow at all. For low concentration, larger fractions of the particles are scattered at the interior with no ring at all. As the concentration increases, wide ring-like deposit is observed at the contact line. For high drying rate, outward velocity was greater than vertical velocity resulting in

a thin ring at the contact line and the rest of particles at the interior of this ring. The Marangoni velocity was on the same magnitude as the sedimentation velocity.

### **6.3 PS-PEO Droplet Drying**

In this chapter the droplets containing PS particles and PEO polymer solution were studied. The concentration of PS particles (1%-5%) and sizes (0.5 $\mu$ m and 5 $\mu$ m) were varied to study their effect on the four stages drying of PEO. Meanwhile the concentration of PEO (100K) ranging from ~2% to 18% were varied to study the effect on the coffee ring stain of PS particles. Drying droplets containing PS microparticles alone form coffee ring stains whereas drying droplets containing PEO polymer solution forms conical-like structures for concentration  $c_1 > 3\%$  in four stages namely pinned drying, pseudo-dewetting, boot-strap building and late stage contraction. Adding PS microparticles in PEO polymer solution of various sizes in this case 0.5 $\mu$ m and 5 $\mu$ m have been shown to completely destroy the conical-like structures below the transition concentration. The coffee stain has been shown to be suppressed for higher PEO concentration and for low PEO concentration below a critical value (transition concentration) puddles are formed. The transition concentration is particle size dependent for similar PEO concentration.

#### **6.3.1 Effect of PS Particle Sizes**

The larger the particles the more the effect in destroying the four stages of PEO polymer solution droplets upon drying. The final deposits in this case puddles and conical-like structures using 0.5 $\mu$ m PS particles are smooth whereas for 5 $\mu$ m PS particles are rough as confirmed with Stylus surface profiler.

#### **6.3.2 Effect of PS-PEO Initial Concentration**

Varying the initial concentration of either PS microparticles (0.5 $\mu$ m or 5 $\mu$ m) keeping the PEO polymer constant or varying initial concentration of PEO polymer keeping

PS microparticles (0.5 $\mu\text{m}$  or 5 $\mu\text{m}$ ) constant affects the transition point. The transition region or point is where the puddle like structure changes to conical-like deposits (pillars). By determining the coefficient of skewness of the deposit the transition concentration (also known as a crossover concentration for which the coefficient of skewness is zero) was found. The transition concentration of PEO polymer has been found to depend on the PS microparticles sizes and its concentration in the PS-PEO mixture. The transition concentration has been observed to shift from 3% (PS microparticles have been taken into account) for PEO polymer alone to  $\sim$ 5% for 1% initial concentration of 0.5 $\mu\text{m}$  PS particles and increases steadily to  $\sim$ 7% for 5% initial concentration the same PS particles sizes. For 5 $\mu\text{m}$  PS particle sizes the transition concentration of PEO polymer has shifted from 3% to  $\sim$ 6% at 1% of PS microparticles and increases steadily to  $\sim$ 9% for 5% of PS microparticles. The shift in transition concentration is largely dependent on PS particle sizes for a fixed PEO concentration in the mixture.

## **6.4 Future Work**

### **6.4.1 How Robust is the Ring Stain**

In the present study the thermal conductivity of the substrate was not varied. It is recommended that future studies use substrates of different thermal conductivity such as aluminium and vary temperature to study their effects on the scaling power laws and the ring formation both at atmospheric and reduced pressures. Controlling self-assembly in printing process is vital for industrial purposes where multiple droplets are used and therefore further studies can be carried out to utilize the low pressure to suppress coffee ring effect and other useful applications. Also studying the effect of different shapes (elliptical rings) and the effect of temperature on the final deposit. A recent study by Li et al [157] found that temperature ( $>40^{\circ}\text{C}$  and up to  $80^{\circ}\text{C}$ ) destroyed the ring in monodisperse PS particles (100nm). Recent

preliminary studies in our group do not support this for 2 $\mu$ m PS particles and temperatures up to 70°C [173]. It will be worthwhile making a careful investigation to study the effect of temperature and particle size on the ring width and height under controlled humidity and temperature conditions using the recently acquired Thermotron SM-1.0-3200 environmental chamber.

#### **6.4.2 Kinematics of Droplet Drying**

While we tried to measure the temperature of the droplet edge and apex at high drying rate inside the low pressure chamber without any success, new and different non-invasive methods can be explored. Experimental studies can utilize a localized heating to control Marangoni flow and control sedimentation of particles by microgravity and centrifuge.

Studying the kinematics of droplets by conventional SDOCT is a relatively quick and easy to use technique and one of the difficulties is their limitations to measuring 2D velocity vectors because it is slow. The new in house built Ultra High Resolution OCT at Nottingham Trent [174] allows 3D scanning of a volume 1 $\times$ 1 $\times$ 1mm region in one second with 10  $\mu$ m sampling in the X-Y planes directions and 1-2  $\mu$ m resolution in the vertical direction (Z direction), which should make it possible to measure first measurements of 3D velocity vectors. If successful this would have wide implication in the understanding of the mechanisms of droplet drying. The kinematics of internal droplet flow using 3D-OCT can also be extended to non-spherical droplets to enable an experimental verification of Sáenz et al, [175] recent theoretical predictions of counter-rotating vortices in the droplets. OCT offers the possibility study the evaporation of binary miscible liquids and of volatile liquids and that it has the potential to be a very powerful technique in imaging droplets.

### **6.4.3 PS-PEO Droplet Drying**

In this study, charged PS microparticles were used which may affect the deposition patterns due to interactions with PEO polymer molecules. To understand further the effect of particles sizes on the drying of PEO droplets, neutral particles such as PMMA colloids in a suitable solvent can be explored. PMMA colloids are known to behave like hard spheres [176] so their interactions are very well controlled. Further studies may explore the effect of particle sizes on the drying of PEO droplets by varying the molecular weights of PEO polymer.

## Bibliography

- [1] Deegan, R.D., 2000. Pattern formation in drying drops. *Physical Review E*, 61 (1), 475.
- [2] Nadkarni, G., and Garoff, S., 1992. An investigation of microscopic aspects of contact angle hysteresis: Pinning of the contact line on a single defect. *EPL (Europhysics Letters)*, 20 (6), 523.
- [3] Chhasatia, V.H., and Sun, Y., 2011. Interaction of bi-dispersed particles with contact line in an evaporating colloidal drop. *Soft Matter*, 7 (21), 10135-10143.
- [4] Deegan, R.D., Bakajin, O., Dupont, T.F., Huber, G., Nagel, S.R. and Witten, T.A., 1997. Capillary flow as the cause of ring stains from dried liquid drops. *Nature*, 389 (6653), 827-829.
- [5] Adachi, E., Dimitrov, A.S. and Nagayama, K., 1995. Stripe patterns formed on a glass surface during droplet evaporation. *Langmuir*, 11 (4), 1057-1060.
- [6] Conway, J., Kornis, H. and Fisch, M.R., 1997. Evaporation kinematics of polystyrene bead suspensions. *Langmuir*, 13 (3), 426-431.
- [7] Fischer, B.J., 2002. Particle convection in an evaporating colloidal droplet. *Langmuir*, 18 (1), 60-67.
- [8] Truskett, V.N., and Stebe, K.J., 2003. Influence of surfactants on an evaporating drop: fluorescence images and particle deposition patterns. *Langmuir*, 19 (20), 8271-8279.
- [9] Kim, J., Ahn, S.I., Kim, J.H. and Zin, W., 2007. Evaporation of water droplets on polymer surfaces. *Langmuir*, 23 (11), 6163-6169.
- [10] Bourges-Monnier, C., and Shanahan, M., 1995. Influence of evaporation on contact angle. *Langmuir*, 11 (7), 2820-2829.

- [11] Picknett, R., and Bexon, R., 1977. The evaporation of sessile or pendant drops in still air. *Journal of Colloid and Interface Science*, 61 (2), 336-350.
- [12] Trantum, J.R., Baglia, M.L., Eagleton, Z.E., Mernaugh, R.L. and Haselton, F.R., 2014. Biosensor design based on Marangoni flow in an evaporating drop. *Lab on a Chip*, 14 (2), 315-324.
- [13] Kaneda, M., Ishizuka, H., Sakai, Y., Fukai, J., Yasutake, S. and Takahara, A., 2007. Film formation from polymer solution using inkjet printing method. *AIChE Journal*, 53 (5), 1100-1108.
- [14] Perelaer, J., Smith, P.J., Wijnen, M.M., van den Bosch, E., Eckardt, R., Ketelaars, P.H. and Schubert, U.S., 2009. Droplet tailoring using evaporative inkjet printing. *Macromolecular Chemistry and Physics*, 210 (5), 387-393.
- [15] Ko, H., Park, J., Shin, H. and Moon, J., 2004. Rapid self-assembly of monodisperse colloidal spheres in an ink-jet printed droplet. *Chemistry of Materials*, 16 (22), 4212-4215.
- [16] Kawase, T., Moriya, S., Newsome, C.J. and Shimoda, T., 2005. Inkjet printing of polymeric field-effect transistors and its applications. *Japanese Journal of Applied Physics*, 44 (6R), 3649.
- [17] Dugas, V., Broutin, J. and Souteyrand, E., 2005. Droplet evaporation study applied to DNA chip manufacturing. *Langmuir*, 21 (20), 9130-9136.
- [18] Smalyukh, I.I., Zribi, O.V., Butler, J.C., Lavrentovich, O.D. and Wong, G.C., 2006. Structure and dynamics of liquid crystalline pattern formation in drying droplets of DNA. *Physical Review Letters*, 96 (17), 177801.
- [19] Larson, R., Perkins, T., Smith, D. and Chu, S., 1999. The hydrodynamics of a DNA molecule in a flow field. In: *The hydrodynamics of a DNA molecule in a flow field. Flexible Polymer Chains in Elongational Flow*. Springer, 1999, pp. 259-282.

- [20] Wang, D., Liu, S., Trummer, B.J., Deng, C. and Wang, A., 2002. Carbohydrate microarrays for the recognition of cross-reactive molecular markers of microbes and host cells. *Nature Biotechnology*, 20 (3), 275-281.
- [21] Heim, T., Preuss, S., Gerstmayer, B., Bosio, A. and Blossey, R., 2005. Deposition from a drop: morphologies of unspecifically bound DNA. *Journal of Physics: Condensed Matter*, 17 (9), S703.
- [22] Carroll, G.T., Wang, D., Turro, N.J. and Koberstein, J.T., 2006. Photochemical micropatterning of carbohydrates on a surface. *Langmuir*, 22 (6), 2899-2905.
- [23] Monteux, C., and Lequeux, F., 2011. Packing and sorting colloids at the contact line of a drying drop. *Langmuir*, 27 (6), 2917-2922.
- [24] Zhang, D., Xie, Y., Mrozek, M.F., Ortiz, C., Davisson, V.J. and Ben-Amotz, D., 2003. Raman detection of proteomic analytes. *Analytical Chemistry*, 75 (21), 5703-5709.
- [25] Ondarcuhu, T., and Joachim, C., 1998. Drawing a single nanofibre over hundreds of microns. *EPL (Europhysics Letters)*, 42 (2), 215.
- [26] Chakrapani, N., Wei, B., Carrillo, A., Ajayan, P.M. and Kane, R.S., 2004. Capillarity-driven assembly of two-dimensional cellular carbon nanotube foams. *Proceedings of the National Academy of Sciences of the United States of America*, 101 (12), 4009-4012
- [27] Cuk, T., Troian, S.M., Hong, C.M. and Wagner, S., 2000. Using convective flow splitting for the direct printing of fine copper lines. *Applied Physics Letters*, 77 (13), 2063-2065.
- [28] Boneberg, J., Burmeister, F., Schäfle, C., Leiderer, P., Reim, D., Fery, A. and Herminghaus, S., 1997. The formation of nano-dot and nano-ring structures in colloidal monolayer lithography. *Langmuir*, 13 (26), 7080-7084.

- [29] Cosgrove, T., 2010. Colloid science: principles, methods and applications. John Wiley & Sons.
- [30] Barnes, G., and Gentle, I., 2011. Interfacial science: an introduction. Oxford University Press.
- [31] De Gennes, P., Brochard-Wyart, F. and Quéré, D., 2004. Capillarity and wetting phenomena: drops, bubbles, pearls, waves. Springer.
- [32] Butt, H., Golovko, D.S. and Bonaccorso, E., 2007. On the derivation of Young's equation for sessile drops: nonequilibrium effects due to evaporation. *The Journal of Physical Chemistry B*, 111 (19), 5277-5283.
- [33] Letellier, P., Mayaffre, A. and Turmine, M., 2007. Drop size effect on contact angle explained by nonextensive thermodynamics. Young's equation revisited. *Journal of Colloid and Interface Science*, 314 (2), 604-614.
- [34] Marmur, A., 2006. Soft contact: measurement and interpretation of contact angles. *Soft Matter*, 2 (1), 12-17.
- [35] Ruiz-Cabello, F.J.M., Kusumaatmaja, H., Rodríguez-Valverde, M.A., Yeomans, J. and Cabrerizo-Vílchez, M.A., 2009. Modeling the corrugation of the three-phase contact line perpendicular to a chemically striped substrate. *Langmuir*, 25 (14), 8357-8361.
- [36] Rodríguez-Valverde, M., Ruiz-Cabello, F. and Cabrerizo-Vilchez, M., 2008. Wetting on axially-patterned heterogeneous surfaces. *Advances in Colloid and Interface Science*, 138 (2), 84-100.
- [37] Eral, H., and Oh, J., 2013. Contact angle hysteresis: a review of fundamentals and applications. *Colloid and Polymer Science*, 291 (2), 247-260.
- [38] Moradi, S., Englezos, P. and Hatzikiriakos, S.G., 2013. Contact angle hysteresis: surface morphology effects. *Colloid and Polymer Science*, 291 (2), 317-328.

- [39] Neumann, A., and Good, R., 1972. Thermodynamics of contact angles. I. Heterogeneous solid surfaces. *Journal of Colloid and Interface Science*, 38 (2), 341-358.
- [40] Cwikel, D., Zhao, Q., Liu, C., Su, X. and Marmur, A., 2010. Comparing contact angle measurements and surface tension assessments of solid surfaces. *Langmuir*, 26 (19), 15289-15294.
- [41] Erbil, H.Y., McHale, G., Rowan, S. and Newton, M., 1999. Determination of the receding contact angle of sessile drops on polymer surfaces by evaporation. *Langmuir*, 15 (21), 7378-7385.
- [42] Hu, H., and Larson, R.G., 2002. Evaporation of a sessile droplet on a substrate. *The Journal of Physical Chemistry B*, 106 (6), 1334-1344.
- [43] Løvoll, G., Méheust, Y., Måløy, K.J., Aker, E. and Schmittbuhl, J., 2005. Competition of gravity, capillary and viscous forces during drainage in a two-dimensional porous medium, a pore scale study. *Energy*, 30 (6), 861-872.
- [44] Bonn, D., Eggers, J., Indekeu, J., Meunier, J. and Rolley, E., 2009. Wetting and spreading. *Reviews of Modern Physics*, 81 (2), 739.
- [45] Saada, M.A., Chikh, S. and Tadrist, L., 2012. Effect of substrate thickness and thermal conductivity on an evaporating sessile drop. In: *Journal of Physics: Conference Series*, IOP Publishing, pp. 012140.
- [46] Xu, W., Leeladhar, R., Kang, Y.T. and Choi, C., 2013. Evaporation kinetics of sessile water droplets on micropillared superhydrophobic surfaces. *Langmuir*, 29 (20), 6032-6041.
- [47] Birdi, K., Vu, D. and Winter, A., 1989. A study of the evaporation rates of small water drops placed on a solid surface. *The Journal of Physical Chemistry*, 93 (9), 3702-3703.
- [48] Green, D.W., 2008. *Perry's chemical engineers' handbook*. McGraw-hill New York.

- [49] Erbil, H.Y., 2012. Evaporation of pure liquid sessile and spherical suspended drops: A review. *Advances in Colloid and Interface Science*, 170 (1–2), 67-86.
- [50] Sobac, B., and Brutin, D., 2012. Thermal effects of the substrate on water droplet evaporation. *Physical Review E*, 86 (2), 021602.
- [51] Popov, Y.O., 2005. Evaporative deposition patterns: spatial dimensions of the deposit. *Physical Review E*, 71 (3), 036313.
- [52] Gleason, K., and Putnam, S.A., 2014. Microdroplet Evaporation with a Forced Pinned Contact Line. *Langmuir*, 30 (34), 10548-10555.
- [53] Schönfeld, F., Graf, K., Hardt, S. and Butt, H., 2008. Evaporation dynamics of sessile liquid drops in still air with constant contact radius. *International Journal of Heat and Mass Transfer*, 51 (13), 3696-3699.
- [54] Marmur, A., 1998. Contact-angle hysteresis on heterogeneous smooth surfaces: theoretical comparison of the captive bubble and drop methods. *Colloids and Surfaces A: Physicochemical and Engineering Aspects*, 136 (1), 209-215.
- [55] Zhang, X., and Mi, Y., 2009. Dynamics of a Stick– Jump Contact Line of Water Drops on a Strip Surface. *Langmuir*, 25 (5), 3212-3218.
- [56] Shanahan, M., and Sefiane, K., 2009. Kinetics of triple line motion during evaporation. *Contact Angle, Wettability and Adhesion*, 6, 19-31.
- [57] Chuang, Y., Chu, C., Lin, S. and Chen, L., 2014. Evaporation of water droplets on soft patterned surfaces. *Soft Matter*, 10 (19), 3394-3403.
- [58] Semenov, S., Starov, V., Rubio, R. and Velarde, M., 2010. Instantaneous distribution of fluxes in the course of evaporation of sessile liquid droplets: computer simulations. *Colloids and Surfaces A: Physicochemical and Engineering Aspects*, 372 (1), 127-134.

- [59] Semenov, S., Starov, V.M., Rubio, R.G. and Velarde, M.G., 2012. Computer simulations of evaporation of pinned sessile droplets: influence of kinetic effects. *Langmuir*, 28 (43), 15203-15211.
- [60] Starov, V., and Sefiane, K., 2009. On evaporation rate and interfacial temperature of volatile sessile drops. *Colloids and Surfaces A: Physicochemical and Engineering Aspects*, 333 (1), 170-174.
- [61] Dunn, G., Wilson, S., Duffy, B., David, S. and Sefiane, K., 2008. A mathematical model for the evaporation of a thin sessile liquid droplet: Comparison between experiment and theory. *Colloids and Surfaces A: Physicochemical and Engineering Aspects*, 323 (1), 50-55.
- [62] Girard, F., Antoni, M. and Sefiane, K., 2008. On the effect of Marangoni flow on evaporation rates of heated water drops. *Langmuir*, 24 (17), 9207-9210.
- [63] Girard, F., and Antoni, M., 2008. Influence of substrate heating on the evaporation dynamics of pinned water droplets. *Langmuir*, 24 (20), 11342-11345.
- [64] Snegirev, A.Y., 2013. Transient temperature gradient in a single-component vaporizing droplet. *International Journal of Heat and Mass Transfer*, 65, 80-94.
- [65] Bringuier, E., and Bourdon, A., 2003. Colloid transport in nonuniform temperature. *Physical Review E*, 67 (1), 011404.
- [66] Duhr, S., and Braun, D., 2006. Why molecules move along a temperature gradient. *Proceedings of the National Academy of Sciences of the United States of America*, 103 (52), 19678-19682.
- [67] Duhr, S., and Braun, D., 2006. Thermophoretic depletion follows Boltzmann distribution. *Physical Review Letters*, 96 (16), 168301.

- [68] Giglio, M., and Vendramini, A., 1977. Soret-type motion of macromolecules in solution. *Physical Review Letters*, 38 (1), 26.
- [69] Putnam, S.A., and Cahill, D.G., 2005. Transport of nanoscale latex spheres in a temperature gradient. *Langmuir*, 21 (12), 5317-5323.
- [70] Iacopini, S., and Piazza, R., 2003. Thermophoresis in protein solutions. *EPL (Europhysics Letters)*, 63 (2), 247.
- [71] Ghofraniha, N., Ruocco, G. and Conti, C., 2009. Collective thermal diffusion of silica colloids studied by nonlinear optics. *Langmuir*, 25 (21), 12495-12500.
- [72] Würger, A., 2009. Temperature dependence of the soret motion in colloids. *Langmuir*, 25 (12), 6696-6701.
- [73] Hu, H., and Larson, R.G., 2005. Analysis of the microfluid flow in an evaporating sessile droplet. *Langmuir*, 21 (9), 3963-3971.
- [74] Tam, D., von ARNIM, V., McKinley, G. and Hosoi, A., 2009. Marangoni convection in droplets on superhydrophobic surfaces. *Journal of Fluid Mechanics*, 624, 101-123.
- [75] Barmi, M.R., and Meinhart, C.D., 2014. Convective Flows in Evaporating Sessile Droplets. *The Journal of Physical Chemistry B*, 118 (9), 2414-2421.
- [76] Bringuier, E., and Bourdon, A., 2003. Colloid transport in nonuniform temperature. *Physical Review E*, 67 (1), 011404.
- [77] Kishikawa, Y., Wiegand, S. and Kita, R., 2010. Temperature dependence of soret coefficient in aqueous and nonaqueous solutions of pullulan. *Biomacromolecules*, 11 (3), 740-747.

- [78] Bhardwaj, R., Fang, X., Somasundaran, P. and Attinger, D., 2010. Self-assembly of colloidal particles from evaporating droplets: role of DLVO interactions and proposition of a phase diagram. *Langmuir*, 26 (11), 7833-7842.
- [79] Hu, H., and Larson, R.G., 2005. Analysis of the effects of Marangoni stresses on the microflow in an evaporating sessile droplet. *Langmuir*, 21 (9), 3972-3980.
- [80] Still, T., Yunker, P.J. and Yodh, A.G., 2012. Surfactant-induced Marangoni eddies alter the coffee-rings of evaporating colloidal drops. *Langmuir*, 28 (11), 4984-4988.
- [81] Sempels, W., De Dier, R., Mizuno, H., Hofkens, J. and Vermant, J., 2013. Auto-production of biosurfactants reverses the coffee ring effect in a bacterial system. *Nature Communications*, 4, 1757.
- [82] Ristenpart, W., Kim, P., Domingues, C., Wan, J. and Stone, H., 2007. Influence of substrate conductivity on circulation reversal in evaporating drops. *Physical Review Letters*, 99 (23), 234502.
- [83] Sefiane, K., and Bennacer, R., 2011. An expression for droplet evaporation incorporating thermal effects. *Journal of Fluid Mechanics*, 667, 260-271.
- [84] Sefiane, K., Wilson, S., David, S., Dunn, G. and Duffy, B., 2009. On the effect of the atmosphere on the evaporation of sessile droplets of water. *Physics of Fluids (1994-Present)*, 21 (6), 062101.
- [85] Sommer, A.P., Ben-Moshe, M. and Magdassi, S., 2004. Size-discriminative self-assembly of nanospheres in evaporating drops. *The Journal of Physical Chemistry B*, 108 (1), 8-10.
- [86] Shmuylovich, L., Shen, A.Q. and Stone, H.A., 2002. Surface morphology of drying latex films: multiple ring formation. *Langmuir*, 18 (9), 3441-3445.

- [87] Keseroğlu, K., and Çulha, M., 2011. Assembly of nanoparticles at the contact line of a drying droplet under the influence of a dipped tip. *Journal of Colloid and Interface Science*, 360 (1), 8-14.
- [88] Bhardwaj, R., Fang, X. and Attinger, D., 2009. Pattern formation during the evaporation of a colloidal nanoliter drop: a numerical and experimental study. *New Journal of Physics*, 11 (7), 075020.
- [89] Sommer, A.P., 2004. Suffocation of nerve fibers by living nanovesicles: A model simulation-Part II. *Journal of Proteome Research*, 3 (5), 1086-1088.
- [90] Deegan, R.D., Bakajin, O., Dupont, T.F., Huber, G., Nagel, S.R. and Witten, T.A., 2000. Contact line deposits in an evaporating drop. *Physical Review E*, 62 (1), 756.
- [91] Dmitriev, A., and Makarov, P., 2015. On liquid evaporation from droplets of colloidal solutions of SiO<sub>2</sub> and Fe<sub>2</sub>O<sub>3</sub> nanoparticles. *Colloid Journal*, 77 (2), 135-142.
- [92] Nguyen, T.A., and Nguyen, A.V., 2012. Increased evaporation kinetics of sessile droplets by using nanoparticles. *Langmuir*, 28 (49), 16725-16728.
- [93] Maenosono, S., Dushkin, C., Saita, S. and Yamaguchi, Y., 1999. Growth of a semiconductor nanoparticle ring during the drying of a suspension droplet. *Langmuir*, 15 (4), 957-965.
- [94] Deegan, R.D., 1998. Deposition at pinned and depinned contact lines: pattern formation and applications.
- [95] Marín, Á.G., Gelderblom, H., Lohse, D. and Snoeijer, J.H., 2011. Order-to-disorder transition in ring-shaped colloidal stains. *Physical Review Letters*, 107 (8), 085502.
- [96] Askounis, A., Sefiane, K., Koutsos, V. and Shanahan, M.E., 2013. Structural transitions in a ring stain created at the contact line of evaporating nanosuspension sessile drops. *Physical Review E*, 87 (1), 012301.

- [97] Zhong, X., and Duan, F., 2014. Evaporation of Sessile Droplets Affected by Graphite Nanoparticles and Binary Base Fluids. *The Journal of Physical Chemistry B*.
- [98] Yunker, P.J., Still, T., Lohr, M.A. and Yodh, A., 2011. Suppression of the coffee-ring effect by shape-dependent capillary interactions. *Nature*, 476 (7360), 308-311.
- [99] Yunker, P.J., Lohr, M.A., Still, T., Borodin, A., Durian, D.J. and Yodh, A.G., 2013. Effects of particle shape on growth dynamics at edges of evaporating drops of colloidal suspensions. *Physical Review Letters*, 110 (3), 035501.
- [100] Weon, B.M., and Je, J.H., 2010. Capillary force repels coffee-ring effect. *Physical Review E*, 82 (1), 015305.
- [101] Hu, H., and Larson, R.G., 2006. Marangoni effect reverses coffee-ring depositions. *The Journal of Physical Chemistry B*, 110 (14), 7090-7094.
- [102] Eral, H.B., Augustine, D.M., Duits, M.H. and Mugele, F., 2011. Suppressing the coffee stain effect: how to control colloidal self-assembly in evaporating drops using electrowetting. *Soft Matter*, 7 (10), 4954-4958.
- [103] Shen, X., Ho, C. and Wong, T., 2010. Minimal size of coffee ring structure. *The Journal of Physical Chemistry B*, 114 (16), 5269-5274.
- [104] Chhasatia, V.H., Joshi, A.S. and Sun, Y., 2010. Effect of relative humidity on contact angle and particle deposition morphology of an evaporating colloidal drop. *Applied Physics Letters*, 97 (23), 231909.
- [105] Bou Zeid, W., and Brutin, D., 2013. Influence of relative humidity on spreading, pattern formation and adhesion of a drying drop of whole blood. *Colloids and Surfaces A: Physicochemical and Engineering Aspects*, 430, 1-7.
- [106] Brutin, D., 2013. Influence of relative humidity and nano-particle concentration on pattern formation and evaporation rate of pinned drying

- drops of nanofluids. *Colloids and Surfaces A: Physicochemical and Engineering Aspects*, 429, 112-120.
- [107] Iaelachvili, J.N., 2011. *Intermolecular and surface forces: revised third edition*. Academic press.
- [108] Sempels, W., De Dier, R., Mizuno, H., Hofkens, J. and Vermant, J., 2013. Auto-production of biosurfactants reverses the coffee ring effect in a bacterial system. *Nature Communications*, 4, 1757.
- [109] Iaelachvili, J.N., 2011. *Intermolecular and surface forces: revised third edition*. Academic press.
- [110] Verwey, E., and Overbeek, J.T.G., 2001. *Theory of the stability of lyophobic colloids*, 1948. Amsterdam: Elsevier, .
- [111] Elimelech, M., Jia, X., Gregory, J. and Williams, R., 1998. *Particle deposition & aggregation: measurement, modelling and simulation*. Butterworth-Heinemann.
- [112] Deshiikan, S., and Papadopoulos, K., 1998. Modified Booth equation for the calculation of zeta potential. *Colloid and Polymer Science*, 276 (2), 117-124.
- [113] Kuncicky, D.M., and Velev, O.D., 2008. Surface-guided templating of particle assemblies inside drying sessile droplets. *Langmuir*, 24 (4), 1371-1380.
- [114] Jung, J., Kim, Y.W., Yoo, J.Y., Koo, J. and Kang, Y.T., 2010. Forces acting on a single particle in an evaporating sessile droplet on a hydrophilic surface. *Analytical Chemistry*, 82 (3), 784-788.
- [115] Yan, Q., Gao, L., Sharma, V., Chiang, Y. and Wong, C., 2008. Particle and substrate charge effects on colloidal self-assembly in a sessile drop. *Langmuir*, 24 (20), 11518-11522.

- [116] Cowie, J.M., 1991. *Polymers: chemistry and physics of modern materials*. CRC Press.
- [117] Rubinstein, M., and Colby, R., 2003. *Polymers Physics*. Oxford.
- [118] Jones, R.A., *Soft Condensed Matter* 2002.
- [119] Fried, J., 2003. *Polymer science and technology*. Pearson Education.
- [120] Seymour, R.B., and Carraher, C.E., 1981. *Polymer chemistry*. Marcel Dekker.
- [121] Ho, D.L., Hammouda, B., Kline, S.R. and Chen, W., 2006. Unusual phase behavior in mixtures of poly (ethylene oxide) and ethyl alcohol. *Journal of Polymer Science Part B: Polymer Physics*, 44 (3), 557-564.
- [122] Bailey, F.J., 2012. *Poly (ethylene oxide)*. Elsevier.
- [123] Mark, J.E., 2007. *Physical properties of polymers handbook*. Springer.
- [124] Jawalkar, S.S., Adoor, S.G., Sairam, M., Nadagouda, M.N. and Aminabhavi, T.M., 2005. Molecular modeling on the binary blend compatibility of poly (vinyl alcohol) and poly (methyl methacrylate): an atomistic simulation and thermodynamic approach. *The Journal of Physical Chemistry B*, 109 (32), 15611-15620.
- [125] Gupta, J., Nunes, C., Vyas, S. and Jonnalagadda, S., 2011. Prediction of solubility parameters and miscibility of pharmaceutical compounds by molecular dynamics simulations. *The Journal of Physical Chemistry B*, 115 (9), 2014-2023.
- [126] Layec, Y., and Layec-Raphalen, M., 1983. Instability of dilute poly (ethylene-oxide) solutions. *Journal De Physique Lettres*, 44 (3), 121-128.

- [127] Ho, D.L., Hammouda, B. and Kline, S.R., 2003. Clustering of poly (ethylene oxide) in water revisited. *Journal of Polymer Science Part B: Polymer Physics*, 41 (1), 135-138.
- [128] Yu, D.M., Amidon, G.L., Weiner, N.D. and Goldberg, A.H., 1994. Viscoelastic properties of poly (ethylene oxide) solution. *Journal of Pharmaceutical Sciences*, 83 (10), 1443-1449.
- [129] Torres, M.F., Müller, A.J., Szidarovszky, M.A. and Sáez, A.E., 2008. Shear and extensional rheology of solutions of mixtures of poly (ethylene oxide) and anionic surfactants in ionic environments. *Journal of Colloid and Interface Science*, 326 (1), 254-260.
- [130] Kalashnikov, V., 1994. Shear-rate dependent viscosity of dilute polymer solutions. *Journal of Rheology (1978-Present)*, 38 (5), 1385-1403.
- [131] Bossard, F., El Kissi, N., D'Aprèa, A., Alloin, F., Sanchez, J. and Dufresne, A., 2010. Influence of dispersion procedure on rheological properties of aqueous solutions of high molecular weight PEO. *Rheologica Acta*, 49 (5), 529-540.
- [132] Dupas, A., Hénaut, I., Argillier, J. and Aubry, T., 2012. Mechanical degradation onset of polyethylene oxide used as a hydrosoluble model polymer for enhanced oil recovery. *Oil & Gas Science and Technology—Revue d'IFP Energies Nouvelles*, 67 (6), 931-940.
- [133] Sung, J.H., Lim, S.T., Am Kim, C., Chung, H. and Choi, H.J., 2004. Mechanical degradation kinetics of poly (ethylene oxide) in a turbulent flow. *Korea-Australia Rheology Journal*, 16 (2), 57-62.
- [134] Odell, J.A., Muller, A.J., Narh, K.A. and Keller, A., 1990. Degradation of polymer solutions in extensional flows. *Macromolecules*, 23 (12), 3092-3103.

- [135] Minoura, Y., Kasuya, T., Kawamura, S. and Nakano, A., 1967. Degradation of poly (ethylene oxide) by high-speed stirring. *Journal of Polymer Science Part A-2: Polymer Physics*, 5 (1), 125-142.
- [136] Willmer, D., Baldwin, K.A., Kwartnik, C. and Fairhurst, D.J., 2010. Growth of solid conical structures during multistage drying of sessile poly (ethylene oxide) droplets. *Physical Chemistry Chemical Physics*, 12 (16), 3998-4004.
- [137] Baldwin, K.A., Granjard, M., Willmer, D.I., Sefiane, K. and Fairhurst, D.J., 2011. Drying and deposition of poly (ethylene oxide) droplets determined by Péclet number. *Soft Matter*, 7 (17), 7819-7826.
- [138] Dasgupta, B.R., Tee, S., Crocker, J.C., Frisken, B. and Weitz, D., 2002. Microrheology of polyethylene oxide using diffusing wave spectroscopy and single scattering. *Physical Review E*, 65 (5), 051505.
- [139] Hu, Y., Zhou, Q., Wang, Y., Song, Y. and Cui, L., 2013. Formation mechanism of micro-flows in aqueous poly (ethylene oxide) droplets on a substrate at different temperatures. *Petroleum Science*, 10 (2), 262-268.
- [140] Choi, Y., Han, J. and Kim, C., 2011. Pattern formation in drying of particle-laden sessile drops of polymer solutions on solid substrates. *Korean Journal of Chemical Engineering*, 28 (11), 2130-2136.
- [141] Deegan, R.D., 1998. Deposition at pinned and depinned contact lines: pattern formation and applications.
- [142] Huang, D., Swanson, E.A., Lin, C.P., Schuman, J.S., Stinson, W.G., Chang, W., Hee, M.R., Flotte, T., Gregory, K. and Puliafito, C.A., 1991. Optical coherence tomography. *Science (New York, N.Y.)*, 254 (5035), 1178-1181.
- [143] Fujimoto, J.G., et al., 2000. Optical coherence tomography: an emerging technology for biomedical imaging and optical biopsy. *Neoplasia*, 2 (1), 9-25.

- [144] Boppart, S.A., 2003. Optical coherence tomography: technology and applications for neuroimaging. *Psychophysiology*, 40 (4), 529-541.
- [145] Trantum, J.R., Eagleton, Z.E., Patil, C.A., Tucker-Schwartz, J.M., Baglia, M.L., Skala, M.C. and Haselton, F.R., 2013. Cross-sectional tracking of particle motion in evaporating drops: Flow fields and interfacial accumulation. *Langmuir*, 29 (21), 6221-6231.
- [146] Jonas, S., Bhattacharya, D., Khokha, M.K. and Choma, M.A., 2011. Microfluidic characterization of cilia-driven fluid flow using optical coherence tomography-based particle tracking velocimetry. *Biomedical Optics Express*, 2 (7), 2022-2034.
- [147] Yaqoob, Z., Wu, J. and Yang, C., 2005. Spectral domain optical coherence tomography: a better OCT imaging strategy. *Biotechniques*, 39.
- [148] Manukyan, S., Sauer, H.M., Roisman, I.V., Baldwin, K.A., Fairhurst, D.J., Liang, H., Venzmer, J. and Tropea, C., 2013. Imaging internal flows in a drying sessile polymer dispersion drop using spectral radar optical coherence tomography (SR-OCT). *Journal of Colloid and Interface Science*, 395, 287-293.
- [149] Brevis, W., Niño, Y. and Jirka, G., 2011. Integrating cross-correlation and relaxation algorithms for particle tracking velocimetry. *Experiments in Fluids*, 50 (1), 135-147
- [150] Thielicke, W. & Stamhuis, E. J. (2014): PIVlab - Time-Resolved Digital Particle Image Velocimetry Tool for MATLAB (version: 1.35). <http://dx.doi.org/10.6084/m9.figshare.1092508>
- [151] Thielicke, W. (2014): The Flapping Flight of Birds - Analysis and Application. Phd thesis, Rijksuniversiteit Groningen.

- [152] Morgan, G.A., Leech, N. and Barret, K., 2005. SPSS For Intermediate Statistics: Use and Interpretations.
- [153] Rowan, S., Newton, M. and McHale, G., 1995. Evaporation of microdroplets and the wetting of solid surfaces. *The Journal of Physical Chemistry*, 99 (35), 13268-13271.
- [154] Askounis, A., Sefiane, K., Koutsos, V. and Shanahan, M.E., 2014. Effect of particle geometry on triple line motion of nano-fluid drops and deposit nano-structuring. *Advances in Colloid and Interface Science*,
- [155] Abramchuk, S., Khokhlov, A., Iwataki, T., Oana, H. and Yoshikawa, K., 2001. Direct observation of DNA molecules in a convection flow of a drying droplet. *EPL (Europhysics Letters)*, 55 (2), 294.
- [156] Jing, J., Reed, J., Huang, J., Hu, X., Clarke, V., Edington, J., Housman, D., Anantharaman, T.S., Huff, E.J., Mishra, B., Porter, B., Shenker, A., Wolfson, E., Hiort, C., Kantor, R., Aston, C. and Schwartz, D.C., 1998. Automated high resolution optical mapping using arrayed, fluid-fixed DNA molecules. *Proceedings of the National Academy of Sciences of the United States of America*, 95 (14), 8046-8051.
- [157] Rasband, W., Image, J. and US National Institutes of Health, Bethesda, Maryland, USA: 1997-2011. <http://Imagej.Nih.gov/ij>. Accessed online on 09/05/2015
- [158] Vella, D., and Mahadevan, L., 2005. The "cheerios effect". *American Journal of Physics*, 73 (9), 817-825.
- [159] Kralchevsky, P.A., and Nagayama, K., 2000. Capillary interactions between particles bound to interfaces, liquid films and biomembranes. *Advances in Colloid and Interface Science*, 85 (2), 145-192.

- [160] Li, Y., Lv, C., Li, Z., Quéré, D. and Zheng, Q., 2015. From coffee rings to coffee eyes. *Soft Matter*.
- [161] Parsa, M., Harmand, S., Sefiane, K., Biggerelle, M. and Deltombe, R., 2015. Effect of Substrate Temperature on Pattern Formation of Nanoparticles from Volatile Drops. *Langmuir*, 31 (11), 3354-3367.
- [162] Foley, A.L., 1910. The Temperature Coefficient of the Surface Tension of Water. In: *Proceedings of the Indiana Academy of Science*, pp. 175-180.
- [163] Sigma Aldrich. [http://www.sigmaaldrich.com/content/dam/sigmaaldrich/docs/Sigma/Product\\_Information\\_Sheet/2/lb1pis.pdf](http://www.sigmaaldrich.com/content/dam/sigmaaldrich/docs/Sigma/Product_Information_Sheet/2/lb1pis.pdf). Accessed online on 15/09/2015
- [164] Pearson, J., 1958. On convection cells induced by surface tension. *Journal of Fluid Mechanics*, 4 (05), 489-500.
- [165] Thokchom, A.K., Swaminathan, R. and Singh, A., 2014. Fluid Flow and Particle Dynamics Inside an Evaporating Droplet Containing Live Bacteria Displaying Chemotaxis. *Langmuir*, 30 (41), 12144-12153.
- [166] Askounis, A., Sefiane, K., Koutsos, V. and Shanahan, M.E., 2014. The effect of evaporation kinetics on nanoparticle structuring within contact line deposits of volatile drops. *Colloids and Surfaces A: Physicochemical and Engineering Aspects*, 441, 855-866
- [167] Li, G., 2007. *Structuring of Polymer Surface by Evaporation of Sessile Microdrops*, .
- [168] Mamalis, D., Koutsos, V., Sefiane, K., Kagkoura, A., Kalloudis, M. and Shanahan, M.E., 2015. Effect of poly (ethylene oxide) molecular weight on the pinning and pillar formation of evaporating sessile droplets: The role of the interface. *Langmuir*.
- [169] Cui, L., Zhang, J., Zhang, X., Huang, L., Wang, Z., Li, Y., Gao, H., Zhu, S., Wang, T. and Yang, B., 2012. Suppression of the coffee ring effect by

- hydrosoluble polymer additives. *ACS Applied Materials & Interfaces*, 4 (5), 2775-2780.
- [170] Zhang, Y., Liu, Z., Zang, D., Qian, Y. and Lin, K., 2013. Pattern transition and sluggish cracking of colloidal droplet deposition with polymer additives. *Science China Physics, Mechanics and Astronomy*, 56 (9), 1712-1718.
- [171] Chen, L., and Bonaccorso, E., 2014. Effects of surface wettability and liquid viscosity on the dynamic wetting of individual drops. *Physical Review E*, 90 (2), 022401
- [172] Perelaer, J., Smith, P.J., Hendriks, C.E., van den Berg, Antje MJ and Schubert, U.S., 2008. The preferential deposition of silica microparticles at the boundary of inkjet printed droplets. *Soft Matter*, 4 (5), 1072-1078.
- [173] Turner, A. (2015): The self-assembly of microstructures for nanoscale application. MSc thesis, Nottingham Trent University.
- [174] Cheung, C., Spring, M. and Liang, H., 2015. Ultra-high resolution Fourier domain optical coherence tomography for old master paintings. *Optics Express*, 23 (8), 10145-10157.
- [175] Sáenz, P., Sefiane, K., Kim, J., Matar, O. and Valluri, P., 2015. Evaporation of sessile drops: a three-dimensional approach. *Journal of Fluid Mechanics*, 772, 705-739.
- [176] Wilson, L., Harrison, A., Schofield, A., Arlt, J. and Poon, W., 2009. Passive and active microrheology of hard-sphere colloids. *The Journal of Physical Chemistry B*, 113 (12), 3806-3812.
- [177] McHale, G., and Newton, M.I., 2002. Frenkel's method and the dynamic wetting of heterogeneous planar surfaces. *Colloids and Surfaces A: Physicochemical and Engineering Aspects*, 206 (1), 193-201.
- [178] Shikhmurzaev, Y.D., 2008. On Young's (1805) equation and Finn's (2006)'counterexample'. *Physics Letters A*, 372 (5), 704-707.

## Appendix A: Derivation of the Young Equation

For smooth and chemically homogeneous planar surfaces, two approaches to the equilibrium contact angle  $\theta$ , exist namely (a) force balance and (b) minimum surface free energy [31, 177]. The former approach will be used to derive the Young's equation.

From figure (A.1), the interfacial surface tensions are regarded as force per unit length. At equilibrium, the horizontal forces balance at the contact line requires that  $\Sigma F_x = 0$  yielding equation (A.1) and the vertical forces balance  $\Sigma F_y = 0$ . The vertical component of the liquid-gas surface tension is balanced by reaction force  $F_R$  exerted on a contact line by the solid [31, 178] and hence  $F_R = \gamma_{lg} \sin\theta$ .

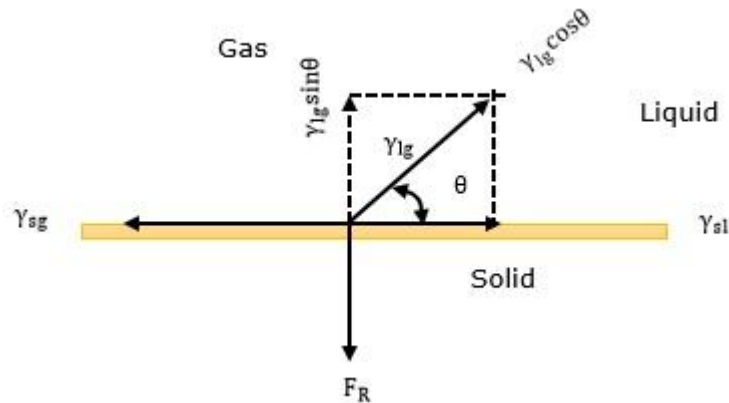


Figure A.1: Schematic illustration of an equilibrium contact angle in terms of force balance.

$$\gamma_{sg} = \gamma_{sl} + \gamma_{lg} \cos\theta \quad (\text{A.1})$$

Rearrangement equation (A.1) lead to a well known the Young equation (A.2).

$$\cos\theta = \frac{\gamma_{sg} - \gamma_{sl}}{\gamma_{lg}} \quad (\text{A.2})$$

## Appendix B: Radial profile plotting using Image J

The radial profile plugin embedded in Image J software was then used to analyse the images by producing a profile plot of normalized integrated intensities around circles as a function of distance from a reference point in the image [157]. On image opened in Image J software, the reference point represents the centre of the region of interest as shown in figure B.1.

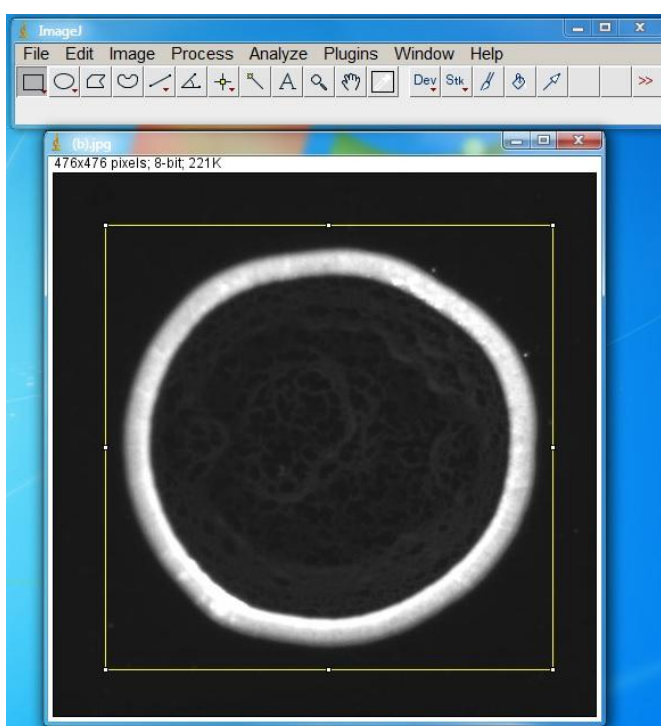


Figure B.1: Defining the region of interest in Image J software.

The position of this reference point could be modified in a dialog box. By running the radial profile plug in, figure B.2 was produced. The intensity at any given distance from the point represents the sum of the pixel values around a circle. This circle has the point as its center and the distance from the point as radius. The integrated intensity is divided by the number of pixels in the circle that was also part of the image, yielding normalized comparable values. The profile x-axis was

plotted as pixel values or as values in millimeters by calibrating the image. It is of note that this method measures the width of the ring by calibrating the images and does not allow the measurement of the height of the ring. Figure B.3 show an example of the radial profile obtained from figure B.2.

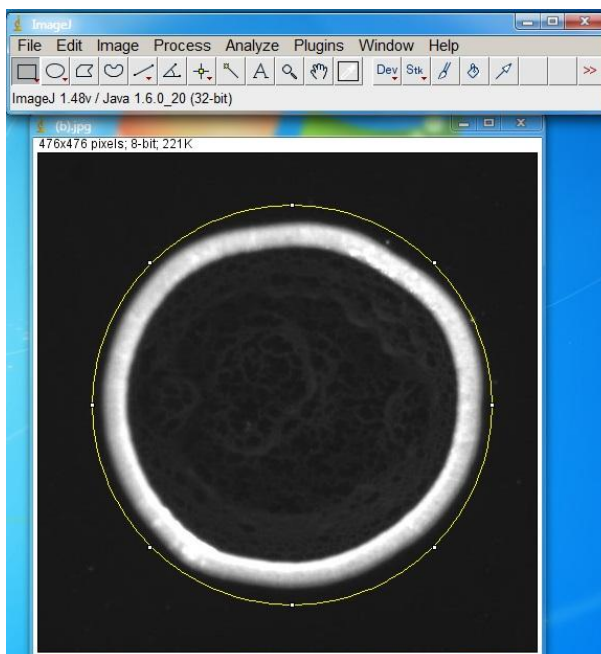


Figure B.2: The circle bounding the region whose integrated intensity was to be determined.

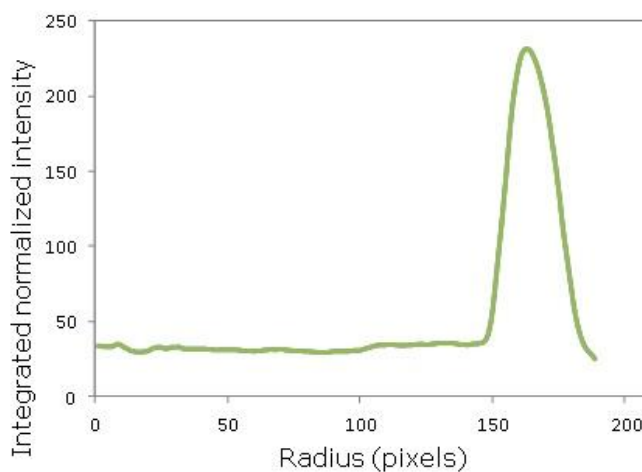


Figure B.3: Radial profile plugin plot radial profile versus radius for 0.5 $\mu$ m particles dried at 0.6 nL/s in upright orientation.

## Appendix C: Derivation of ring stain power law predictions

Consider a pinned droplet of radius  $R$  containing microparticles making a contact angle  $\theta$  with a glass cover slip as shown in figure C.1.

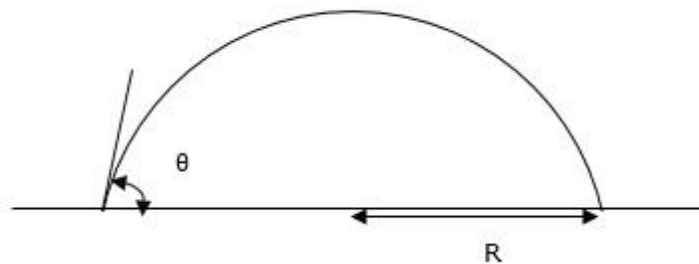


Figure C.1: Schematic illustration of a droplet containing microparticles on a glass cover slip

In order to derive the relationship between the ring width/height ( $w_r / h_r$ ) with initial concentration  $c_0$  (in  $\text{g}/\text{cm}^3$ ) of the particles by in droplet, the following assumptions are made:

- a) All the particles end up in the ring,
- b) The cross-sectional shape of the deposit does not depend on the initial concentration  $c_0$  of the particles in the droplet.
- c) The packing fraction  $\phi$  of the final deposit is constant.

Let the initial volume of the droplet and initial concentration of the microparticles in the droplet is be  $V_0$  and  $c_0$  respectively. Then the total mass of the microparticles will be  $V_0 c_0$  while the corresponding total volume of a dried deposit given by

$V_o c_o \phi / \rho$  where  $\rho$  is the density of the microparticles. Assuming all microparticles end up in the ring after evaporation of the droplet, the final deposits takes the shape shown in figure C.2 where  $h_r$ ,  $w_r$  and  $r$  is the ring height, ring width and inner radius respectively.

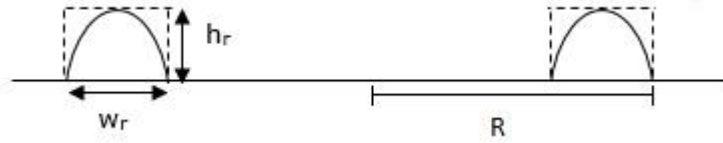


Figure C.2: Schematic illustration final deposit shape after droplet evaporation. The dashed line shows the theoretical prediction of the ring dimensions.

The volume of circular ring  $V_{ring}$  is given by equation (C.1) as :

$$V_{ring} = \text{Area} \times \text{height} \quad (C.1)$$

$$V_{ring} = (w_r \times 2\pi R)(h_r) \quad (C.2)$$

Assuming  $w_r \propto h_r$  then  $w_r = kh_r$  where  $k$  is a constant and upon substituting in equation (C.2), equation (C.3) is obtained.

$$V_{ring} = (k_r h_r^2)(2\pi R) \quad (C.3)$$

Equation (C.3) can be written in terms of the initial volume of the droplet and initial concentration of the microparticles as given in equation (C.4).

$$\frac{V_o c_o \phi}{\rho} = (k_r h_r^2)(2\pi R) \quad (C.4)$$

Hence the height of the ring  $h_r$  is given as ;

$$h_r^2 = \frac{V_o \phi}{2\pi R \rho k_r} \times c_o \quad (C.5)$$

Since the droplet is considered to be pinned in the entire droplet life time and that  $k_r$ ,  $\rho$  and  $V_o$  are constant, it follows that  $h_r^2 \propto c_o$  and since  $w_r \propto h_r$  then equations (C.6) and (C.7) are obtained which are the basis of simple argument.

$$h_r \propto \sqrt{c_o} \tag{C.6}$$

$$w_r \propto \sqrt{c_o} \tag{C.7}$$

## Appendix D: Determination of coefficient of skewness

The macros embedded in excel was used to determine the mean, mode, standard deviation and hence the coefficient of skewness using data in figure 2.14 and 2.15 in section 2.4.2. The LHS and RHS coefficient of skewness was determined separately and averaged. Figure D.1 and D.2 show the excel screen shot how the coefficients of skewness were obtained.

BU	BV	BW	BX
<b>4% PS</b>	<b>1.6% PEO (LHS)</b>	<b>1.6% PEO (RHS)</b>	<b>Radius (<math>\mu\text{m}</math>)</b>
<b>Number</b>	<b>98860455.2</b>	<b>106958420.2</b>	
<b>Sum</b>	<b>36491095560</b>	<b>40230393409</b>	
<b>Mean</b>	<b>369.1172116</b>	<b>376.1311483</b>	
<b>Mode</b>	<b>548.21</b>	<b>538.98</b>	
<b>STDEV</b>	<b>202.1697353</b>	<b>200.5391458</b>	
<b>skew</b>	<b>-0.885853603</b>	<b>-0.812055178</b>	
<b>SKEW2</b>	<b>-0.644167863</b>	<b>-0.697022405</b>	
0	53611.3	53640.8	0.38
1	53581.9	53712.1	1.15
2	53510.6	53866.9	1.92
3	53481.1	54105.3	2.69
4	53451.7	54385.4	3.46
5	53505.7	54665.5	4.23
6	53643.4	54945.7	5
7	53822.8	55100.5	5.77
8	54002.2	55171.8	6.54
9	54139.8	55159.4	7.31
10	54152.1	55063.6	8.08



Coefficient of skewness for LHS peak



Coefficient of skewness for RHS peak

Figure D:1: A screen shot showing the determination of the coefficient of skewness for deposit containing  $c_1 = 1.6\%$  (PEO) and  $c_0 = 4\%$  ( $0.5\mu\text{m}$  PS particles) giving a Coefficient Skewness  $-0.64$  (LHS) and  $-0.70$  (RHS). The average Coefficient of skewness is  $\sim -0.67$ .

AT	AU	AV	AW
<b>4% PS</b>	<b>9.6% PEO (LHS)</b>	<b>9.6% PEO (RHS)</b>	<b>Radius (<math>\mu\text{m}</math>)</b>
<b>Number</b>	<b>752150222.1</b>	<b>759114781.7</b>	
<b>Sum</b>	<b>1.90226E+11</b>	<b>1.94418E+11</b>	
<b>Mean</b>	<b>252.9094594</b>	<b>256.1111804</b>	
<b>Mode</b>	<b>6.93</b>	<b>52.32</b>	
<b>STDEV</b>	<b>198.7910818</b>	<b>202.4606509</b>	
<b>skew</b>	<b>1.237376733</b>	<b>1.006571793</b>	
<b>SKEW2</b>	<b>0.284014987</b>	<b>0.294245483</b>	
0	1052137.9	1049055.3	0.77
1	1053929.9	1047722.8	1.54
2	1055763.6	1046599.3	2.31
3	1057513.8	1045726.4	3.08
4	1058846.3	1045020.7	3.85
5	1059760.9	1044523.8	4.62
6	1060341.3	1044194.1	5.39
7	1060712.8	1043947.9	6.16
8	1060833.6	1043827.1	6.93
9	1060703.9	1043664.4	7.69
10	1060281.6	1043501.8	8.46

Coefficient of  
skewness for LHS  
half of the peak

Coefficient of  
skewness for RHS  
half of the peak

Figure D.1: A screen shot showing the determination of the coefficient of skewness for deposit containing  $c_1 = 9.6\%$  (PEO) and  $c_0 = 4\%$  ( $5\mu\text{m}$  PS particles) giving a Coefficient Skewness  $+0.28$  (LHS) and  $+0.29$  (RHS). The average Coefficient of skewness is  $\sim +0.29$

## **Publications**

1. Msambwa, Y., Fairhurst, D.J. and Ouali, F., 2013. How robust is the ring stain for evaporating suspension droplets? *Interfacial Phenomena and Heat Transfer*, 1 (3).
2. Msambwa, Y., Shackleford, A., Ouali, F. and Fairhurst, D., 2016. Controlling and characterising the deposits from polymer droplets containing microparticles and salt. *The European Physical Journal E*, 39 (2), 1-8.

The copies of these publications have been attached in the next page.

# HOW ROBUST IS THE RING STAIN FOR EVAPORATING SUSPENSION DROPLETS?

Y. Msambwa, D. J. Fairhurst, & F. Ouali\*

School of Science and Technology, Nottingham Trent University, Clifton Lane, Nottingham, NG11 8NS, United Kingdom

\*Address all correspondence to F. Ouali, E-mail: fouzia.ouali@ntu.ac.uk

*The ring stain is commonly seen when droplets containing particles, such as coffee, are left to dry on a surface: a pinned contact line leads to outward radial flow, which is enhanced by the diverging evaporative flux at the contact line. As shown by Deegan et al. (1997) particles are swept outwards in this flow and create a ring which grows according to a simple power law with time. The final dried width and height of the ring should also be given by power laws of concentration, with both exponent equal to 0.5 provided all particles are in the ring, and the packing factor and ring profile are constant. We use suspensions of polystyrene particles in water with sizes ranging from 200 to 500 nm and initial concentrations  $c_0$  from 0.009% to 1% deposited on glass substrates to investigate these scaling predictions. We vary the drying rate from 0.5 to 5 nl/s using humidity and reduced pressure, use a range of substrates to vary the initial contact angle between  $5^\circ$  and  $35^\circ$ , and invert the droplets to change the direction of gravity. We find that for all but the very lowest pressures, the ring height follows the predicted power law, with exponent equal to  $0.50 \pm 0.04$  and the ring width having an exponent of  $0.33 \pm 0.05$ . The discrepancy between the measured and predicted width exponent is accounted for by an observed variation of droplet radius with concentration, and the presence of particles in the center of the droplet. In addition, for low pressures (fast evaporation) the scaling laws no longer hold: the ring is much narrower and there is significant deposition in the center of the droplet, possibly due to reduced particle-enhanced pinning.*

**KEY WORDS:** droplet, evaporation, particle, deposit, ring stain

## 1. INTRODUCTION

The work of Deegan et al. (1997) proposed a simple explanation for the common occurrence of coffee-ring stains with just two requirements: first, the triple line at the edge of the droplet must remain pinned to the substrate throughout (nearly all of) the drying process, known as constant contact area drying (Picknett and Bexon, 1977); second the evaporative flux over the droplet varies with radius  $r$  away from the center of the droplet and diverges at the contact line  $r = r_d$  following a power law:

$$J(r) \propto (r_d - r)^{-\lambda}, \quad (1)$$

where  $\lambda$  depends on the contact angle  $\theta$  as  $\lambda = (\pi - 2\theta)/(2\pi - 2\theta)$ . These two requirements lead to an outward flow to replenish solvent loss at the contact line, which sweeps suspended material to the contact line where it is deposited as a ring stain. By integrating the evaporation flux and balancing this with radial flow within the droplet, the authors showed that the total mass  $M$  of the deposited ring should grow with power law behavior:

$$M(t) \propto t^{2/(1+\lambda)}. \quad (2)$$

They found good experimental agreement for droplets with initial radius  $r_d = 2$  mm, contact angle  $\theta = 14^\circ$ , initial concentration  $c_0 \approx 0.01\%$ , and average evaporation rate of 1.2 nl/s, with roughly 90% of the particles ending up in the ring.

### NOMENCLATURE

$c_0$	initial concentration of droplet	$p$	exponent for droplet radius variation with concentration
$D$	particle diffusion coefficient	$r$	radial coordinate
$d_p$	particle diameter	$r^*$	rescaled radius coordinate
$h_r$	height of ring deposit	$r_d$	radius of droplet contact area
$J$	evaporative flux	$u_c$	critical particle speed for crystalline deposits
$L$	typical separation between particles	$V_0$	initial droplet volume
$M$	mass of deposit	$\dot{V}$	droplet evaporation rate
$m$	exponent for ring width variation with concentration	$w_r$	width of ring deposit
$n$	exponent for ring height variation with concentration	$z^*$	rescaled height coordinate
$\theta$	(equilibrium) contact angle	$\lambda$	exponent of evaporation
$\theta_a$	advancing contact angle	$\rho$	density of a particle
$\theta_r$	receding contact angle	$\phi$	particle packing fraction in the deposit

In subsequent work by the same authors (Deegan, 1998; Deegan et al., 2000), additional relationships are found between the width  $w_r$  and height  $h_r$  of the ring at the moment when the liquid depins in terms of  $r_d$  and  $c_0$ :

$$w_r \propto c_0^m, \quad h_r \propto w_r^{n/m} \propto c_0^n \quad (3)$$

Experimental values of the exponents were  $m = 0.78 \pm 0.10$  for  $0.1 \mu\text{m}$  spheres and  $m = 0.86 \pm 0.10$  for  $1 \mu\text{m}$  spheres and  $n/m = 0.85$ . The authors also point out that although they find good qualitative agreement between theory and experiment, “the theory predicts that the material arrives at the contact line earlier than it actually does,” by a factor of 2. It should also be noted that although ring widths were measured directly, ring heights are only ever inferred using assumed values of the contact angle.

A simple theoretical approach, however, leads to different predictions. By conserving particles, the final mass of the deposit should be proportional to the initial volume  $V$  multiplied by  $c_0$ :  $M(t = t_f) = \rho V_0 c_0 \phi$ , where  $\rho$  is the density of a particle and  $\phi$  is the average packing fraction in the deposit. If we assume that (i) all the particles end up in the ring, (ii) the cross-sectional shape of the deposit does not depend on  $c_0$ , and (iii) the packing fraction  $\phi$  is constant, then different scaling predictions are found for both  $w_r$  and  $h_r$ :

$$w_r \propto c_0^{0.5}, \quad h_r \propto c_0^{0.5}. \quad (4)$$

It turns out that there are deficiencies with this simple approach. First, the packing fraction is not constant throughout the ring. For droplets containing particles with diameter  $d_p = 2 \mu\text{m}$ , evaporating with a constant contact area (pinned triple line), Marín et al. (2011) showed that the arrangement of particles in the ring stain is controlled by the speed with which they are carried to the periphery: in slow flow, dense, crystalline regions are built with either square or hexagonal packing; during the “rush hour” particle speeds increase above a critical speed  $u_c$  and particles do not have time to rearrange so the ring is randomly structured. The crystalline regions are also more densely packed than the random structure, as determined by the average Voronoi area around each particle. The critical speed is found by equating the diffusive and hydrodynamic time scales and is given by

$$u_c \sim \frac{LD}{d_p^2} \sim \frac{1}{c_0^{1/3}} \frac{1}{d_p^3}, \quad (5)$$

where  $L$  is the typical separation between particles, and  $D$  is the particle diffusion coefficient. There is a weak dependency on initial concentration but a much stronger dependency on particle size, which led the authors to comment that nanofluid droplets should always form crystalline deposits as the flow velocity will never exceed  $u_c$ .

Popov (2005) presents a complex calculation to predict the spatial dimensions of the ring stain, which agrees with the simple physical argument presented above, but not the measurements of Deegan. His resolution to this discrepancy is that as the depinning time is also a function of initial concentration, scaling as  $\sim c_0^{0.26}$ , more concentrated solutions will remain pinned for longer and more of the particles will end up deposited in the ring. By addition of the exponents, he recovers Deegan's  $m = 0.78$  exponent for ring width.

Askounis et al. (2013) investigated droplets containing particles with  $d_p = 80$  nm, evaporating with a stick-slip motion of the triple line, and observed concentric deposits due to the periodic motion of the triple line. Each circular deposit had a further structure showing four distinct regions: disordered outside, then a region with both square and hexagonal crystals, next a purely hexagonal region, and finally another disordered region. The authors proposed that as the smaller particles can approach much closer to the triple line where the evaporative flux accelerates above beyond  $u_c$ , and the effects of the disjoining pressure will be enhanced, these particles are frozen into position before they have time to crystallize. By reducing pressure, they increased particle flow and observed an increase in crystallinity. In contrast to Marín, here with much smaller particles, the flow is causing the ordering rather than disrupting it.

Yunker et al. (2011) have recently investigated the effect of varying the aspect ratio of prolate spheroidal particles on the structure and growth mechanisms of the particle deposits at the edge of a droplet. The width of the deposit was seen in all cases to increase linearly in time, but the roughness depended very sensitively on the eccentricity of the particles. Spherically-shaped particles created a compact, smooth deposit, whereas rodlike particles formed a rough, sparse, dendritic deposit. Interestingly, these suspension droplets are one of the first systems whose growth dynamics can be easily switched experimentally from one universality class to another (Yunker et al., 2011). This observation, and the other recent findings summarized above, underline the fact that there is still much to learn about the formation of the coffee ring.

In contrast, one of the aims of ongoing research into drying sessile droplets is often to remove the coffee-ring stain entirely, as many commercial processes require a uniform deposit. Several effects have been observed to achieve this goal, including: capillary forces (Weon and Je, 2010); Marangoni flow induced by surface tension gradients (Hu and Larson, 2002); electrowetting (Eral et al., 2011); and droplets smaller than a critical size (Shen et al., 2010). Many of these effects are summarized in a recent review (Sefiane et al., 2013).

Unlike the previous work mentioned above, here we seek to neither remove the coffee stain entirely, nor to thoroughly quantify its detailed structure. Instead, we investigate how robust the ring-stain scaling predictions are with respect to five experimental parameters: particle size and concentration, evaporation rate, contact angle, and droplet orientation.

## 2. MATERIAL AND METHODS

The particle suspensions used in this study were surfactant-free polystyrene spheres commercially available from Sigma-Aldrich with particle diameters of  $100 \pm 30$  nm,  $200 \pm 30$  nm, and  $500 \pm 50$  nm, supplied as 2% solids by volume and a particle density of  $1.050 \text{ gcm}^{-3}$  at  $20^\circ\text{C}$ . The suspensions were used as supplied, then diluted with deionized water to obtain samples with weight fractions equal to 0.009%, 0.002%, 0.02%, 0.1%, 0.25%, 0.5%, and 1%. The samples were left on a SRT6-Stuart roller mixer for 12 h to minimize the agglomeration of particles. The mixing process continued for 30 min prior to every experiment.

Three different glasses with different wetting properties were used as substrates in experiments, and the wetting properties of each were characterized by measuring equilibrium, and advancing and receding contact angles ( $\theta$ ,  $\theta_a$ , and  $\theta_r$ ) for three different droplets using a Krüss DSA system: glass coverslips from Chance Proper, Ltd., with dimensions of  $0.15 \times 24 \times 50$  mm and  $\theta = 35^\circ$ ,  $\theta_a = 38.4 \pm 0.4^\circ$ ,  $\theta_r = 34.0 \pm 0.5^\circ$ ; microscope glass slides from Sail Lab Co. Ltd., (China) with  $1.1 \times 25.4 \times 76.2$  mm dimensions, and  $\theta = 18^\circ$ ,  $\theta_a = 19.1 \pm 0.3^\circ$ ,  $\theta_r = 16.3 \pm 0.7^\circ$ ; and microscope glass slides from Thermo Scientific (Menzel-Glaser) with  $1.1 \times 26 \times 76$  mm and  $\theta = 5^\circ$  dimension (which were not possible to measure receding angles for). Before use all substrates were cleaned by blowing with nitrogen gas to remove dust particles and any other contaminants. The zeta potentials of the glass coverslips and the

500 nm particles were measured to be  $-65.3 \pm 7$  mV and  $-57.6 \pm 0.7$  mV, respectively, using a Malvern Nano S Zetasizer.

Samples were placed inside a cylindrical vacuum chamber (diameter 8.6 cm, height 5.4 cm) and connected through a valve to a Cole Parmer MD 4NT vacuum pump (Baldwin et al., 2012). The pressure was recorded using a transducer (KJLC 902) interfaced with controller and readout (KPDR 900) to provide accurate control over the pressure within the chamber. Baffles were positioned within the chamber to reduce the air flow, but there is the possibility that some small air flow or vibration of the air was present due to the cyclic action of pump. On a prepared substrate, 1  $\mu\text{L}$  droplets of each sample concentration were carefully deposited using a Microman positive displacement pipette from Gilson, Inc. Experiments were also repeated with the droplets on the underside of the substrate. The droplets were monitored and the average drying rate calculated by recording the total drying time for each droplet and dividing the initial droplet volume by this time.

Samples were imaged after drying with an Imaging Source CCD camera with IC Capture software, using a Stocker Yale diffuse backlight (ML-045) in both reflected and transmitted modes. ImageJ was used to integrate the measured intensity around the circular deposits to create a radial profile of each deposit. Although the vertical intensity scale is only loosely related to deposit height, this measurement does enable the width of the ring  $w_r$  to be determined with good accuracy. Optical and scanning electron microscopy were also used to examine the deposits.

The height profile of the deposits was analyzed using a Dektat 150 surface profiler with a 1 mg scan force to reduce the chance of damage to the delicate samples. The profiler recorded a line profile of each deposit with around 3  $\mu\text{m}$  horizontal resolution and almost 1 nm vertical resolution. For each droplet, six scans were taken along diameters spaced evenly around the deposit. From the six sets of scan data, average values for the droplet radius  $r_d$ , ring height  $h_r$ , and width  $w_r$  were determined. It should be emphasized that here we are measuring the final dried dimensions of the ring, whereas previous work (Deegan, 1998; Deegan et al., 2000) measured ring width at the moment of depinning. The entire profile was also used to calculate the fraction of particles which ended up in the ring. Representative images and profiles of deposits from two droplets with 500 nm particles and  $c_0 = 1\%$  drying at two different rates (0.6 and 3.3 nl/s), measured using both the profiler and with imaging, are shown in Fig. 1. Very good agreement is seen for the slower drying droplet over the entire droplet. For the faster drying droplet, the position and width of the outermost ring also agree, but there are discrepancies closer to the center. The height values obtained from the profiler are more reliable and are the only data used for quantitative measurements of height.

### 3. RESULTS AND DISCUSSION

Figure 2 shows data points for the measured values for the ring width and height as a function of  $c_0$  for droplets containing 200nm particles, at atmospheric conditions, in an upright orientation. The solid lines show power law curves with fitted exponents of  $m = 0.336 \pm 0.016$  for the width and  $n = 0.55 \pm 0.03$  for the height. Overall, similar fits were performed for 34 combinations of particle size, atmospheric pressure, contact angle, and droplet orientation. Experiments were repeated with up to four identical droplets, and the measured values of ring height and width were within the statistical uncertainties of one droplet (indicated by the error bars on Fig. 2). The fitted exponents are presented in Fig. 3. In addition, the droplet radius was observed to increase weakly with concentration,  $r_0 \propto c_0^p$ , presumably due to attraction between the particles and the substrate. The values for  $p$  are also plotted in Fig. 3. The average values for the three exponents are found to be  $m = 0.33 \pm 0.05$  for the deposit width,  $n = 0.50 \pm 0.04$  for the deposit height [in agreement with theoretical prediction of the height from Eq. (4)], and  $p = 0.03 \pm 0.01$  for the droplet radius.

As can be seen from Fig. 3, the scaling law exponents are independent of drying rate and show no additional dependency on contact angle, particle size, or droplet orientation. Colloidal particles are only weakly effected by gravity, so it is perhaps unsurprising that the orientation of the droplet does not alter the drying pattern. However, an often overlooked effect in evaporating droplets is the buoyancy of the vapor (Kelly-Zion et al., 2013), the flow of which, relative to the droplet and the substrate, will be altered by changing the relative direction of gravity. Our results, however, show that this effect is insignificant.

The constants of proportionality do show slight dependence on particle size and drying rate and a significant variation with contact angle, as flatter rings are seen as the contact angle decreases with a fixed volume. However, the

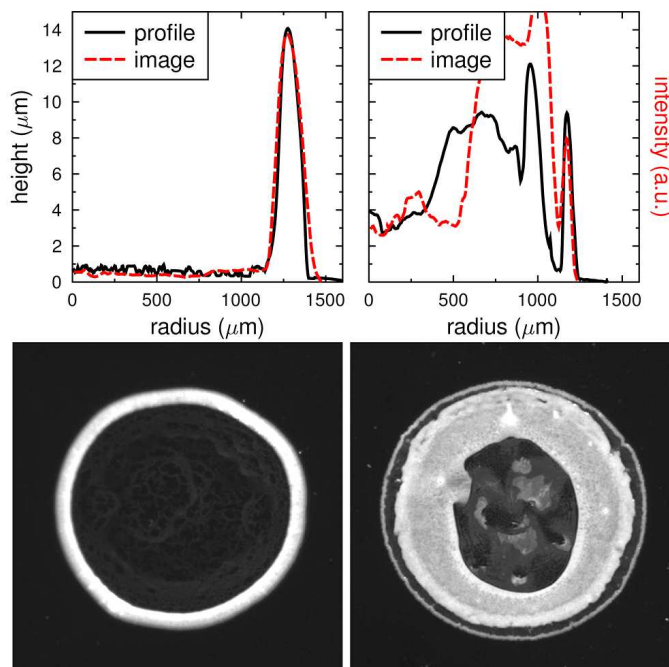


**FIG. 1:** Comparison of deposit profiles measured using a surface profiler (solid black lines) and imaging (red dashed lines) at two different drying rates,  $\dot{V} = 0.6$  nL/s (left) and  $\dot{V} = 3.3$  nL/s (right). The two images are shown underneath. Both droplets contained 500 nm particles at initial concentration  $c_0 = 1\%$ .

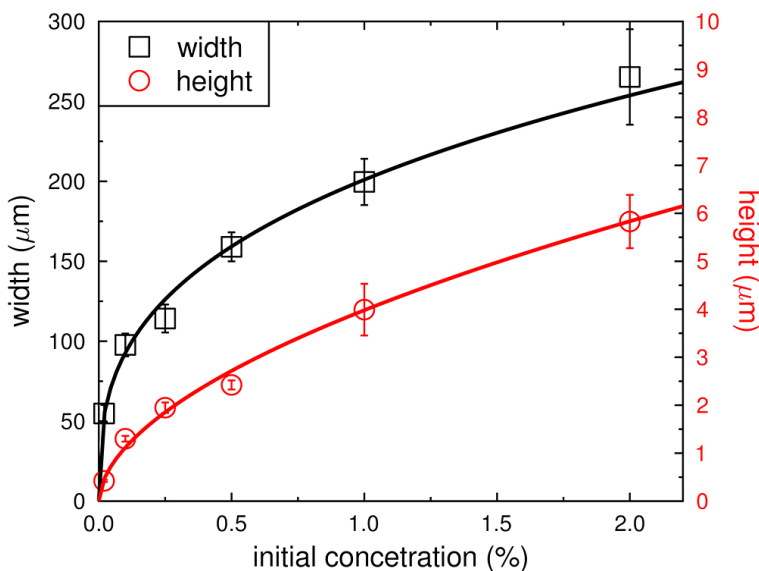


**FIG. 2:** Concentration dependency of the height  $h_r$  (circles, red online) and width  $w_r$  (black squares) of the ring stain deposited from droplets containing 200 nm particles, drying upright at atmospheric pressure with  $\theta = 5^\circ$ . The data is fitted by the equations  $w_r$  ( $\mu\text{m}$ ) =  $201 c_0^{0.336 \pm 0.016}$  and  $h_r$  ( $\mu\text{m}$ ) =  $3.98 c_0^{0.55 \pm 0.03}$ . Error bars indicate variation of the measured values within one droplet.

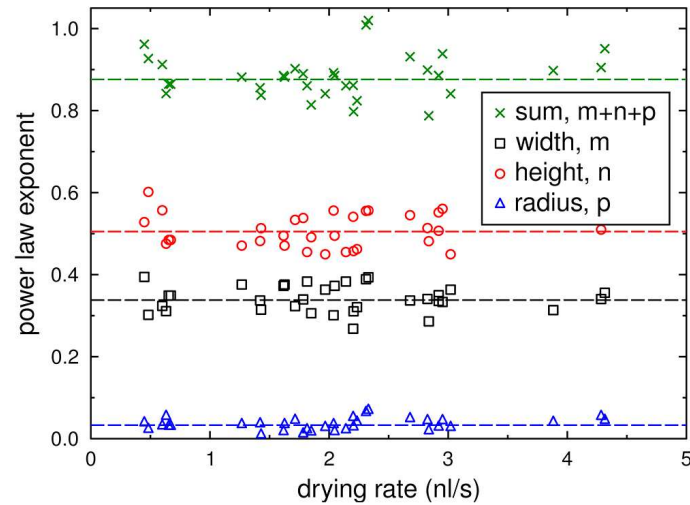


**FIG. 3:** Data points show the fitted values for the power law exponents describing how the ring width ( $m$ , black squares), ring height [ $n$ , red circles (online)] and initial droplet radius [ $p$ , blue triangles (online)] vary with drying rate. Also shown is the sum of all three exponents  $m + n + p$ . Exponents are determined for a range of particle sizes, contact angles, and orientations.

width of the ring does not vary as noticeably with contact angle. Steric repulsion at the interface, which can prevent particles from entering a region very close to the triple line, can explain the flatter deposit: an annulus containing a fixed number of particles close to the triple line will be flatter for lower contact angles. The increased droplet perimeter along which the particles are deposited may compensate for the smaller change in width.

To further investigate the validity of the scaling laws, we center the profilometer data on the peak of the deposit and rescale in the horizontal and vertical coordinates using the 1% data as the unscaled values:

$$r^* = r \left( \frac{0.02}{c_0} \right)^m, \quad z^* = z \left( \frac{0.02}{c_0} \right)^n. \quad (6)$$

As can be seen in Fig. 4, using values of  $m = 0.42$  and  $n = 0.55$ , the scaled profiles are similar, although the detailed shape of the deposit shows some variation with concentration.

As discussed above, conservation of the total volume of particles dictates that the overall deposit volume should be proportional to  $c_0$ , a power law of exponent 1. Experimentally, the deposit volume is proportional to the product of the ring height, ring width, and droplet radius. Therefore we expect that the sum of the three respective exponents  $m + n + p$  should be equal to 1. In Fig. 3 we also plot this sum, which has a value of  $0.86 \pm 0.07$ . Although this is close to the predicted value of unity, it is consistently smaller. The discrepancy could be accounted for by one of several explanations and is most likely to be a combination of (i) the particle packing fraction  $\phi$  increases at higher concentrations so these ring deposits have misleadingly small dimension (Marín et al., 2011); (ii) the shape of the deposit varies slightly with concentration, which is not accounted for in the predictions; and (iii) a small fraction of the particles are deposited in the center of the droplet and are therefore not included in the volume calculations. Optical and electron microscopy observations show that not all of the particles are deposited in the ring. To quantify this, we used both profilometry and image analysis to estimate the fraction of particles in the ring, and for a sample with  $c_0 = 1\%$  and  $\theta = 35^\circ$ , around 90% of the particles were in the ring [in agreement with previous observations (Deegan et al., 1997)] and the remaining 10% were deposited in a monolayer of particles covering much of the initial contact area. Owing to the  $3 \mu\text{m}$  horizontal sensitivity of the profilometer, we were unable to reliably determine the fraction in the ring for lower concentrations.

For all samples, at the very lowest pressures investigated (10 mbar, corresponding to evaporation rates over 4 nl/s) a much lower fraction of the particles were deposited in the peripheral ring: it has a height around 50% and width

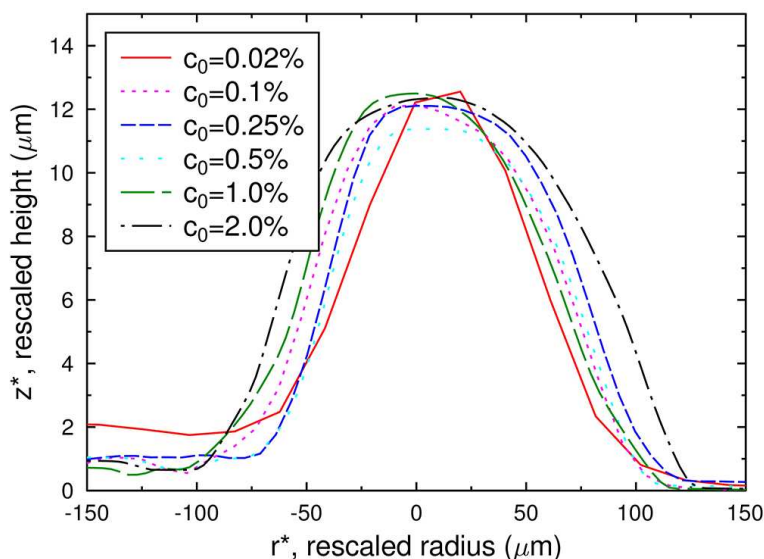


**FIG. 4:** Ring profile data for droplets containing 500 nm particles drying at 800 mbar for a range of initial concentrations. Radius and height coordinates are rescaled with concentration using exponents  $m = 0.42$  and  $n = 0.55$ , respectively. The outside of the droplet is in the positive  $r^*$  direction.

30%, the values predicted from the scaling laws, and only around 15% of the particles are deposited here. As shown in Fig. 1, significant deposition was seen over the contact area. There appeared to be a sharp transition between ring deposition and the fast drying behavior and preliminary investigations suggest a possible mechanism: a pinned contact line leads to preferential deposition, which creates roughness at the contact line which in turn enhances the pinning. However, at the high drying rates, although the solvent is flowing rapidly to the edge as a result of the evaporation, the particles may not be swept along at the same rate, due perhaps to electrostatic interactions with other particles or with the substrate. Whatever the mechanism, fewer particles arrive at the contact line so the pinning is weaker and the interface depins earlier, reminiscent of the argument of Popov (2005). The observed sharp transition occurs due to the positive feedback in the deposition/pinning behavior. We are currently performing experimental work to investigate this further.

#### 4. CONCLUSIONS

We have performed droplet evaporation experiments to determine how robust the scaling laws are which describe the height and width of the deposited ring stain. Using polystyrene particles in water on glass substrates, we have varied particle size and concentration, and droplet orientation and evaporation rate (via atmospheric pressure), and used optical and profilometric methods to determine the ring dimensions. We find that for all sizes and orientations, and all but the very fastest evaporation rates (lowest pressures), there is a robust scaling of the ring dimensions with concentration: ring width is given by  $w_r \propto c_0^{0.33 \pm 0.05}$  and the height is given by  $h_r \propto c_0^{0.50 \pm 0.04}$ . That droplet orientation does not alter the scaling laws suggests that they should also hold under microgravity conditions. At pressures around 10 mbar, the deposit is seen across the entire contact area, which we believe is due to weaker particle-induced pinning at these high evaporation rates.

#### ACKNOWLEDGMENT

Y. Msambwa is funded by the Tanzanian government through the Dar Es Salaam University College of Education.

## REFERENCES

- Askounis, A., Sefiane, K., Koutsos V., Shanahan, and Martin E. R., Structural transitions in a ring stain created at the contact line of evaporating nanosuspension sessile drops, *Phys. Rev. E*, vol. **87**, p. 012301, 2013.
- Baldwin, K. A., Roest, S., Fairhurst, D. J., Sefiane, K., and Shanahan, M. E. R., Monolith formation and ring-stain suppression in low-pressure evaporation of poly (ethylene oxide) droplets, *J. Fluid Mech.*, vol. **695**, pp. 321–329, 2012.
- Deegan, R. D., Deposition at pinned and depinned contact lines: Pattern formation and applications, PhD Thesis, Science, 1998.
- Deegan, R. D., Bakajin, O., Dupont, T. F., Huber, G., Nagel, S. R., and Witten, T. A., Capillary flow as the cause of ring stains from dried liquid drops, *Nature*, vol. **389**, no. 6653, pp. 827–829, 1997.
- Deegan, R. D., Bakajin, O., Dupont, T. F., Huber, G., Nagel, S. R., and Witten, T. A., Contact line deposits in an evaporating drop, *Phys. Rev. E*, vol. **62**, no. 1, p. 756, 2000.
- Eral, H. B., Augustine, D. M., Duits, M. H. G., and Mugele, F., Suppressing the coffee stain effect: How to control colloidal self-assembly in evaporating drops using electrowetting, *Soft Matter*, vol. **7**, no. 10, pp. 4954–4958, 2011.
- Hu, H. and Larson, R. G., Evaporation of a Sessile Droplet on a Substrate, *J. Phys. Chem. B*, vol. **106**, no. 6, pp. 1334–1344, 2002.
- Kelly-Zion, P. L., Pursell, C. J., Hasbamer, N., Cardozo, B., Gaughan, K., and Nickels, K., Vapor distribution above an evaporating sessile drop, *Int. J. Heat Mass Transfer*, vol. **65**, no. 0, pp. 165–172, 2013.
- Marín, A. G., Gelderblom, H., Lohse, D., and Snoeijer, J. H., Order-to-disorder transition in ring-shaped colloidal stains, *Phys. Rev. Lett.*, vol. **107**, no. 8, p. 085502, 2011.
- Picknett, R. G. and Bexon, R., The evaporation of sessile or pendant drops in still air, *J. Colloids Interface Sci.*, vol. **61**, pp. 336–350, 1977.
- Popov, Y. O., Evaporative deposition patterns: Spatial dimensions of the deposit, *Phys. Rev. E*, vol. **71**, no. 3, p. 036313, 2005.
- Sefiane, K., Patterns from drying drops, *Adv. Colloid Interface Sci.*, no. 0001–8686, doi: 10.1016/j.cis.2013.05.002, 2013, in press.
- Shen, X., Ho, C. M., and Wong, T. S., Minimal size of coffee ring structure, *J. Phys. Chem. B*, vol. **114**, no. 16, pp. 5269–5274, 2010.
- Weon, B. M. and Je, J. H., Capillary force repels coffee-ring effect, *Phys. Rev. E*, vol. **82**, no. 1, p. 015305, 2010.
- Yunker, P. J., Still, T., Lohr, M. A., and Yodh, A. G., Suppression of the coffee-ring effect by shape-dependent capillary interactions, *Nature*, vol. **476**, no. 7360, pp. 308–311, 2011.
- Yunker, P. J., Lohr, M. A., Still, T., Borodin, A., Durian, D. J., and Yodh, A. G., Effects of particle shape on growth dynamics at edges of evaporating drops of colloidal suspensions, *Phys. Rev. Lett.*, vol. **110**, no. 3, p. 035501, 2013.

# Controlling and characterising the deposits from polymer droplets containing microparticles and salt<sup>\*</sup>

Y. Msambwa, A.S.D. Shackelford, F.F. Ouali, and D.J. Fairhurst<sup>a</sup>

Nottingham Trent University, Clifton Lane, Nottingham, NG11 8NS, UK

Received 14 July 2015 and Received in final form 29 January 2016

Published online: 26 February 2016

© The Author(s) 2016. This article is published with open access at Springerlink.com

**Abstract.** A coffee ring-stain is left behind when droplets containing a wide range of different suspended particles evaporate, caused by a pinned contact line generating a strong outwards capillary flow. Conversely, in the very peculiar case of evaporating droplets of poly(ethylene oxide) solutions, tall pillars are deposited in the centre of the droplet following a boot-strapping process in which the contact line recedes quickly, driven by a constricting collar of polymer crystallisation: no other polymer has been reported to produce these central pillars. Here we map out the phase behaviour seen when the specific pillar-forming polymer is combined with spherical microparticles, illustrating a range of final deposit shapes, including the standard particle ring-stain, polymer pillars and also flat deposits. The topologies of the deposits are measured using profile images and stylus profilometry, and characterised using the skewness of the profile as a simple analytic method for quantifying the shapes: pillars produce positive skew, flat deposits have zero skew and ring-stains have a negative value. We also demonstrate that pillar formation is even more effectively disrupted using potassium sulphate salt solutions, which change the water from a good solvent to a theta-point solvent, consequently reducing the size and configuration of the polymer coils. This inhibits polymer crystallisation, interfering with the bootstrap process and ultimately prevents pillars from forming. Again, the deposit shapes are quantified using the skew parameter.

## 1 Introduction

The work of Deegan *et al.* [1] first thoroughly investigated the properties of the coffee ring-stain, commonly seen when suspension droplets are left to evaporate on a solid surface. They proposed a simple explanation for these deposits with just two requirements: firstly, the triple line at the edge of the droplet must remain pinned to the substrate throughout (nearly all of) the drying process, known as constant contact radius drying (CCR) [2]; secondly the evaporative flux over the droplet varies with radius  $r$  measured from the centre of the droplet and diverges at the contact line  $r = R$  following a power law. These two requirements lead to an outward flow to replenish solvent loss at the contact line, which sweeps suspended material to the contact line where it is deposited as a ring-stain. The size and shape of the deposit is robust over a range of experimental parameters and follows simple power-law predictions [3]. One of the aims of ongoing research into drying sessile droplets is to control and

prevent the formation of the coffee ring-stain as many commercial processes require a uniform deposit. Several mechanisms have been observed to achieve this goal including: non-spherical particles [4], capillary forces [5]; Marangoni flow induced by surface tension gradients [6]; electrowetting [7]; using droplets smaller than a critical size [8] and heated substrates [9]. Many of these effects are summarised in a recent review [10].

In many cases, ring-stains are also suppressed if the liquid in the droplet undergoes a phase-change during evaporation. For example, in drying droplets of both dextran [11] and bitumen [12] the contact line becomes pinned, a flexible glassy skin with fixed surface area forms and as evaporation continues the film buckles leaving a final deposit in the shape of a sombrero.

The polymer used in this study is the very widely used linear polymer PEO, poly(ethylene oxide) [13–16]. It is unique amongst its homologues for its unusual solubility properties [17]: it dissolves in water, although at high concentrations or molecular weights, solutions can appear cloudy due to micron-sized clusters of undissolved polymer [18]. The origin of these clusters is still a point of contention [18]. The properties of PEO are very well known including data on its viscosity [19], solubility [20], phase behaviour [21] and crystallisation [22]. In water, PEO

<sup>\*</sup> Contribution to the Topical Issue “Wetting and Drying: Physics and Pattern Formation”, edited by Duyang Zang, Ludovic Pauchard and Wei Shen.

<sup>a</sup> e-mail: david.fairhurst@ntu.ac.uk

molecules adopt an expanded coil structure as water is considered a good solvent for PEO. These fully expanded coils have sufficient space to arrange into a crystalline network with the neighbouring chains to form spherulites when the polymer concentration increases. The solvent quality can be reduced by adding salts which disrupt the water structure, reducing the favourable interaction between monomers and water until the theta point is reached, where the molecule is somewhat condensed and described by the statistics of an ideal coil. On the addition of further salt, the polymer will precipitate out of solution as it undergoes a coil-globule transition; several works have studied the effectiveness of various salts [23, 24]. An interesting follow-up paper studied the change in polymer conformation using optical tweezers to show the elasticity of a single PEO molecule as the salt concentration is altered [25].

In a previous work [26] we observed for the first time that aqueous droplets of PEO follows a unique drying route. The liquid droplet is squeezed inwards by a constricting ring of crystallising polymer at the contact line which eventually lifts the remaining liquid from the surface, forming polymer pillars which may be taller than the original droplet. The polymer crystallisation is an essential part of this process and explains why this effect has not been seen in other, non-crystallising polymers. Further work [27] examined in detail the mechanisms controlling this behaviour, showing that the effects of droplet volume, contact angle, temperature and vapour pressure could be combined into a dimensionless Péclet number which correctly predicts whether a given droplet will form a pillar or not. The physical mechanism was later expanded to also include the effects of polymer concentration [28] and polymer molecular weight [29]. More recently very similar pillar-forming behaviour was observed in droplets of blood evaporating at pressures below 10% atmospheric pressure. The striking similarities between the two cases were used to develop a generalised classification of droplet evaporation modes [30], determined by the constant  $A$  which relates the instantaneous droplet radius  $R$  to the speed of motion of the contact line  $\dot{R}$  in the equation  $\dot{R} = -\frac{A}{R}$ . For  $A = 0$ , the contact line is pinned and evaporation is through CCR mode, resulting in classic ring-stain deposit. For  $0 < A < A_{CCA}$ , less than  $A_{CCA}$  a specific rate at which the droplet evaporates with constant contact angle, the deposit is a doughnut shape due to the slow receding of the contact line during evaporation. For  $A > A_{CCA}$ , “fast receding” of the contact line is seen, resulting in the deposition of a tall pillar. In ref. [30] the parameter  $A$  was varied using polymer concentration.

An aesthetically similar observation is seen in freezing water droplets. Liquid water expands as it solidifies, leading to cusped solid deposits [31]. Droplets of salt solutions do not typically form ring-stains due to modified wettability once salt crystals begin to precipitate [32], and can often be seen to “creep” across the surface, leaving a deposit that is larger than the original droplet [33, 34].

Others have also studied the drying behaviour of PEO droplets. Mamalis *et al.* [35] varied the molecular weight

and substrate chemistry to highlight the role of interfacial friction on pillar formation. Hu *et al.* [36] placed 5% concentration droplets of molecular weight  $M_W = 280 \text{ kg mol}^{-1}$  PEO on both isothermal and heated substrates and found evidence of Marangoni flow at higher temperatures. Choi *et al.* [37] added  $1 \mu\text{m}$  and  $6 \mu\text{m}$  hollow glass spheres to very dilute (maximum of 0.1%) PEO solutions with  $M_W = 200 \text{ kg mol}^{-1}$  and  $900 \text{ kg mol}^{-1}$  in order to alter the viscous drag on the moving particles. They found that even at such low concentrations, the effect of the polymer was sufficient to disrupt formation of the ring-stain.

In this work we investigate two methods to control the pillar formation in aqueous PEO droplets, and propose a simple method to characterise the basic shape of the deposit. Firstly we study mixtures of PEO with polymer microparticles, mapping out how the droplet deposits change from ring-stain to pillars as the relative concentration of the two components are varied. We use two different sized particles and compare their effects, to determine whether polymer crystallisation and hence pillar formation is disrupted more by particle volume fraction, or number density. Secondly we disrupt the water structure by adding to the PEO solutions small quantities of the salt potassium sulphate,  $\text{K}_2\text{SO}_4$ , as this ranks relatively highly in both the Hoffmeister series (indicating a strong tendency to induce protein precipitation) and in the data in ref. [23] on the effect of various salts on PEO solubility. With added salt the solution is not as good a solvent for the polymer, so its *quality* as a solvent has reduced. We study how the pillar formation is disrupted when the solvent quality is reduced leading to a reduction in the size of the dissolved polymer coil and a restriction on the freedom of the coils to form ordered crystalline structures. To quantify our findings from both sets of experiments, we present a novel and versatile technique, using the skewness of a height profile, to distinguish quantitatively between the various deposits.

## 2 Methods

Polymer solutions were prepared by dissolving PEO powder (from Sigma Aldrich with average molecular weight  $M_w = 100 \text{ kg mol}^{-1}$  and  $200 \text{ kg mol}^{-1}$ , referred to as PEO100 and PEO200) in distilled, deionized water with a range of mass concentrations  $c_0$  and left to equilibrate for at least 24 hours. The particle suspensions used in this study were surfactant-free polystyrene spheres commercially available from Sigma-Aldrich with particle diameters of  $0.50 \pm 0.05 \mu\text{m}$  and  $5.0 \pm 0.5 \mu\text{m}$ , supplied at up to 10% solids by volume and a particle density of  $1.050 \text{ g cm}^{-3}$  at  $20^\circ\text{C}$ . The suspensions were diluted with deionized water, if necessary, and added to the PEO solutions to obtain samples with particle concentrations by mass  $c_p$  between 1% and 5%. Due to the difficulties of dissolving PEO into the particle solutions, the highest polymer concentrations possible were around 16%. The salt  $\text{K}_2\text{SO}_4$  was added to other PEO solutions to give salt concentrations by mass  $c_s$  between 0.1% and 1.0%. As the salt comes in dry powdered form, it is possible to mix solutions

with polymer concentrations as high as 25%. All samples were left on a SRT6-Stuart roller mixer for 12 hours to minimise the agglomeration of particles. The mixing process was repeated for at least 30 minutes prior to every experiment.

For the evaporation experiments, droplets of initial volume  $V_0$  between  $0.4\ \mu\text{l}$  and  $5\ \mu\text{l}$  were slowly pipetted onto clean glass slides using a positive displacement Gilson pipette to ensure accurate dispensing of the viscous solutions. Previous work [27] has shown that, provided the droplet dimensions are smaller than the capillary length (around 2 mm), droplet volume does not affect deposition patterns. Samples were imaged from the side during drying using an Imaging Source CCD camera with IC Capture software, illuminated by a Stocker Yale diffuse back light (ML-045). ImageJ was used to analyse the images and extract the profile coordinates of the deposit from the images of the final deposit. Images of the final deposits were also taken using a Nikon Eclipse TE2000-S inverted microscope and an Olympus BX51 upright microscope using crossed-polarisers to highlight the crystallised polymer spherulites.

For the droplets containing polymer plus salt, ten droplets at each combination were deposited, and although not all were usable for analysis, in total 380 dried droplets were imaged and analysed. For the droplets of polymer plus particles, ten droplets were deposited at each composition, with profile images taken of three. As some of the samples formed ring-stains, in which the centre was lower than the edge, images taken from the side were not able to capture the profile accurately. In these situations, the height profile of the deposits was analysed using a Dektat 150 surface profiler with a 1mg scan force to reduce the chance of damage to the delicate samples. The profiler recorded a line profile for each deposit with around  $3\ \mu\text{m}$  horizontal resolution and almost 1nm vertical resolution. For each droplet, 6 scans were taken along diameters, spaced evenly around the deposit.

### 3 Results

Tables showing representative final images for the deposits, both profile and overhead, for both particle sizes and salt, are presented in figs. 1 to 6. The axes of the table for the salt samples have been transposed owing to the large number of different concentrations used. Repeatability for all droplets was very good, as illustrated by the superimposed profiles presented in fig. 1. Although measurements were not taken from all droplets, the ten repeats for each combination were compared by eye and in nearly all cases the deposits were very similar, with slightly more variation seen with droplets at the boundary between flat and pillar structures.

Pillar formation, which is typically seen above 3% in pure PEO droplets, is shifted to higher concentrations with the addition of particles, with the  $5\ \mu\text{m}$  particles in particular disrupting the pillars. Between 6% and 10% the pillars are more rounded and at their base extend to the full width of the initial droplet. For all samples, steep, tall pillars are seen at high polymer concentrations. As shown

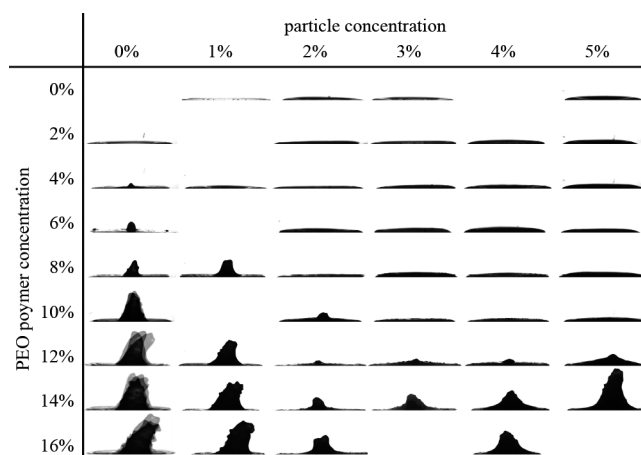


**Fig. 1.** Final profile images for  $0.7\ \mu\text{l}$  droplets containing PEO100 and  $5\ \mu\text{m}$  particles with  $c_0$  between 0% and 16% and  $c_p$  between 0% and 5%. The lower four pure polymer images show superimposed profiles from repeated droplets to indicate experimental repeatability.

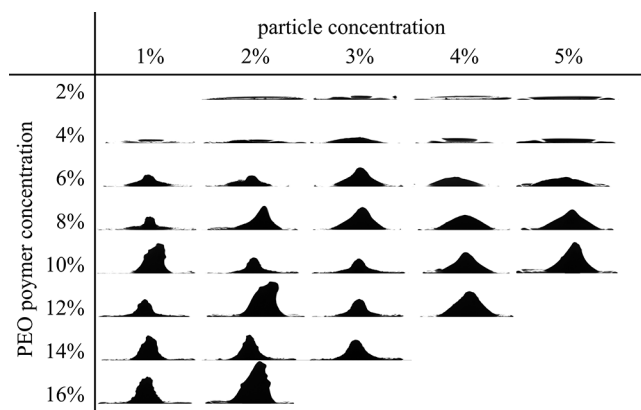


**Fig. 2.** Final profile images for  $0.7\ \mu\text{l}$  droplets containing PEO100 and  $0.5\ \mu\text{m}$  particles with  $c_0$  between 2% and 16% and  $c_p$  between 1% and 5%.

in fig. 2, the disruption is less pronounced for the  $0.5\ \mu\text{m}$  particles.

The overhead images of the droplets with  $5\ \mu\text{m}$  particles are uniformly dark and did not reveal any particular variations between droplets, so are not included here. However, higher magnification microscopy close to the contact line shows that for low polymer concentrations, particles were deposited at the edge in a ring-stain, whereas at higher  $c_0$ , particles were more evenly distributed, as illustrated in fig. 4.

The results for samples with no polymer and shown in fig. 5. The particle and water droplets show classic ring-stains while the salt and water solutions show the more complicated crystal rings seen in such “creeping” solutions where the liquid spreads out over the deposited solid [32, 33]. The particles deposits were also characterised using a stylus profilometer.

The total drying time did not vary significantly between the various droplets and was around 600 seconds at standard atmospheric conditions.

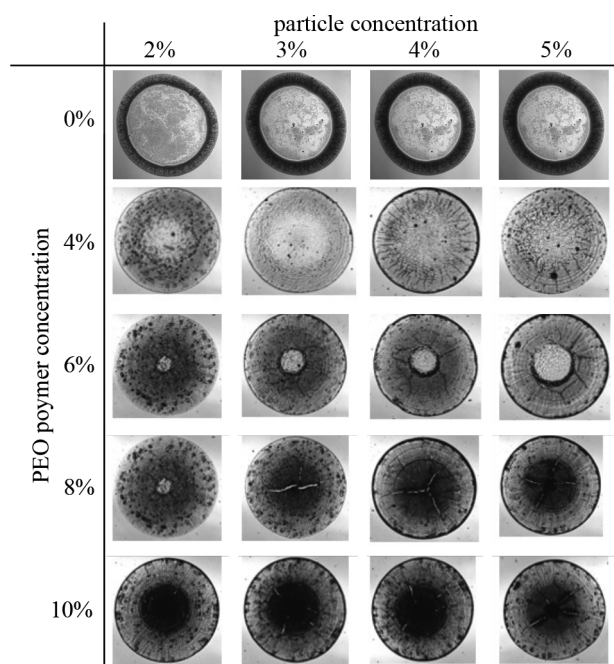


**Fig. 3.** Final overhead images taken through crossed polarisers of  $0.4 \mu\text{l}$  droplets containing PEO100 and  $0.5 \mu\text{m}$  particles with  $c_0$  between 0% and 10% and  $c_p$  between 2% and 5%. Ring-stains are clear at low values of  $c_0$  and at higher values (above around 6%) pillars are present, seen as a central circle in the images.

The deposit shapes are more usefully quantified using surface profile data giving the height of the deposit  $h(r)$  as a function of distance from the droplet centre  $r$ . As we have shown previously [3], robust ring-stains are observed over a range of experimental conditions, and here we confirm this result, finding clear ring-stains for all particle droplets without PEO,  $c_0 = 0\%$ , as evidenced by the  $c_0 = 0\%$  curve in fig. 7 for  $0.5 \mu\text{m}$  particles. Note that both the height profiles and microscopy reveal that there is at most a monolayer of particles deposited in the centre of the ring. The other curves in this figure show the effect of increasing PEO concentration: at low values of  $c_0$ , we still observe a ring-stain however with non-zero height in the centre. Figure 4 suggests that there may be separation between particles and polymer, as the ring preferentially contains particles, and the centre contains polymer. For higher concentrations,  $c_0 \geq 6.0\%$ , a central pillar is clearly defined, which increases in height with polymer concentration. The measured profiles using  $5 \mu\text{m}$  particles are not presented, but show a similar transition from ring-stain to pillar on the addition of PEO.

## 4 Discussion

We have shown qualitatively in the previous section that the addition of either particles or salt can disrupt the formation of PEO polymer pillars. It has been established previously [26] that pillars are deposited following a four-

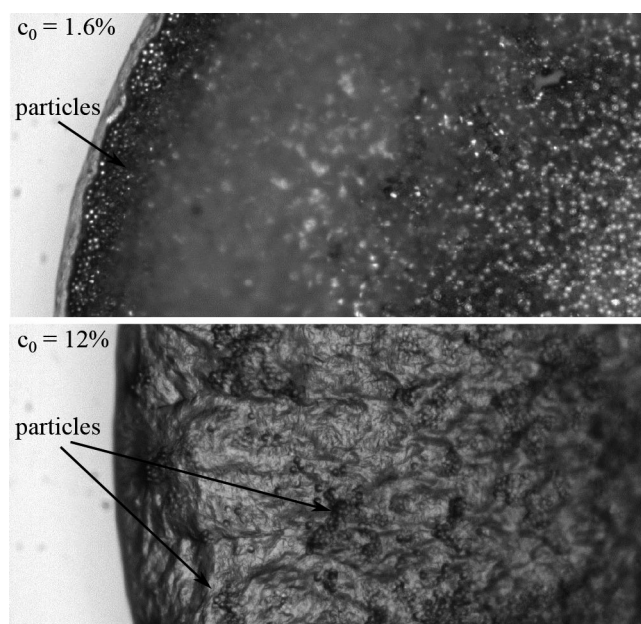


**Fig. 4.** Close-up images of the contact line of  $0.4 \mu\text{l}$  droplets with  $c_0$  of 1.6% and 12% and concentration of  $5 \mu\text{m}$  particles  $c_p = 4\%$ . At low  $c_0$ , particles are preferentially deposited at the edge, like a classic ring-stain despite the presence of polymer. At higher concentrations, the polymer disrupts the particle movement and consequently, particles are distributed more evenly.

stage process, where the critical step in the vertical growth of the structures is the “bootstrap” step in which crystalline polymer spherulites are deposited at the contact line and bind preferentially to the glass substrate creating a solid collar around the remaining liquid. Due to additional loss of water, the collar contracts, squeezing the droplet towards the centre. As the droplet recedes, the collar begins to squeeze the liquid upwards, away from the substrate, which is particularly dramatic at low pressures [27]. When the crystallisation process is hindered, the collar will not form, the contact line will not recede and pillars will not be able to form [29]. The addition of  $\text{K}_2\text{SO}_4$  disrupts the structure of PEO in aqueous solutions and is known to initiate precipitation of the polymer, by decreasing the affinity of the polymer monomers for water compared to the polymer-polymer attractions. The polymer chains collapse from their open, expanded coil state, in which they are described by the statistics of a self-avoiding chain to a more compact ideal random walk before precipitating out of solution in the very compact globule state [25]. This configurational change of the polymer should prevent pillar formation at low salt concentrations, well below 1%. Although not of primary focus in this work, a very low concentration of polymer ( $c_p < 2\%$ ) was observed to disrupt the creeping behaviour of pure salt droplets.

In the polymer plus particle system, the polymer has a dramatic effect on the formation of the ring-stain. The overall deposit becomes flat at low polymer concentrations, although there does appear to be some evidence for

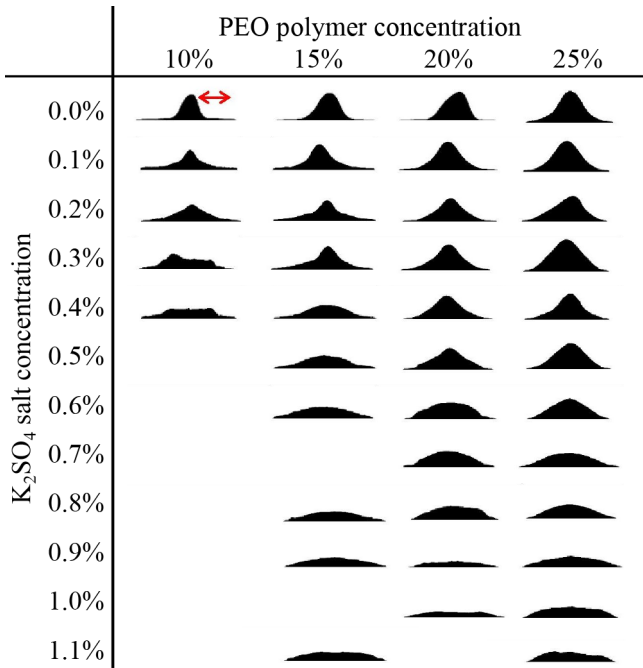


**Fig. 5.** Final profile images for  $5\mu\text{l}$  droplets containing PEO200 and  $\text{K}_2\text{SO}_4$  with  $c_0$  between 10% and 25% and  $c_s$  between 0% and 1.1%.

fractionation within the droplet, with particles preferentially deposited at the edge for  $c_p < 2\%$ . The effect discussed above, in which polymer crystallisation at the contact line drives the droplet inwards, is sufficiently strong to overcome the self-pinning that occurs typically at the edge of evaporating suspension droplets, preventing the ring-stain. The effect of the particles on pillar formation is less dramatic than the effect of salt, with the  $5\mu\text{m}$  particles shifting the threshold concentration for pillars up from 3% to around 12%, and the smaller  $0.5\mu\text{m}$  particles making very little difference to the threshold values of  $c_p$ . This suggests that pillar formation is relatively immune to physical impurities, which only provide a steric rather than a configurational hindrance to polymer crystallisation. Even the smallest particles are significantly larger than the polymer molecules themselves, so do not interfere with the molecular process of crystallisation. There may in fact be an optimum concentration of particles around 3% to disrupt pillar formation, as shown in fig. 1, as at 5% the pillars seem to be becoming larger again.

In order to quantify how the shape of the deposits are altered we chose to measure the skewness of the droplet profile, and in keeping with statistical textbooks assign the variable  $\gamma_1$ . Skewness, which is related to the third moment of a distribution (as mean is related to the first moment and standard deviation to the second moment), indicates whether a distribution function leans to the left or right. As illustrated in fig. 7, this parameter distinguishes the three main types of pillar deposit: profiles which are peaked towards  $r = 0$  have a positive skewness; ring-stain deposits in which the profile is peaked towards the edge at  $r = R$  have a corresponding negative

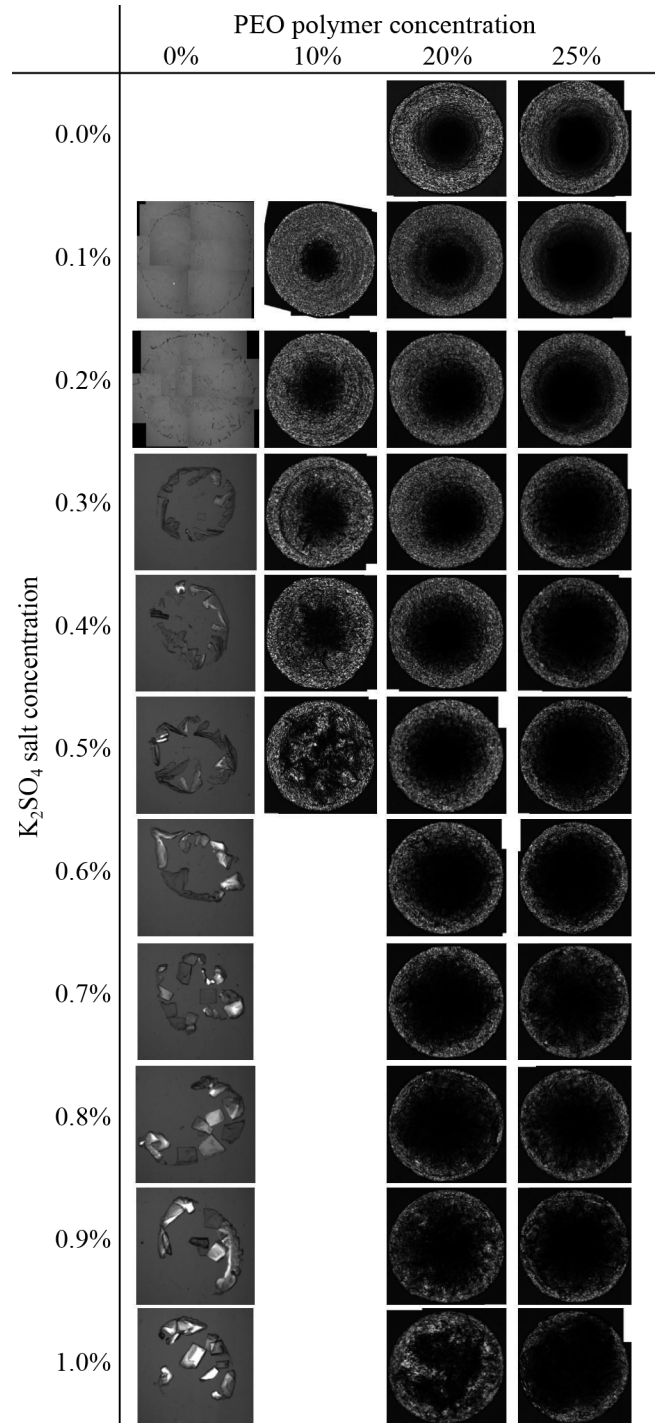


**Fig. 6.** Final overhead images taken through crossed polarisers for  $5\mu\text{l}$  droplets containing PEO200 and  $\text{K}_2\text{SO}_4$  with  $c_0$  between 0% and 25% and  $c_s$  between 0% and 1.0%.

skew; and symmetrical flat deposits have a skewness close to zero. The simpler approach of using the value of  $r$  at which the droplet height  $h(r)$  is a maximum does not take into account the height of the peak, and therefore fails to consistently identify flattish deposits, where the maximum is not clearly defined. The use of skewness overcomes this problem.

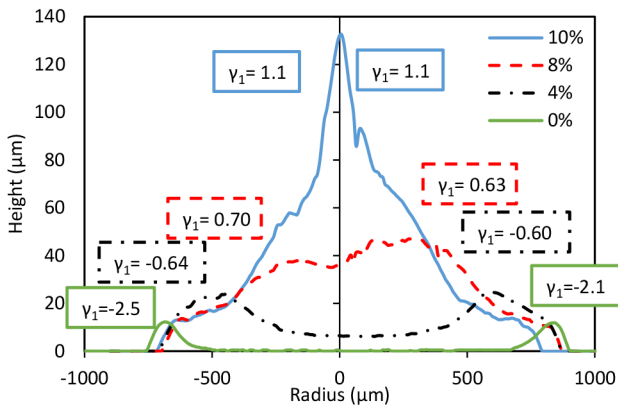


**Fig. 7.** Deposit profiles for  $0.4 \mu\text{m}$  droplets with polymer concentration  $c_0$  between 0% and 10% and concentration of  $0.5 \mu\text{m}$  particles fixed at  $c_p = 4\%$ . The values of the skewness  $\gamma_1$  for both left and right sides of each profile are also indicated on the figure. With no polymer,  $c_0 = 0\%$ , the profile of a classic ring-stain is seen, with negative skewness  $\gamma_1 < -2$ . For  $c_0 = 4\%$  a ring-like deposit at the edge is seen, with additional deposit in the centre and  $\gamma_1 \approx -0.6$ . For  $c_0 = 8\%$ , the deposit is a short pillar with  $\gamma_1 \approx 0.66$  and for  $c_0 = 10\%$  a tall pillar is seen with  $\gamma_1 = 1.1$ .

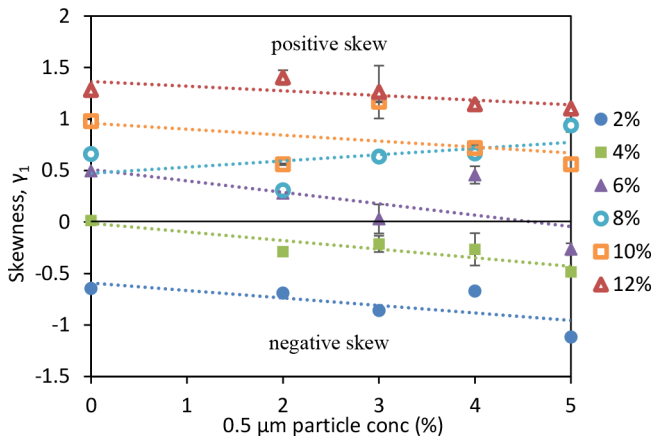


**Fig. 8.** Skewness of final deposit as a function of added concentration of  $0.5 \mu\text{m}$  particles into  $0.7 \mu\text{m}$  droplets containing PEO100 at various concentrations. Vertical error bars indicate the difference in skew between the two sides, average over three droplets. Uncertainties in PEO concentration are around 0.5%.

The simplest definition of skew is the non-parametric skew, defined as the difference between the median and the mean  $\bar{r}$  of the distribution, divided by the standard deviation. However, this approach did not reliably capture the shape of the distributions, so for our analysis we used the standardised third moment of the radial profile. As the data obtained from both image analysis of the interface and surface profilometry is discrete with values of  $r_i$ ,  $h_i$  (and an increment  $\delta_i = r_{i+1} - r_i$  to account for data that are not necessarily equally spaced), we used the following formulae to calculate the skew:

$$\gamma_1 = \frac{\sum (r_i - \bar{r})^3 h_i \delta_i}{[\sum (r_i - \bar{r})^2 h_i \delta_i]^{3/2}}.$$

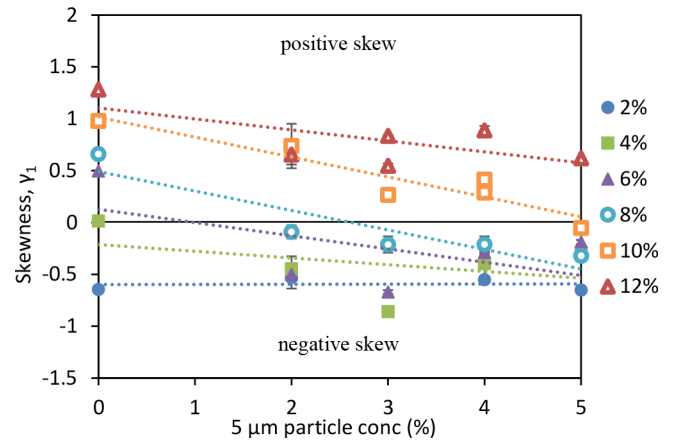


**Fig. 9.** Skewness of final deposit as a function of added concentration of  $5 \mu\text{m}$  particles into  $0.7 \mu\text{m}$  droplets containing PEO100 at various concentrations. Vertical error bars indicate the difference in skew between the two sides, averaged over three droplets. Uncertainties in PEO concentration are around 0.5%.

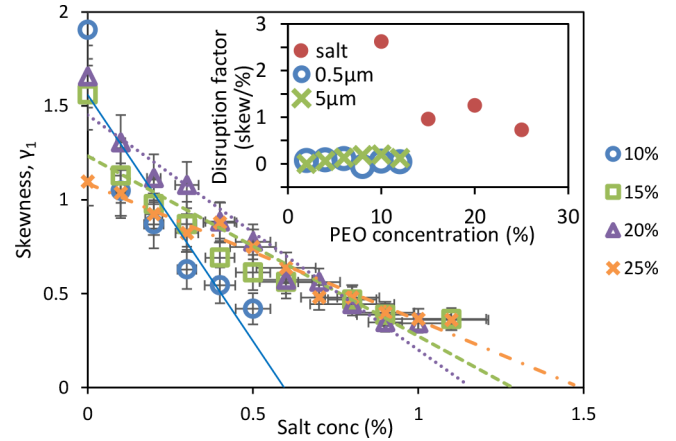


**Fig. 10.** Skewness of final deposit as a function of added concentration of  $\text{K}_2\text{SO}_4$  salt to droplets containing PEO200 at various concentrations. Vertical error bars indicate the standard deviation of skewness measured over 8 droplets. Uncertainties in PEO concentration are around 0.5%. The inset shows the disruption factor for each of the three systems as a function of PEO concentration, showing salt to have a larger effect than either size of particle.

For a given distribution, with  $r$  ranging from  $-R$  to  $+R$  we calculated the average of  $\gamma_1$  for  $0 < r < R$  for the right-hand side and  $-\gamma_1$  for  $-R < r < 0$  for the left hand side, the difference between the two halves characterising the uncertainty in the skewness.

The results for the skew analysis for all three systems are shown in figs. 8–10. Nearly all data sets show that the skewness of the deposit reduces with increasing additives, indicating that pillars become flatter. To quantify the effect of the additives, to a first approximation we fit the data for each value of  $c_0$  with a straight line, acknowledging that a linear dependency does not necessarily give the best agreement with the data, particularly for the salt, and that in one or two cases the skew may even increase

at higher concentrations. We recognise that there are limitations with this simple characterisation of the shape of the droplet deposit, which for example does not capture the observed segregation between particle and polymer, as this does not affect the overall height of the deposit.

We calculate a *disruption factor* to quantify this effect, equal to the negative of the slope of the best-fit lines. These are plotted in the inset to fig. 10 and emphasise that only a small quantity of salt is required to prevent pillar formation, with an average disruption factor around 1.4 skew/%. The disruption factors for the polymer plus particle systems are significantly less, 0.05 for the 0.5  $\mu\text{m}$  particles and 0.12 for the 5  $\mu\text{m}$  particles, with the smaller particles having less of an effect on the pillar formation process in agreement with the qualitative observations made from the droplet profiles.

## 5 Conclusions

We have investigated the effect of adding two different sizes of micro-particles to evaporating droplets of poly(ethylene oxide) solution. In pure solutions, PEO forms tall pillars above around 3% concentration and micro-particles typically leave ring-stain deposits. We have shown particles disrupt pillar formation and polymer disrupts ring-stain formation. Pillar formation is shifted to slightly higher polymer concentrations when large 5  $\mu\text{m}$  particles are added, but is less affected by the addition of 0.5  $\mu\text{m}$  particles. We also show preliminary evidence for particle segregation at higher polymer concentrations. This observation opens up the possibility of using PEO pillars to create functional pillars containing bespoke particles, with the confidence that the additional impurities, particularly small particles, are not likely to interfere with pillar formation. Potassium sulfate is known to reduce the affinity of PEO with water, causing the coils to collapse. By adding this salt to evaporating PEO droplets we see significant interference of the pillar formation. To quantify the different deposits observed we introduce the use of the normalised third moment of the deposit profile, commonly known as the skewness. We show that this simple parameter seems to capture the three deposit types, with a positive skewness for pillars, close to zero for flat deposits and negative skewness for ring-stains. The skew values can also be used to define a disruption factor which quantifies how effect different additives are at changed the shape of the deposit. We believe skewness has the potential to be very useful for characterisation of deposits in a wide variety of systems.

Y. Msambwa is funded by the Tanzanian government through the Dar Es Salaam University College of Education. D.J. Fairhurst would like to thank NTU for funding a research sabbatical. We also acknowledge useful discussions initiated through COST Action MP1106. We are very grateful to the referees for making several insightful comments.

**Open Access** This is an open access article distributed under the terms of the Creative Commons Attribution License (<http://creativecommons.org/licenses/by/4.0>), which permits unrestricted use, distribution, and reproduction in any medium, provided the original work is properly cited.

## References

1. R.D. Deegan, O. Bakajin, T.F. Dupont, G. Huber, S.R. Nagel, T.A. Witten, *Nature* **389**, 827 (1997).
2. R.G. Picknett, R. Bexon, *J. Colloids Interface Sci.* **61**, 336 (1977).
3. Yohana Msambwa, David J. Fairhurst, Fouzia Ouali, *Interfacial Phenom. Heat Transf.* **1**, 207 (2013).
4. Peter J. Yunker, Tim Still, Matthew A. Lohr, A.G. Yodh, *Nature* **476**, 308 (2011).
5. B.M. Weon, J.H. Je, *Phys. Rev. E* **82**, 015305 (2010).
6. H. Hu, R.G. Larson, *J. Phys. Chem. B* **106**, 1334 (2002).
7. H.B. Eral, D. Mampallil Augustine, M.H.G. Duits, F. Mugele, *Soft Matter* **7**, 4954 (2011).
8. X. Shen, C.M. Ho, T.S. Wong, *J. Phys. Chem. B* **114**, 5269 (2010).
9. Yanshen Li, Cunjing Lv, Zhaohan Li, David Quéré, Quanshui Zheng, *Soft Matter* **11**, 4669 (2015).
10. Khellil Sefiane, *Adv. Colloid Interface Sci.* **206**, 372 (2014).
11. L. Pauchard, C. Allain, *Europhys. Lett.* **62**, 897 (2003).
12. M.A. Rodríguez-Valverde, P. Ramón-Torregrosa, A. Páez-Dueñas, M.A. Cabrerizo-Vílchez, R. Hidalgo-Álvarez, *Adv. Colloid Interface Sci.* **136**, 93 (2008).
13. L. Wallstromm, K.A.H. Lindberg, *Wood Sci. Technol.* **29**, 109 (1995).
14. A.A. Collyer, *Phys. Educ.* **10**, 305 (1975).
15. Andre C. Dumetz, Rachael A. Lewus, Abraham M. Lenhoff, Eric W. Kaler, *Langmuir* **24**, 10345 (2008).
16. A. Abuchowski, T. Vanes, N.C. Palczuk, F.F. Davis, *J. Biol. Chem.* **252**, 3578 (1977).
17. Boualem Hammouda, *J. Polym. Sci. Part B - Polym. Phys.* **44**, 3195 (2006).
18. B. Hammouda, D.L. Ho, S. Kline, *Macromolecules* **37**, 6932 (2004).
19. M. Mohsen-Nia, H. Modarress, H. Rasa, *J. Chem. Engin. Data* **50**, 1662 (2005).
20. Stefan Bekiranov, Robijn Bruinsma, Philip Pincus, *Phys. Rev. E* **55**, 577 (1997).
21. Ana Saraiva, Ole Persson, Aage Fredenslund, *Fluid Phase Equilib.* **91**, 291 (1993).
22. Ni Ding, Eric J. Amis, *Macromolecules* **24**, 3906 (1991).
23. F.E. Bailey Jr., R.W. Callard, *J. Appl. Polym. Sci.* **1**, 56 (1959).
24. Ebba Florin, Roland Kjellander, Jan Christer Eriksson, *J. Chem. Soc. Faraday Trans. 1: Phys. Chem. Condens. Phases* **80**, 2889 (1984).
25. A. Dittmore, D.B. McIntosh, S. Halliday, O.A. Saleh, *Phys. Rev. Lett.* **107**, 148301 (2011).
26. David Willmer, Kyle Anthony Baldwin, Charles Kwartnik, David John Fairhurst, *Phys. Chem. Chem. Phys.* **12**, 3998 (2010).
27. Kyle Anthony Baldwin, Manon Granjard, David I. Willmer, Khellil Sefiane, David John Fairhurst, *Soft Matter* **7**, 7819 (2011).

28. Kyle A. Baldwin, Samuel Roest, David J. Fairhurst, Khellil Sefiane, Martin E.R. Shanahan, *J. Fluid Mech.* **695**, 321 (2012).
29. K.A. Baldwin, D.J. Fairhurst, *Colloid. Surf. A* **441**, 867 (2014).
30. Kyle Anthony Baldwin, David John Fairhurst, *Soft Matter* **11**, 1628 (2015).
31. Alvaro G. Marin, Oscar R. Enriquez, Philippe Brunet, Pierre Colinet, Jacco H. Snoeijer, *Phys. Rev. Lett.* **113**, 054301 (2014).
32. D.J. Fairhurst, *Droplets of Ionic Solutions*, chapt. 20 in *Droplet wetting and evaporation: from pure to complex fluids*, edited by David Brutin (Elsevier, 2015) pp. 295-314.
33. Willem J.P. van Enckevort, Jan H. Los, *Crystal Growth Design* **13**, 1838 (2013).
34. Noushine Shahidzadeh, Marthe F.L. Schut, Julie Desarnaud, Marc Prat, Daniel Bonn, *Sci. Rep.* **5**, 5908 (2015).
35. Dimitrios Mamalis, Vasileios Koutsos, Khellil Sefiane, Antonia Kagkoura, Michail Kalloudis, Martin E.R. Shanahan, *Langmuir* **428**, 39 (2015).
36. Yin-Chun Hu, Qiong Zhou, Hai-Mu Ye, Yu-Feng Wang, Li-Shan Cui, *Colloids Surf. A: Physicochem. Engin. Aspects* **428**, 39 (2013).
37. Yongjoon Choi, Jeongin Han, Chongyoun Kim, *Korean J. Chem. Engin.* **28**, 2130 (2011).